Dissertation for the Degree of Doctor of Philosophy

Development of 1 kW Class Novel HTS Rotating Machine Operated by Contactless Superconducting Field Exciter

Ji Hyung Kim

Faculty of Applied Energy System
Major of Electrical Engineering

GRADUATE SCHOOL
JEJU NATIONAL UNIVERSITY

February 2020

Development of 1 kW Class Novel HTS Rotating Machine Operated by Contactless Superconducting Field Exciter

Ji Hyung Kim

(Supervised by Professor Ho Min Kim)

A dissertation submitted in partial fulfillment of the requirements
for the degree of Doctor of Philosophy
2019. 12

This dissertation has been examined and approved

....

Dissertation director, Eel-Hwan Kim, Prof. of Electrical Engineering

Se Ho Kim..

Gaemyung Lee..

Tae Kuk Ko ....

Ho Min Kim..

Faculty of Applied Energy System
Major of Electrical Engineering
GRADUATE SCHOOL
JEJU NATIONAL UNIVERSITY

CONTENTS

ABSTRACT

Development of 1 kW Class Novel HTS Rotating Machine Operated by Contactless Superconducting Field Exciter

Name: Ji Hyung Kim
Affiliation: Faculty of Applied Energy System
Major of Electrical Engineering
Jeju National University
Dissertation Advisor: Ho Min Kim, Professor

This dissertation deals with the design, fabrication, and performance testing of a prototype machine for the world's first implementation of a new type high-temperature superconducting rotating machine (HTSRM), which is charged and operated by the application of a contactless excitation technique with a rotary-type HTS flux pump based on a permanent magnet (PM). HTS conductors can provide a large current stably without attenuation of transport current by exhibiting the inherent characteristic of “zero resistance” at higher temperatures and magnetic fields than low-temperature superconductors. Thus, HTS conductors are highly suitable for large-scale rotating machineries that require a high energy density, such as low-speed and high-torque rotating machines. Some examples of these are direct drive-type generators for off-shore wind turbines or propulsion motors for electric ships. Among HTS conductors, rare-earth barium copper oxide tape, which is a second generation (2G) coated conductor, provides high current density to rotor-field coils (FCs). This enables the manufacturing of machines with smaller volumes and lower weights compared with conventional rotating machinery of equal capacity. However, to achieve these objectives, electrical and mechanical connections are required between a direct-current (DC) power supply (PS) at room temperature and an FC at cryogenic temperature through a slip-ring/brush set and metal current leads, constituting the contact-type field excitation device. The use of such contact-type excitation device has the following technical limitations.

1. Mechanical noise and vibration in a slip-ring/brush set decrease the system-reliability, -economics, and -productivity owing to frequent maintenance requirement.
2. Thermal losses in metal current leads decrease the thermal stability of HTS coil owing to local temperature rise, and decease in system efficiency due to the increased

cryogenic cooling load and corresponding cooling cost.

3. External DC power sources decrease the system-efficiency, -economics, and -maintainability because of the use of additional DC PSs.

Therefore, the development of a contactless excitation system is required to fundamentally solve the abovementioned problems of conventional contact-type excitation system. Thus, a contactless superconducting field exciter (CSFE) with a 2G HTS flux pump is very promising for realizing a more economic HTSRM with high efficiency and stability for various industrial applications, compared with mechanical contact excitation.

By using this exciter, the slip-ring/brush set, metal current lead, and external PS in the contact excitation system can be eliminated by the onboard exciter system that can generate and supply its DC power inside the HTS rotor. The HTS flux pump applied as a field exciter can completely block the thermal intrusion from the conventional contact-type field excitation devices at room temperature and strongly suppress the internal Joule heating during current excitation. Thus, this apparatus enables high efficiency, strong reliability, and cost saving in superconducting rotating machine systems by removing the mechanical connection between the contact excitation system at room temperature. The general technical advantages of CSFE with the flux pump are as follows.

1. To provide high system-efficiency and -economics by omitting the metal current leads, slip-ring/ brush assembly, and external power source.
2. To provide high electrical and thermal stability of HTS FCs by perfectly eliminating heat intrusions through metal current leads.
3. To considerably reduce refrigeration cost by almost completely eliminating thermal losses in metal current leads.
4. To provide high-durability, -economic efficiency, -maintainability, and -productivity of system by perfectly eliminating noise and vibration from mechanical frictions at slip sing/ brush assembly.

Although this ability of HTS flux pump is expected to enable the commercial application of the HTSRM because of the abovementioned technical advantages, any practical demonstration of an HTS noncontact excitation system in rotary superconducting applications, specifically, HTS rotating machines, has not yet been conducted or reported on. Therefore, this dissertation presents a novel structure design for HTSRM equipped with CSFE. This exciter originates from the so-called rotating magnet-based HTS flux pump and is a noncontact PS for superconducting DC magnets. The novelty of the core technologies proposed in this dissertation and the corresponding advantages are as follows.

1. An integrated rotor structure with HTS field poles of rotating machine and DC power generation unit of CSFE; Increased cooling efficiency by simplifying cryogenic cooling

structure.

2. A structure that does not need additional rotor drive for generating time-varying magnetic field, which is required to excite DC power; Increased system-maintainability and -efficiency by simplifying system structure.
3. A structure with a cylindrical time-varying magnetic field supply unit at room temperature; Increased controllability of charged current by readily controlling the number of PMs at room temperature.
4. Novel structures (toroidal-head and magnetic back plate) and winding method (serial multiple winding with no junction) in CSFE rotor; Increased non-contact charge current within limited rotor size.

In dissertation, to verify and evaluate the feasibility of CSFE for practical operation of HTSRM, an HTS rotor with an integrated DC power source in field exciter and HTS FCs was designed, fabricated, and tested. The prototype HTSRM with 1 kW class capacity was mechanically, thermally, and electromagnetically designed and analyzed using numerical design process. The current pumping mechanism using external time-varying magnetic field was introduced to develop CSFE. The fabricated CSFE was experimentally tested on full-scale HTS FCs to analyze and evaluate the contactless current charge characteristics and its performances, respectively. The test results showed that although it was partially passive, current control is possible within a certain range by changing the number of PM, rotating speed, and air-gap length. In addition, the self-controlling behavior in charged current by CSFE was observed in the thermal transient state in which the liquid cryogen is insufficient, and it is considered that the reliability in current supply and the thermal stability in HTS FCs can be improved.

Finally, motor-generator setup was built based on the developed rotating machine system. A non-contact excitation performance was successfully confirmed in generator operation, and its charge behaviors were experimentally analyzed. The test results verified that the developed field exciter can improve the system efficiency by approximately 1% by considerably decreasing the excitation loss, compared with the field charge using metal current leads. Further, an output of 1086 W and field current of 101 A were achieved at a rated rotating speed of 400 rpm. Moreover, the design results from the 2D finite element analysis were 90% consistent with the experiment results under the same operating conditions. Total harmonic distortion of HTSG was measured at the 1% level, which experimentally confirmed that the pulsation of the non-contact charging current by the flux pump is not reflected in the output of HTSG. For charge behaviors of 100-A-class CSFE, it is suggested that the developed field exciter is suitable for applications requiring constant speed operation because it operates like a permanent magnet generator or motor within a certain speed range.

LIST OF FIGURES

LIST OF TABLES

LIST OF ABBREVIATIONS

AC	Alternating current
BSCCO	Bismuth strontium calcium copper oxide
CSFE	Contactless superconducting field exciter
Cu	Copper
CSC	Constant speed characteristic
CLC	Constant load characteristic
DAQ	Data-acquisition
DC	Direct-current
DPC	Double pancake coil
EM	Electro-magnet
EMF	Electromotive force
FRP	Fiber reinforced plastic
FC	Field coil
1G	First generation
GN2	Gas nitrogen
GFRP	Glass fiber reinforced plastic
HTS	High-temperature superconducting
HTSG	High-temperature superconducting generator
HTSM	High-temperature superconducting motor
HTSRM	High-temperature superconducting rotating machine
LN2	Liquid nitrogen
LTS	Low temperature superconducting
MRI	Magnetic resonance imaging
MMF	Magnetomotive force
MTPA	Maximum-torque-per ampere
M-G	Motor-generator
NMR	Nuclear magnetic resonance
OCC	Open circuit characteristic
PM	Permanent magnet
PCM	Persistent current mode
PS	Power supply
REBCO	Rare-earth barium copper oxide
RMS	Root mean square

2G	Second generation
SCC	Short circuit characteristic
SCR	Short circuit ratio
SMES	Superconducting magnetic energy storage
2D	Two-dimensional
3D	Three-dimensional
THD	Total harmonic distortion
VTHD	Voltage total harmonic distortion

Chapter 1. Introduction

1.1. Background and motivation of the study

Superconductivity exhibits two major properties, i.e., zero-resistance and perfect diamagnetism characteristics of a conductor, under particular critical properties governing superconductivity; critical temperature (T_c), critical magnetic field (H_c), and critical current density (J_c). Superconductivity is classified into two conductor applications, i.e., low-temperature superconducting (LTS) and high-temperature superconducting (HTS) conductors based on the boiling temperature of liquid nitrogen (77.2 K) [1].

LTS conductors are regarded as metallic superconductors. Generally, they exhibit superconductivity at low critical temperatures (below 30 K) and operate at 4 K level with liquid helium. They are made of a metal-based material; thus, it is easy to join conductors by heat treatment, which results in a long piece of conductor spool. Moreover, they exhibit high reliability in detection and protection against quench, i.e., “phase change to normal state,” because of fast normal zone propagation velocity caused by high thermal conductivity of conductor [2].

The LTS technology is reliable because of long-term research periods, efforts, and technical knowledge accumulation; thus, nuclear magnetic resonance (NMR), magnetic resonance imaging (MRI), particle accelerator, fusion power generation, and other such techniques, which are not possible with a conventional conductor technology (copper magnets), have already been realized using LTS magnets, thereby contributing significantly to medical and scientific technology. Considerable advancement in LTS technology has been achieved; however, it is difficult to apply in electric power applications of various industry fields because of its cooling cost with very expensive liquid helium [1]–[4]. LTS conductors are easy to manufacture because of the simplicity of the conductor structure, which makes it possible to fabricate a conductor with long piece length. This helps in decreasing the number of joints inside superconducting magnets, thereby resulting in decrement of joint resistance. It is possible to design and manufacture superconducting magnets that can operate in persistent current mode (PCM) without current decay. Generally, a level below 10^{-12} Ω is considered for the superconducting joint to operate in PCM [5], [6]. The initial charging is performed by an external power supply (PS) and metal current leads, and a steady state operation is performed in PCM through a switch changeover. Therefore, LTS magnets are successfully commercialized by their applications in NMR and MRI systems, which are recommended to operate in PCM to assure the homogeneity of the magnetic field.

HTS conductors are classified into two types; bismuth strontium calcium copper oxide (BSCCO) and rare-earth barium copper oxide (REBCO), which correspond to first generation

(1G) and second generation (2G) HTS conductors, respectively. HTS conductors exhibit superconductivity at relatively higher critical temperatures (above 90 K) and can operate at approximately 77 K level, which is achievable using inexpensive liquid nitrogen. Furthermore, it can operate in a relatively higher magnetic field than that of LTS conductors. These enable a developer to design and manufacture various application devices with high capacity, compact volume, light weight, and low cooling cost. As compared to LTS conductors, 2G HTS conductor (REBCO) exhibit attractive performances to sustain high current density in large external magnetic fields over a wide range of temperatures. They are able to realize ultra-high field magnets over 25 T for NMR, thermonuclear reactor, and so on; as well as for large-scale electric power applications, such as energy storage system, power cables, fault current limiters, transformers, and rotating machineries [7]–[13].

The 2G HTS technology a has very promising potential in various large-scale applications, such as medical, scientific, space, energy, and military fields; however, a few challenges in magnet operation still exist. One such challenge is the difficulty of PCM operation. A joint resistance of 2G HTS conductor (a level 10^{-9} Ω) is higher than that of LTS conductor (a level 10^{-12} Ω), thereby resulting making persistent current operation difficult or impossible. A 2G HTS conductor is a ceramic oxide; thus, it is manufactured in a multilayered structure of a composite material (in the form of a tape) to reinforce the brittle mechanical strength. This laminated structure expands the process and facilities for conductor manufacturing, thereby making it difficult to manufacture conductors with long piece length. Consequently, the maximum piece length of most 2G HTS wires that are currently commercialized is about 500 m level.

Therefore, in actual magnet applications, it is inevitable to join wires, which makes it difficult to operate in PCM because of increase in the joint resistance. Studies are being conducted to enable persistent current operation by reducing the joint resistance using joints between the superconducting layer and layer of 2G HTS conductor; however, in-depth research and technological advances are required for actual applications using 2G HTS magnet [5], [6]. Therefore, it is virtually impossible to operate 2G HTS magnets in PCM because of the above-mentioned disadvantages in the conductor structure and manufacturing.

The contact-type charging devices are limited to operate 2G HTS magnets in rotary and stationary applications because PCM operation is still impossible. To initially charge, compensate, and control the current or magnetic flux in an HTS magnet during the overall operation mode, the electrical and physical connection using the metal current leads is essentially required between HTS magnet at cryogenic temperature and the external PS at room temperature. This type of physical and electrical connection causes conduction and Joule-heating because of temperature difference between the cryogenic and room temperatures, and transporting current in current leads, respectively. Thus, heat transfer caused by thermal conduction and Joule-heating losses is inevitable, and they are always present and adversely affect the HTS magnet system. This is a common problem in both stationary and rotary power devices using HTS magnets. The use of this type of contact-type excitation device inevitably faces the following technical problems:

1. Mechanical noise and vibration in a slip-ring/brush set: These decrease the reliability, economic value, and productivity of systems because of frequent maintenance.
2. Thermal losses in metal current lead: These decrease the thermal stability of HTS coil by increasing the local temperature and decease the system efficiency by increasing cryogenic cooling load and corresponding cooling cost.
3. External direct-current (DC) power sources (PSs): These decrease the efficiency, economic value, and maintainability of systems because of use of additional DC PSs.

Fig. 1.1 shows the thermal loss estimations of various HTS rotating machines (HTSRMs) [14]−[16]. The thermal losses through the metal current lead were reported to be approximately 15%, 19%, and 28% of the total rotor losses of the 10 MW class HTS generator (HTSG) and 3 and 1.5 MW class HTS motors (HTSMs), respectively. These thermal losses decrease the thermal stability of the HTS magnet and increase the cooling capacity of a cryocooler for HTS magnet cooling, which means that the temperature increases and is unstably maintained in the heated HTS magnet.

The various thermal-anchoring technologies for cooling the metal current leads have been introduced to reduce the cooling load of the cryocooler and enhance the thermal stability of the HTS magnet [17]. Especially, the concept of cooling anchor can effectively cool the metal current leads, as shown Fig. 1.2 [18].

The technical concept of the cooling anchor is simultaneously chilling and supporting the current leads resulting from the direct coupling of the current leads with the cryogen return pipelines inside the HTSRM. Thus, the cooling anchors can minimize heat intrusion toward the HTS magnet, because it can prevent overheating of the current leads by conduction cooling from the returning cryogen. Technically, the difference between the use of this device and the conventional thermal-anchoring technique is the use of the returned vaporized cryogen as a cooling source.

By applying G10 cooling anchors, the maximum temperature in the HTS magnet was 10.594 K (25.46%), lesser than that without cooling anchors, as shown Figs. 1.2(c) and 1.2(d). In this case, the current lead loss was reduced by 68% as compared to that achieved without the cooling anchors. There are effective advantages of thermal-anchoring technologies on metal current lead; however, the thermal drawbacks of the contact-type excitation method, which deteriorates the technical and economic reliability of the HTSRM, still remain.

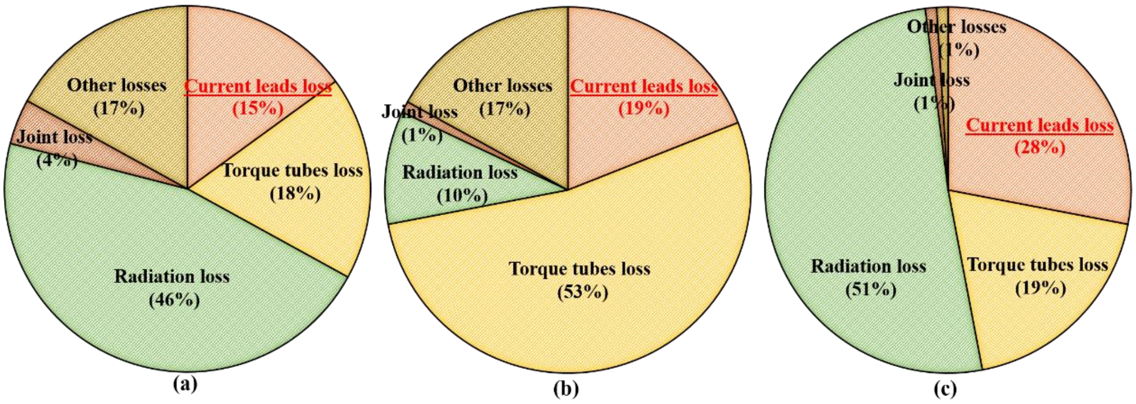

Fig. 1.1. Thermal loss estimation of various HTSRMs. (a) 10 MW class HTSG, (b) 3 MW class HTSM, and (c) 1.5 MW class HTSRM

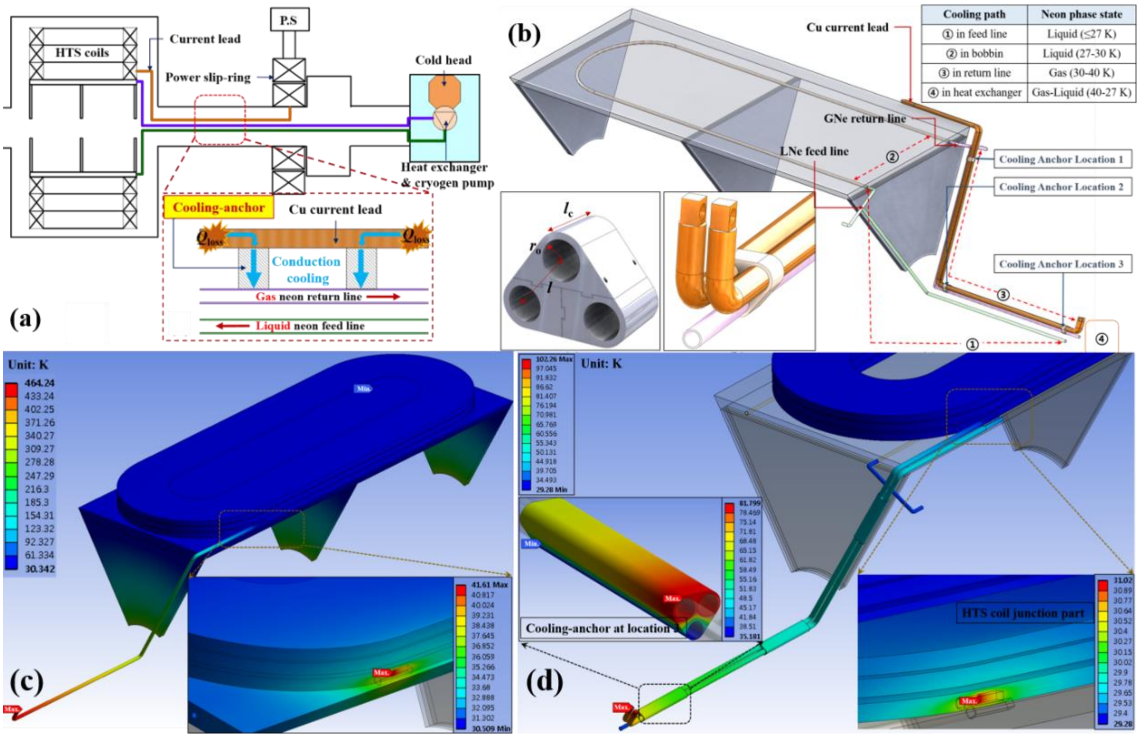

Fig. 1.2. Conceptual design of cooling anchor. (a) Schematic diagram of the HTSRM with the cooling anchor, (b) design of the cooling anchor, (c) temperature distribution without the cooling anchor, and (d) temperature distribution with the G10 cooling anchor

Furthermore, unlike superconducting magnet systems that operate in a stationary state, such as NMR, MRI, and superconducting magnetic energy storage (SMES), the rotating system, i.e., superconducting rotating machines, require not only metal current leads but also slip-ring assembly with brush, which deliver the transport current from DC PS in the stationary state to the HTS magnet in the rotary state.

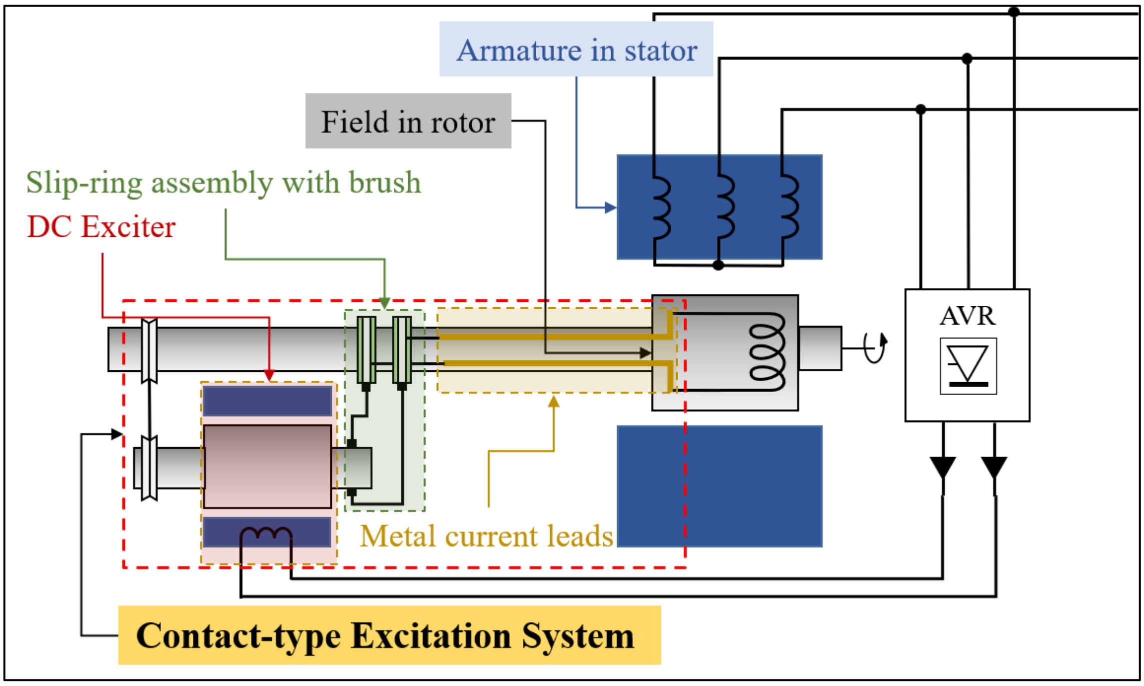

(a) Schematic diagram of the contact-type excitation system

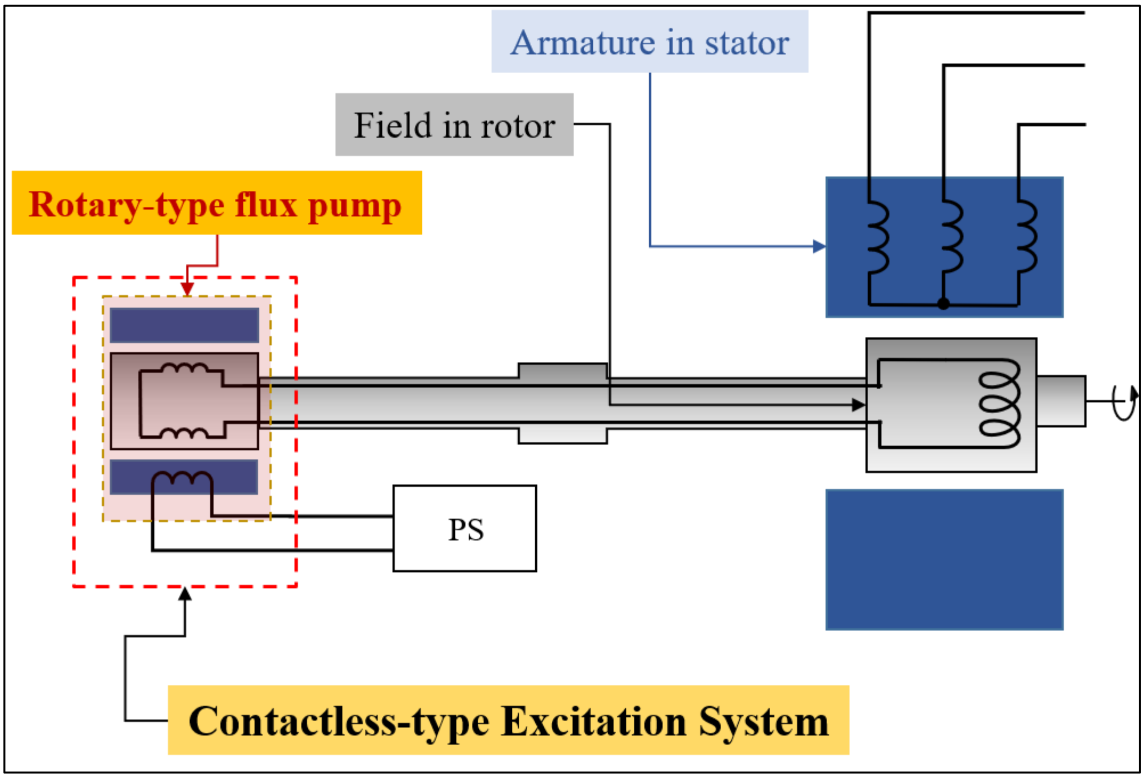

(b) Schematic diagram of the contactless-type excitation system

Fig. 1.3. Schematic diagrams of excitation system for the superconducting rotating machine

In other words, the HTS magnets in the rotor are charged by the contact-type excitation system, which is composed of metal current leads, slip-ring assembly with brush, and DC PS, as shown in Fig. 1.3(a). These physical excitation system causes severe mechanical problems, such as durability deterioration, noise and vibration generation, electrical arcing-fire because of mechanical friction between slip-ring and the brush, and the aforementioned thermal problems. Thus, it can economically harm the reliability, availability, maintainability of the rotating machine system in the commercialization operation. In particular, noise and vibration of the contact type excitation system are not suitable for electric propulsion ship systems that require silence, such as luxury cruise ships and warships.

Therefore, a technical alternative, which can complement the shortcomings of the contact-type excitation system, must be proposed to increase the possibility of commercialization of superconducting rotating machines.

1.2. Necessity and significance of the study

To fundamentally and qualitatively solve the problems of contact-type excitation systems in conventional HTSRMs, this dissertation proposes the novel concept of HTSRM and its world's first implementation. This novel idea introduces HTS contactless superconducting field exciter (CSFE) via "rotating-magnet-type HTS flux pump," to replace the conventional contact-type excitation system, as shown in Fig. 1.3(b). It is observed that the "HTS" in this dissertation refers to "2G HTS" for both HTSRM and CSFE. This HTS flux pump, which use DC voltage by Faraday's law and dynamic resistance concepts in superconducting circuit under time-varying magnetic field, is one of the superconducting power supplies and is classically used to wirelessly charge the superconducting magnet system operated in stationary states, such as NMR, MRI, and SMES.

An HTS flux pump applied as a field exciter can generate and supply its own DC power inside the HTS rotor. This ability can completely block the thermal intrusion from conventional contact-type field excitation devices at room temperature and strongly suppress the internal Joule heating during current excitation by eliminating the slip-ring/brush assembly, metal current lead, and external PS. These characteristics indicate that higher efficiency and stability can be achieved in HTS FCs as compared to those obtained with mechanical contact excitation. The general technical benefits of CSFE with HTS flux pump are as follows:

1. The thermal stability of HTS field winding is improved by eliminating the metal current leads that deliver conduction and joule-heating losses toward cryogenic temperature.

2. The refrigeration cost can be reduced by considerably reducing the total cooling loads of the cryogenic cooling system by completely eliminating the thermal losses in metal current leads.
3. The metal current leads, slip-ring/ brush assembly, and external PS are omitted, thereby improving the system efficiency and economic value.
4. The system durability is significantly improved by eliminating the noise and vibration caused by mechanical friction completely, thereby improving the economic efficiency by enhancing maintainability and productivity of system.

This type of flux pump has been actively applied in stationary superconducting applications; however, its practical demonstration on rotary superconducting applications (rotating machines) has not been conducted or reported on because the application of flux pumps on rotating superconducting FCs is technically more difficult than that of stationary superconducting magnets. The design of a flux pump structure, which should be integrated with a cylindrical rotor and should be electrically compatible with the HTS FCs, is a challenge that should be addressed to develop an optimized HTS rotor. Thus, a suitable flux pump design should be confirmed through practical development and testing to determine its applicability intuitively. Therefore, laboratory-scale hardware implementation is required to investigate the feasibility of using a CSFE as the field exciter of an HTS rotating machine.

1.3. Novelty of the study

The proposed and developed machine in this dissertation, is a small-scale prototype for an integrated system with HTSRM and CSFE, which is structurally connected to the same rotor shaft of the rotating machine. The HTS FCs are charged by DC power generation at the rotary part of the CSFE because of injection of time-varying magnetic field from PMs of the stationary part of the CSFE.

The originality of the core technologies applied for world’s first development of an HTSRM charged and operated by CSFE, and its corresponding benefits are as follows:

1. An integrated rotor structure with HTS field poles of the rotating machine and DC power generation unit of the CSFE: This increased the cooling efficiency by simplifying the cryogenic cooling structure.
2. A structure that does not require an additional rotor drive for generating time-varying magnetic field. This increased system-maintainability and efficiency by simplifying the system structure.

3. A structure having a cylindrical time-varying magnetic field supply unit at room temperature. This increased the controllability of the charged current by readily controlling the number of PMs at room temperature.
4. Novel structures (toroidal-head and magnetic back plate) and novel winding method (serial multiple winding with no junction) in the CSFE rotor. These increased the contactless charge current within the limited rotor size.

1.4. Outline of the study

The main research objectives of this dissertation are as follows:

1. To design and fabricate a small-scale prototype HTSRM equipped with CSFE.
2. To experimentally analyze the charging characteristics of HTS FCs using CSFE.
3. To experimentally verify the application feasibility of CSFE on the HTSRM system.

The major research contents and scope of this dissertation are described as follows:

1. Design and fabrication of the 1 kW class HTSRM.
    - The structure of the 1 kW class HTSRM was analytically and numerically designed and analyzed.
    - The electromagnetic characteristics of the 1 kW class HTSRM was numerically analyzed using the commercial FEM software.
    - The components of the 1 kW class HTSRM are fabricated and assembled together with CSFE.
2. Design, fabrication, and characteristic test of CSFE.
    - CSFE is empirically designed and fabricated considering a suitable structure and charging method for maximizing the charged current.
    - Current charge characteristics of HTS FCs are experimentally analyzed using developed CSFE.
3. Hardware implementation and performance test of the 1 kW class HTSRM.
    - The motor-generator (M-G) setup including the cryogenic cooling system was fabricated to demonstrate the feasibility of CSFE.
    - The noncontact current charge behaviors in HTS FCs are experimentally analyzed using the induced voltage characteristics of HTSRM.
    - The operational characteristic using CSFE are evaluated in test of generating power characteristic.
    - The application feasibilities of CSFE on HTSRM are investigated and discussed with the results of characteristic test.

This dissertation is organized based on the following research objectives and contents:

In Chapter 1, the background knowledge for the excitation system of HTSRM, necessity and significance of the proposed novel idea in this dissertation, i.e., contactless excitation system using 2G HTS flux pump, and major contents of the dissertation were described in detail.

In Chapter 2, the basic operational mechanism of a rotary-type 2G HTS flux pump was introduced and its operational characteristics for designing CSFE were investigated with a simple flux pump system governed for a superconducting R-L circuit. Moreover, research trends of the contactless excitation system with various type of HTS flux pumps were overviewed and their pros and cons were investigated. Finally, a novel structure of the HTS rotor combined with CSFE was proposed based on the above investigations, i.e., operational characteristics and technical pros and cons of other developments.

In Chapter 3, 1 kW class HTSRM, which employs 2G HTS race-track coils as rotor-field magnets, was numerically analyzed and designed based on the two-dimensional (2D) finite element (FE) method. The HTS rotor structure was designed considering mechanical and thermal characteristics. In particular, a salient pole structure for HTS FCs was optimized using parametric 2D FE simulations. The final structures and its design drawing were derived to fabricate a prototype machine and the electrical output characteristics of the prototype design were analyzed to estimate machine performance considering unexpected current charge performances of CSFE.

In Chapter 4, a salient field pole structure and four HTS coils were fabricated based on the design results achieved in Chapter 3. In addition, CSFE was empirically designed and manufactured based on proto-type research works. Further, a full-scale rotor assembly was preliminarily tested and its controllable currents excited by the contactless method were investigated to evaluate its application feasibility on variable speed operations.

In Chapter 5, the various core components of HTSG, such as rotor, stator, and cryogenic cooling system, were finally fabricated, assembled, and tested to configure the 1 kW class HTSG system. Further, the HTSG operating characteristics and performance were evaluated using the M-G test setup, which was built based on the developed rotating machine system. In the no load test of generator operation, the characteristics of the induced voltage of the HTSG were tested and measured. Moreover, a contactless excitation in HTS FCs was confirmed in generator operation and its charge and discharge behaviors were analyzed experimentally. Further, the HTSG output characteristics were tested and measured by performing experiments on the constant load and constant speed characteristics, respectively.

In Chapter 6, the results of this dissertation were comprehensively described. Moreover, the technical constraints of the developed excitation device were given, and possible solutions were proposed and discussed for further study.

Chapter 2. Novel Superconducting Field Exciter for HTS Rotating Machine

This chapter introduced the novel concept of HTSRM, wherein its HTS field winding is charged and operated by CSFE. First, the operating mechanism of 2G HTS flux pump based on the rotating time-varying magnetic field, which is the CSFE in this dissertation, was briefly described and the key operational parameters required to design, operate, and control were discussed to reflect their influence on HTSRM application. Further, various development cases, which are application of 2G HTS flux pump on the HTSRM system in progress or completed, were reviewed to investigate the feasible design and development of the novel rotating machine system integrated with HTS field winding and HTS flux pump. Finally, a conceptual structure of HTSRM integrated with CSFE were proposed considering the design issues discussed in relevant applications above. The key design issues of the novel structure proposed in this dissertation were described to highlight the novelty of this study.

2.1. Introduction of contactless excitation technique based on rotary-type HTS flux pump

2.1.1. Operational mechanism of rotary-type HTS flux pump

This subsection briefly introduced the operating mechanism of the 2G HTS flux pump using rotating time-varying magnetic field. Flux pumps are regarded as superconducting direct current (DC) power source (PS) by using the inherent characteristics of the superconducting phenomenon and they include functions in both power generation and conversion from alternating current (AC) to DC. Thus, it is possible to develop a high efficiency PS that can replace the power semiconductor device in a conventional PS. Moreover, the superconducting closed loop consists of a flux pump as a PS and a superconducting coil as a load can generate and transport DC power by itself; thus, it can eliminate the external PS, metal current leads, and slip-ring/brush set which are required for conventional technology, thereby resulting in improvement in the efficiency, stability, and economic value of power applications.

Traditionally, LTS flux pumps have been commercialized for magnetic resonance imaging and nuclear magnetic resonance applications requiring PCM operation. These type of LTS flux pumps explain its operating mechanism of contactless current charge through the “flux conservation law,” which states that the total flux passed into a non-resistive closed circuit does not change as long as the circuit remains in the non-resistive state. A persistent current is induced in the superconducting loop by the magnetic flux trapped in normal conducting zones, which are generated through repeated apparent phase changes from normal to superconducting states. Thus, they usually employ a type-I superconductor (Niobium) to trap the fluxes easily, and thus, induce the current because type-I superconductors have one critical field intensity (H_c) boundary with low strenth, thereby resulting in easy creation of normal zones using external magnetic field from permanent magnets (PMs) [19]−[23].

However, HTS consuctors are not only type-II superconductors with two H_c boundaries, i.e., lower H_c (H_{c1}) and upper H_c (H_{c2}), unlike type-I supercondoctors, but also the strength of H_{c2} is relatively high wherein PMs cannot generate the normal zones above H_{c2} easily. Thus, they are not applicable to the currnet charging mechanism of the LTS flux pump using certain phase changes from normal to superconducting states.

M. Sander and T. Coombs found that magnetization of yttrium barium copper oxide (YBCO) bulk can be produced without creating a normal zone within type-II superconductor, which has flux flow regime in a mixed state between H_{c1} and H_{c2}. [25], [26]. A 2G HTS flux pump based on rotating magnets was first proposed by C. Hoffmann et al. [23], [24]. They experimentally confirmed that HTS load coil could be energized by DC voltage, which is generated in flux flow regime of the 2G HTS conductor and by the time-varying magnetic field from the mechanically rotating PM. After Hoffmann's work, many relevant studies have actively followed their valuable contribution to fully prove and understand the operating behaviors and mechanism of 2G HTS flux pump based on rotating magnets [27]−[44].

The operating mechanism of the 2G HTS flux pump, which has been studied currently, can be described by DC open-circuit voltage (V_{dc}) and dynamic resistance (R_d) connected in series with the superconducting loop. Figs. 2.1(a) and 2.1(b) show the schematic diagrams that consist of HTS magnet and rotary-type 2G HTS flux pump, and its corresponding equivalent circuit to explain the fundamental principle of current charge by the 2G HTS flux pump, respectively.

The rotary-type 2G HTS flux pump consists of a 2G HTS wire in the stator part and one or more PMs that are arranged on the circumference of the rotor part. When the PMs rotate with constant S_r, the open circuit voltage (V_{oc}) is generated in 2G HTS wire in the stator by the time-varying magnetic field injected from rotating PMs.

Fig. 2.1(c) shows the evolution process from AC V_{oc} to DC V_{oc} (V_{dc}) with comparion at 300 K and 77 K. This generation of AC voltage is a general phenomenon that fully follows Faraday's law in superconducting state at 77 K as well as in normal state at 300 K. The 2G HTS flux pump is considered as a simple AC alternator while operating at 300 K because it ouputs AC voltage, which is directly governed by Faraday's law and then induced in the 2G HTS wire, thereby resulting in drive of AC current into the loaded HTS coil.

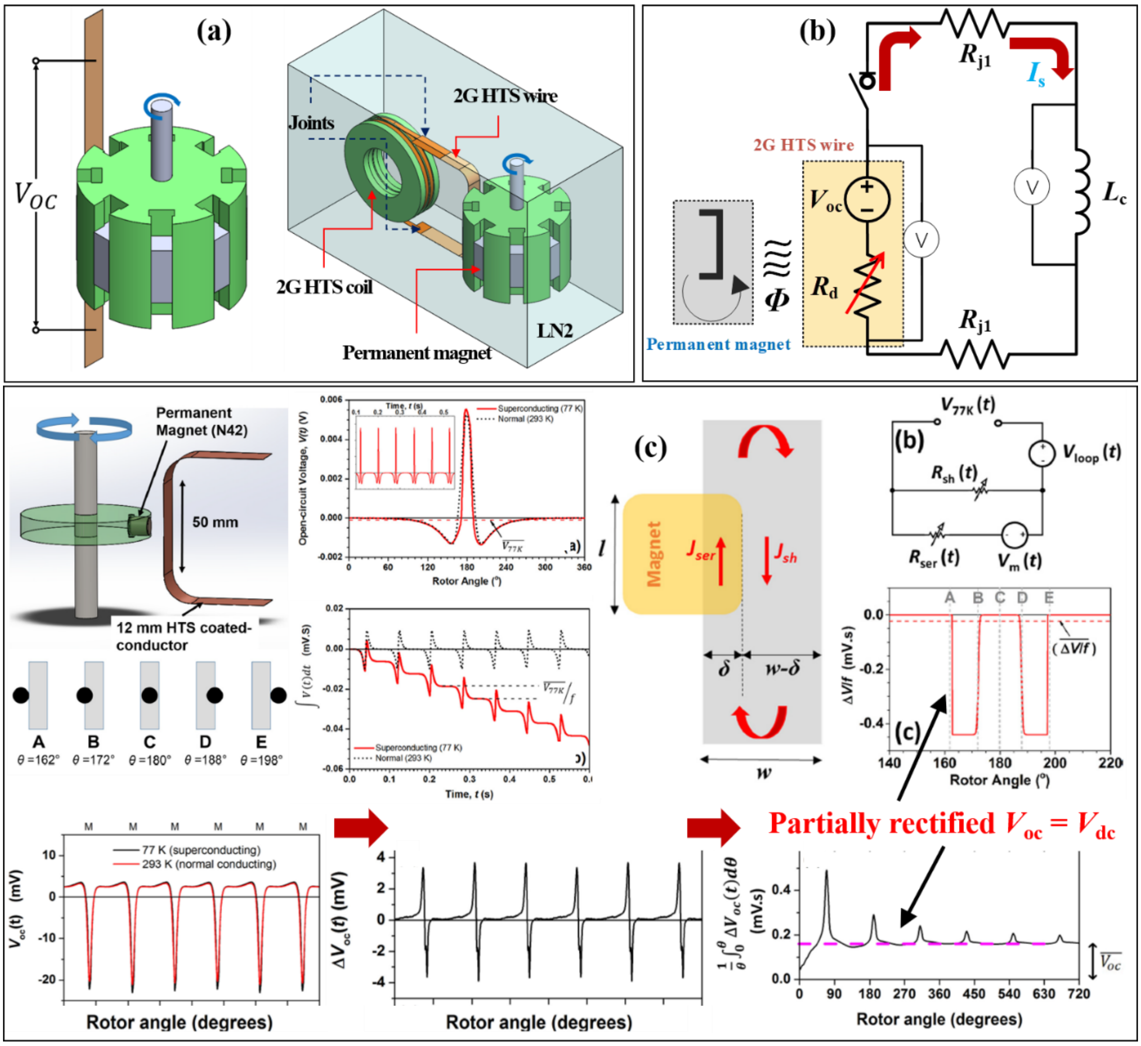

Fig. 2.1. Concept of 2G HTS flux pump based on rotating magnet. (a) 3D configuration, (b) equivalent R-L circuit, and (c) rectification process from AC V_{oc} to DC V_{oc} (V_{dc})

However, a 2G HTS flux pump exhibits the opposite output characteristic in superconducting state at 77 K. It is considered as a DC generator or DC PS, which are equiped with rectifier circuits, while operating at 77 K. The AC voltage is induced in open circuit of the 2G HTS wire (switch-off state in Fig. 2.1(b)); however, time-averaged AC voltage, i.e., DC voltage, is obtained as output connected in series with the HTS coil (switch-on state in Fig. 2.1(b)).

The transition of AC to DC is the fundamental source to drive the current in only the superconducting loop. The value of V_{dc}, which arises and increases because of time-averaging of the V_{oc} across 2G HTS wire for a cycle, is governed as follows [30], [32], [35], [44]:

$$V_{dc} = f_r \int_0^{\frac{1}{f_r}} V_{oc}(t)\,dt = f_r \int_0^{\frac{1}{f_r}} \Delta V_{oc}(t)dt \tag{2.1}$$

where V_{oc} (t) is the open circuit AC voltage according to elapsed time, which is defiend to -dΦ_{l}/dt. f_{r} is the rotating frequency of the flux pump and $\Delta V_{\mathrm{oc}}(t) = V_{\mathrm{oc(77K)}}(t) – V_{\mathrm{oc(300K)}}(t)$. V_{dc} is zero in normal conducting state at 300 K while V_{ac} is non-zero. However, V_{dc} is non-zero in superconducting state at 77 K while V_{ac} is zero. Through a series of studies by C. W. Bumby et al. [30], [32], [35], [44], it is reasonably believed that such rectification from AC to DC is a inherent characteristic of 2G HTS wire, which shows non-linear resistivity of the circulating eddy current path in the flux flow regime. This resistivity is anomalous according to the passing angle of the time-varying magnetic field from the rotating PM and acts as a shunt resistor periodically at a certain angle of PM, thereby causing partial rectification of V_{oc}, as shown in Fig 2.1(c). It is observed that a complete quantitative explanation of this behavior is still being investigated.

R_{d} represents the internal varying-resistance in the HTS flux pump, as shown in Fig. 2.1(b), and is a well-known characteristic of type-II superconductors. This varying resistance is caused by dissipative losses arising from flux flow because of motions of time-varying magnetic flux. When the magnetic field penetrates into the 2G HTS wire perpendicularly while interacting with the DC current transported in the flux flow regime, Lorentz force is produced, which acts on the penetrated magnetic flux, thereby resulting in motion of magnetic field pinned in mixture state of type II superconducting conductor. A magnitude of R_{d} is analytically presented as follows [45]:

$$R_{\mathrm{d}} = \frac{4aL_{\mathrm{e}}f_{\mathrm{r}}}{I_{\mathrm{c0}}}\left(B_{\mathrm{a}}+\frac{B_{\mathrm{a}}^{2}}{B_{0}}\right) \text{ at } B_{\mathrm{a}} \gg 2B_{\mathrm{th}} \tag{2.2}$$

where $2a$, L_{e}, B_{a}, and I_{co} are the width of 2G HTS wire, effective interaction length of the time-varying magnetic field with 2G HTS wire, magnitude of the applied magnetic field, and critical current of the 2G HTS wire without external applied magnetic field, respectively. B_0 is the relationship between I_{c0} and B_{a} within the HTS wire, which is obtained from Kim model and is governed by $I_{\mathrm{cm}} = I_{\mathrm{c0}} /(1 + B_{\mathrm{a}}/B_0)$ [46]. Here, I_{cm} is critical current of the 2G HTS wire with external applied magnetic field. It is observed that this equation is applicable when the B_{a} is larger than twice the threshold magnetic field (B_{th}) and its magnitude is proportional to f_{r} and B_{a} [27], [46].

The 2G HTS flux pump can be considered as a DC voltage source, which includes V_{dc} and R_{d} based on DC behaviors described above. If any load coil is connected with terminals of the HTS flux pump in series, the DC current flows into the closed electric circuit. When it begins to rotate the PMs, it indicates that the injection of time-varying magnetic field into 2G HTS wire in the stator, V_{dc} appears across the 2G HTS wire, thereby resulting in a gradual ramp up of the current in the loaded HTS coil to a saturation value. This type of flux pump can be equivalently modeled using a simple R-L electric circuit, as shown in Fig. 2.1(b) and is governed as follows [27], [28], [31] :

$$V_{\mathrm{dc}} = L_{\mathrm{c}}\frac{dI_{\mathrm{t}}}{dt} + I_{\mathrm{t}}R_{\mathrm{e}} \tag{2.3}$$

where R_e is total resistance in the superconducting loop and sum of R_d and joint resistance by soldering (R_j), i.e., $R_e = R_j + R_d$. L_c denotes the inductance of the HTS coil for electric load. DC transport current (I_t) that flows through the circuit and terminal voltage of HTS coil (V_{coil}), which are exponentially dependent on the elapsed time, are given as follows [28], [29], [31]−[33]:

$$I_{\mathrm{t}}\,(t) = \frac{V_{\mathrm{dc}}}{R_{\mathrm{e}}}\left(1 - e^{-\frac{R_{\mathrm{e}}}{L_{\mathrm{c}}}t}\right) = I_{\mathrm{sc}}\left(1 - e^{-\frac{R_{\mathrm{e}}}{L_{\mathrm{c}}}t}\right) \tag{2.4}$$

$$V_{\mathrm{coil}}\,(t) = L_{\mathrm{c}}\frac{\mathrm{d}I_{\mathrm{t}}}{\mathrm{d}t} = V_{\mathrm{dc}}\cdot e^{-\frac{R_{\mathrm{e}}}{L_{\mathrm{c}}}t} \tag{2.5}$$

where L_c/R_e denotes a time constant (τ) and determines the charge time of the ramped-up I_t. I_{sc} is defined as V_{dc}/R_e, which is the maximum available current that can be transferred into the loaded HTS coil by the HTS flux pump.

Fig. 2.2(a) shows the typical behaviors of I_t and V_{coil} of HTS coils charged by the HTS flux pump. The I_t and V_{coil} characteristics according to charge frequency and flux-gap were experimentally validiated by [27] and [28], respectively. Fig. 2.2(b) shows the calculation example for V_{coil} and I_t behaviors in the superconducting R-L circuit shown in Fig. 2.1(b). These simple calculations were referred from [28], assuming the case of pink curves (3 mm) in the right picture of Fig. 2.2(a); $V_{dc} = 2.3$ mV, $R_d = 511$ mΩ, $R_j = 0.88$ μΩ, and $L_c = 2.4$ mH. The maximum value of occurs at $t = 0$. However, I_t is at its minimum value, i.e., zero. Further, these values, V_{dc} and I_t exponentially increase and decrease, respectively, to a limiting saturation point for each value at $t = \infty$. This point is decided when the output voltage of the flux pump (V_{fp}) matches V_{coil}. For the steady state of the R-L circuit, V_{fp} measured across the flux pump is presented as follows:

$$V_{\mathrm{fp}} = V_{\mathrm{coil}} = V_{\mathrm{dc}} - I_{\mathrm{t}}R_{\mathrm{e}} \tag{2.6}$$

It is observed that the above relation is only satisfied for $I_t < I_{c,coil}$ because if $I_t > I_{c,coil}$, the HTS coil is no longer a pure inductor because of the rising additional voltage drop caused by flux flow resistance of the 2G HTS wire. Thus, Eq. (2.5) is no longer valid and V_{coil} should follow the

I-*V* relationship of the superconducting coil [32], [33], [44].

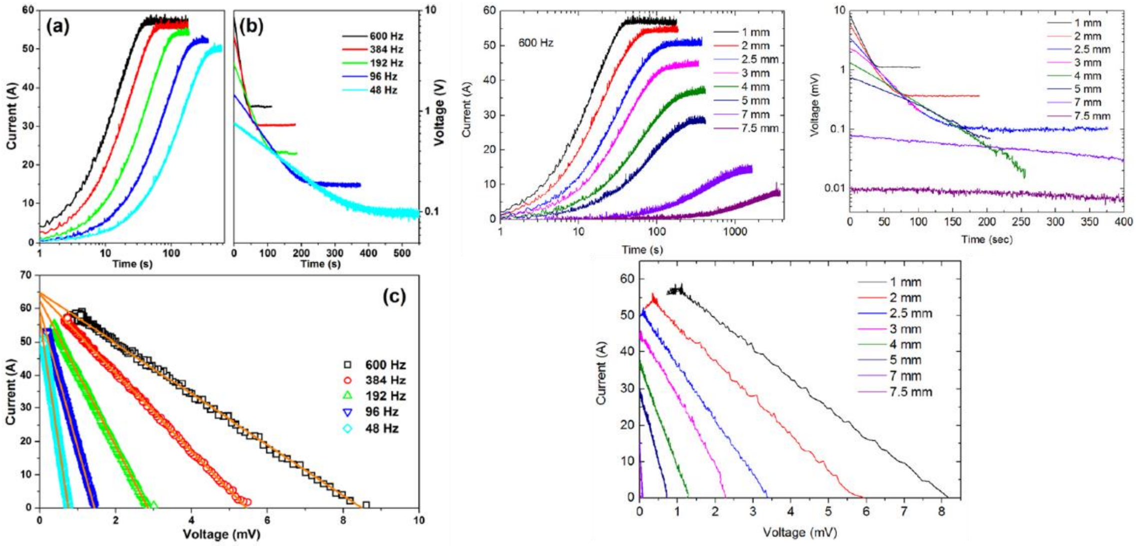

(a) V_t and I_t behaviors according to frequency (left) and air-gap (right)

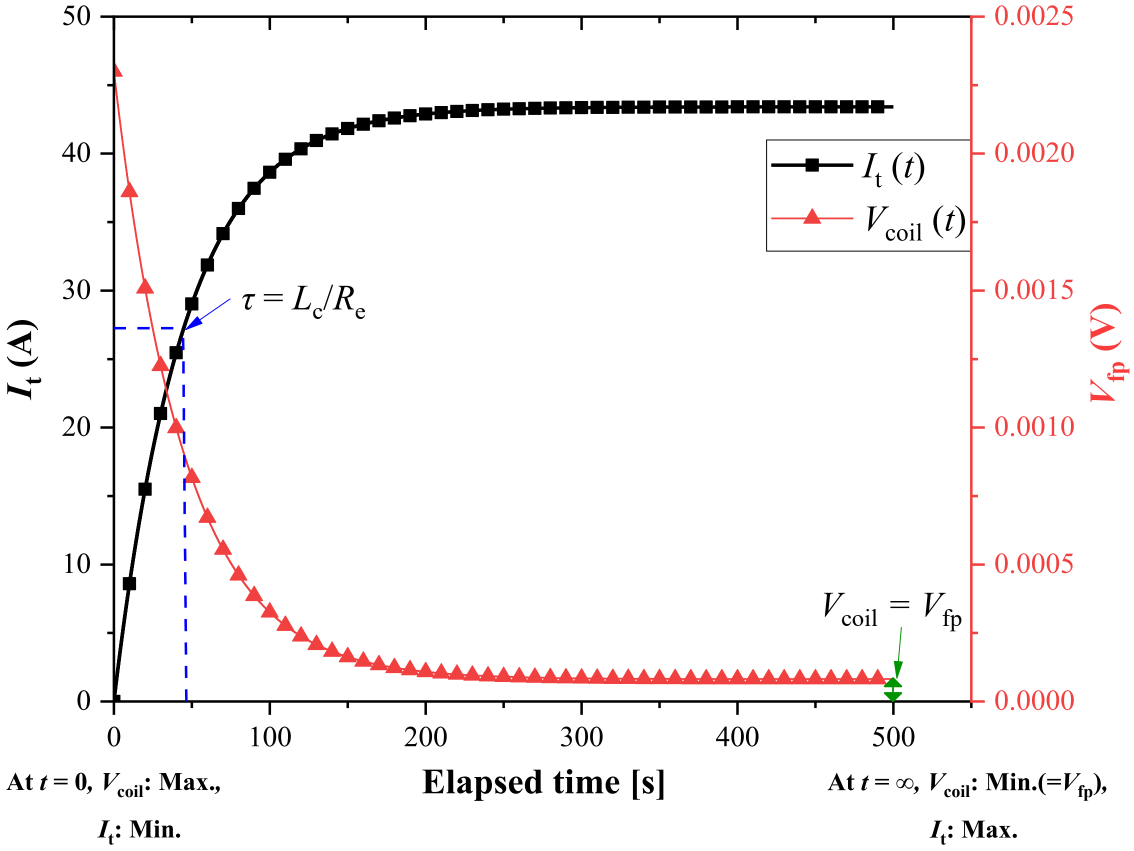

(b) V_{coil} and I_t behaviors of the superconducting R-L circuit according to elapsed time

Fig. 2.2. Typical behaviors of V_t and I_t of HTS coils charged by HTS flux pump

2.1.2. Operational characteristic of rotary-type HTS flux pump

Fig. 2.3 shows a simple relationship between the design and control parameters of the 2G HTS flux pump based on time-varying rotating magnets. It observed that all denotaions for Fig. 2.3 are as follows:

- V_{dc}: time-averaged DC voltage
- I_s: saturation current
- R_e: effective resistance
- R_d: dynamic resistance
- R_j: joint resistance
- Φ_l: linkage flux
- f_r: charge frequency
- B_m: magnetic fluxdensity of PM
- g_a: air-gap beween rotor and stator
- m_p: magnetization property
- t_e: charging time
- A_c: cross-area passing Φ_l
- n_c: the number of 2G HTS wire
- T_h: type of 2G HTS wire
- S_r: rotating speed
- n_p: the number of PM
- n_j: the number of joint
- A_j:cross-area of joint
- L_c: load coil inductance
- N_c: the number of turns in coil

It focuses on relatively higher I_s and faster t_e as the key parameters for design and control of rotary-type flux pump. For maximizing I_s, first more higher V_{dc} is considered and it is achieved by increasing ①Φ_l and ②f_r. They are critically effective for generating V_{dc} and quantification in its magnitude, because V_{oc} is governed by Φ_l and f_r, i.e., $V_{oc} = L_c \times d\Phi_l /dt$ and $V_{dc} = f_r \Delta\Phi_l$. The methodological considerations to increase Φ_l and f_r are as follows:

ⓐ↑B_m: Using a very strong permanent magnet to increase the penetrating Φ_l by injecting strong B_m. A weak Φ_l formed by a relatively low B_m is blocked in the 2G HTS wire by the screening current.

ⓑ↓g_a: Decreasing the flux air gap to as small as possible to increase the penertrating Φ_l by reducing the leaked Φ_l. A weak Φ_l formed by a relatively long air gap is blocked in the

2G HTS wire by the screening current.

ⓒ↑m_p: Using iron material in the flux pump structure and increasing the magnetization characteristic of iron core to increase the penetrating Φ_l by reducing the reluctance in the magnetic path. It is observed that iron loss should be carefully considered because V_{dc} decreases because of energy loss in iron material at a relatively higher f_r [31],[34].

ⓓ↑A_c: Expanding the cross area passing PMs to increase the penetrating Φ_l by using a 2G HTS wire with wide width, i.e., 12 mm width [47]. Moreover, 12 mm width is effective for maximizing I_s because it is restricted by the I_c of the 2G HTS wire.

ⓔ↑n_c: Increasing the number of 2G HTS wires as much as possible within a limited space to increase the number of V_{dc} sources by multiple winding of the 2G HTS wire. It seems to have an effect similar to that of ⓓ.

ⓕ T_h: Using a non-coated 2G HTS wire by metal stabilizer to eliminate the eddy current loss occuring in metal stabilizer [27]–[28], [34].

ⓖ↑S_r: Increasing f_r directly to increase the change in time-varying Φ_l per cycle by increasing the rotating speed of PMs.

ⓗ↑n_p: Increasing f_r (= (n_p × S_r)/60) to increase the change in time-varying Φ_l per cycle by increasing n_p in the rotating part.

A much smaller R_e is considered for maximizing I_s, which can be achieved by decreasing ③ R_d and ④ R_j.

ⓘ↓f_r, ⓙ↑I_c, and ⓚ↓B_m : Decreasing, increasing, and decreasing f_r, I_c, and B_m, respectively to reduce R_d in the flux flow regime when PMs pass across the 2G HTS wire. R_d is governed by Eq. (2.2).

ⓛ↓n_j and ⓜ↑A_j: Decreasing and increasing n_j and A_j, respectively to reduce R_j by winding the2G HTS wire in series connection and expanding overlapped area between the two conductors.

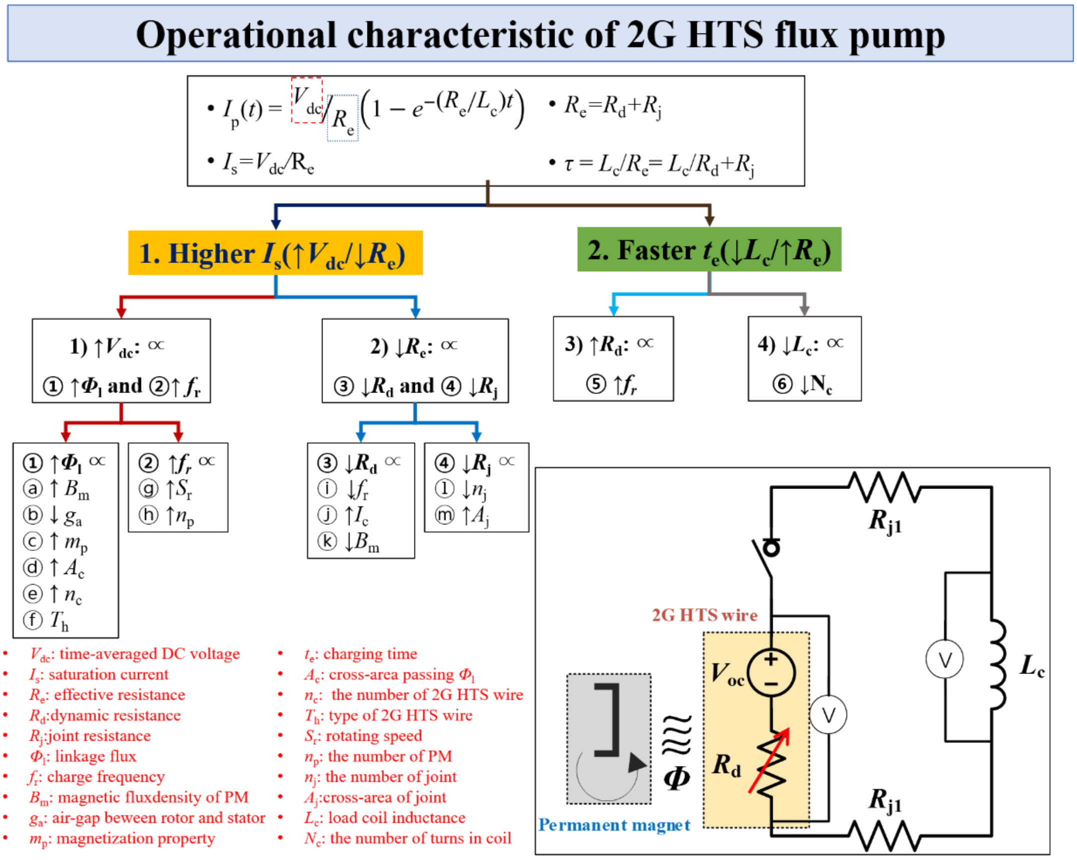

Fig. 2.3. Relationships in design and control parameters of the HTS flux pump based on a rotating magnet

For minimizingthe t_e, more higher R_d and lower L_c are considered, and this can be achieved by increasing ⑤ f_r and decreasing ⑥ N_c, respectively. These parameters are critically effective for decision on ↓τ (=↓L_c/↓R_e) of the superconducting circuit. Here, R_j is constant; thus, R_e is dependent only on R_d while operation. The methodological considerations to realize faster t_e are as follows:

⑤ ↑f_r: Increasing S_r and n_p to increase R_d, which is proportional to f_r as presented in Eq. (2.2), thereby resulting in decrease in τ (=L_c/R_e) [27]. The charged current is saturated at maximum value; thus, the increase in R_d because of increase in f_r speeds up t_e. However, for a certain range of increased f_r, the magnitude of R_d increases non-linearly and sharply, thereby resulting in a decrease in charging current [33]. In addition, the losses dissipated at rapidly increased R_d reduce the efficiency of the flux pump.

⑥ ↓N_c: Decreasing L_c to reduce t_e by decreasing N_c. HTS coils with the smallest possible inductance while satisfying its performances can reduce t_e. However, it is very passive parameter because this is mostly dependent on design of HTSRM.

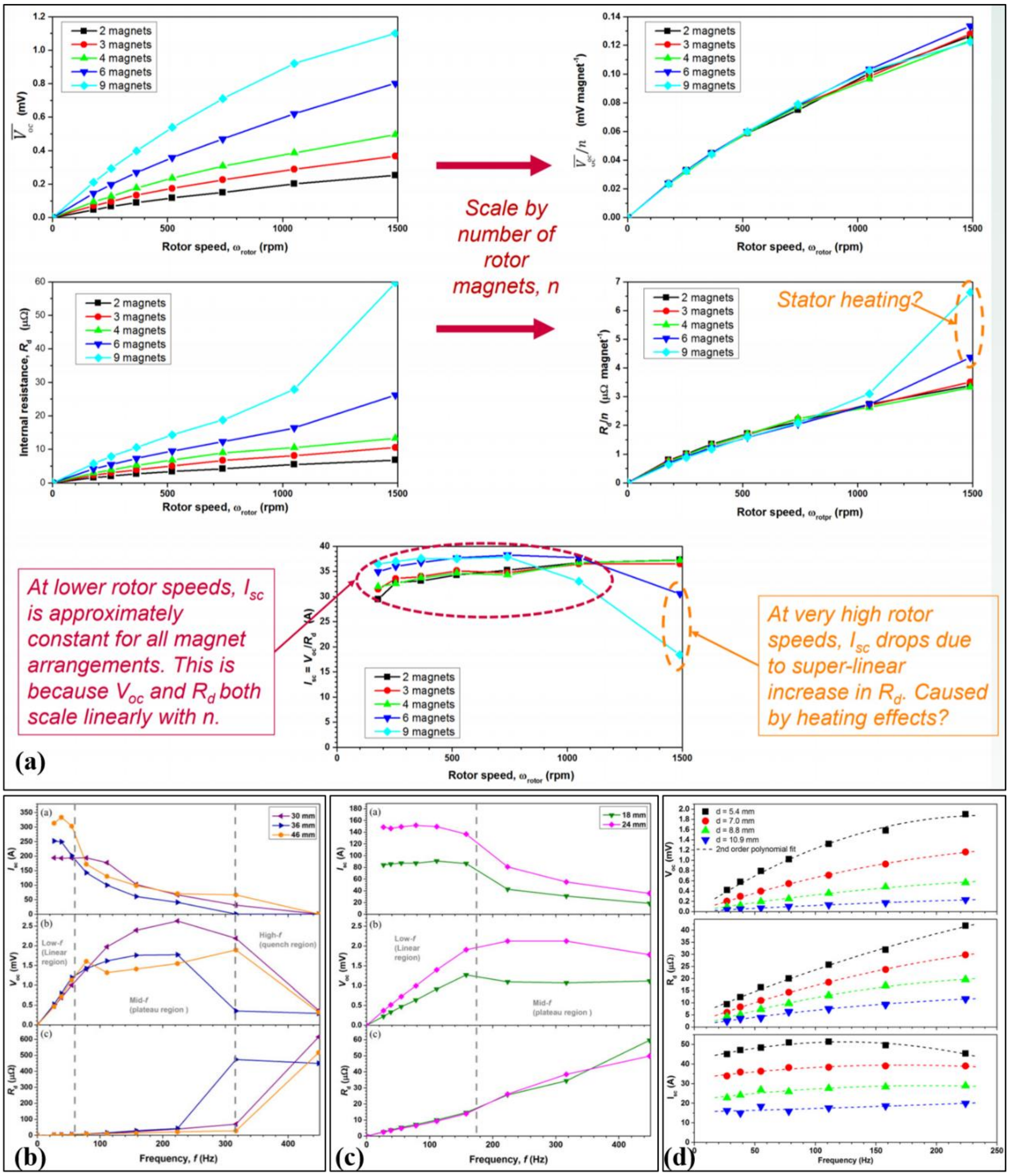
Scale by number of rotor magnets, n

Stator heating?

At lower rotor speeds, I_{sc} is approximately constant for all magnet arrangements. This is because V_{oc} and R_d both scale linearly with n.

At very high rotor speeds, I_{sc} drops due to super-linear increase in R_d. Caused by heating effects?

Fig. 2.4. Anomalous curves of I_{sc}, V_{oc}, and R_{d} versus f_{r} studied from (a) “Optimizing rotor speed and geometry for an externally-mounted HTS dynamo,” (b) and (c) “Impact of stator wire width on the output of a dynamo-type HTS flux pump,” and “Development of a brushless HTS exciter for a 10 kW HTS synchronous generator”

As a summary on design parameters, valuable precautions are investigated for design and control of the 2G HTS flux pump. It should be noted that the increments in V_{dc} and R_{d} are generally almost constant with equal f_{r}; thus, the charging current remains nearly constant at a lower value of f_{r}, which increases it slightly, as shown in all sub-images of Fig. 2.4, thereby indicating that

I_s is determined by V_{oc}/R_d and its magnitude is independent of the f_r at lower S_r of flux pump. However, it shows that I_s tends to decrease at higher f_r because of saturaltion or decrease in V_{dc} and sharp increase in R_d at higher f_r, especially, as shown in Figs. 2.4(b) and 2.4(c). Such anomalous behaviors are reasonably expected to be caused by eddy currents ,which generate heat loss in iron structures and 2G HTS wire, thereby resulting in reduction in both V_{dc} and R_d by decreasing the Φ_l and I_c values, respectively. Therefore, f_r is carefully decided considering available S_r of the flux pump [29], [33], [44], [48]. Moreover, it is considered that the only controllable parameters during device operation are S_r, g_a, n_p, and B_m in the PM. The remaining parameters are passive parameters that are fixed when designing the devices.

2.2. Development trend of contactless excitation technique

This subsection introduces several researches and developments on HTSRM excited by contactless excitation techniques, i.e., various types of HTS flux pump. The key-design technologies applied to developments in progress were investigated and analyzed to design a novel and suitable structure for the rotating machine integrated with CSFE.

The research and development of Type-II HTS flux pump using external time-varying magnetic field have recently been started. However, till now the research scopes are mainly limited to investigation of current pumping mechanism and the analysis of basic characteristic [27]−[28], [30]−[36]. The several feasibility studies have been attempted for practical application on superconducting devices, but this has also been limited to application for the superconducting magnets operating in a stationary state [49]. Moreover, a few studies have been conducted to excite the superconducting magnets which is operated in a rotation state, such as field windings in synchronous rotating machine. The ongoing or completed R & D in worldwide have been investigated and their key-techniques were analyzed. Further, the pros and cons as well as their key parameters of corresponding technologies were discussed through own interpretation, which are summarized in Table 2.1.

The R & D group in Sichuan University of china has been successfully carrying out a feasibility study for the development of a 16.9 kW class HTS synchronous motor using the HTS flux pump. So far, only the design and analysis of the motor system and characteristic experiment for the small-scale flux pump have been conducted in [50]−[52], respectively. Currently, the demonstration of this machine still works in progress. Therefore, they officially present the results of design and analysis of HTSM. The electromagnetic characteristic of HTSM was analyzed using 2D FEM and thermal loss of HTSM was estimated by analytical calculation.

They considered the linear-type flux pump using travelling magnetic wave to excite HTS field winding in rotor, as shown in Fig. 2.5(a). The four flux pumps were used to charge four field-poles. In other words, a unit field-pole can be individually excited and controlled by a flux pump module. These flux pumps are embedded in the rotor thermal shield together with the HTS field winding. This type of installation is possible to increase the saturation current I_s by minimizing physical gap between flux pump and HTS wire, as shown in Fig. 2.5(a). The four HTS FCs were cooled to 30 K by conduction cooling using first stage of cryocooler and excited to be 200 A through the HTS flux pump, which is cooled to 65 K by second stage of cryocooler.

In an international conference on magnet technology 26 (2019), they reported results on design, fabrication, and test of full-scale HTS racetrack coil as shown in Fig. 2.5(b). A no-insulation type racetrack coil was successfully charged by rotating magnet HTS flux pump at 77K and its current was saturated to 48.3 A with current ramp-up speed of 0.01923 A/s [53].

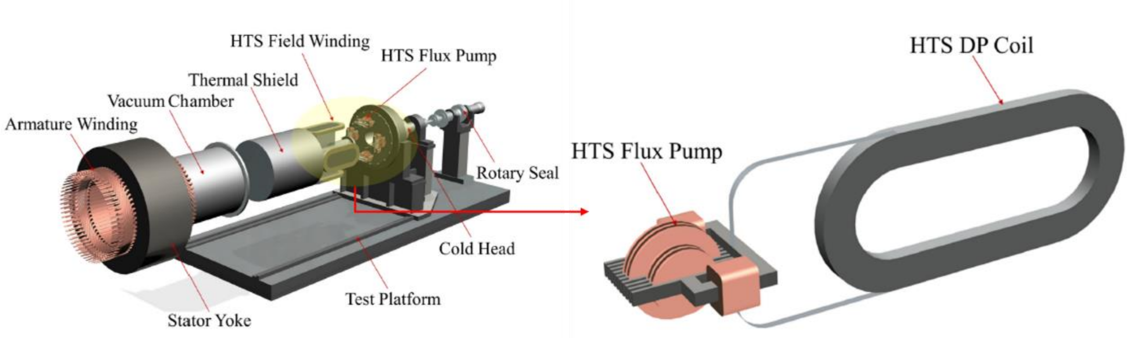

(a) 3D configuration diagram

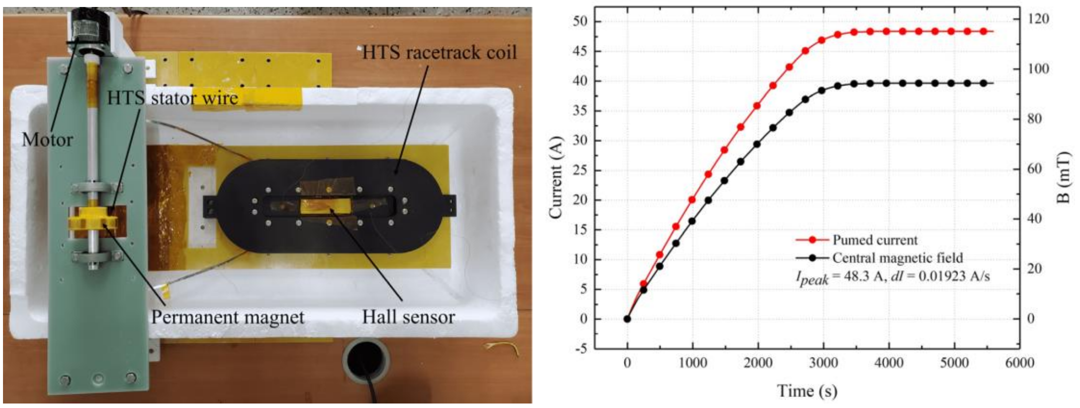

(b) Contactless charging experiment and results

Fig. 2.5. Schematic diagram of the 16.9 kW class HTS synchronous motor using linear-type HTS flux pump in Sichuan University

The linear-type flux pump using electromagnets (EMs) enables us to easily and freely charge and control the current of HTS field winding without any mechanical rotation of the flux pump.

However, an additional PS is required to operate the EM in linear-type flux pump. If own PSs, such as a battery or small-alternator, is not equipped inside the rotor, this once again brings the technical shortcomings, which must supply DC power to the EMs via a conventional contact excitation system consisting of current leads, slip ring, brush, and DC PS. In addition, Joule heating in EMs can increase the cooling capacity of the HTS rotor. Only a single superconducting wire is magnetically coupled to the HTS flux pump, as shown in Fig. 2.5(a); thus, the quasi DC voltage source is generated in only one point. Therefore, the charging efficiency of this structure may be lower than that of flux pump with multiple quasi DC voltage sources in series HTS wire.

The collaborative R & D group in Victoria University of Wellington and Auckland University of Technology in New Zealand and Changwon National University in S. Korea has successfully completed the design research for a 10 kW HTSG integrated with rotating-type HTS flux pump [29], [37], [54]. Fig. 2.6(a) shows configuration of their design for 10 kW class HTS synchronous generator and field exciter based on HTS flux pump.

The stator of flux pump, which generates the quasi DC voltage, is positioned only inside the rotor cryostat and is cooled at 75 K by conduction from cryogenic rotor through thermal links. Moreover, the rotor of flux pump including the several PMs is located at outside of rotor cryostat and independently rotated by external motor drive, resulting in active controlling the excitation frequency [29]. The value of field current (I_f) is set at 85 A at 30 K using pumping of liquid neon from external cooling system. They investigated excitation performances of full-scale HTS FCs using experiment results on small-scale prototype of rotating-type HTS flux pump. In particular, the required parameters for designing full-scale exciter, such as total resistance in superconducting loop, power loss, and charging time, were calculated in [29]. It is expected to decrease saturation current caused by increase in joint the resistance because of the parallel joint of HTS flux pump with metal bus-bar. The charging reliability may be deteriorated because of non-uniform conduction cooling using temperature gradient from cryogenic rotor, a reliability verification on charging performance is considered for the practical demonstration.

In relevant research [37], various characteristics of 10 kW class HTSG were numerically analyzed using field current input data achieved from protype experiments. Currently, the demonstration test bed is under construction for the 10 kW HTSG with an HTS flux pump exciter. In addition, the contactless current charge of a full-scale HTS FC was experimentally tested and its results were reported at an international conference on magnet technology 26 (2019), as shown in Fig. 2.6(b) [54]. The value of I_f is charted for about 6 h and finally saturated at 35 A with T_{op} = 77 K, S_r = 2500 rpm, and g_a = 7 mm.

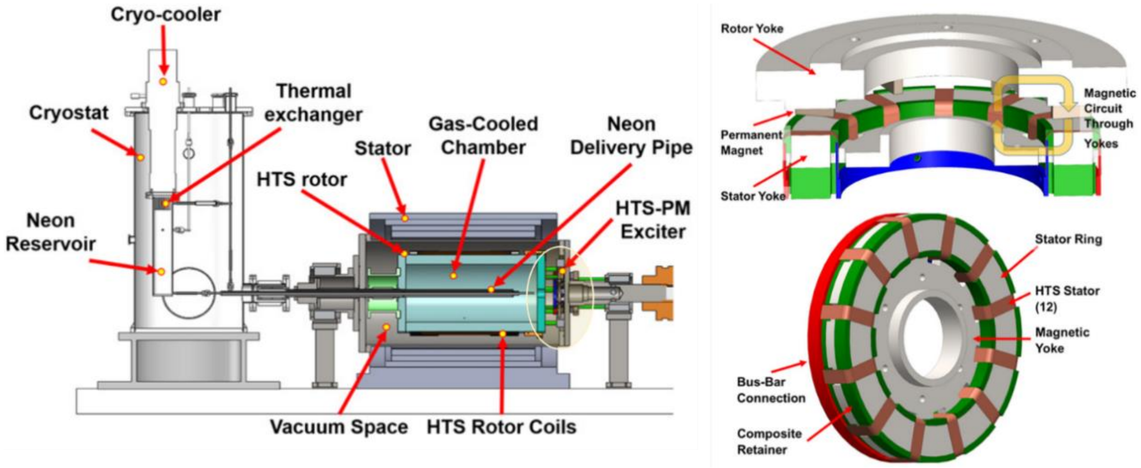

(a) 3D configuration diagram

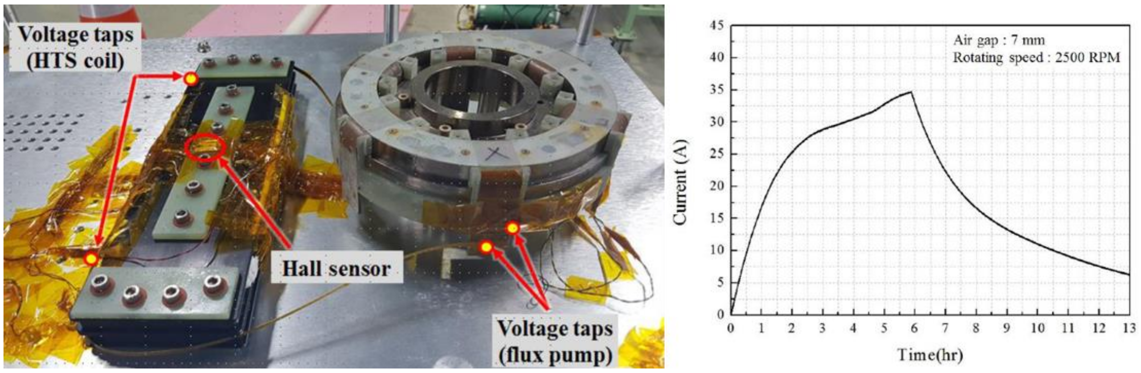

(b) Contactless charging experiment and results

Fig. 2.6. Schematic diagram of the 10 kW class HTS synchronous generator using rotating-type HTS flux pump in Victoria University of Wellington, Auckland University of Technology and Changwon National University

The R & D group in Changwon National University of S. Korea has successfully completed the design research for a 12 MW class HTSG for wind turbine [55], [56]. Structurally, each HTS FC is modularized by a cryostat, as shown in Fig. 2.7. They considered the rotating-type flux pump using travelling magnetic wave, which is similar structure to the application in 10-kW-class HTSG discussed in sub-chapter 2.2.2. The stator of flux pump is only positioned inside the rotor cryostat and cooled by conduction through connection with HTS FC. Moreover, the rotor of flux pump which includes the several PMs is located at rotor cryostat outside. When the generator rotor is rotated by movement of turbine blades, the PMs in flux pump rotor can be rotated by reaction force generated between bilateral circular gears, as shown in Fig. 2.7. Therefore, HTS wires in the flux pump stator are subjected to time-varying magnetic field. The frequency of the time-varying magnetic field is constantly determined by the generator rotation speed, i.e., the constant gear ratio. The electromagnetic characteristic was analyzed by three-dimensional (3D)

FEA to design the flux pump. The charging and discharging times for full-scale HTS filed coil were estimated with prediction of R_d of flux pump. It is assumed that 14 and 45 h will be required to charge and discharge the current of 317 A, respectively.

In the design of a flux pump stator, the use of multiple HTS wires generate multiple quasi DC voltages and thereby it can help to enhance the performance of saturation current in flux pump. However, the parallel connection of multiple HTS wires with metal bus-bar may reduce the maximum saturation current because of relatively higher R_j in superconducting loop than that of serial connection. The flux pump stator is indirectly cooled through conduction heat-transfer from HTS FCs. The un-uniform or -stable cooling conditions can cause the performance degradation of saturation current in flux pump. Further, use of iron core and metal bus bar encourage this because of additional thermal losses, i.e., iron and ohmic losses. In the design of flux pump rotor, the rotation of flux pump that use mechanical gears may lead to low reliability and maintainability because of its mechanically complicated configuration. If control of charged current is considered, it may be extremely passive or impossible because frequency of time-varying magnetic field, i.e., source of quasi DC voltage, can be not continuously changed because of its constant S_r. Moreover, individual charge structure may cause unbalanced current charge in each modular HTS FC because of differences in manufacturing, operating, and joining conditions of the HTS flux pump. Consequently, any demonstration of designed flux pump exciter has not been conducted till now for the practical application of a few MW class HTSG system.

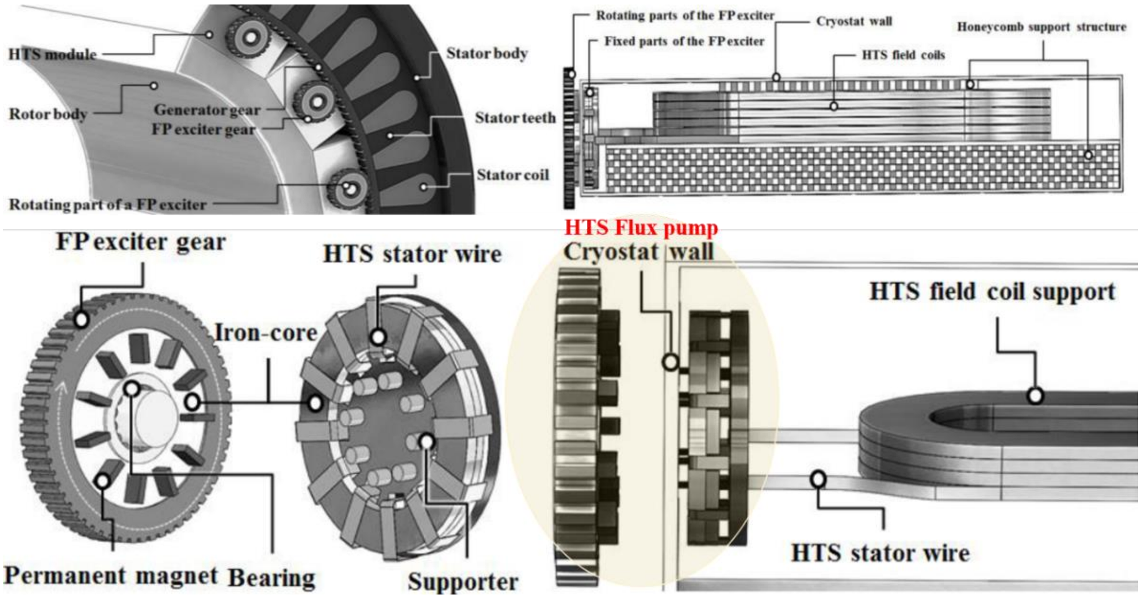

Fig. 2.7. Schematic diagram of the 12 MW class HTS synchronous generator using rotating-type HTS flux pump in Changwon National University

Table 2.1. Design features of HTS rotating machine equipped with the various type HTS flux pump

Parameters	**Sichuan University**	**Victoria and Changwon National Universities**	**Changwon National University**	**Jeju National University**
Cooling method	Conduction cooling using 2nd cryocooler	Conduction cooling using LNe	Conduction cooling using 2nd cryocooler	Bath cooling LN2
Operating temperature	30 K in field winding /65 K in flux pump	30 K in field winding /75 K in flux pump	20 K in field and flux pump	77 K in field and flux pump
HTS flux pump-type/-arrangement	Linear-type with EMs /Axial to F.C.	Rotating type with PMs /Axial to F.C.	Rotating type with PMs /Axial to F.C.	Rotating type with PMs /Radial to F.C.
Connection of flux pump to field winding	Single exciter to single FC	Single exciter to several FCs	Single exciter to single FC	Single exciter to several FCs
Joint type in flux pump	-	Series and Parallel	Series and Parallel	Series
The number of quasi DC voltage sources	1	-	-	8
Control ranges of field current	Broadness	Narrowness	Narrowness	Narrowness
Controllability of field current	Active (Fully independent control to B_m and f_r)	Active (Fully independent control to f_r)	Passive (Partially independent control to f_r)	Passive (Partially independent control to f_r)
System configuration	Complicacy	Complicacy	Complicacy	Simplicity
Maintainability	Bad	Bad	Bad	Good
Cooling capacity	Large	Small	Small	Small
Research progress	Design and analysis complete (2018) Exciter component testing complete (2019) Prototype development in progress (2019)	Design and analysis complete (2016) Exciter component testing in progress (2019) Prototype development in progress (2019)	Design and analysis complete (2016)	Development complete (2019) Performance test complete (2019) Follow-up research in progress (2019)

2.3. Novel structure design for HTS rotating machine with contactless superconducting field exciter

2.3.1. Design issue and purpose for novel excitation device

As investigated and discussed in subsection 2.2, several attempts have been made and reported applications of HTS flux pump on rotating machine globally; however, so far, those are still in the design, analysis, and basic test stages of the system. Therefore, there is not much the results of practical implementation research on suitable structure design for HTS flux pump based on rotating magnet, which is called "CSFE" in this dissertation. From the application perspective of the HTSRM with a typical structure, the practical research is required to enhance the technical feasibility of CSFE on rotating machine applications. Therefore, the novel structure of HTSRM operated by CSFE is proposed in this dissertation considering the suitable technical design factors on application to typical structure of HTSRM, such as structure, material, and winding method, of CSFE.

The design purposes and technical countermeasures for a novel structure of HTSRM with CSFE in this dissertation are discussed ahead. It is observed that design purposes were derived with references in parameter analysis and development investigation in subsections 2.1.2 and 2.2.2, respectively.

1. Efficient cryogenic cooling: Rotor structure integrated with field pole and exciter.
2. Enhanced system maintainability and efficiency: Simplified structure and configuration of exciter.
3. Current controllability: Exciter structure to control the charge characteristic and performance.
4. Maximized exciter capacity: Series multiple winding of 2G HTS wires without junction at exciter.

2.3.2. Novel structure for HTS rotating machine with contactless superconducting field exciter

Figs. 2.8(a) and 2.8(b) conceptually show the cross-sectional side view of HTSRM integrated with CSFE and front view of CSFE, which are newly proposed in this dissertation. Similar to a rotating machine, the structure of CSFE equally consists of stator part in room temperature and rotor part in cryogenic temperature. The key design features for HTSRM and CSFE structures are described as follows considering design purposes mentioned in subsection 2.3.1:

1. To satisfy the design purpose 1, the rotary part of CSFE is located on the same rotating axis of HTSRM and covered by same cryostat in rotor of HTSRM. Therefore, the cooling structure, which cools the HTS strands on CSFE and HTS coils on field pole,

can be simplified by sharing cryogen chamber inside rotor, as shown in Fig. 2.8(a). This results in more efficient cryogenic cooling than separated cooling structure.

2. To satisfy the design purpose 2, this structure, wherein the time-varying magnetic field is applied by relatively rotated rotor part, does not require the additional driving device for generating the external time-varying magnetic field. This allows mechanically simple system configuration that improve the maintainability as well as increase in system efficiency by saving energy for driving device.
3. To satisfy the design purpose 3, several PMs are disposed on the inner surface of the stator in the circumferential direction to inject a time-varying perpendicular magnetic field to 2G HTS wires in rotor part, as shown in Fig. 2.8(b). The number of PMs in the CSFE stator (n_p) can be changed to control the frequency of time-varying magnetic field (f_r) from PM because not only rotating speed (S_r) but also n_p affects f_r, which is governed to ($n_p \times S_r$)/60. Finally, the amount of magnetic energy or saturation current to be charged to HTS FCs are determined by magnetic intensity of PM, f_r, and the air-gap length (g_a) which is a spatial distance between PM in CSFE stator and 2G HTS wires in CSFE rotor. By positioning the stator of CSFE at rotor outside in room temperature, not only the cooling load can be reduced but also the controllability of the time-varying magnetic field or charged current can be improved.
4. To satisfy the design purpose 3, the g_a is adjustable using changeable thin fiber reinforced plastic (FRP) sheets, thereby resulting in controlling the amount of field current. The magnetic field density from PM in the 2G HTS wires, which can determine the amount of current charged from the CSFE is affected by the g_a. In other words, the charged current increases and decreases as the g_a decreases and increases, respectively.
5. To satisfy the design purpose 4, multiple DC voltage sources are created by implementation of multiple winding of 2G HTS wires, as shown in Fig. 2.8(b), thereby maximizing the magnitude of charged current within the limited rotor size. The serial or parallel connections of the HTS strands can be considered to generate the multiple voltage sources in superconducting circuit. The parallel connection of multiple HTS strands creates some electrical and physical joints between HTS strands to form the superconducting circuit. This may increase the magnitude of joint resistance in superconducting circuit and then, reduce the saturation current. Therefore, the multiple winding method with serial connection is considered to maximize the saturation current in a limited space of HTSRM rotor. For this implementation of series multiple winding in 2G HTS wires without junction, the winding method and structure shape

with toroidal-type are proposed in the rotor design of CSFE. They can guide and support the winding path of HTS wire as well as improve the cooling efficiency through conduction heat transfer. In addition, such toroidal structure of CSFE rotor is structurally suitable for cylindrical rotor structure of HTSRM.

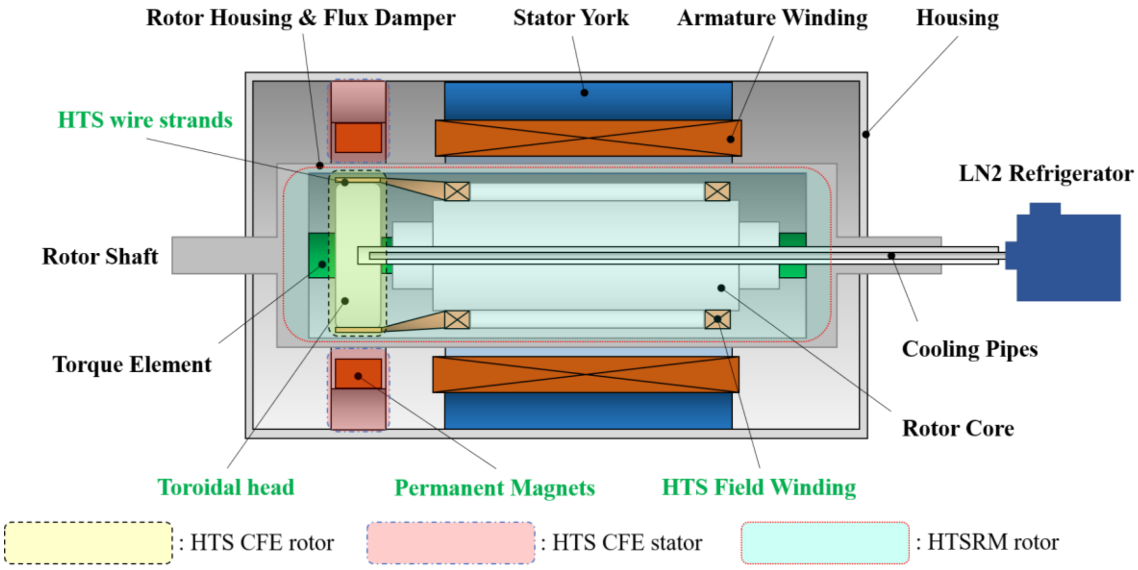

(a) Side view of the conceptual HTSRM integrated with CSFE

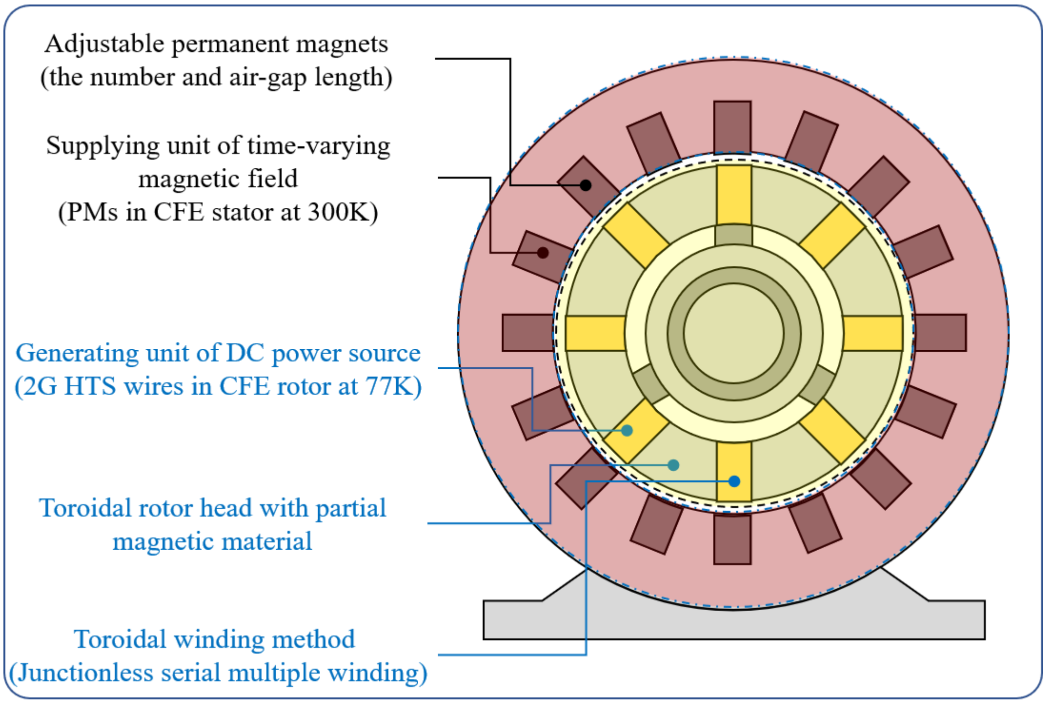

(b) Front view of CSFE

Fig. 2.8. Cross-sectional schematic diagrams of the conceptual HTSRM integrated with CSFE

Chapter 3. Structure Design and Operational Characteristic for HTS Rotating Machine

This chapter presents the results of design and analysis of the 1 kW class HTSRM for manufacturing the prototype machine applied to CSFE. A draft machine of the 1 kW class HTSRM was conceptually designed using loading distribution method. A practical design in the electromagnetic point of view was pursued considering the various limitations in development budget, compatibility with design of CSFE, and others.

The structure of HTS rotor was conceptually designed considering mechanical and thermal characteristics. A torque tube is considered as a core structure among various other thermal insulation structures because it can dramatically minimize heat intrusion from room temperature in the cryogenic environment. However, the mechanical rigidity of a torque tube is inversely proportional to its thermal conduction loss. Thus, the structural design of a torque tube including thickness (t_{tu}) and axial length (l_{tu}) should be seriously considered in structure design process. The correlation characteristics between mechanical and thermal design process was considered to develop a thermally and mechanically stable concept of 1 kW class HTSRM.

To increase the economic efficiency during the development stage and the performance of the 1 kW class HTSRM, various salient-pole structures of the rotor and magnetic materials of both the rotor and stator were considered. Using the time-transient solver of the 2D FEA, various key design parameters were electromagnetically investigated and compared by considering the different stator-winding coil pitches and structural dimensions of the salient-field pole. Further, the final 2D FEA model was determined based on the parametric-analysis results, and a performance analysis was performed to determine the various machine characteristics in motor operation of the 1 kW class HTSRM.

The 1 kW class HTSRM, which is finally manufactured as a prototype machine, was modeled and analyzed using 3D CAD and 2D FEA with various considerations in practical design and fabrication. For non-loaded and loaded operations in the generator mode, the steady-state FE simulations were performed to assure and estimate the electrical output characteristics according to I_{f} charged by CSFE.

3.1. Structure design and electromagnetic analysis of HTS rotating machine

3.1.1. Fundamental design of HTS rotating machine

A. Electromagnetic design of HTSRM

A draft machine was designed using loading distribution method to develop the 1 kW class HTSRM. The stator core of a commercialized induction motor was considered as the stator of this machine to reduce the development budget. For choosing a commercialized stator core, the volume of a cryogen tank inside the rotor was considered to store sufficient liquid nitrogen (LN2). Thus, the stator core of totally enclosed motor with 7.5 kW capacity and 160 M frame from HYOSUNG was finally reused.

Table 3.1. Parameter specifications of draft design of the 1 kW class HTSRM

Parameters	**Unit**	**Value**
Rated power	kW	1
Rated torque	N·m	23.9
Rated rotating speed	rpm	400
Rotor pole number	-	4
Rated stator current /density	A_{rms}/ A/mm^2	2.62/1.85
Number of slots	-	48
Pole pitch	-	12
Stator coil number per slot/phase	-	52/416
Fill factor of stator slot	%	58
Operating field winding current	A	≥30
FC inductance	mH	≤35
Winding turns per field pole	-	60
HTS coil type	-	Race-track DPC
Winding type	-	Polyimide tape insulated co-winding
Operating temperature	K	77
Cooling method	-	LN_2 batch

Based on the structural dimensions and material properties of the commercial stator core, the number of turns of the HTS FC (N_{fc}) on the rotor was calculated by estimating the full-load magnetomotive force (MMF or $F_{fc}=N_{fc}I_f$) to generate the targeted magnetic flux density in the air gap. Moreover, the conductor diameter and number of armature winding on the stator were designed by considering the fill factor based on slot dimensions of stator core. The iron core was laminated with thin steel plate (50PN470 or S18) along the rotating-shaft direction and consisted of 48 slots. Four slots were allocated as the number of slots per pole per phase. Therefore, the winding turns per phase were distributed in the four slots. The 2G HTS wire was used only to fabricate the field-pole winding in the rotor, whereas a conventional copper stranded conductor was used for armature winding in the stator. The 2G HTS field windings were designed as a racetrack type and double pancake coil (DPC) using a 2G HTS wire from SuperPower Inc. A magnetic air gap between the inner and outer radii of the stator core is set to be 7 mm.

Table 3.1 lists the design parameter specifications of a 1 kW class HTSRM. The rated S_r and I_f are designed to consider compatibility with CSFE design. In a prototype research, a current of 25 A was charged into HTS DPC with inductance of 29.5 mH, using prototype rotating type HTS flux pump, which is specified to N_s = 300 rpm and g_a = 8 mm, eight HTS strands in rotor, and eight PMs in stator [47]. By considering experimental verification, rated rotating speed of machine (N_s) = 400 rpm and $I_f \geq 30$ A were set for initial design of the 1 kW class HTSRM. Such reasonable considerations are expected to give a qualitative understanding of the application feasibility of HTS flux pump on field excitation system of HTSRM.

B. Structure design of HTS rotor

In this subsection, the structure design of HTS rotor was conceptually conducted with design considerations in thermal loss estimation which is to minimize LN2 consumption as much as possible, as well as mechanical stability estimation for various structure components on HTS rotor. The core structures of HTS rotor, such as torque tube and rotating shaft, are conceptually designed by analytical design codes considering to mechanical strength, mechanical rigidity and thermal heat losses of HTS rotor. Further, conceptual modelling is built using SolidWorks 3D CAD to refer detail design process for practical development of prototype machine.

The heat from the room temperature should not be penetrated in the rotor inside; thus, the HTS rotor should be designed as a thermal insulation structure to stably operate HTS coils on rotor body. A torque tube is one of the effectively thermal insulation structures for HTS rotor. The electromagnetic torque, which is generated by the interaction between magnetic field of the stator and rotor, should be transferred to the rotor shaft through torque tubes. Therefore, G10 FRP is a great potentially material for torque tubes because of its excellent thermal insulation and mechanical strength performances [57].

The total heat losses (Q_{total}) in the HTS rotor are conveniently derived by the following equation:

$$Q_{total} = Q_{cd} + Q_r + Q_e + Q_h \tag{3.1}$$

where Q_{cd} is the conduction heat losses, which is transferred from room temperature (300 K) to cryogenic temperature, i.e., 77 K in this dissertation, through both sides of the torque tubes. Q_r is a radiation heat loss, which is invaded into rotor pole (77 K) from the thermal shield (300 K) located in rotor outermost side. Q_e is the eddy current loss, which is electromagnetically generated in the thermal shield during the steady-state operation of HTSRM. Finally, Q_h is the internal heat loss in HTS coils, such as AC loss, and mechanical lab joints loss. In this dissertation, three major heat losses, Q_{cd}, Q_r, and Q_e, were mainly considered to conceptually design the rotor structure of the 1 kW class HTSRM.

A thickness of torque tube (t_{tu}) is considered as a core parameter for designing the torque tube because it can determine the conduction heats transferred from room temperature and mechanical strength and rigidity against the rotational moment applied to the rotor. These relations can be explained as follows [58]−[60]:

$$Q_{\mathrm{cd}} = \frac{\tilde{k} A_{\mathrm{tu}} \Delta T}{l_{\mathrm{tu}}} = \frac{\tilde{k} A_{\mathrm{tu}} (T_{\mathrm{h}} - T_{\mathrm{l}})}{l_{\mathrm{tu}}} \tag{3.2}$$

$$d_{\mathrm{i}} = \sqrt[4]{d_{\mathrm{o}}^4 - \frac{16 d_{\mathrm{o}} T_{\mathrm{m}}}{\pi \tau_{\mathrm{max}}}} \tag{3.3}$$

where $\tilde{k}$, A_{tu}, and l_{tu} are the average thermal conductivity from T_h (300 K) to T_l (77 K), conduction surface of the torque tube, and effective length of torque tube, respectively. Moreover, d_i, d_o, T_m, and τ_{max} are the inner diameter, outer diameter, torsion moment, and maximum shear stress, respectively. If the greater t_{tu} (d_o−d_i) of the torque tube is selected, the larger of the conduction heat from room temperature is generated. However, the greater t_{tu} (d_o−d_i) of the torque tube is designed, the larger mechanical load that it can withstand.

In the structural design of torque tubes, mechanical rigidity design of was first performed and then, the conduction heat loss was estimated because the first one of the main functions of a torque tube is to transfer torque to the load shafts. The torque tubes were designed based on rigidity design method because it is known that design standard in torsional rigidity is more mechanically stable than that of torsional shear strength in consideration of safety design for member of framework, i.e., G10 FRP. The torsional rigidity should be evaluated, even if torsional strength is sufficient enough. The reason of evaluation is that it may cause torsional vibration in the member of framework because of elastically generated torsional deformation. Thus, t_{tu} is calculated by Bach's torsional angle formula which is restricting the torsion angle (θ_t) within a specific range of T_m. Further, it can be expressed as follows [57], [60]−[61]:

$$\theta_{\mathrm{t}} = \frac{T_{\mathrm{m}} l_{\mathrm{tu}}}{G I_{\mathrm{p}}} = \frac{5760 T_{\mathrm{m}} l_{\mathrm{tu}}}{\pi^2 G\left(d_{\mathrm{o}}^4 - d_{\mathrm{i}}^4\right)} \tag{3.4}$$

where G is the shear modulus of the used material and I_{p} is the polar moment of inertia, which depends on the cross-sectional shape of the member.

Fig. 3.1 shows the variations in t_{tu}, θ_{t}, Q_{cd}, and $\tau_{\max}$ of the torque tube versus safety factors (S_{f}), which is defined to ratio allowable stress (Y_{s}) to shear stress ($\tau_{\max}$). It is observed that d_{o} of torque tube is set at 70 mm because of connection with CSFE rotor. While T_{m} is assumed to be 47.8 N·m in all design regions for a sufficient design margin. In addition, the mechanical and thermal properties of G10 FRP material were referred in [60], [62]. To maintain high S_{f} values of torque tube, the t_{tu} value of torque tube should be thick. However, it means that Q_{cd} is increased from room temperature. In terms of strength design standard, the S_{f} at around 50 can satisfy both design parameters, namely, $\tau_{\max}$ and Q_{cd} as shown in Fig. 3.1. However, S_{f} value should be over 180 to restrict θ_{t} value under 0.2° in rigidity design standard of the torque tubes.

Fig. 3.2 shows the variations in t_{tu}, θ_{t}, Q_{cd}, and $\tau_{\max}$ of the torque tube that vary with different value of T_{m}. As mentioned above, S_{f} is assumed to be 182 in all design regions. The t_{tu} values of torque tube should be thick to increase the design margin of T_{m} so that the torque tube can sufficiently withstand the load torques, and maintain the value of S_{f} at 182, as well. In addition, Q_{cd} values are increased with increase in t_{tu} of the torque tubes.

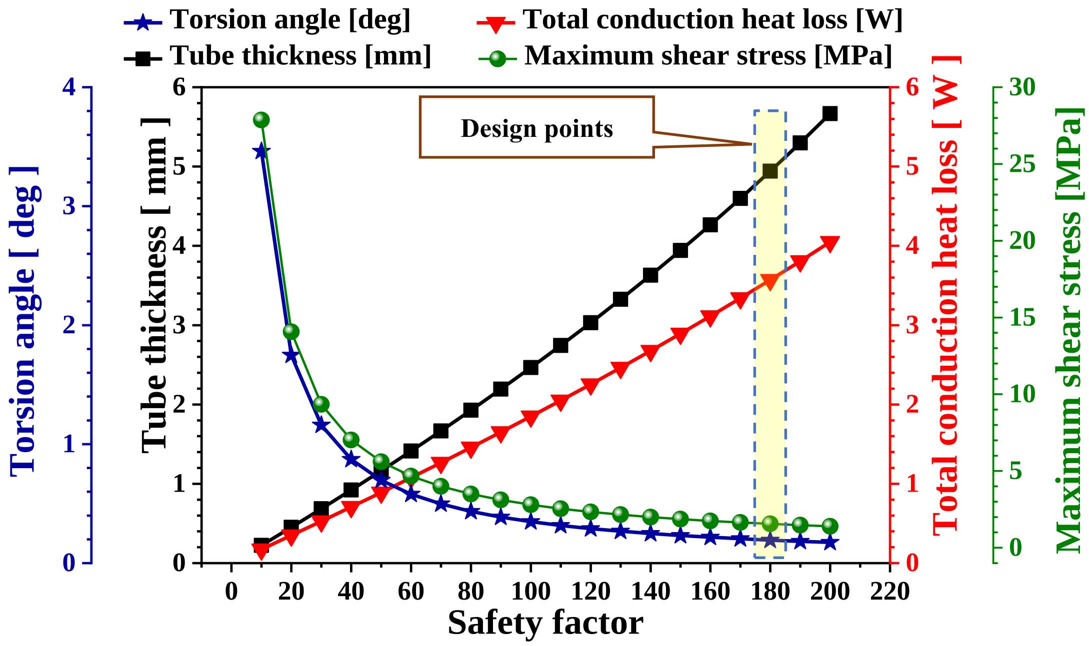

Fig. 3.1. Variations in t_{tu}, θ_{t}, Q_{cd}, and $\tau_{\max}$ of torque tube versus S_{f} with the same T_{m}

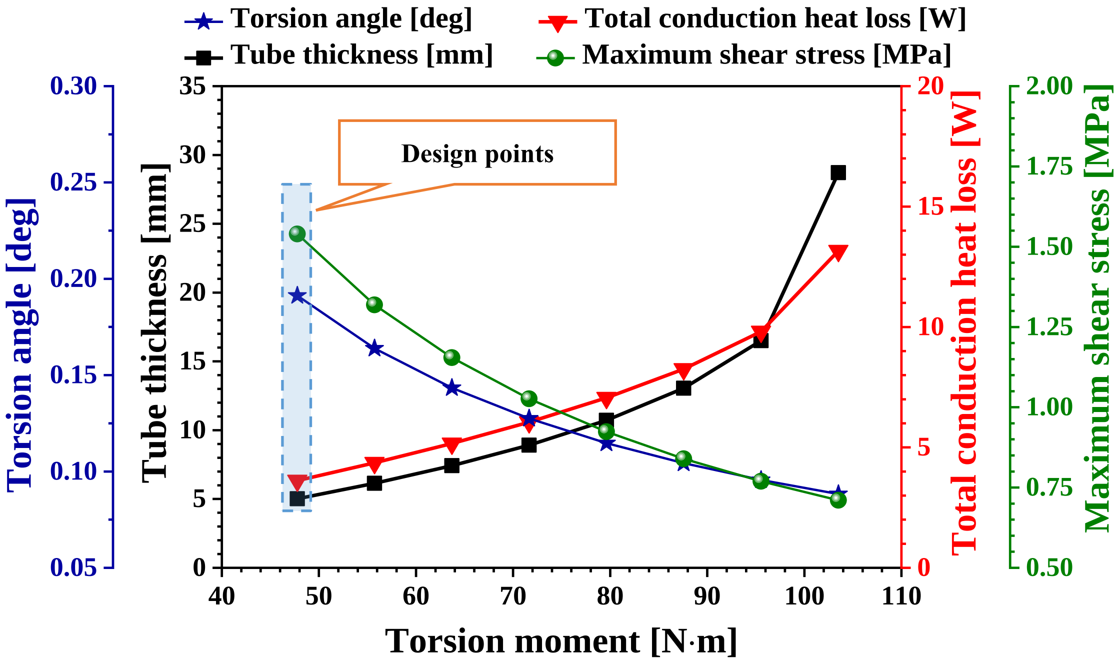

Fig. 3.2. Variations in t_{tu}, θ_t, Q_{cd}, and τ_{max} of torque tube versus T_m with the same S_f

Table 3.2 lists the design conditions and results of the torque tubes in consideration with $Q_{cd.}$ and θ_t value. Finally, d_i and Q_{cd} of the torque tube were calculated to be 60 mm with θ_t of 0.19° and 1.81 W, respectively. The largest heat loss of the HTS rotor is generally considered to be Q_r in thermal design of HTSRM; however, it can be significantly reduced by wrapping the rotor pole with multi-layer insulation. The largest radiative heat flux (q_r) with multi-layer insulation is conveniently estimated by follows [57]–[59], [63]:

$$q_r = \frac{Q_r}{A_r} = \frac{\varepsilon\sigma\left(T_h^4 - T_l^4\right)}{(N_i + 1)A_r} \tag{3.5}$$

where ε, σ, N_i, A_r, T_h, and T_l are the effective thermal emissivity of the materials used at rotor structure, Stefan–Boltzmann constant, number of superinsulation layer, radiative surface area, thermal shield temperature (300 K), and rotor pole temperature (78 K), respectively.

To investigate the thermal effects of change in material on thermal shield (cryostat) and rotor body, several cases were considered with stainless steel and aluminum materials for thermal shield and rotor pole. Table 3.3 summarizes the estimated results of Q_r considering six different cases. It is observed that Q_r values in Case I, II, and III were estimated with the absence of multi-layer insulation and torque tubes at both sides. If the rotor pole is surrounded by superinsulation of 10 layers, Q_r values can be one tenth smaller than that of case in non-use of superinsulation layer. Thus, 1 mm gap between the thermal shield and rotor pole was considered for multi-layer insulation.

Table 3.2. Design conditions and results of torque tube for the 1 kW class HTSRM

Design conditions		**Design results**	
Items	**Values**	**Items**	**Values**
d_o/d_i [mm]	70/60	Q_{cd}/ Q_{cd}[‡] [W]	1.81/3.61
T_h/T_l [K]	300/78	Q_{rt}/Q_{rr}[W]	1.80/0.71
L_{tu} [mm]	54	t_{tu} [mm]	5
A_{tu} [mm^2]	1020	θ_t [°]	0.19
Y_s[†] [MPa]	280	τ_{max} [MPa]	1.54
$\tilde{k}$ [W/m·K]	0.43	S_f	182
T_m [N·m]	47.8	Weight[†] [kg]	0.22

[†]: Yield strength, [‡]: both side of rotor

Table 3.3. Comparison results of radiation loss considering materials

	Cases	ε	Q_r **[W]**
Case I	Stainless steel in thermal shield Aluminum in rotor pole	ε_h: 0.16[†] ε_l: 0.1[‡]	6.47
Case II	Stainless steel in thermal shield Stainless steel in rotor pole	ε_h: 0.16[†] ε_l: 0.12[*]	7.39
Case III	Aluminum in thermal shield Stainless steel in rotor pole	ε_h: 0.1[‡] ε_l: 0.12[*]	6.11
Case IV	Case I with 10 superinsulation layer[#]	ε_h: 0.16[†] ε_l: 0.1[‡]	0.59
Case V	Case II with 10 superinsulation layer[#]	ε_h: 0.16[†] ε_l: 0.12[*]	0.67
Case VI	Case III with 10 superinsulation layer[#]	ε_h: 0.1[‡] ε_l: 0.12[*]	0.56

[†]: At 300 K (SUS304, mechanical polish), [‡]: from 290 K to 77 K, (Al, mechanical polish), [*]: at 77 K (SUS304, mechanical polish), [#]: using RUAG Coolcat 2 model (1 mm per 10 layer)

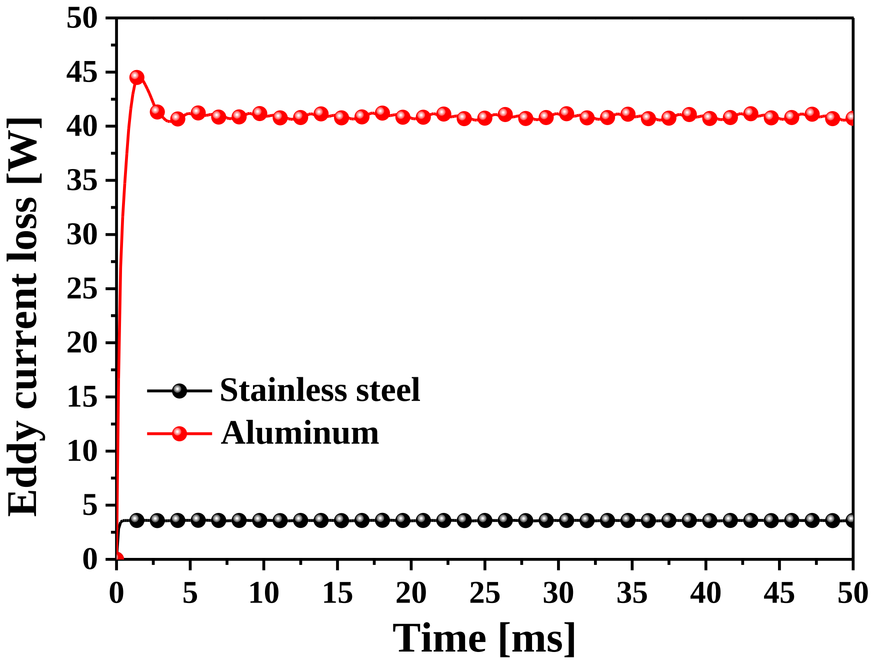

Fig. 3.3. Comparison of Q_e in thermal shield with stainless steel and aluminum materials

The Q_r value in Case III with aluminum material for the thermal shield was the smallest one; however, stainless steel was chosen as the thermal shield material. The resistivity of stainless steel (740 nΩ·m) is relatively higher than that of aluminum (0.399 nΩ·m). Therefore, thermal shield with aluminum material generates larger Q_e than that of thermal shield with stainless steel, as shown in Fig. 3.3. The eddy current generated in thermal shield with stainless steel is suppressed by its high resistivity. Q_e values for aluminum and stainless-steel materials are calculated at 41 and 3.6 W, respectively, using the ANSYS-Maxwell electromagnetic FEA software.

The value of Q_{cd} in the torque tube can be reduced by increasing l_{tu}. However, this increases Q_r because surface area heat-transferred by radiation is proportional to increase in l_{tu}. Therefore, the changed values in Q_{cd} and Q_r are finally calculated according to changes in l_{tu}, as shown in Fig. 3.4. These calculations were based on ε of 0.7 for G10 FRP in torque tube and design properties of Case II presented in Table 3.3. Although the optimal value of l_{tu} is at 150 mm (both ends: 300 mm) leading to the minimized value of total heat loss, 54 mm (both ends: 108 mm) is chosen as the final value for l_{tu} because of consideration in mechanical problem, such as vibration of rotor while increasing l_{tu}. In particular, the radiation loss in torque tube (Q_{rt}) is higher than radiation loss in rotor pole body (Q_{rr}) because of higher value of ε of G10 FRP, as listed in Table 3.3.

Table IV summarizes the design results of rotating shafts in loaded side and non-loaded side of HTS rotor. The length of rotor was designed to be 1560 mm. For the non-loaded side, the minimum shaft length at 500 mm is considered to make enough temperature gradient because it can reduce the risk of freezing magnetic fluid seal in case of insufficiently length between LN2 temperature and room temperature. Further, the diameters of rotating shafts were designed by using (4). In addition, the shaft in loaded side, which is directly connected with the load of rotating machine, is designed in solid shaft in consideration with mechanical stability of the rotor shaft. While the shaft in the non-loaded side is designed in hollow type because of installation of cooling pipes for supplying LN2. Finally, both stainless steel and aluminum materials are considered for rotating shafts. They satisfy the reliable recommendation in Bach's torsional angle formula because calculated θ_t values were much smaller than 0.25°.

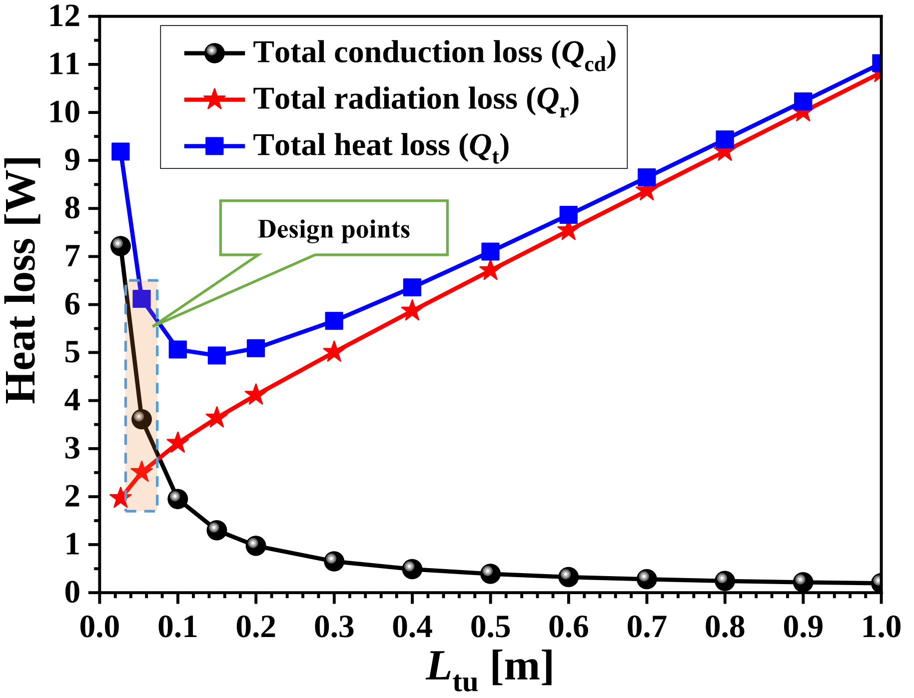

Fig. 3.4. Variations in heat losses of HTS rotor versus l_{tu} with materials of Case II presented in Table 3.3

Table 3.4. Design results of rotating shaft for the 1 kW class HTSRM

	Rotating shaft design results			
Items	**Loaded side (Solid shaft)**		**Non-loaded side (Hollow shaft)**	
Materials	Stainless steel	Aluminum	Stainless steel	Aluminum
d_o/d_i [mm]	60/0	60/0	60/51	60/51
t_{tu} [mm]	60	60	4.5	4.5
θ_t [°]	0.03	0.08	0.06	0.17
S_f	150.9	244.9	72.1	117.1
Weight† [kg]	4.6	1.5	3.16	1.05

†: Without flanges

Fig. 3.5 shows the conceptual modelling of the 1 kW class HTSRM, which is designed based on subsections 3.1.1.A and 3.1.1.B, using SolidWorks CAD. The rotor body, which supports HTS FCs and serves as a cryogen tank for LN2, is uniaxially coupled to the rotor of CSFE and is then connected to the rotor shafts through torque tubes on both sides. The cooling pipes flow LN2 pass inside the rotor body through hollow shaft. HTS field windings are considered to design DPCs using 2G HTS wire with width of 4 mm. Moreover, a 2G HTS wire is wound at rotor of CSFE in series and bonded to HTS FCs to form a superconducting series circuit.

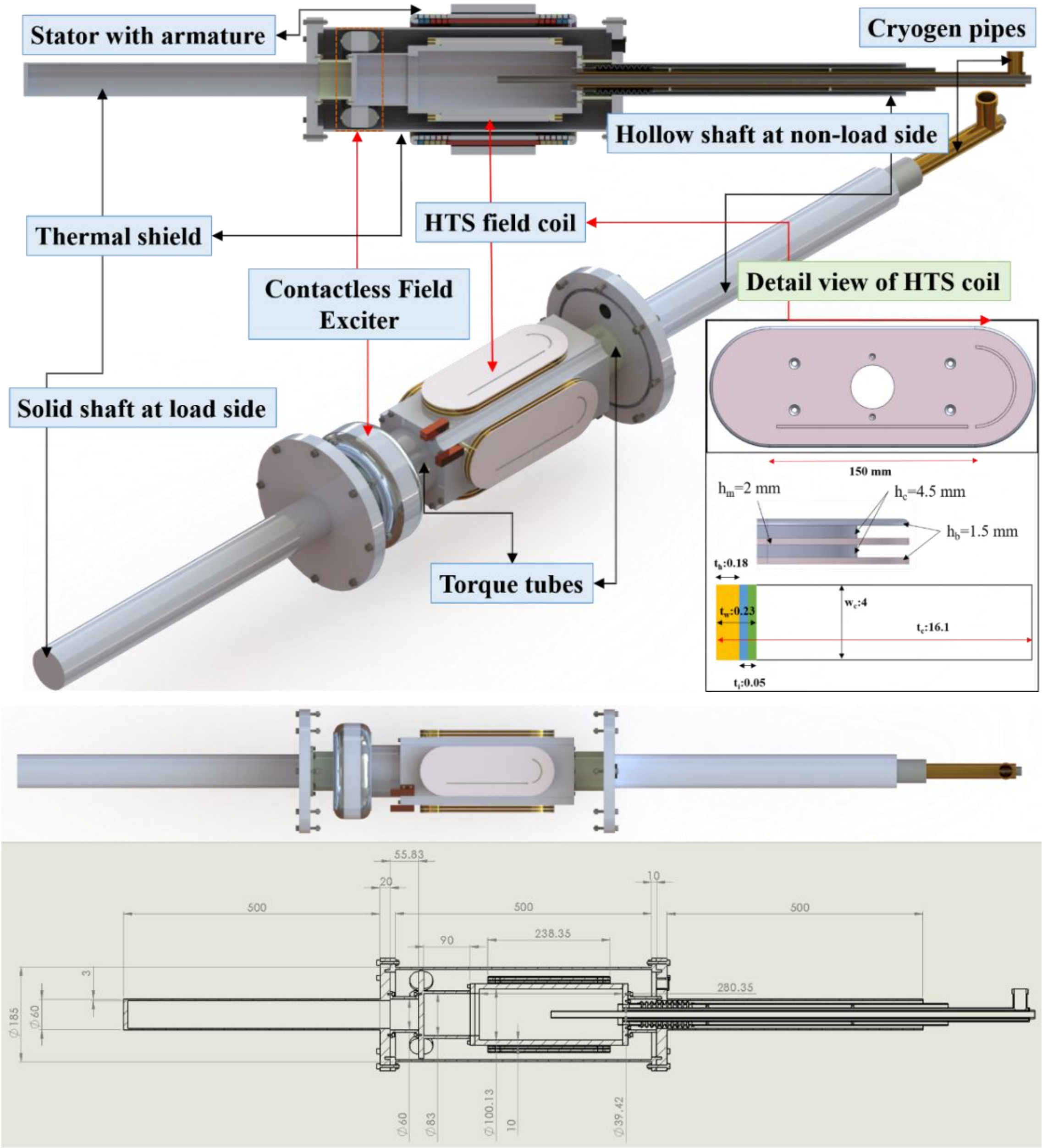

Fig. 3.5. Conceptual design configuration of the 1 kW class HTSRM

3.1.2. Structure optimization design of HTS rotating machine

This subsection mainly focuses on the structure design and analysis of the 1 kW class HTSRM, which will be assembled with the CSFE. The key parameters of the HTS FC, such as field-coil inductance (L_{fc}), N_{fc}, and etc. were designed based on the CSFE operating conditions similar to the N_s and I_f setting in subsection 3.1.1.A. The charging time to excite HTS FCs using CSFE is dependent on the L_{fc}. The larger L_{fc} is, the longer charging time is. Thus, specification of 2G HTS wire was changed from use with width of 4 mm to 12 mm to reduce L_{fc} by decreasing the N_{fc}. 2G HTS wire with 12 mm width is more effective for increasing fully saturated current on FCs charged by HTS flux pump because it's critical current (I_c) is approximately three time higher than that of HTS wire with 4 mm width. In addition, magnetic material was considered for the rotor structure to compensate the F_{fc} caused by the decreased N_{fc}. In particular, N_{fc} was finally set to 60 turns considering the F_{fc} estimation in loading distribution design, and budget for 2G HTS wire as well as L_{fc}. It is believed that such reasonable design considerations can secure a qualitative understanding of the application feasibility of HTS flux pump on field excitation system of HTSRM.

A salient-pole type and carbon steel, which can assist the concentration of magnetic flux and hence generate additional output, were employed as a rotor structure and material, respectively, to reduce the length of an expensive 2G HTS wire. However, these factors can electromagnetically harm the performance of the rotating machine and HTS coils in the rotor field winding. Therefore, the electromagnetic effects because of the changes in the salient-pole shape on the performance characteristics of the rotating machine and HTS coils should be carefully investigated.

First, a parametric simulation using the time-transient solver of 2D FEA was performed to select a suitable coil pitch for the stator winding of the 1 kW class HTSRM in terms of the space-harmonic contents of the machine output. Using a constant stator coil pitch, the parametric designs of the salient-pole shape then were developed for the 1 kW class HTSRM and the influences of various structural dimensions of the salient-field poles were analyzed using the time-transient solver of 2D FEA. In addition, carbon steel (SAE-AISI 1045 or S45C) was used as the material for the salient-pole rotor. Fig. 3.6 shows the magnetic field density (B) versus intensity (H), i.e., the B–H characteristic curves of the stator and rotor cores, which are referred from [64]–[65]. The magnetization grade of S18 electrical steel is higher than that of S45C carbon steel under the same F_{fc}. For comparison, various critical electromagnetic design parameters such as total harmonic distortion (THD) of the voltages, ripple ratio of the rated torque (T_{rc}), and maximum magnetic field perpendicularly applied to the 2G HTS conductor (B_p), were investigated and compared to determine a suitable dimension of the salient-field pole. Finally, an optimized 1 kW class HTSRM was built based on the parametric-analysis results and its various output performances were analyzed to estimate the machine characteristics.

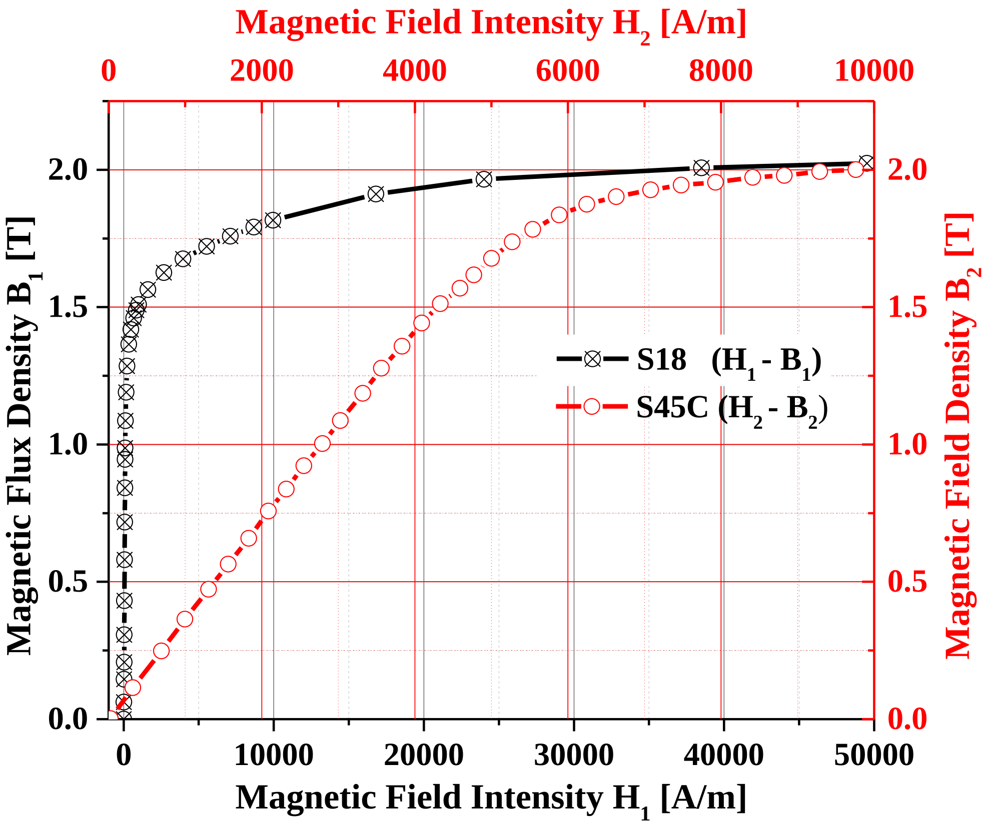

Fig. 3.6. *B*–*H* characteristics curves for stator core (S18) and rotor core (S45C)

A. Parametric analysis of the stator-winding coil pitch

The harmonic characteristic is very important in the rotating-machine design process because if the phase voltage includes harmonic waves, the non-sinusoidal current causes a torque ripple in the rotating machine, resulting in noise, vibration, and mechanical loss. Basically, the harmonic components in the air gap magnetic-field density and back-electromotive force (EMF, E_b) wave can effectively be reduced by considering the distributed and fractional-pitch windings [66]. Therefore, the effects of the application of fractional-pitch winding were analyzed to reduce the spatial harmonic components, which are caused by the structural characteristics of the teeth and slots in the magnetic cores of stator and rotor.

Table 3.5 lists the parametric-analysis results on the analysis of the effects of various stator-winding coil pitches on the output characteristic at no-load and loaded operations. It is observed that the coil pitches varied from 8 to 12 in the parametric analysis. When the coil pitch was 12, it was considered as a full-pitch winding and was used as a reference model for comparison with the other models. The results of the no-load analysis revealed that the induced voltage (E_i) and machine input (P_{in}) were inversely proportional to the decrease in the coil pitch. However, the copper loss (P_c) was proportional to the decrease in the coil pitch and then decreased, as presented in Table 3.5, because of the reduction in the copper length at the end winding. It is noted that the length of the end windings in each coil pitch and the corresponding phase resistance (R_a) values were simply estimated using 3D models of the armature windings and P_c values were simply calculated assuming armature current (I_a) of 4 A_{rms}. The machine efficiency (η) decreased with the increase in the coil pitch.

Table 3.5. Parametric analysis results considering stator coil pitch

Coil Pitches	**Unit**	**8/12$^{\#}$ (2/3)**	**9/12$^{\#}$ (3/4)**	**10/12$^{\#}$ (5/6)**	**11/12$^{\#}$**	**12/12$^{\#\#}$**
Items		**Values**				
No-load operation analysis						
E_i	V_{rms}	92.27	98.40	102.87	105.61	106.60
VTHD	%	3.26	1.78	1.09	2.55	3.33
R_a	Ω	2.51	2.66	2.81	2.96	3.11
P_c	W	120.6	127.7	134.9	142.0	149.2
I_a	A_{rms}	4	4	4	4	4
P_{in}	W	1107.3	1180.8	1234.4	1267.3	1279.2
P_{out}	W	986.7	1053.1	1099.6	1125.3	1130.0
η	%	89.11	89.18	89.07	88.79	88.34
Load operation analysis						
VTHD†	%	3.38	1.84	1.19	2.70	3.53
T_r	Nm	26.30	28.06	29.35	30.12	30.38
T_c	Nm	2.23	1.33	0.67	1.88	2.53
$T_{r.c}$	%	8.47	4.75	2.29	6.23	8.33

$^{\#}$: Fractional-pitch winding, $^{\#\#}$: full-pitch winding, †: without 3rd harmonics

The load-analysis results listed at the bottom in Table 3.5 indicate that the voltage THDs (VTHDs) of E_b for all coil pitches were generally lower because the stator core was not saturated by low field excitation. The third harmonic component and its multiples, such as the ninth and fifteenth harmonic components, did not appear in the line-to-line star-connected armature winding because they are cancelled in symmetrical three-phase machines. Thus, the fifth and seventh harmonics remained as the main harmonic components [66]. The rated-torque (T_r) profiles according to various coil pitches are shown in Fig. 3.7. A 10/12 coil pitch was a suitable stator coil pitch in terms of the T_{rc} characteristic, and its VTHD and T_{rc} were 1.19% and 2.29%, respectively.

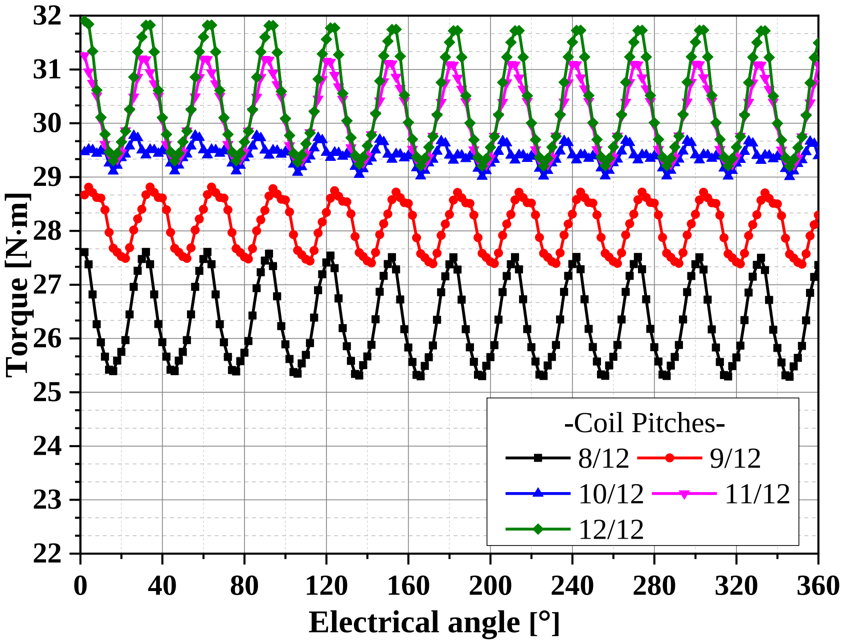

Fig. 3.7. Comparison of torque profiles according to stator coil pitches

B. Parametric analysis of the salient-pole shapes

In a motor operation driven by a sinusoidal pulse width modulation input, E_b of the salient-pole synchronous machine, which generally has a square-wave form, should be a sinusoidal wave. Thus, the machine torque ripple can be reduced. In addition, the HTS coils, which are inserted into the pole leg in the form of a race-track, are magnetically affected by the salient-field pole structure with magnetic materials. This magnetic effect can decrease the HTS coil performance, i.e., its I_c capability. Therefore, parametric analysis that considers the shapes of the salient-field pole is necessary.

Fig. 3.8(a) shows the reference model for comparison with the parametric FEA models shown in Figs. 3.8(b)–3.8(e). The salient-field pole mainly consists of a racetrack-type HTS single pancake coil (SPC) for the field winding inserted in the salient-pole structure and the pole shoe, leg, and body of the rotor supporting structure. In addition, the stator basically consists of a three-phase armature winding with a 10/12 coil pitch and a laminated iron core as armature supporting structure. The four parametric geometric variables are considered to investigate the effects of the salient-pole shapes on the HTSRM performance. All sizes of the geometric variables were parameterized within the rotor-design space and listed in Table 3.6.

In an HTS rotating machine, with a magnetic core in the rotor or stator, the I_c performance of the HTS coils may be decreased by B_p because a high-magnetic concentration or saturated pole can introduce an external magnetic field to the HTS coils that surround the salient field pole structure, as shown in Figs. 3.8(b)–3.8(d). Thus, suitable sizes for the pole-leg width (W_l), pole-leg height (H_l), and pole-shoe width (W_s) of the salient-field pole must be determined by parametric analysis. In addition, the pole-shoe height (H_s) at the shoe end determines the maximum air gap length (G_{max}) at the end of the pole arc [67]. As H_s becomes shorter, G_{max} increases; therefore, the air gap shape becomes unbalanced along the pole-face arc, as shown in Fig. 3.8(e). H_s 1 is applicable only for a constant air gap; however, the other sizes (H_s 2 and H_s 5) are applicable for unbalanced air-gap. It is observed that the reference model shown in Fig. 3.8(a) is built with W_l 5=54.8 mm, H_l 5=14 mm, W_s 1=77.2 mm, and H_s 1=4.87 mm. All parametric models shown in Figs. 3.8(b)–(e) are derived from Fig. 3.8(a).

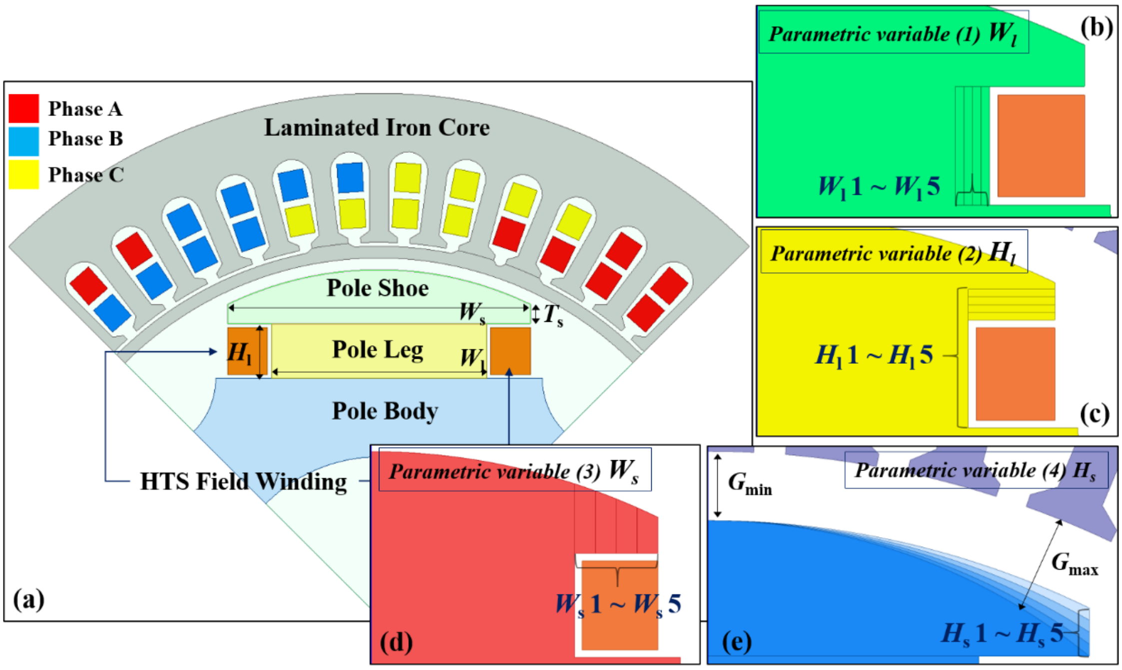

Fig. 3.8. Structures of the FEA models considering the parametric salient-field pole shapes

All the models mentioned above were modeled and analyzed using the time-step FEA in ANSYS-Maxwell 2D version 17.2. Moreover, to simplify the analyses, the motor operating mode with operating current (I_{op}) = 30 A, I_a = 4 A_{rms}, and N_s = 400 rpm was simulated using approximately 69000 finite elements. In addition, carbon steel (SAE-AISI 1045 or S45C) and a silicon steel plate (50PN470 or S18), as shown in Fig. 3.6, were used as the material for the salient-field pole and laminated stator core, respectively. The key parameters considering the parametric variables of the salient-pole shapes are summarized and listed in Table 3.6.

First, the parametric-analysis results of W_l generally show that W_l changes do not affect the machine characteristics.

Further, the results of the change in H_l, which determines the spacer gap (g_s) between the HTS SPC and the bottom of the salient-field pole shoe, reveals that it affects the B_p characteristic of the HTS SPC. As H_l decreases from 18 to 14 mm, the B_p values increases in the range from 0.184 to 0.308 T because the g_s values also decreases as H_l decreases. Therefore, the highly concentrated magnetic flux across the pole shoe perpendicularly passes and influences the upper area of the HTS SPC adjacent to the pole shoe, as shown in Fig. 3.9. Moreover, notable changes in the other machine parameters in the absence of B_p are not observed.

Table 3.6. Parametric analysis results considering salient-field pole shapes

Variables	**Values [mm]**	**Machine-parameter values**					
Parametric variable (1) W_l							
		$E_i^{\#}$ [V_{rms}]	THD$^{\#}$ [%]	$B_p^{\#\#}$ [T]	$L_f^{\#\#}$ [mH]	$T_r^{\#\#}$ [N·m]	$T_{rc}^{\#\#}$ [%]
W_l 1	54.8	102.9	1.088	0.308	37.98	29.35	2.29
W_l 2	52.8	102.7	1.082	0.310	37.93	29.30	2.3
W_l 3	50.8	102.5	1.08	0.310	37.84	29.24	2.29
W_l 4	48.8	102.3	1.08	0.308	37.75	29.18	2.29
W_l 5	46.8	102.1	1.078	0.308	37.65	29.11	2.29
Parametric variable (2) H_l							
H_l 1	18	102.1	1.291	0.184	36.27	28.94	2.43
H_l 2	17	102.0	1.224	0.198	36.74	29.08	2.41
H_l 3	16	102.4	1.169	0.217	37.17	29.19	2.39
H_l 4	15	102.7	1.123	0.247	37.58	29.28	2.35
H_l 5	14	102.9	1.088	0.308	37.98	29.35	2.29
Parametric variable (3) W_s							
W_s 1	77.2	102.9	1.088	0.308	37.98	29.35	2.34
W_s 2	71.6	99.53	1.357	0.297	35.50	28.38	2.62
W_s 3	66	96.36	1.434	0.254	33.04	27.29	3.19
W_s 4	60.4	91.90	1.281	0.210	30.76	26.11	2.49
W_s 5	54.8	87.85	0.951	0.172	28.72	24.88	2.29
Parametric variable (4) T_s							
H_s 1	4.87	102.9	1.088	0.308	37.98	29.35	2.29
H_s 2	3.65	98.56	0.853	0.314	36.30	28.12	1.75
H_s 3	2.43	94.86	0.691	0.324	34.84	27.06	1.34
H_s 4	1.21	91.70	0.573	0.343	33.55	26.15	1.03
H_s 5	0	88.89	0.492	0.384	32.29	25.34	0.81

$^{\#}$: No load operation, $^{\#\#}$: Loaded operation

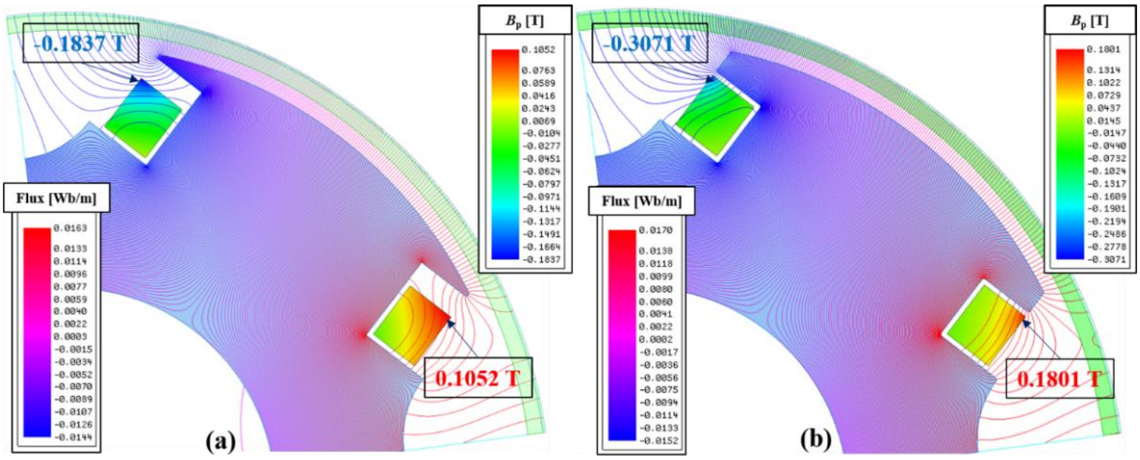

Fig. 3.9. B_p distribution and magnetic flux line plots for (a) H_l 1 and (b) H_l 5.

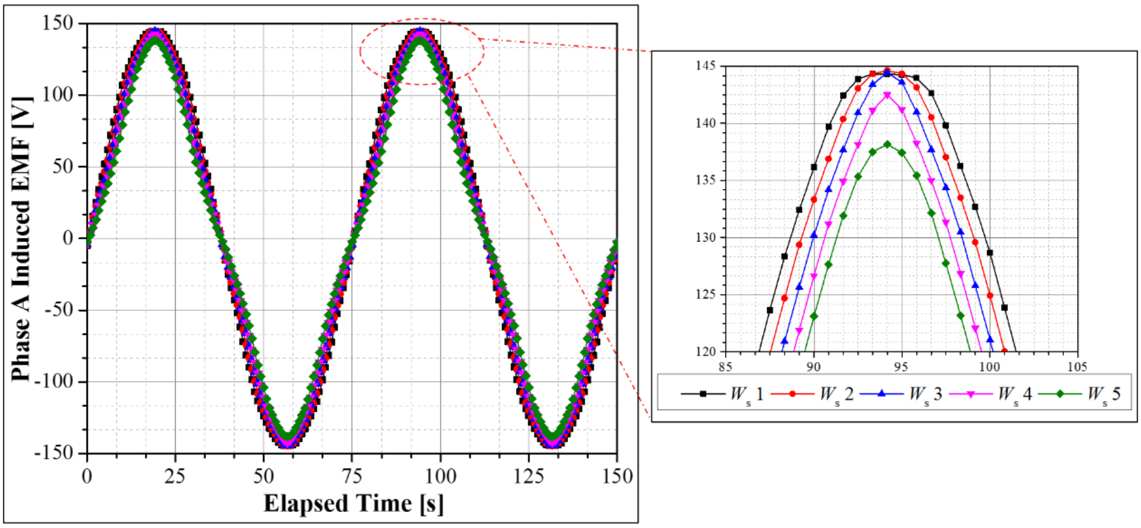

Fig. 3.10. Comparison of phase-A induced-EMF waves according to the W_s values

Furthermore, to review the analysis results according to the changes in W_s, the root mean square (RMS) values of the induced voltage (E_i) corresponding to each W_s are calculated and then reduced from 102.9 to 87.85 V_{rms}. From the results of W_s 1 to W_s 3, as W_s become shorter, the maximum value of E_i increases; however, the RMS value of E_i decreased, as shown in Fig. 3.10, because the linkage flux was concentrated at the pole-shoe center and leaked at the end of the shortened pole shoe. Moreover, the B_p and L_f values decrease when W_s become shorter for the same reason as that of the effects of the change in H_l.

Finally, the effects of the change in H_s on the machine characteristics are investigated. As H_s of the shoe end decreases, the air gap length between the stator-teeth end and shoe face of the salient-field pole become unbalanced.

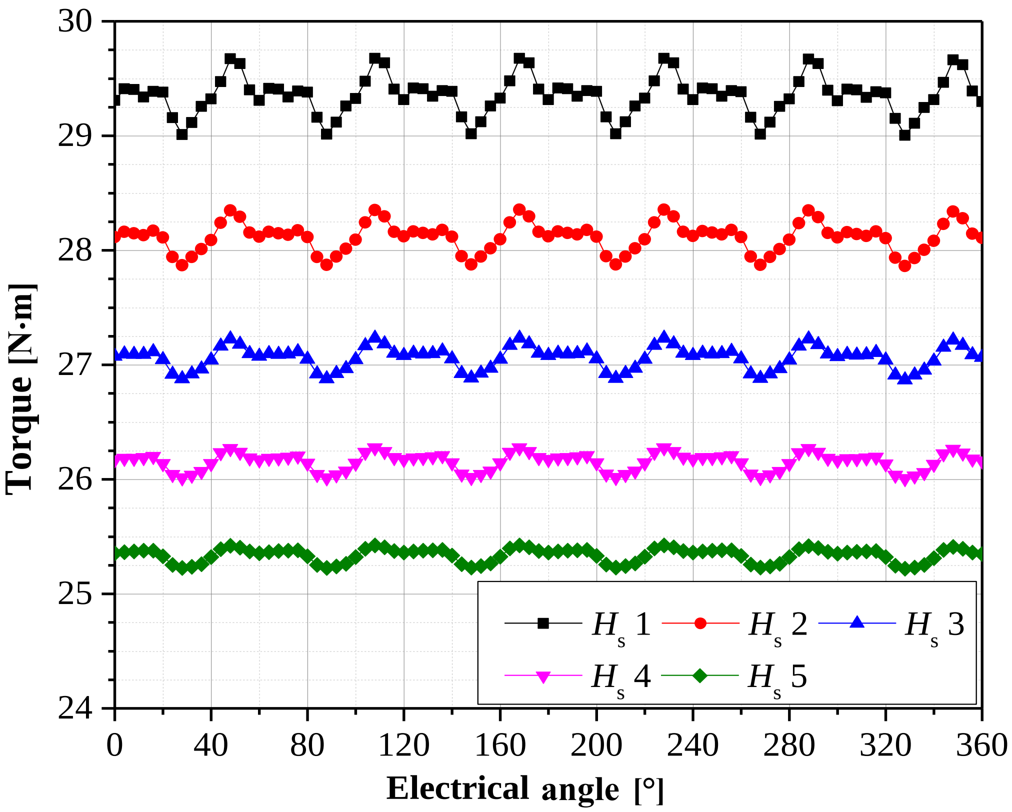

Fig. 3.11. Comparison of the torque profiles according to the H_s values

This result means that the shapes of the magnetic-flux wave in the radial direction changed from a square wave to a sinusoidal wave because the leakage flux is increased by the shortened H_s at the pole-shoe ends. Thus, the linkage flux or EMF waveforms are much closer to a sinusoidal waveform. The characteristics of the voltage THDs and T_{rc} improves with the decrease in H_s according to this explanation. However, the E_i and T_r magnitudes decrease with the decrease in H_s, as shown in Fig. 3.11, because of the larger air gap length, i.e., higher magnetic reluctance at the shoe ends [67].

The performances of the 2G HTS coil, such as I_c and AC loss, are critically dependent on the magnitude of B_p, i.e., I_c and AC loss decreases and increases, respectively, with increasing B_p. Thus, for all results of parametric-analysis described above, it concluded that the optimization of H_l and W_s is considered to be most effective way to enhance performance of 2G HTS coil in iron-core type HTSRM, especially with large-scale capacity.

C. Machine-performance analysis

For the optimized structure of the salient-pole shape of the 1 kW class HTSRM, the geometric dimensions were determined based on the parametric-analysis results presented in Table 3.6. The magnitudes of W_l, H_l, W_s, and H_s were set to 56, 16, 77.2 and 1.21 mm, respectively, by considering the parameter specifications presented in Table 1. In particular, we considered the values of the T_{rc}, B_{p}, and L_{f} parameters to be as low as possible. The final model with the specified dimensions was analyzed and compared with the reference model.

Table 3.7 lists the comparison results of the reference and final models under a steady-state motor operation. E_{i} and T_{r} of the optimal model were approximately 7% lower than those of the reference model. However, the other parameters, i.e., T_{rc}, B_{p}, and L_{f} characteristics of the optimal model, were enhanced and were better than those of the reference model in terms of the vibration and noise of the machine, stability of the HTS coil operation, and smooth excitation of the HTS coil fed by CSFE, respectively. Especially, using I_{c} versus B_{p} curve of 2G HTS wire from SuperPower Inc., as shown in Fig. 3.12 [68], the magnitude of I_{c} increased from 168 to 185 A as magnitude of B_{p} decreased from 0.308 to 0.22 T by comparing the estimated I_{c} values between reference and optimal models. The electrical power in the rated operation was calculated as 1144 W, and the maximum power under the overloaded operation can be increased up to 2290 W, with a maximum stator current of approximately 8 $\mathrm{A_{rms}}$.

Fig. 3.13 shows the characteristic curves of the optimal model to estimate the induced-EMF (K_{E}) and torque (K_{T}) constants, which are defined as the curve slopes $\mathrm{d}V/\mathrm{d}\omega$ and $\mathrm{d}T/\mathrm{d}I_{\mathrm{a}}$, respectively. The calculated K_{E} and K_{T} values of the optimal model were 2.28 $\mathrm{V_{rms}/(rad{\cdot}s)}$ and 6.84 $\mathrm{N{\cdot}m/A_{rms}}$, respectively. This confirmed that the magnitudes of E_{b} and T_{r} were directly proportional to N_{s} and I_{a}, respectively, and no saturation influence of both the rotor and stator according to the increase in I_{a} was observed.

In the motor-operation case, the 1 kW class HTSRM was driven by a voltage-source inverter and controlled using a maximum-torque-per ampere (MTPA) control method for efficient operation in a constant torque region [69]–[72]. Thus, the T_{r} and T_{rc} characteristics according to various current phase angles (β) were analyzed to generate a maximum torque with constant I_{a}, as shown in Fig. 3.14. The maximum torques in both 4 and 8 $\mathrm{A_{rms}}$ armature-current cases were generated at β values of -10° and -20°, and the torque magnitudes were 27.87 and 58.61 N·m, respectively. However, the torque ripples were minimized above the β values for MTPA control. All analysis results in this chapter will be used as a technical reference for further works, i.e., no-load and loaded tests to evaluate the output performance of the 1 kW class HTSRM.

Table 3.7. Comparison-analysis results considering salient-pole shapes

Comparison models	**Machine-parameter values**					
	$\boldsymbol{E_{\mathrm{i}}}^{\#}$ **[$\mathbf{V_{rms}}$]**	**THD**$^{\#}$ **[%]**	$\boldsymbol{B_{\mathrm{p}}}^{\#\#}$ **[T]**	$\boldsymbol{L_{\mathrm{f}}}^{\#\#}$ **[mH]**	$\boldsymbol{T_{\mathrm{r}}}^{\#\#}$ **[N·m]**	$\boldsymbol{T_{\mathrm{rc}}}^{\#\#}$ **[%]**
Reference model	102.9	1.088	0.308	37.98	29.35	2.29
Optimal model	95.72	0.864	0.221	34.51	27.30	1.66

$^{\#}$: No-load operation, $^{\#\#}$: Loaded operation

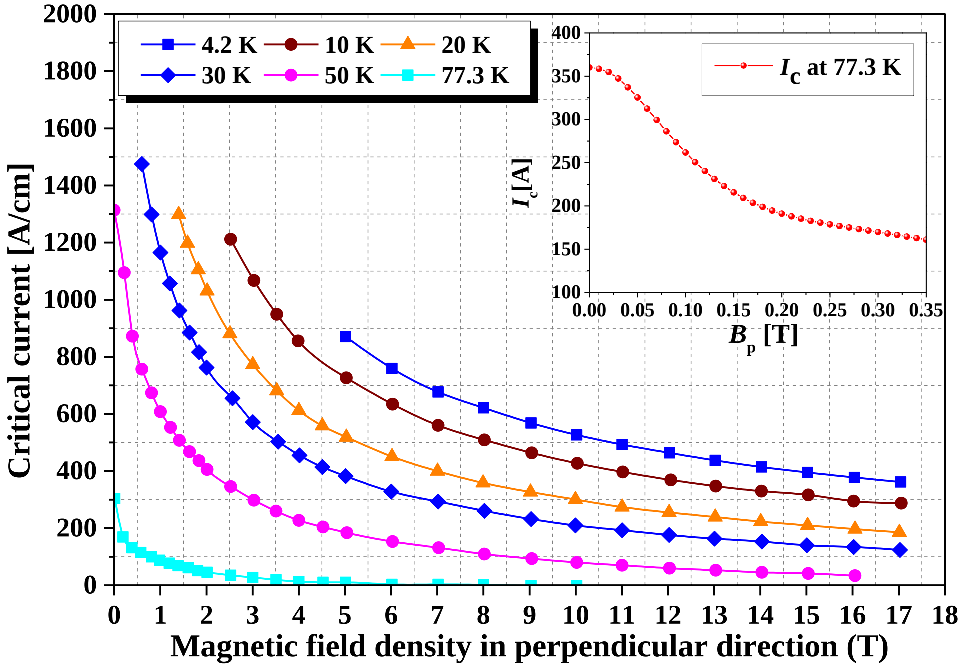

Fig. 3.12. I_c versus B_p curve of the 2G HTS wire from SuperPower Inc.

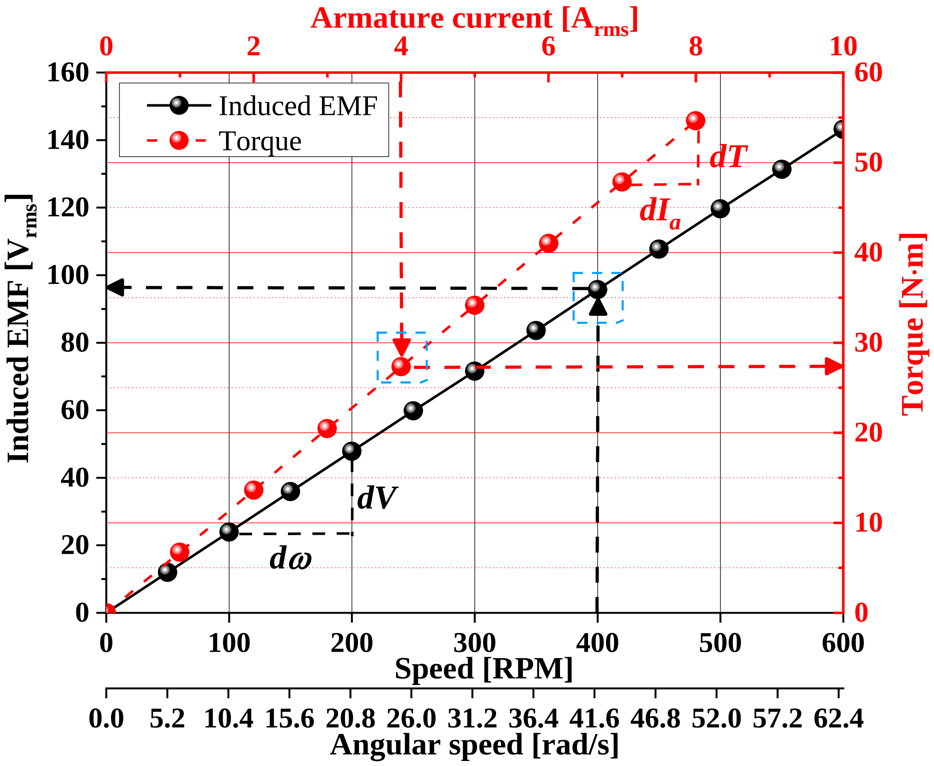

Fig. 3.13. Changes in induced EMF and T_r according to N_s and I_a

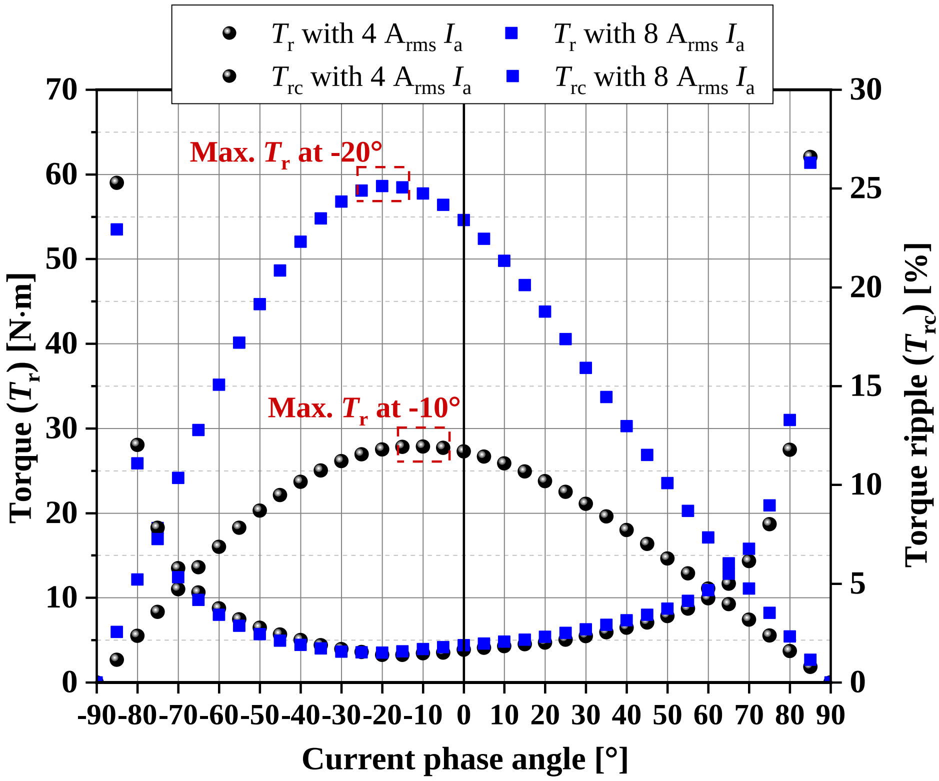

Fig. 3.14. Changes in T_r and T_{rc} according to various current phase angles

3.2. Analysis of operational characteristic for the prototype HTS rotating machine

3.2.1. Optimal configuration of HTS rotating machine

A. Overall structure

Figs. 3.15 and 3.16 show the cross-sectional view and 3D configuration of the 1 kW class HTSRM, respectively, which are modeled using SolidWorks CAD and are manufactured as the final prototype for the 1 kW class HTSRM. A magnetic air gap between the inner and outer radii of the stator core was set to 7 mm considering structural air-gaps, thickness of cryogenic structure, i.e., cryostat, LN2 cylinder-can. A structural air gap between stator inside and rotor outside is designed to be 1 mm.

Based on the rotor structure where the rotor part of CSFE and HTS field pole are combined on one shaft axis, a load side of HTS rotor to connect the prime mover is designed and fabricated with the assembly of torque tube and solid shaft to maintain suitable mechanical rigidity. An opposite load side of HTS rotor is designed and manufactured with torque disk and hollow shaft in considerations of the space for LN2 cooling pipes and the indirect rotational torque of the prime mover. In particular, the structure change to the torque disk at the opposite load side of HTS rotor can be expected to decrease the conduction heat by lengthening the heat transferred path without increasing the length in the axial direction as shown in Fig. 3.16(b) [57].

Moreover, a vacuum port for maintaining the vacuum state inside the HTS rotor, a signal feedthrough for drawing out the signal lines inside the rotor, signal slip-ring for transmission to stationary data acquisition (DAQ) equipment, and magnetic ferro-fluid seal for supplying liquid nitrogen to the rotating rotor at constant speed and vacuum are positioned on the hollow shaft at the opposite load side of HTS rotor. The cooling pipelines is located at the center of HTS rotor inside through the hollow shaft, thereby resulting in supply and discharge of LN2, which is to cool down the rotor assembly integrated with CSFE and HTS field pole.

The rotor pole, which is numerically designed in subsection 3.1.2, is specifically embodied in consideration of the junction structure between each field pole. The smaller joint resistance in superconducting loop is more effective for increasing fully saturated current on FCs charged by HTS flux pump. Thus, to decrease the joint resistance between each field poles, they are connected to use of 2G HTS wires without metal current leads. The joints between inner sides of HTS SPC is necessary to form series circuit inside HTS field poles. For this purpose, an asymmetric cross-sectional shape of field pole is designed as shown in Fig. 3.16(c).

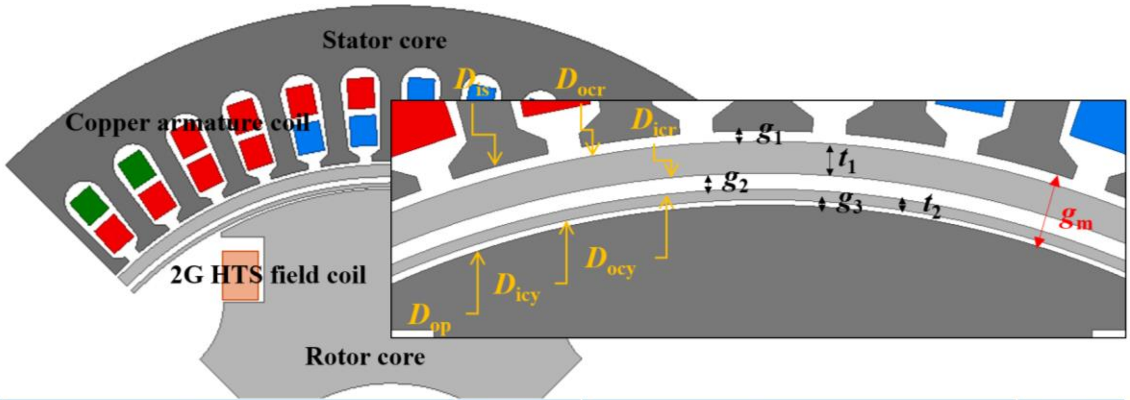

Parameters	Value	Parameters	Value
Inner diameter of stator core, D_{is}	191 mm	Magnetic air-gap, g_m	7 mm
Outer diameter of cryostat (rotor), D_{ocr}	189 mm	Air gap of stator core-cryostat, g_1	1 mm
Inner diameter of cryostat (rotor), D_{icr}	183 mm	Cryostat thickness, t_1	3 mm
Outer diameter of LN2 cylinder, D_{ocy}	180 mm	Air gap of cryostat-LN2 cylinder, g_2	1.5 mm
Inner diameter of LN2 cylinder, D_{icy}	178 mm	LN2 cylinder thickness, t_2	1 mm
Outer diameter of field pole, D_{op}	177 mm	Air gap of LN2 cylinder-field pole, g_3	0.5 mm

Fig. 3.15. Cross-sectional diagram of the 1 kW class HTSRM

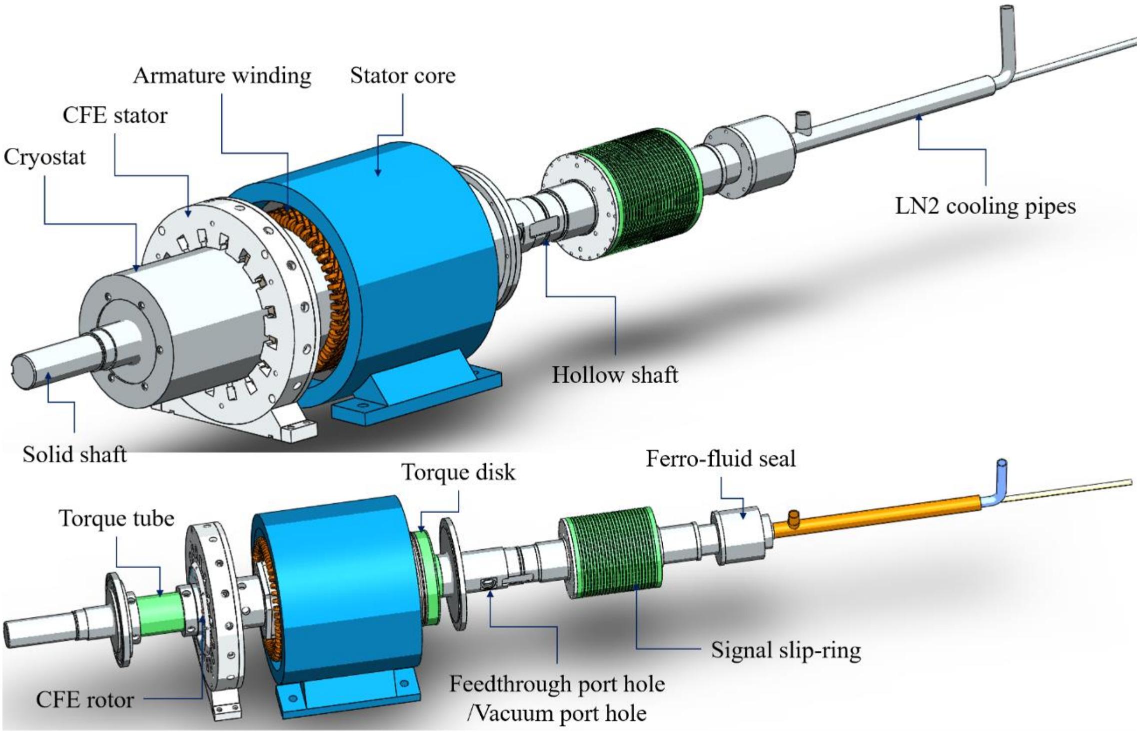

(a) 3D assembly of the 1 kW class HTSM with CSFE

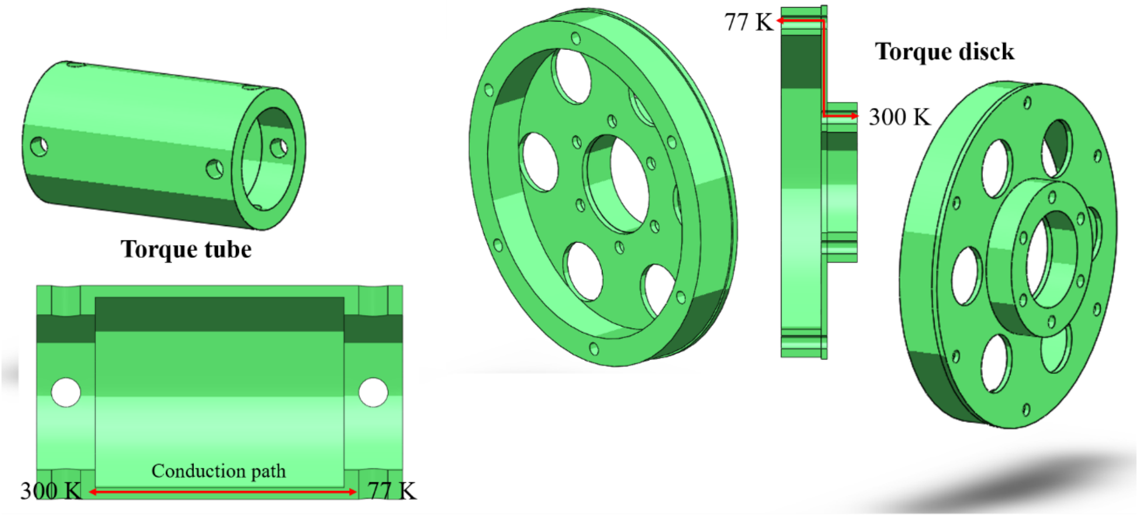

(b) Torque tube and torque disk components

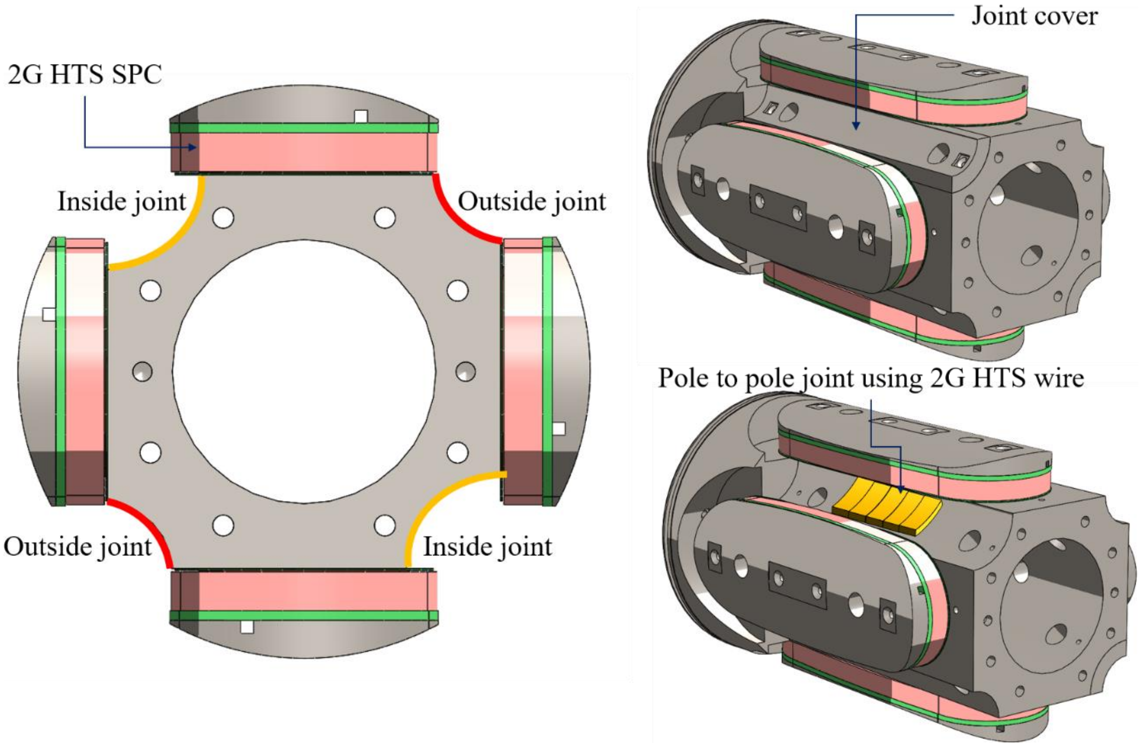

(c) Salient field pole configuration and concept of joint between two poles

Fig. 3.16. 3D configuration of the 1 kW class HTSRM

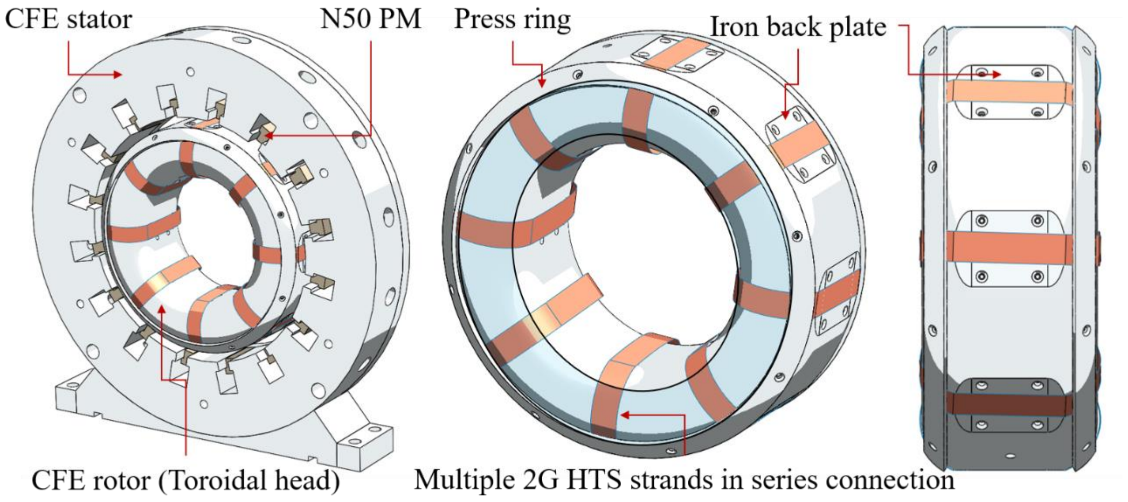

Fig. 3.17. 3D configuration of CSFE

In the structure design of CSFE, the toroidal head structure is devised to wind multiple 2G HTS strands on the rotor of CSFE in series connection, as shown in Fig. 3.17. This is very effective for the series winding method because 2G HTS wire can be wound on round surface of toroidal head without any resistive joints, resulting in maximization of the saturation current charged by CSFE.

In addition, the iron back plates were considered to increase linkage flux from permanent magnets (PMs), resulting in contribution to maximize the saturation current. PMs which are located on the circumference of CSFE stator, injects the periodic magnetic field to HTS strands in the rotor through the relative rotational movement of the rotor.

B. Cooling structure

The open loop thermosyphon cooling method was considered to simply cooling HTS rotor parts (HTS SPCs and CSFE rotor) without any complex device for generation and circulation of cryogen. This method enables easier development of cryogenic cooling system because the vaporized N2 is not returned to the external cooling system for re-cooling in the open-loop cooling mechanism. Any analytical and numerical approaches to estimate the volume, time, and etc. for cryogen re-condensation were not conducted to save the development resources. Therefore, cooling structure was empirically designed for the 1 kW class HTSRM.

Fig. 3.18 shows the cross-sectional side view of the 1 kW class HTSRM to explain the concept of cooling method. The rotary part of CSFE is located on the same rotating axis of HTSRM rotor as shown in Fig. 3.18(c). Therefore, the cooling structure can be simplified by sharing cryogen chamber inside rotor. The HTS field pole is directly connected to the toroidal head of the CSFE. Thus, both rotor parts are cooled together by LN2 and simultaneously rotated in the same rotor shaft. However, the stator of CSFE is located and operated outside the rotor cryostat at room temperature.

Finally, a batch-cooling method using LN2 is adopted to cool the four HTS SPCs mounted on the salient-field pole structure and rotary part of CSFE. LN2 is transferred to the rotor inside of HTSRM through a ferro-fluid seal and triple cooling pipes, as shown in Fig. 3.18(b). The ferro-fluid seal allows the non-rotating state of the triple pipes even while the rotor is rotating. Therefore, the LN2 is flow into inline pipe and gradually starts to be stored in LN2 cylinder that surrounds the HTS coils, as shown in the transparent red rectangular box in Fig.3.18(c). When HTSRM starts to rotate, LN2 is initially concentrated to the cylinder wall surface by the centrifugal force, as shown by the green dashed-arrows in Fig. 3.18(c). Thus, the rotor structures including HTS SPCs and CSFE rotor are directly batch-cooled by the heat transfer of LN2. Therefore, LN2, which is heated and vaporized by rotor thermal losses, i.e., gas nitrogen (GN2), is released outside the HTSRM through discharge pipe, as shown by the red dashed-arrows in Figs. 3.18(b) and 3.18(c). This vaporized N2 after cooling the HTS rotor can be immediately and naturally discharged by the pressure difference between the inside and outside of the generator.

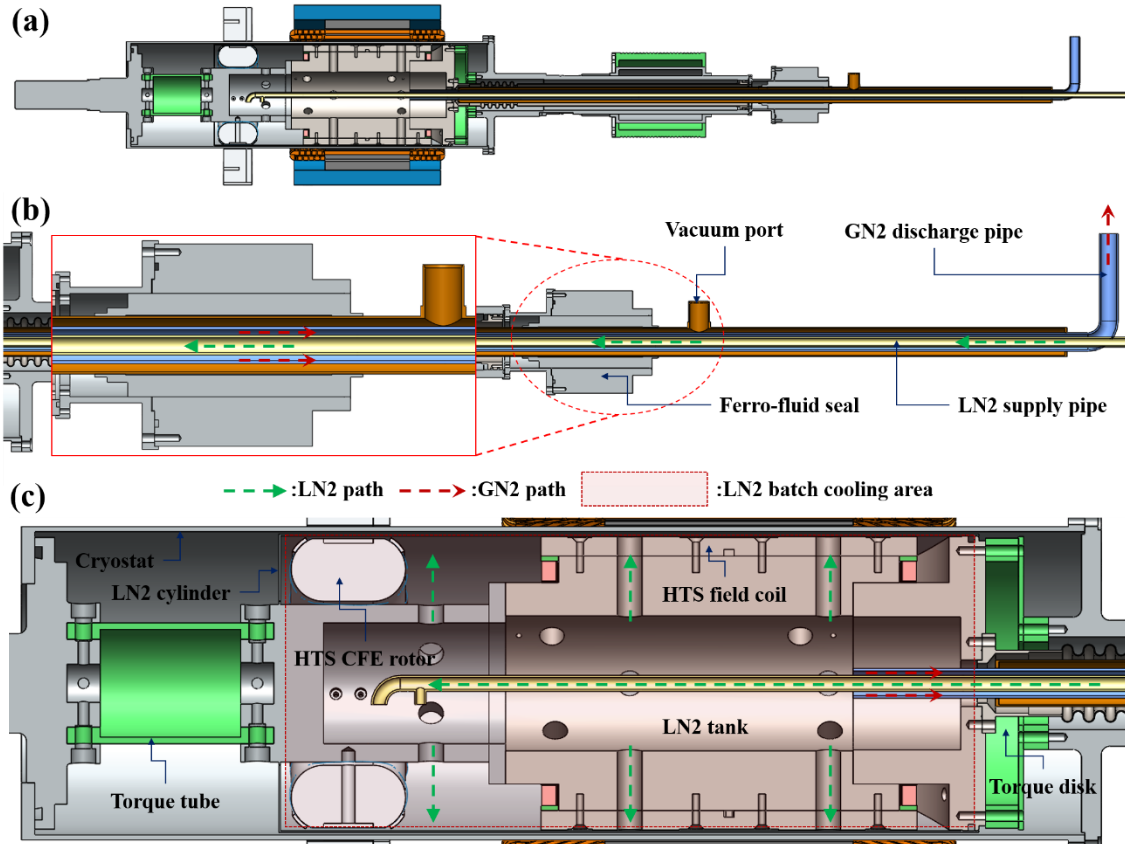

Fig. 3.18. LN2 cooling structure of the 1 kW class HTSG. (a) Overall cross-sectional view of the 1 kW class HTSRM with CSFE, (b) inside view of cryogen transfer pipes, and (c) enlarged inside view of rotor assembled with cooling pipes

3.2.2. Electrical output characteristic analysis of HTS rotating machine

To estimate the machine characteristics and performances according to unexpected I_f charged by CSFE, the electrical output characteristics of the 1 kW class HTSRM, which was structurally decided from sub-chapter 3.2.1, are analyzed by 2D electromagnetic FE simulation. 2D transient solver using the time-step FEA in ANSYS Electromagnetics Suite 19.0 release was considered to save analysis time because leakage magnetic flux in air-gap is very small because of use of magnetic materials and relatively shorter lengths in air-gap and ends of armature and field, resulting in just little bit differences on analysis results between 2D and 3D simulations.

A. Open and short circuits characteristics in no load test

Fig. 3.19 shows the 2D FEA model, which is originated and simplified from final 3D configuration, as shown in Fig. 3.16. This model is defined with permeability of 1 for 2G HTS wire and copper materials and *B*-*H* curves in magnetic materials of rotor and stator cores as shown in Fig. 3.6. A total of 15646 mesh elements are considered as shown in Fig. 3.19(b). In analyses for open and short circuit characteristics (OCC and SCC), the external electric circuits as shown in Fig. 3.20 are connected to three phase armature winding in 2D FE model. The values of leakage reactance at armature ends and phase resistance, which represent the impedance of armature winding are considered to be 1.64 Ω at the S_r of 13.3 Hz and 3.29 Ω, respectively, for both electric circuits.

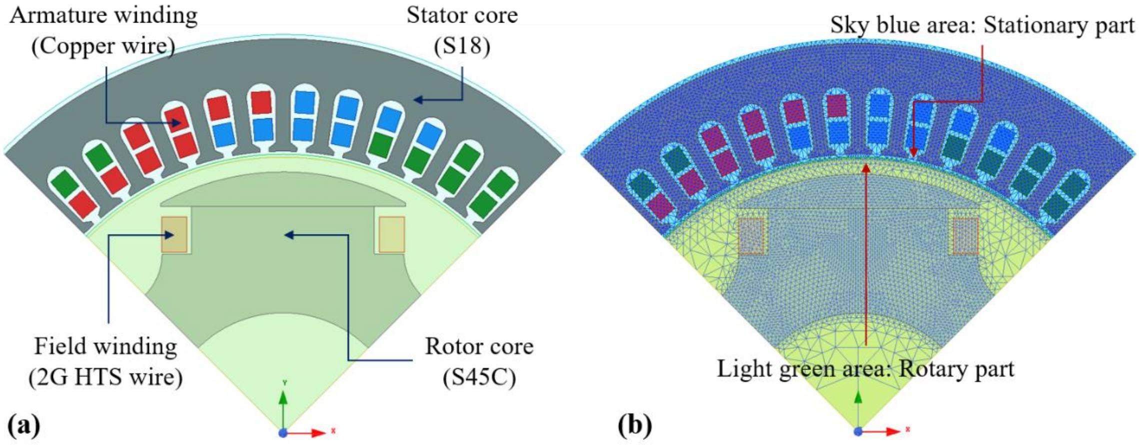

Fig. 3.19. CAD geometry and (b) 2D finite-element splits of a 1 kW class HTSRM

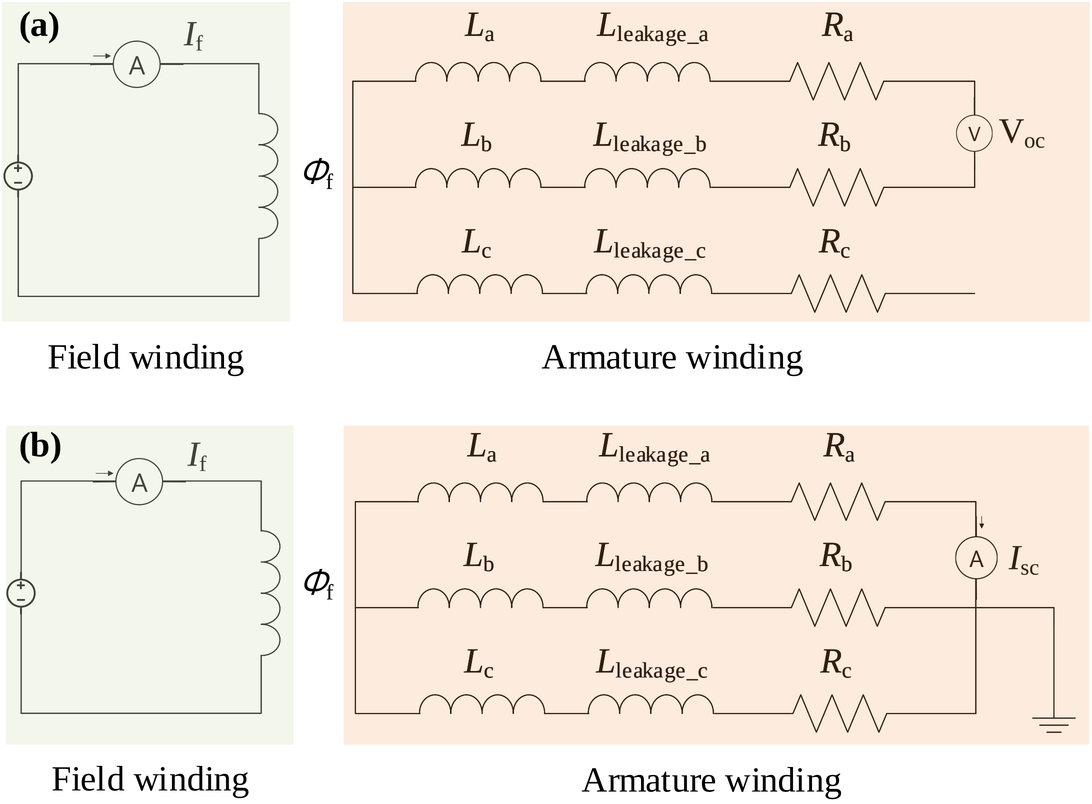

Fig. 3.20. External electric circuit diagrams in (a) OCC and (b) SCC simulations

For OCC analysis, I_f increases from 0 to 120 A at constant S_r and then, terminal phase voltage in open circuit (V_{oc}) is calculated according to changes in the I_f. The ranges from 200 to 800 rpm with 200 rpm interval are considered as the S_r in OCC analysis. Fig. 3.21 shows OCC curves, three phase waveforms of V_{oc} at $S_r = 400$ rpm, and phase-B waveforms of V_{oc} according to changes in the S_r. Up to I_f of 45 A, the value of V_{oc} is linearly proportional to increase in the I_f. However, above I_f of 45 A, V_{oc} starts to saturate according to increase in the I_f because of magnetic saturations in rotor and stator cores. As shown in Figs. 3.22(b) and 3.22(c). Moreover, no noticeable phase imbalance is observed at all S_r, as shown in Fig. 3.21(b). The distortion of the waveforms is observed above the I_f of 90 A as shown in Fig. 3.21(c) because of magnetic saturations in rotor pole shoe and stator teeth. For OCC analysis at the rated S_r, i.e., 400 rpm, I_f should be increased from 30 to ≥ 36 A to generate rated V_{oc}, i.e., 127 V_{rms} (line-to-line 220 V_{rms}).

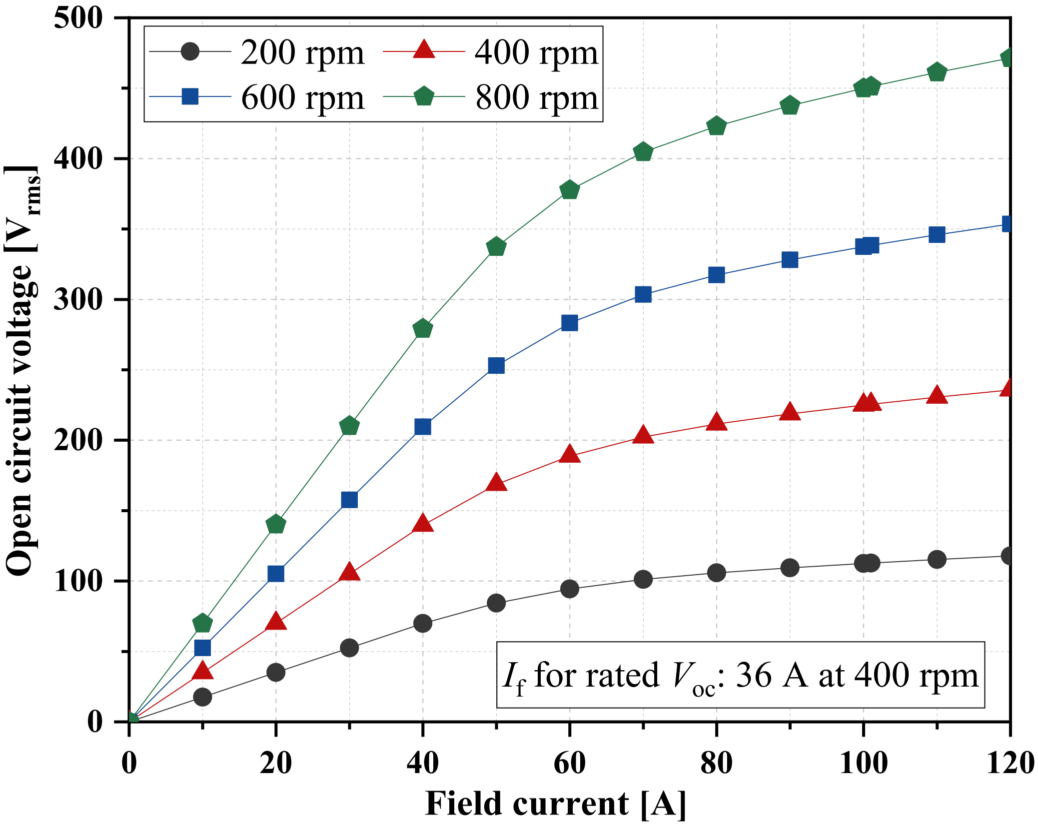

(a) OCC curves according to changes in S_r

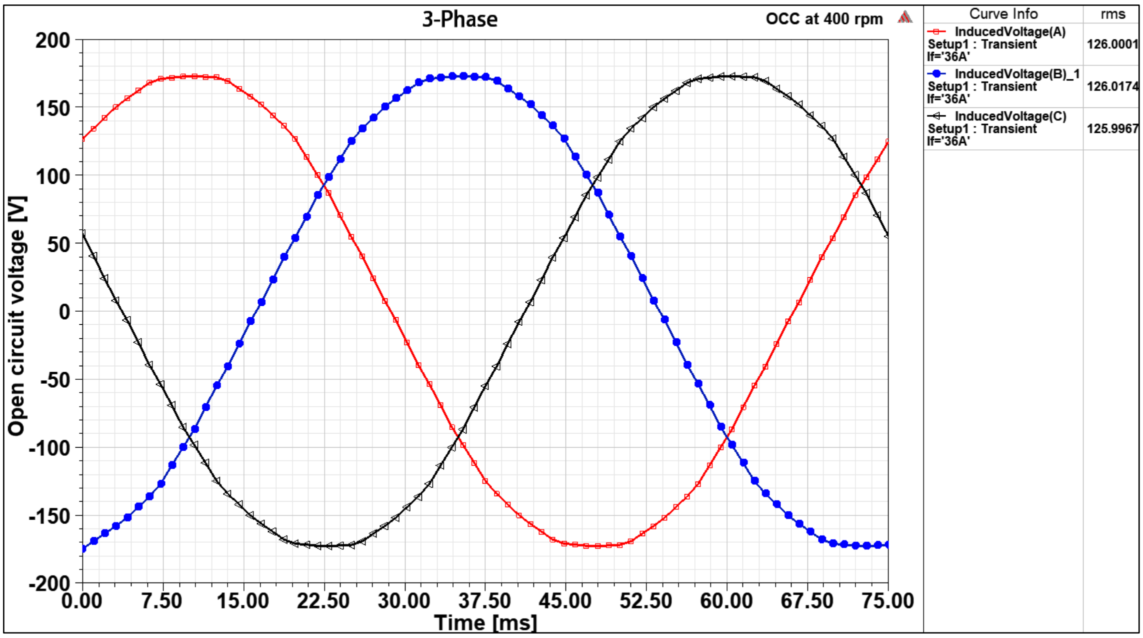

(b) Three phase waveforms of V_{oc} at I_f of 36 A

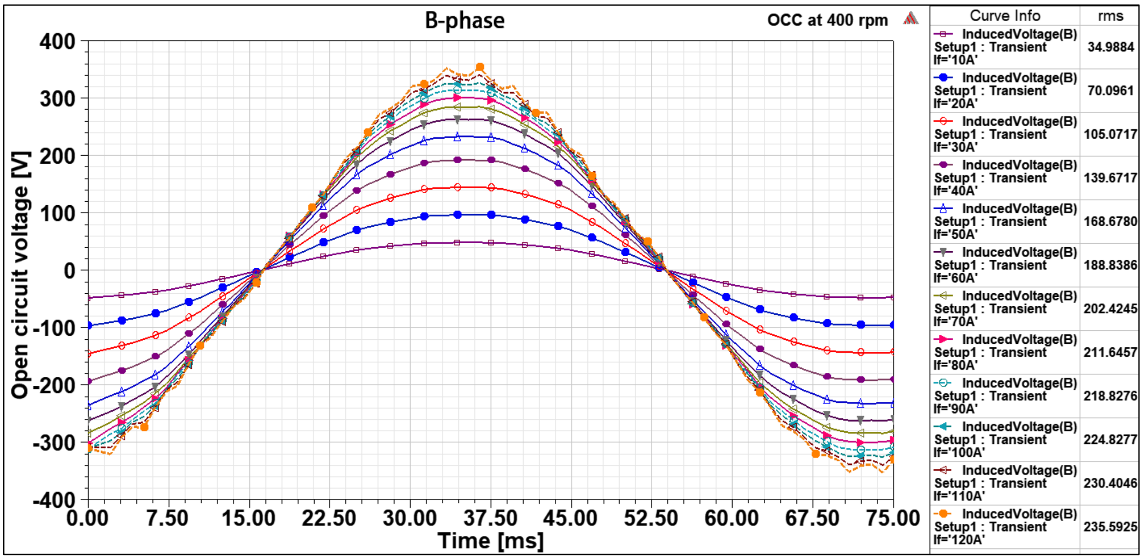

(c) B-phase waveforms of V_{oc} at S_r of 400 rpm according to changes in I_f

Fig. 3.21. OCC curves according to changes in the S_r and phase-B waveforms of V_{oc} according to changes in the I_f

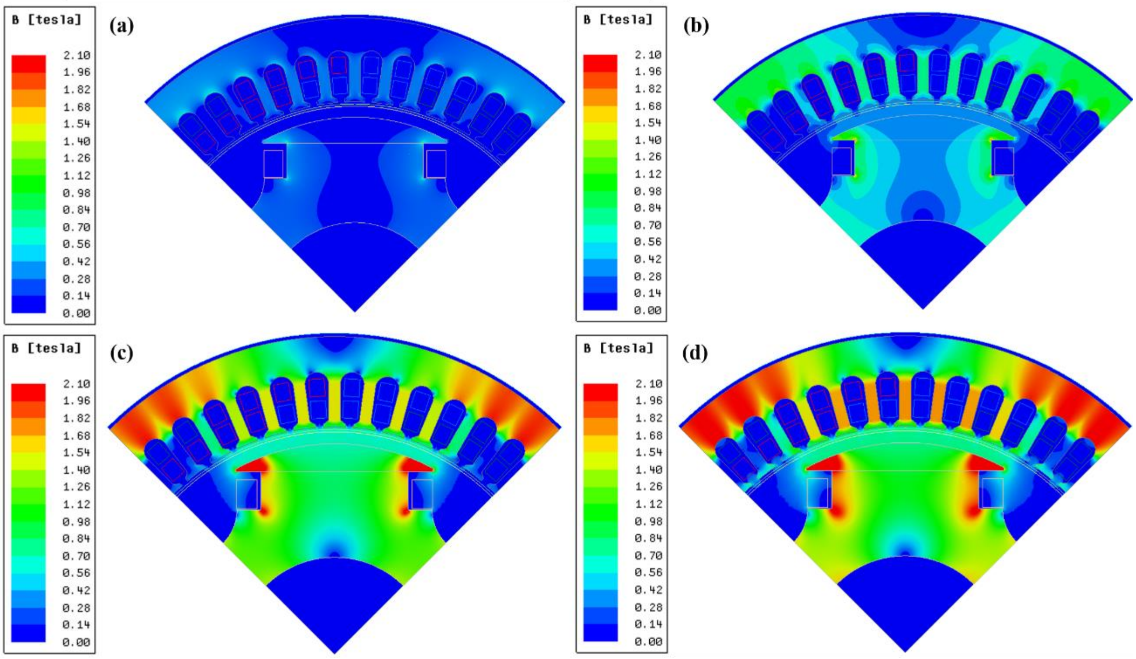

Fig. 3.22. 2D magnetic field distribution with field excitation of (a) 10, (b) 30, (c) 70, and (d) 100 A, respectively, at S_r = 400 rpm

For SCC analysis, the I_f increases from 0 to 120 A at the s_r of 400 rpm and three phase short circuit of armature winding, and then, phase short current (I_{sc}) in armature winding is calculated according to changes in the I_f. Fig. 3.23 shows the SCC curves, three phase waveforms of I_{sc} at S_r = 400 rpm, and phase-B waveforms of I_p according to changes in the I_f. The value of I_f is 12.5 A to flow the rated I_p of 2.64 A. Moreover, the very sinusoidal waveforms and balanced three-phase in the I_p are obtained as shown in Figs. 3.23(b) and (c).

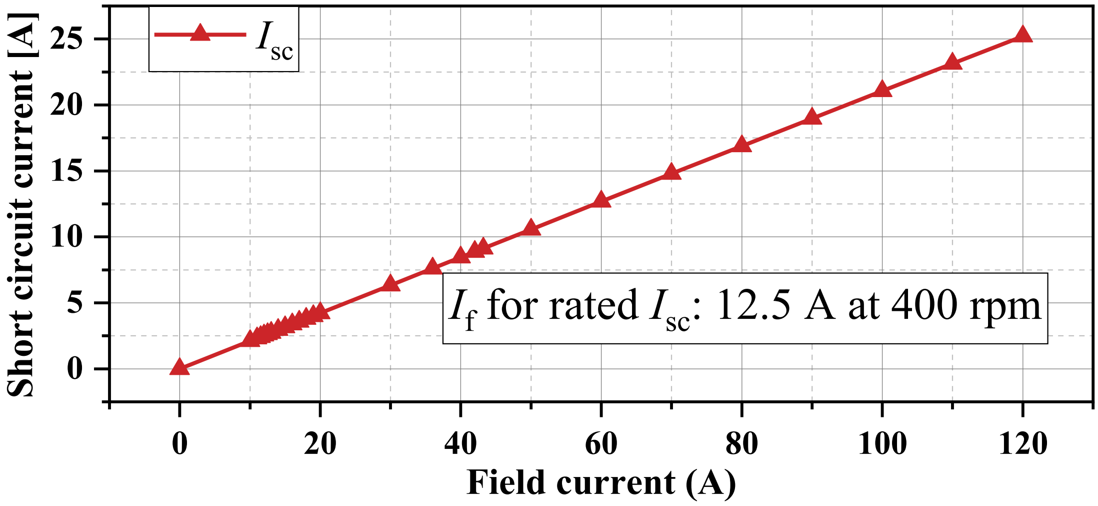

(a) SCC curves according to changes in I_f

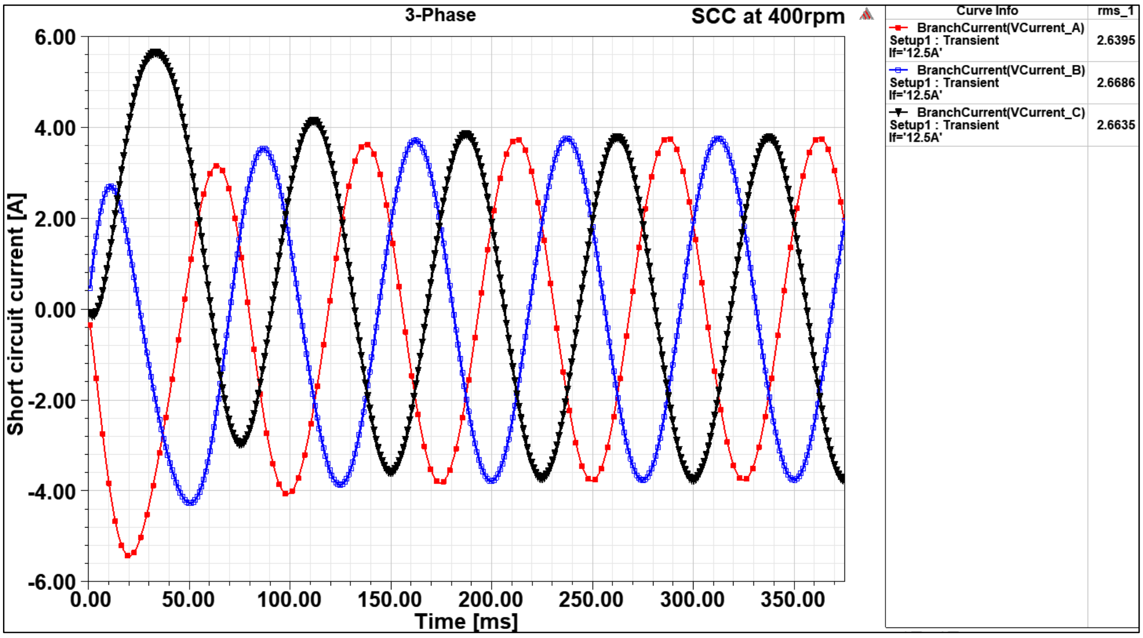

(b) Three phase waveforms of I_{sc} at I_f of 12.5 A

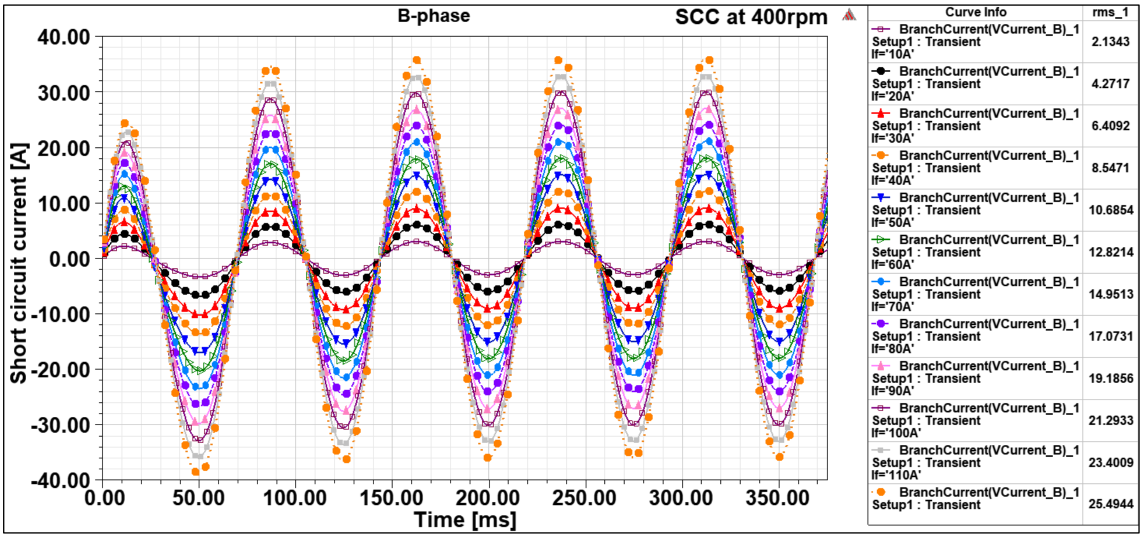

(c) Phase-B waveforms of I_{sc} according to changes in I_f

Fig. 3.23. (a) SCC curves and (b) B-phase waveforms of I_{sc} at S_r of 400 rpm according to changes in I_f

Fig. 3.24 shows OCC and SCC curves at the S_r of 400 rpm according to changes in the I_f. A synchronous impedance (Z_s=V_{oc}/I_{sc}) and corresponding reactance (X_s) as well as short circuit ratio (SCR), which is defined as the ratio of the I_f to reach the rated current in the short circuit and the I_f to reach the rated voltage in the open circuit, are calculated through OCC and SCC curves. The Z_s starts to decrease above the I_f of 45 A because the V_{oc} start to saturate caused by the magnetic saturation in iron cores while the I_{sc} linearly increases because of armature reaction. SCR at S_r of

400 rpm is calculated to be 2.88.

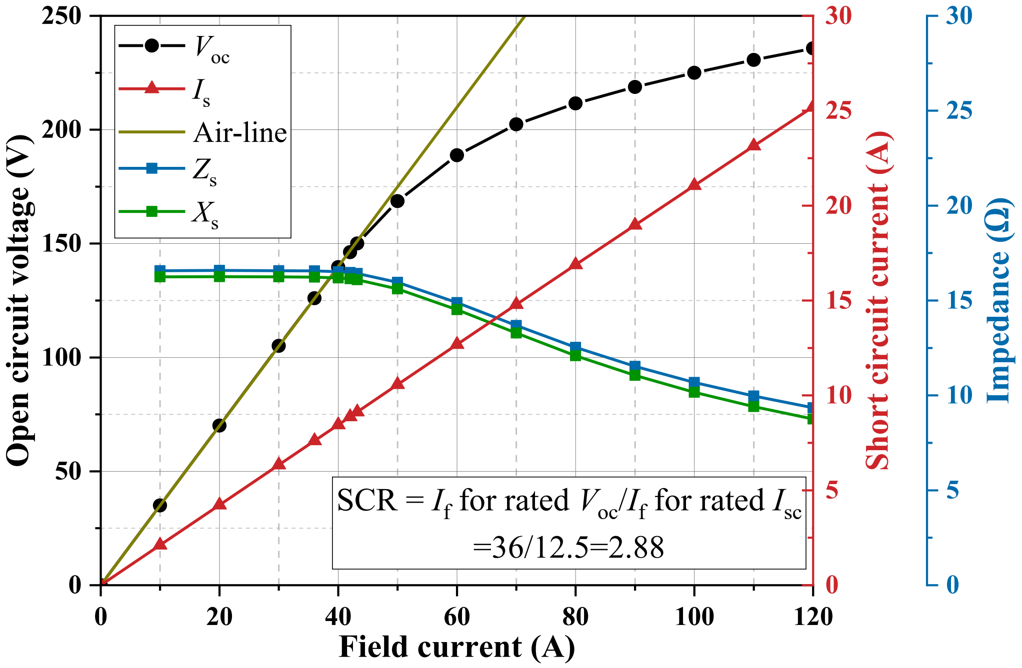

Fig. 3.24. OCC, SCC, Z_s, and X_s curves at S_r of 400 rpm according to changes in I_f

B. Voltage regulation characteristics in resistive load test

The terminal phase voltage in load circuit (V_t) is affected by changes in electrical load because the armature current (I_a) flows and the corresponding voltage drop occurs according to the load. Through coupling of the electrical load circuit, as shown in Fig. 3.25, the active power (P_r), I_a efficiency (η), V_t, and voltage regulation (V_r) characteristics, are analyzed at S_r = 400 rpm according to changes in resistive load, as shown in Figs.3.26−3.30. It is observed that the ranges of load resistance (R_l) from 50 to 500 Ω are considered and η is calculated only considering copper loss in three-phase armature winding.

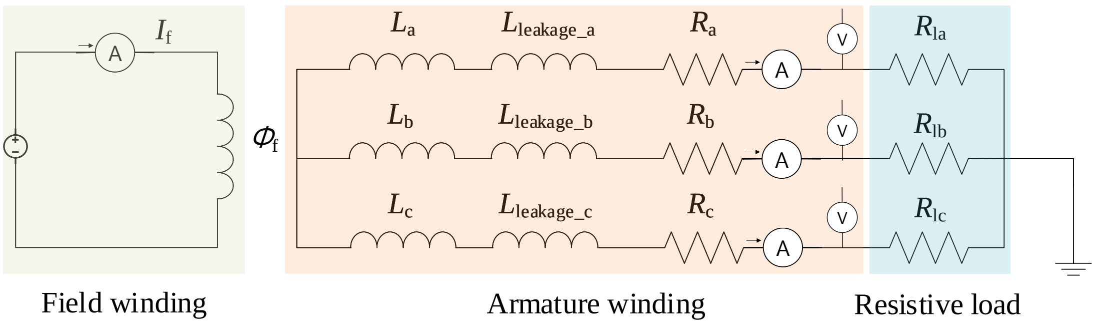

Fig. 3.25. External electric circuit diagram in loaded test

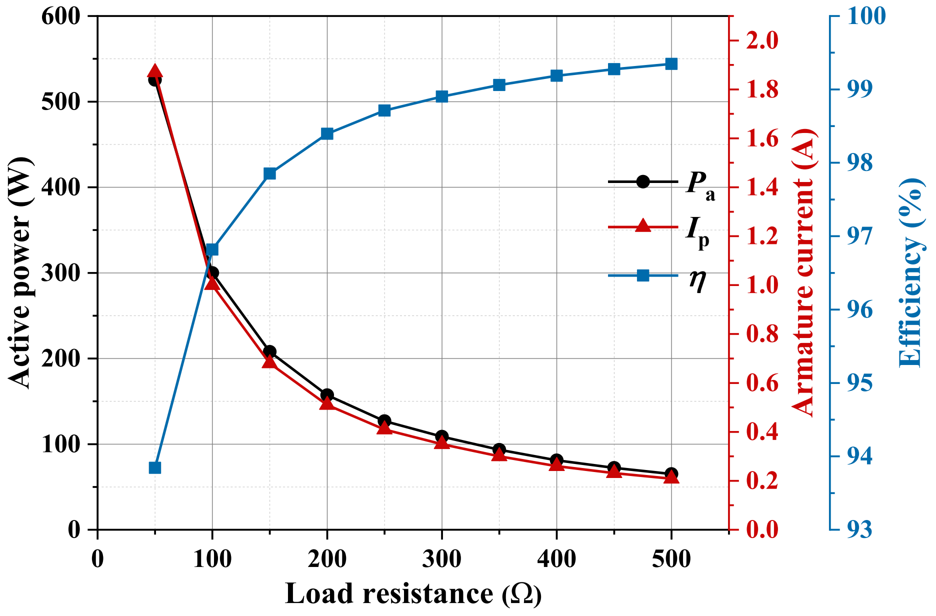

(a) P_a, I_p, and η according to changes in R_l

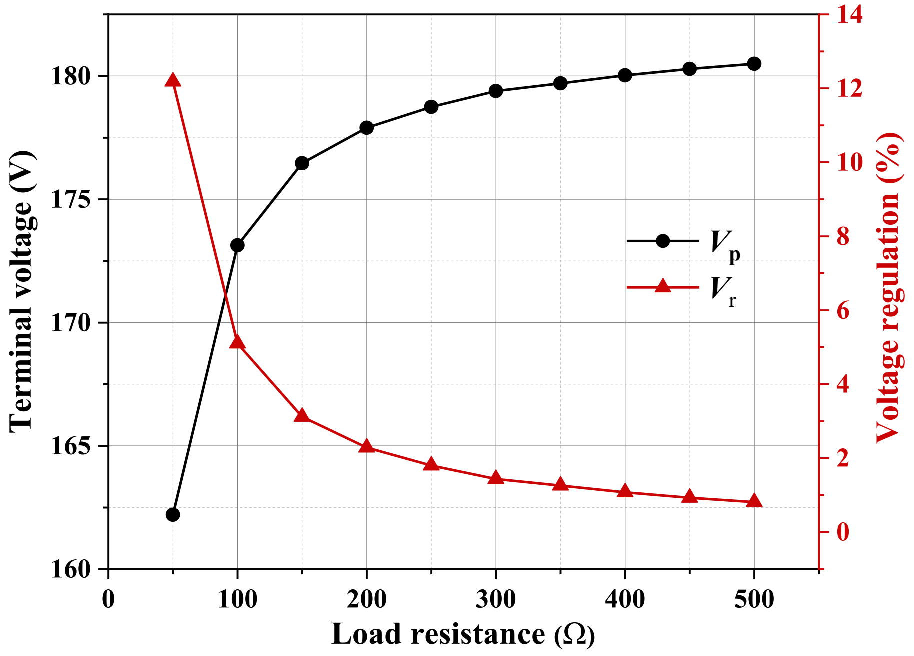

(b) V_p and V_r according to changes in R_l

Fig. 3.26. Load test results at S_r of 400 rpm and the I_f of 30 A according to changes in R_l

For the results obtained with 30 A charge as I_f, as shown in Fig. 3.26, the rated power of this machine (1000 W class) is not generated at all values of R_l. The maximum value of P_r (525 W) is generated at $R_l = 50\ \Omega$, where η of 93.8% is estimated with copper loss of 34.5 W and the largest value of V_r (12.18%) is produced by the largest voltage drop and armature reaction caused by I_p of 1.87 A_{rms}.

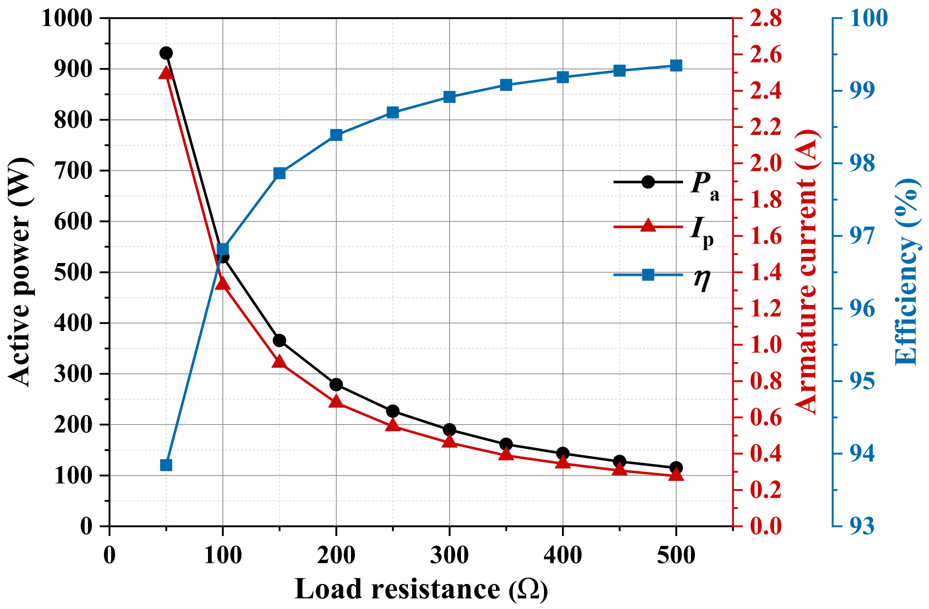

(a) P_a, I_p, and η according to changes in R_l

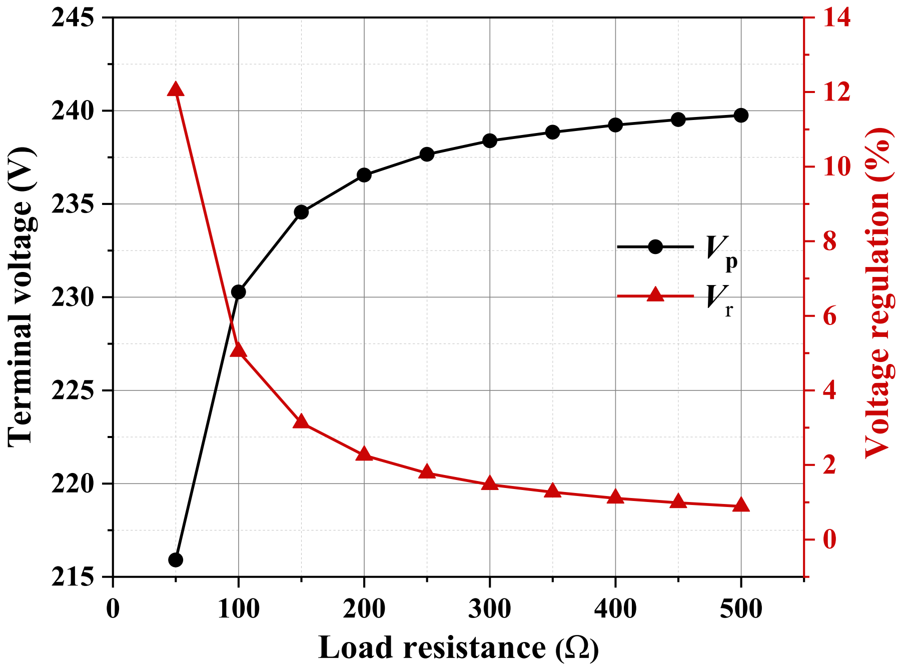

(b) V_p and V_r according to changes in R_l

Fig. 3.27. Load test results at S_r of 400 rpm and the I_f of 40 A according to changes in R_l

For the results obtained with 40 A charge as I_f, as shown in Fig. 3.27, the rated power of this machine (1000 W class) is not generated at all values of R_l like a case of I_f of 30 A charge. The maximum value of P_r (931 W) is generated at $R_l = 50\ \Omega$, where η of 93.8% is estimated with copper loss of 61.1 W and the largest value of V_r (12%) is produced by the largest voltage drop and armature reaction caused by I_p of 2.49 A_{rms}.

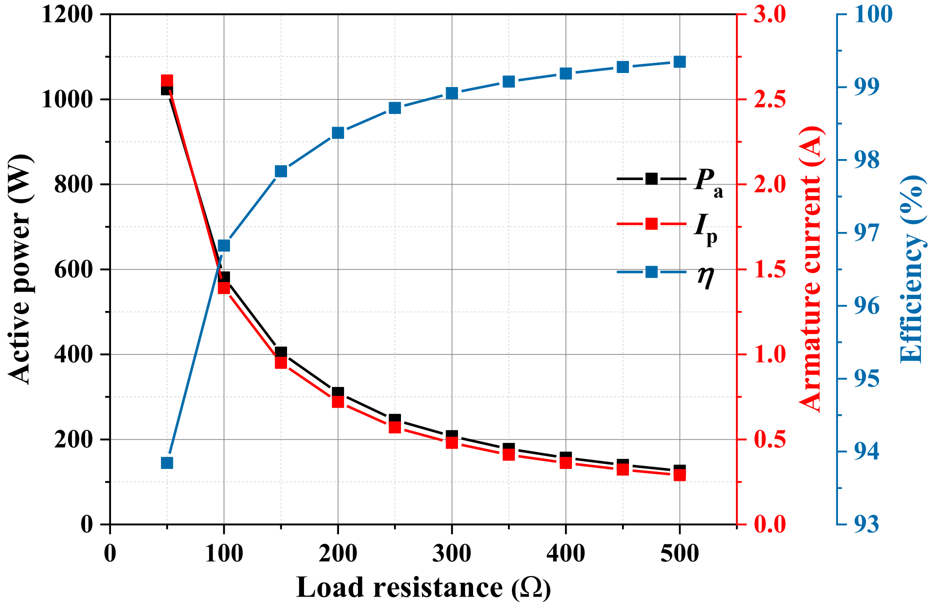

(a) P_a, I_p, and η according to changes in R_l

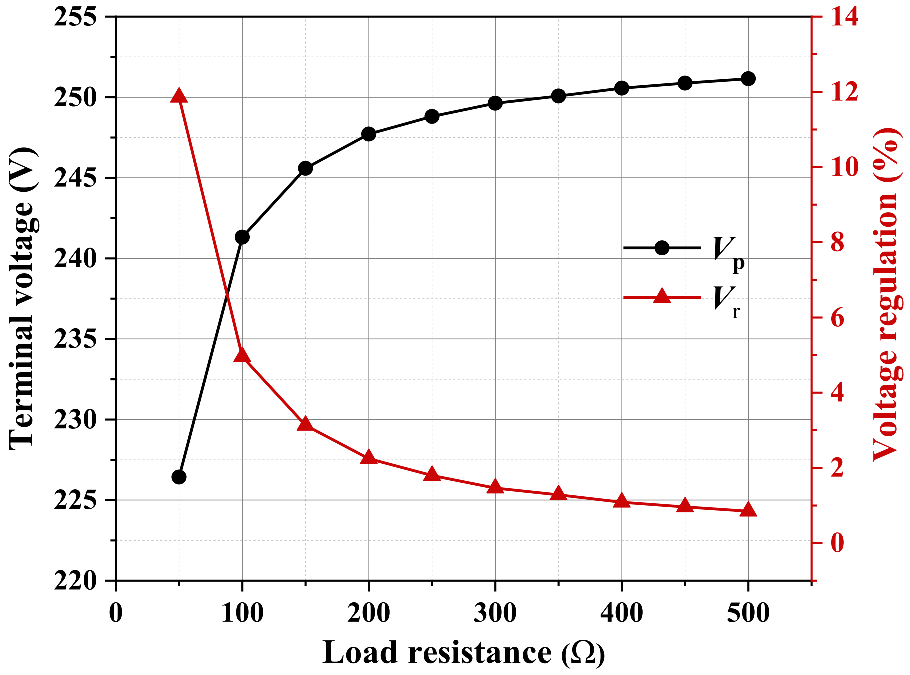

(b) V_p and V_r according to changes in R_l

Fig. 3.28. Load test results at S_r of 400 rpm and the I_f of 42 A according to changes in R_l

It observed that the I_f of 30 A in draft design should be changed to 42 A to generate rated V_t and P_r, namely, 220 V_{rms} and 1000 W, respectively at the R_l of 50 Ω where calculated V_t and P_r are 226 V_{rms} and 1023 W, respectively as shown in Fig. 28.

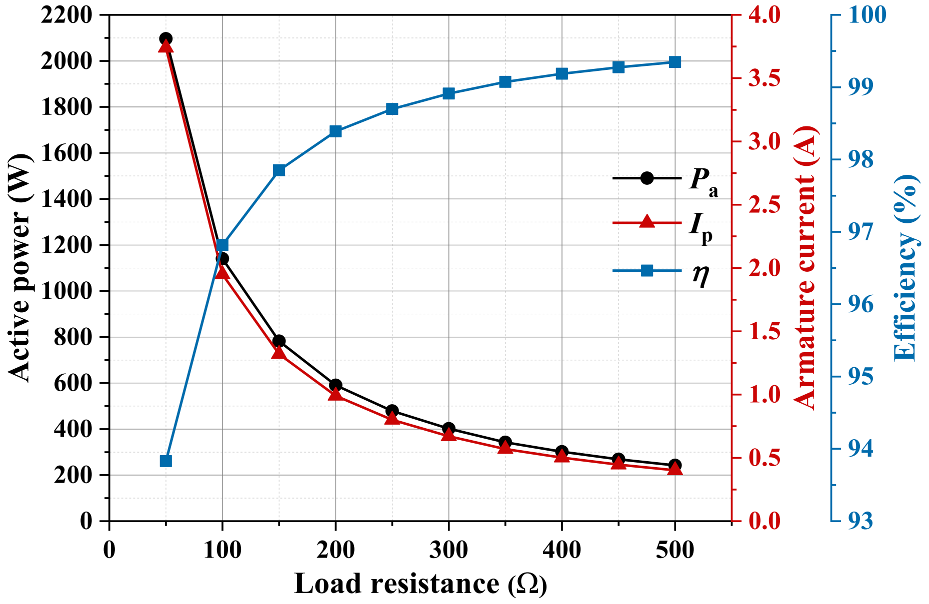

(a) P_a, I_p, and η according to changes in R_l

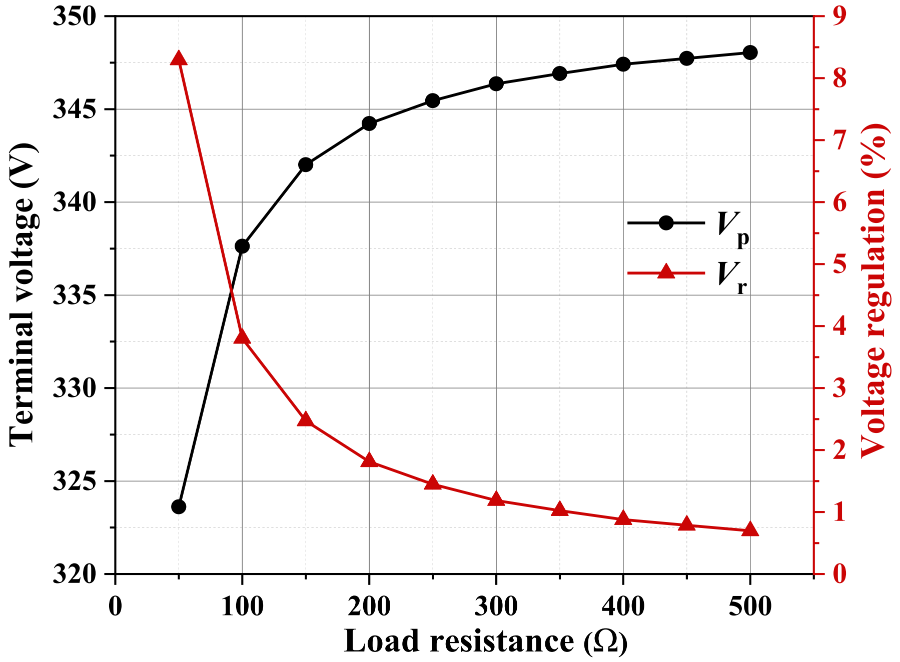

(b) V_p and V_r according to changes in R_l

Fig. 3.29. Load test results at S_r of 400 rpm and the I_f of 70 A according to changes in R_l

For the results with I_f = 70 A charge, as shown in Fig. 3.29, P_r = 1140 W is generated at R_l = 100 Ω, where η = 96.8% and V_r = 3.8% are estimated with copper loss of 37.48 W and voltage drop of 12.8 V_{rms}, respectively, caused by the I_p of 1.95 A_{rms}.

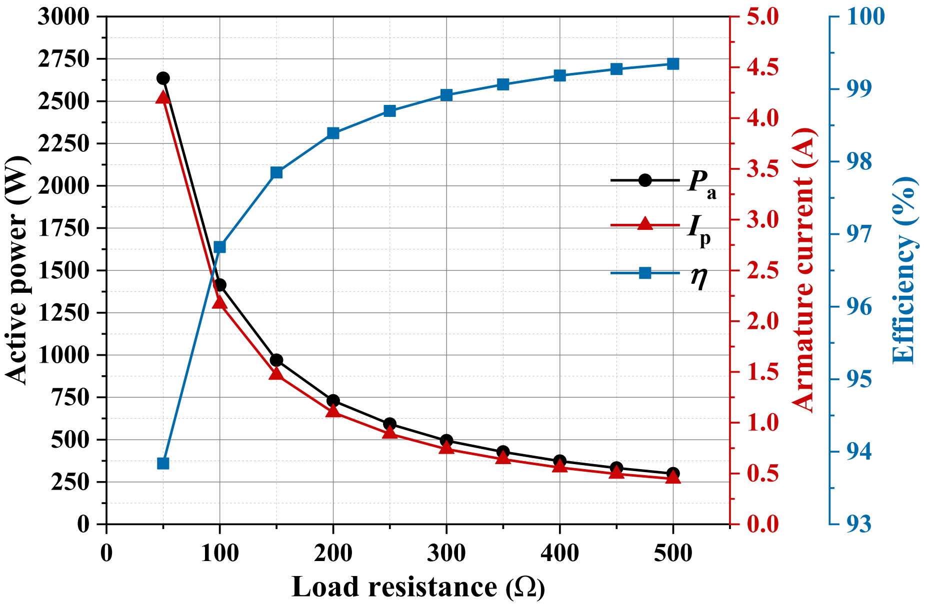

(a) P_a, I_p, and η according to changes in R_l

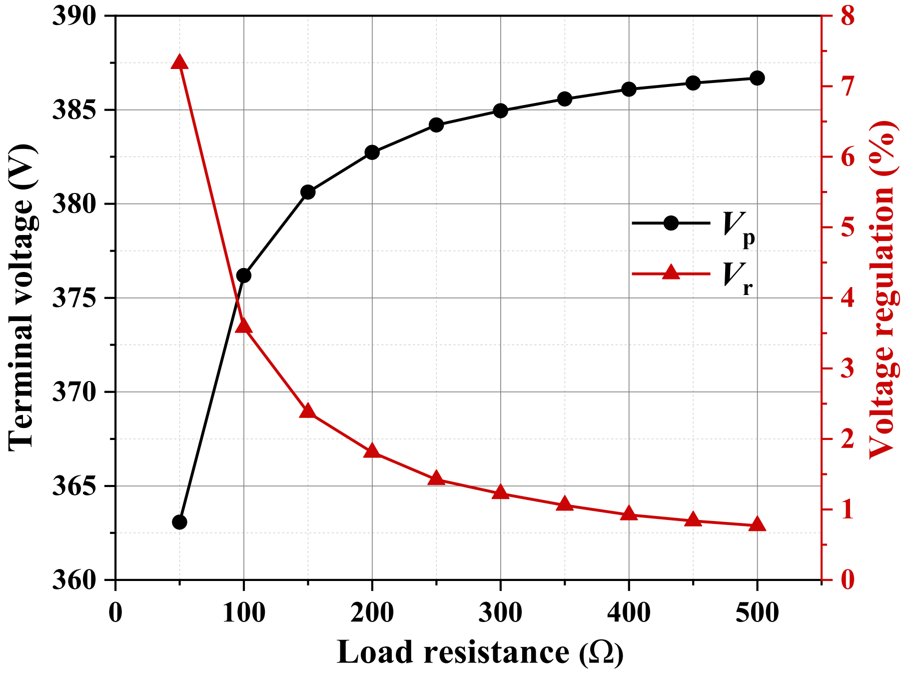

(b) V_p and V_r according to changes in R_l

Fig. 3.30. Load test results at S_r of 400 rpm and the I_f of 100 A according to changes in R_l

For the results of $I_f = 100$ A charge, as shown in Fig. 3.30, $P_r = 1414$ W is generated at $R_l = 100$ Ω, where $\eta = 96.8\%$ and $V_r = 3.6\%$ are estimated with copper loss of 46.41 W and voltage drop of 13.5 V_{rms}, respectively, caused by the I_p of 2.17 A_{rms}.

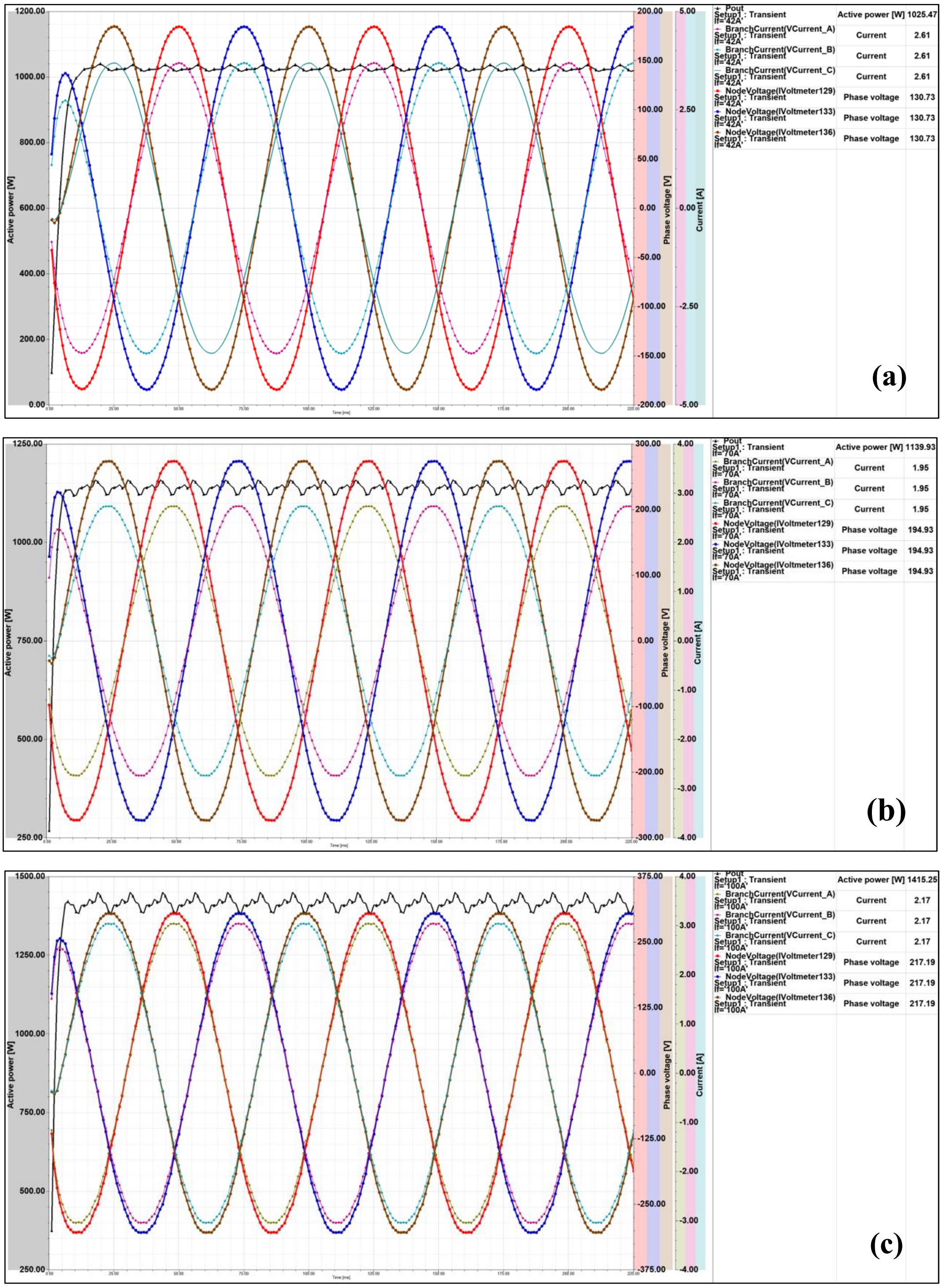

Fig. 3.31. V_t, I_p, and P_r waveforms at $S_r = 400$ rpm and I_f as (a) 42, (b) 70, and (c) 100 A

Fig. 3.31 shows V_t, I_p, and P_r waveforms at the I_f of 42, 70, and 100 A and $S_r = 400$ rpm. The very sinusoidal waveforms and balanced three-phase in the V_t and I_p are observed at all simulated cases. However, ripples in P_r are observed above 70 A charge because of distortions in V_t and I_p caused by magnetic saturation in the iron cores.

3.3. Results and discussion

In this chapter, the 1 kW class HTSM was designed and analyzed based on numerical approach using 2D FEA (ANSYS Electromagnetic Suite) and finally modeled by 3D CAD (SolidWorks).

In the HTS rotor structure, main structures of HTS rotor, such as torque tube, rotating shaft, and rotor cryostat, were conceptually designed considering the mechanical and thermal characteristics of HTS rotor and then, 3D configuration was modeled considering ease of assembly and practical manufacturability.

In the electromagnetic design, structural shape of salient field-pole in HTS rotor was designed and optimized by parametric 2D FEA to meet the I_c performance and required specification from CSFE. Further, the final 3D configuration of field-pole was modeled to build the 1 kW class prototype HTSRM. 2D FE simulations were conducted to analyze output characteristics of prototype HTSRM. Through OCC and SCC analyses in non-loaded test, and VRC analysis in resistive load test, various operating conditions (I_f, S_r, and R_l) were investigated to estimate output performance of the 1 kW class HTSRM in generator mode. In addition, to understand machine characteristics, various machine constants, such as SCR, Z_s, X_l, V_r, P_r, η, and etc. were investigated according to performance of I_f charged by CSFE. It observed that the I_f of 30 A in draft design should be changed to 42 A to achieve the rated V_t and P_r, namely, 220 V_{rms} and 1000 W, respectively. Therefore, it concluded that the rated operating conditions of prototype HTSRM should be carefully considered based on practical performance of full-scale CSFE and simulation results of output characteristic. Moreover, all results can be used as a technical reference for practical implementation and characteristic test of prototype HTSRM.

Chapter 4. Fabrication and Current Charging Experiment of HTS Field Winding

This chapter presents the results of the fabrication and preliminary charging test of 2G HTS coils for the rotor field winding of a 1 kW class HTSRM using the contactless excitation method. The final configuration of the salient field-pole was derived from optimized structural design results presented in chapter 3. Further, all components of the salient field-pole were fabricated and assembled using four race-track HTS SPCs and its basic characteristics, namely, I_c and joint resistance between field poles (R_{pj}), were tested and measured at 77 K.

Moreover, a CSFE was designed based on research results of characteristic investigation in [38]–[41], [47]. Further, the major components of CSFE, such as HTS strands with a toroidal head for the rotary part of CSFE and stationary part of CSFE, were fabricated and assembled with the salient-field pole in same rotor shaft. Furthermore, the charging performance of the I_f was tested in preliminary experiments. In particular, to confirm the technical feasibility of this contactless excitation method i.e., CSFE, on application to the 1 kW class HTSRM, the HTS SPCs on the salient-field pole were charged under various operating conditions of the CSFE in a stationary flux-pump mode before the final fabrication and assembly of HTSRM.

4.1. Design and fabrication of HTS field winding

4.1.1. Design of the rotor pole configuration

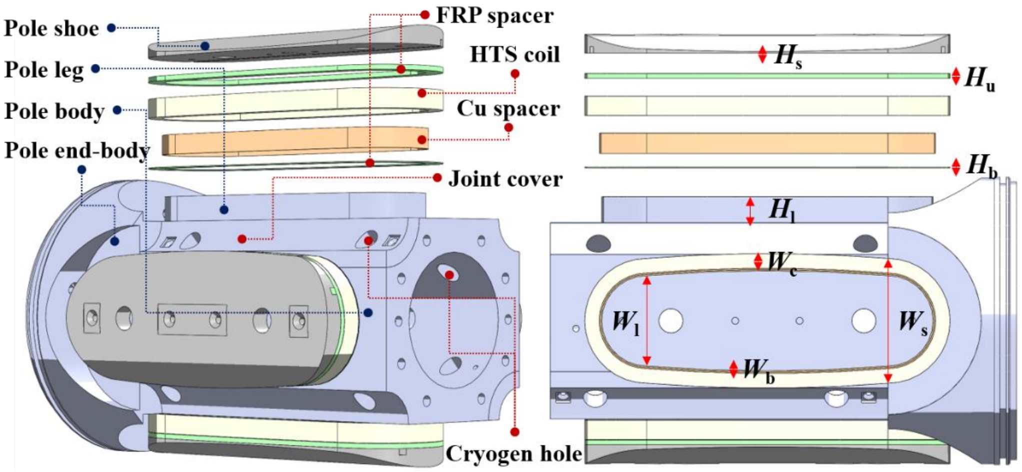

Fig. 4.1. 3D configuration of the salient-field pole structure with HTS race-track SPCs

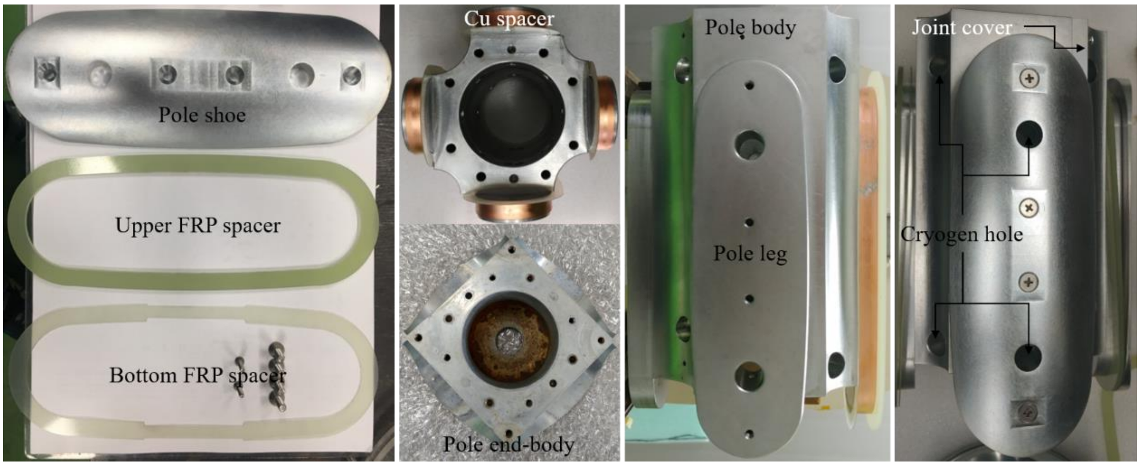

Fig. 4.2. Images of fabricated configuration parts and temporarily assembled field pole

The rotor-field pole with four HTS SPCs was finally designed and fabricated based on the optimized structural design results presented in Chapter 3. This rotor structure was designed to the salient-pole shape using a magnetic material (S45C) to increase the output power density of the rotating machine and reduce the HTS wire length used for the SPCs.

Fig. 4.1 shows the 3D modeling to fabricate the salient-field pole for the 1 kW class HTSRM, which consists of four poles with HTS race-track SPCs wound at each pole leg. Moreover, Fig. 4.2 shows machined and temporarily assembled parts of the salient field-pole structure. The final structural dimensions, which were determined using the FEA results presented in subsection 3.1.2 of Chapter 3, are listed in Table 3.1. The insulation spacers, which were manufactured by glass fiber-reinforced plastic (GFRP) and copper (Cu), respectively, were used to electromagnetically insulate the HTS SPCs from the magnetized salient-field pole structures such as the pole shoe, leg, and body.

The important roles of the pole shoe, i.e., coil cover, are to maximize the flux linkage between the rotor and stator i.e., air gap, and to guide and fix the HTS SPCs from the centrifugal force during rotation. Joint covers are positioned between first and second poles, and third and fourth poles to fix and protect the HTS wires, which is to join the pole to pole. The total sixteen-cylindrical holes are considered as the rotor cooling structure. When the rotor starts to rotate, LN2 is passed to HTS SPCs through the cylindrical holes and start to cool the HTS SPCs as well as pole shoe in earnest by direct heat transfer in LN2 bath. The detailed cooling mechanism and structure were presented in subsection 3.2.1 in Chapter 3. Total weight and volume of this structure were estimated to 33.94 kg and 4.34 m^3, respectively using respective material's density.

Table 4.1. Major design parameters of the salient-pole structure

Parameters	**Unit**	**Values**
Pole structure material	-	S45C (SAE-AISI 1045)
Length of coil straight (pole-leg)	[mm]	150
Upper FRP spacer height H_u	[mm]	3
Bottom FRP spacer height H_b	[mm]	0.5
Pole-shoe height H_s	[mm]	1.21
Pole-leg height H_l	[mm]	16
Pole-leg width W_l	[mm]	56
Pole-shoe width W_s	[mm]	77.2
Copper spacer width W_b	[mm]	1.6
Total weight	[kg]	33.94
Total volume	[m^3]	4.34

4.1.2. Fabrication of HTS field winding

The winding work of the four HTS SPCs and their assembly work with the rotor pole structure were successfully completed, as shown in Fig. 4.6. The four race-track SPCs for the field-pole winding were wound by an SCS 12050 conductor model from SuperPower Inc. The detailed specifications of the 2G HTS wire and SPCs are listed in Tables 4.2 and 4.3, respectively. The wire dimensions were 12 mm wide and 0.064 mm thick. I_c values of the conductor used for the four SPCs were different because of the 100 m spool length.

Table 4.2. Major specifications of 2G HTS wire

Parameters	**Unit**	**Values**
Manufacturer	-	SuperPower Inc.
Conductor type	-	(RE)BCO coated conductor
Conductor model	-	SCS 12050
Conductor width/thickness	[mm]	12/0.064
(RE)BCO thickness	[mm]	1
Stabilizer thickness	[μm]	10
Substrate thickness	[μm]	50
Ave. I_c@77K, 0 T	[A]	350†/339$^\#$
Min. I_c@77K, 0 T	[A]	343†/335$^\#$
STDEV	[%]	1.96†/0.93$^\#$
Ave. n-value	-	33
Stabilizer material	-	Copper

†: used for 1st, 2nd, 3rd poles, $^\#$: used for 4th pole

Table 4.3. Major design parameters of 2G HTS SPCs

Parameters	**Unit**	**Values**
Insulation material/thickness	[mm]	Kapton Polyimide film/0.07
Field winding type	-	Racetrack SPC
Length of coil straight	[mm]	150
HTS Coil width W_c	[mm]	8.04
Winding turns per SPC	-	60
Used conductor length	[m]	$30^{\dagger}/120^{\#}$
Quench voltage V_q	[mV]	$3^{\dagger}/12^{\#}$
Winding force	[N]	143.18

†: used for unit pole, $^{\#}$: used for four poles

Figs. 4.3 and 4.4 show I_c profiles and n values along the 100 m spool, which were used for the first, second, and third SPCs and fourth SPC, respectively. A 2G HTS wire was wound at the magnetic pole body to build the four field windings and the SPCs were co-wound using a 0.07 mm thick polyimide film (Kapton) to provide insulation between the turn and turn layer, and the same winding tension of 143.18 N (14.6 kg-f) was considered for the four SPCs. The total 2G HTS wires used for the four SPC windings was approximately 120 m (30 m × 4 poles). The quench voltage (V_q) values of 3 and 12 mV were considered for the unit and total poles, respectively, using the V_q criterion of 1 μV/cm.

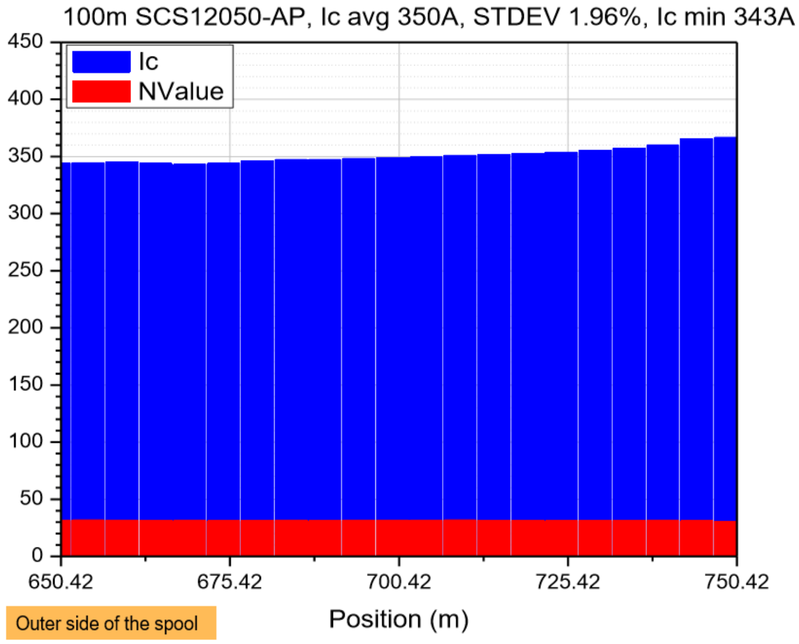

Fig. 4.3. I_c information of 2G HTS wire used in SPCs at 1st, 2nd, and 3rd poles

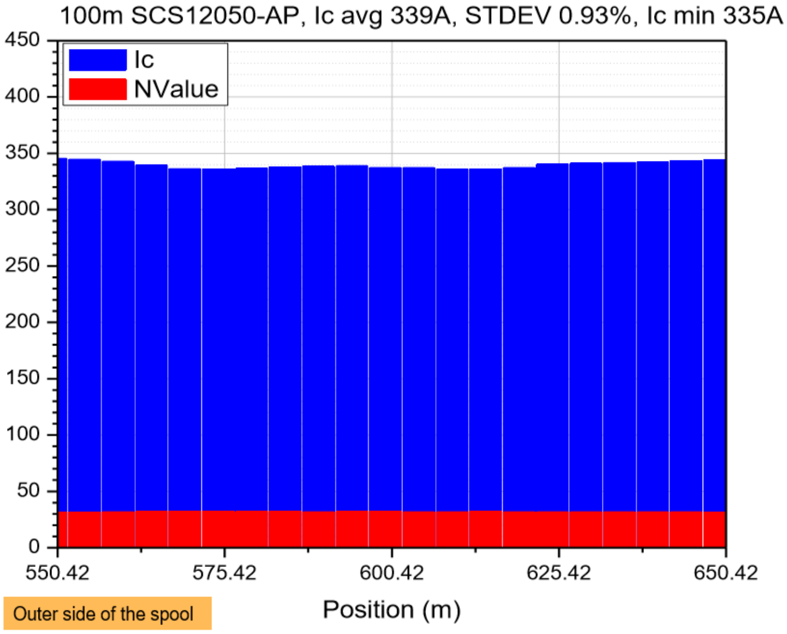

Fig. 4.4. I_c information of 2G HTS wire used in SPC at 4th pole

Fig. 4.5 shows the schematic diagram of the field-pole connection of the 1 kW class HTSRM. To maximize the saturation current of the SPCs from the CSFE, the R_{pj} values should be minimized as much as possible [38], [41]. Therefore, the four poles were connected in series without any metal current leads through the parallel bridge wires to minimize the R_{pj} values, as shown in Fig. 4.5. Finally, these parallel bridges consisted of six HTS wires to join the two poles because we confirm that reducing R_{pj} over a joint length of approximately 7 cm, i.e., 12 mm width x 6 wire, did not show any effect. The second and third SPCs are joined at the outside of each SPC, as shown in Fig. 4.5. However, the first and second SPCs, and third and fourth SPCs are each other joined at the inside of each SPC. Thus, an unbalanced shape between poles is considered in cross-sectional view of the salient-field pole, as shown in Fig. 4.2.

Figs. 4.6(a)–4.6(e) show the photographs of the winding work and fabrication process for HTS field poles of the 1 kW class HTSRM. It is observed that order of each work starts from left- to right-photographs in all figures (Figs. 4.6(a)–4.6(e)). The detailed winding process of the four HTS SPCs and their assembly work are described as follows.

Step 1) To electromagnetically insulate the HTS SPCs from the magnetized salient-field pole structures, inner-side insulation work was conducted in pole body and leg, as shown in Fig. 4.6(a). The bottom FRP spaces were inserted into four-pole legs and simultaneously Kapton and Cu tapes were wound at four-pole legs to form Cu spacers. Further, Kapton tape once again was wound outside the Cu spacers to insulate the HTS wires.

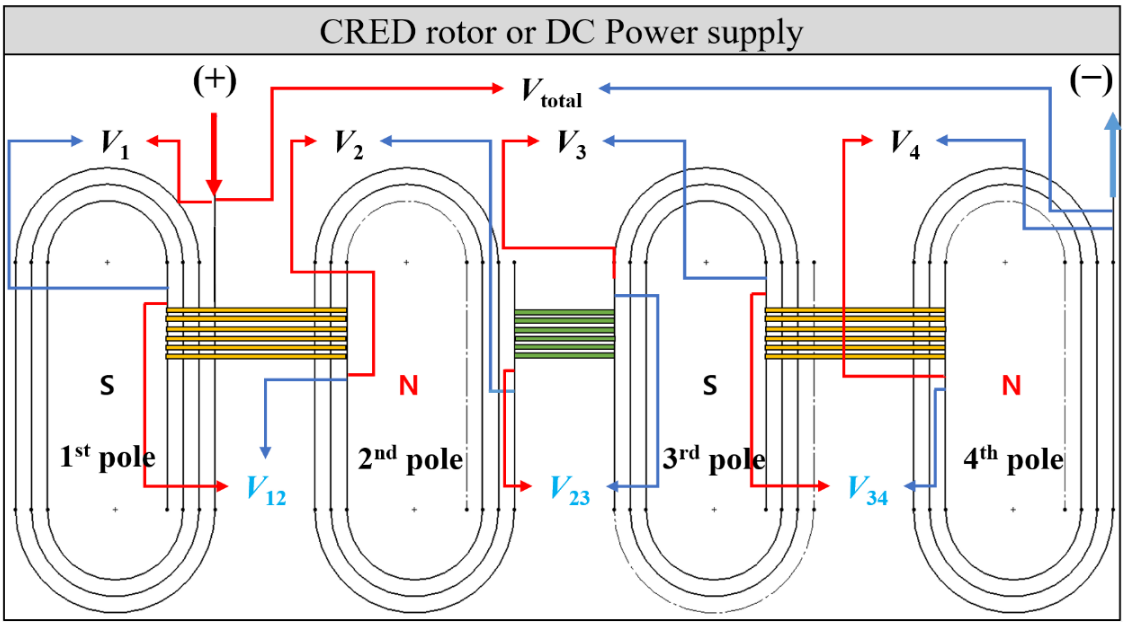

<table>
<tr><th></th><th>1st pole</th><th>2nd pole</th><th>3rd pole</th><th>4th pole</th></tr>
<tr><td>Current direction /Pole direction</td><td>CW (S)</td><td>CCW (N)</td><td>CW (S)</td><td>CCW (N)</td></tr>
<tr><td rowspan="2">Pole Connections</td><td colspan="2">Inside to Inside joint
(Six HTS bridge wires in parallel)</td><td colspan="2">Inside to Inside
(Six HTS bridge wires in parallel)</td></tr>
<tr><td>CRED rotor
or DC PS (+)</td><td colspan="2">Outside to Outside
(Six HTS bridge wires in parallel)</td><td>CRED rotor
or DC PS (−)</td></tr>
</table>

Fig. 4.5. Schematic diagram of four pole connection using the six-HTS bridge wires

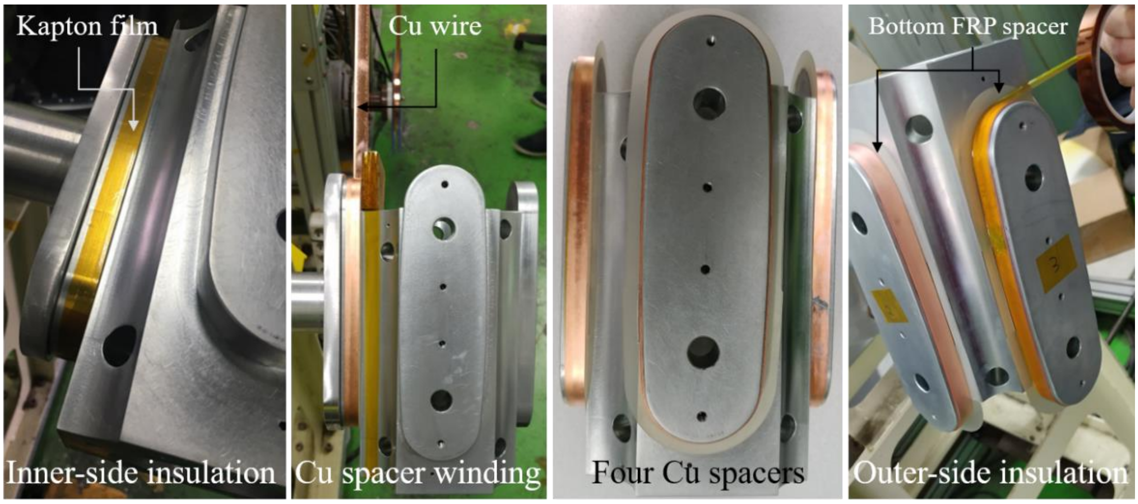

(a) Electromagnetic insulation work on rotor body using Kapton and copper tape

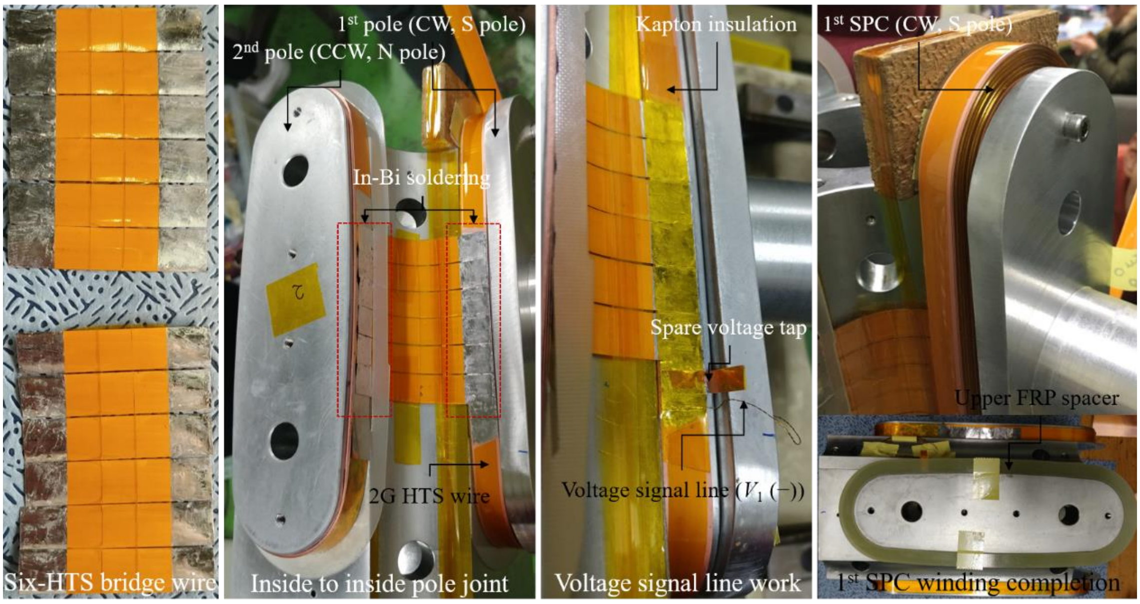

(b) Field winding work of the 1st pole with HTS SPC

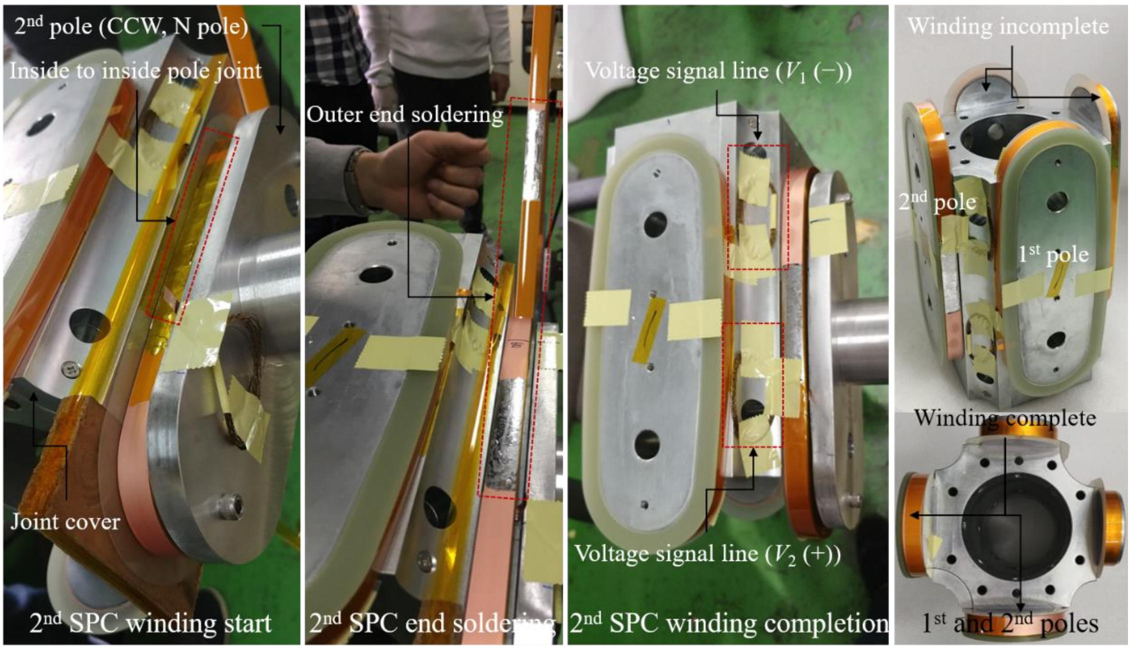

(c) Field winding work of the 2nd pole with HTS SPC

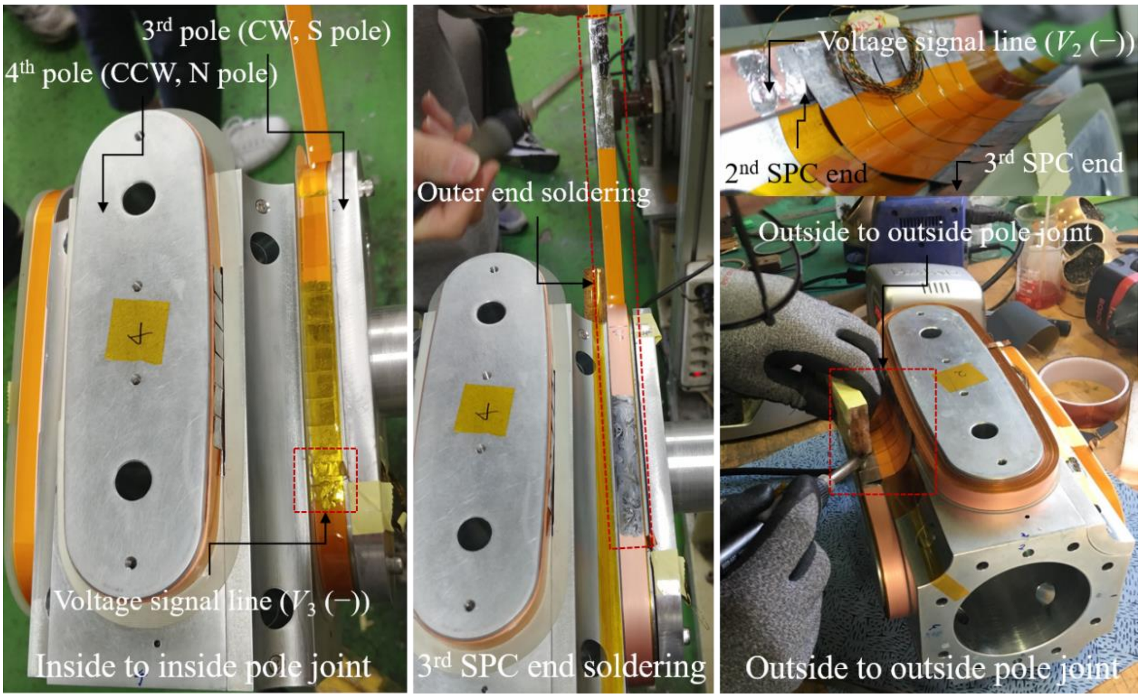

(d) Field winding work of the 3rd pole with HTS SPC

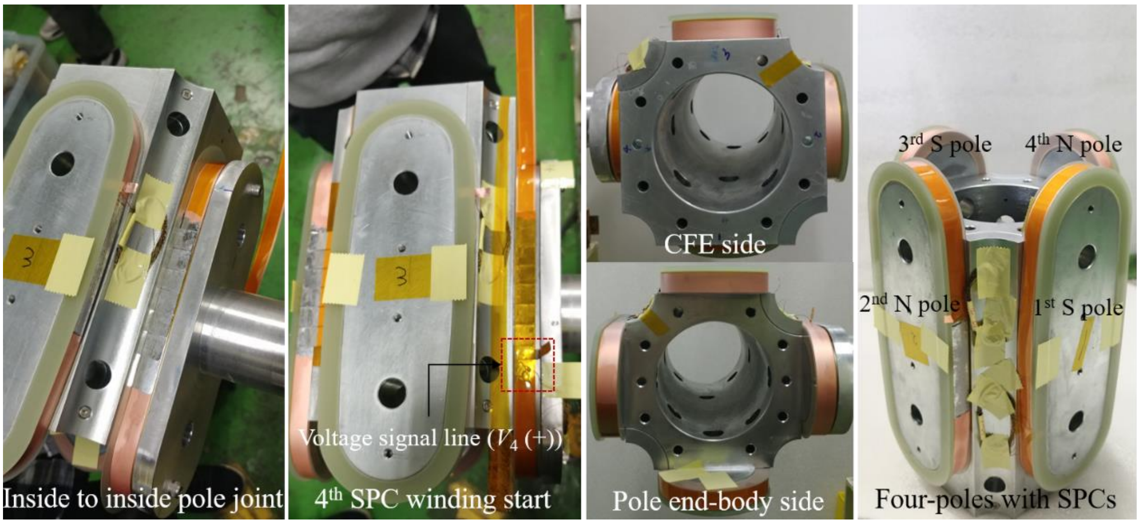

(e) Field winding work of the 4th pole with HTS SPC

Fig. 4.6. Winding and fabrication process of the HTS field pole

Step 2) The six-HTS bridge wires were soldered to first turn of first HTS SPC to electrically join the first and second poles from insides of two HTS SPCs, as shown in Fig. 4.6(b). Further, the twisted pair wire and spare voltage tap, i.e., Cu thin-sheet, were installed to measure the voltage signals of first SPC. In addition, Kapton tape covered surface of HTS bridge wires, signal wire, and Cu sheet to insulate the second turns of HTS SPC. Furthermore, total sixty-five turns were wound with turn to turn Kapton insulations and winding tension of 143.18 N. Note that extra five turns were additionally wound to consider the employment for HTS strands of CSFE. In other words, only sixty-turns contribute to MMF in field winding. Finally, the upper FRP spacer was inserted onto the top of HTS SPC after the winding completion, to electromagnetically insulate HTS SPC from the magnetized pole shoe.

Step 3) When the second HTS SPC begins to be wound, the far ends of HTS bridge wires used in Step 2 were soldered to the first turn of second HTS SPC and simultaneously the signal wire and the voltage tap were installed as shown in Fig. 4.6(c). Further, joint cover was installed to cover the HTS bridge wires between first and second poles. Similar to the first SPC winding, upper FRP spacer was installed after the winding of sixty turns.

Step 4) To join the third and fourth SPCs, the six-HTS bridge wires were soldered to the innermost turn of the third HTS SPC, as shown in Fig. 4.6(d). Moreover, the outside to outside pole joint work was conducted to join the second and third SPCs at outermost of both SPCs after the winding of sixty turns.

Step 5) When fourth HTS SPC begins to be wound, the far ends of HTS bridge wires used in Step 4 were soldered to innermost turn of fourth HTS SPC, as shown in Fig. 4.6(e). The total sixty-five turns were wound at fourth SPC because of the same reason in case of the first SPC winding as described in Step 2.

4.1.3. Characteristic experiment

The salient-field pole with four HTS race-track SPCs was finally fabricated as shown in Figs. 4.6(e) and 4.7, and its basic characteristic experiment was performed using DC PS and under immersion in LN2 after the winding work of the HTS SPCs.

To measure the coil I_c and R_j values, voltage taps were installed in the HTS SPCs, as shown in Figs. 4.5 and 4.6(b)–4.6(e). V_{total}, V_1, V_2, V_3, and V_4 voltage taps were used to measure the I_c values of the total SPCs and the first, second, third, and fourth SPCs, respectively. Moreover, the V_{12}, V_{23}, and V_{34} voltage taps were employed to measure the joint resistances between the first and second poles (R_{pj12}), between the second and third poles (R_{pj23}), and between the third and fourth poles (R_{pj34}), respectively. The transverse-type Hall sensors, i.e., HGCT–3020 model from LakeShore, were installed at the center of the first and second pole shoes, as shown in Fig. 4.7, to measure the axial-center magnetic field density (B_z) of the SPC. These different voltage signals were monitored and measured using a data-acquisition system with LabVIEW software.

Table 3.4 lists the summarized test results of the basic characteristic experiment in LN2. Fig. 4.8 shows the I_c versus V_q curves of the four SPCs, which were measured in test environment as shown in Fig. 4.7. Using the V_q criterion of 1 μV/cm, the measured I_c values of the first, second, third, and fourth SPCs were measured as 125.9, 126.9, 129.1, and 130 A, respectively, at 3 mV V_q. Finally, the overall I_c value of the serial four field poles was 127.5 A at 12 mV V_q.

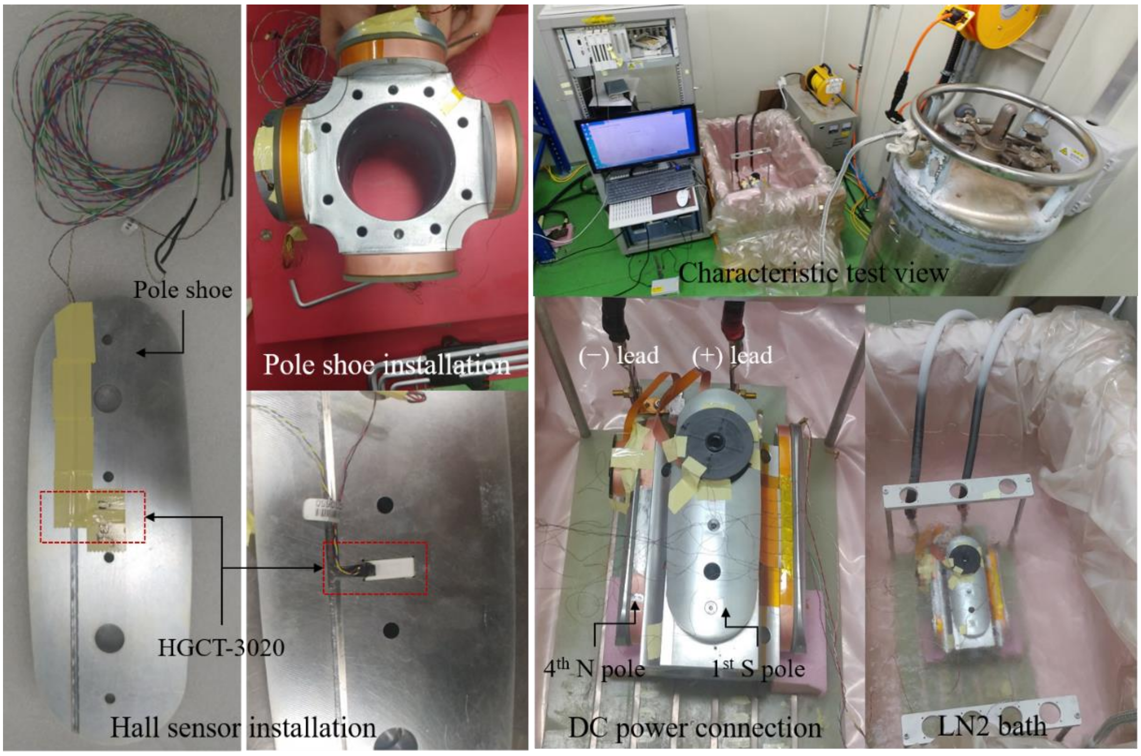

Fig. 4.7. Basic characteristic test of HTS SPCs in LN2 immersion

Table 4.4. Basic characteristic test results of 2G HTS SPCs for the salient-field pole

Items	Unit	4-poles	1st pole	2nd pole	3rd pole	4th pole
I_c	[A]	127.5	125.9	126.9	129.1	130
n-value	-	26	29	26	27	23
E_L	[μV]	3290	776.3	825.45	816.93	855.58
L_c	[mH]	32.9	7.76	8.25	8.17	8.56
R_{pj12}	[nΩ]	-	23		-	-
R_{pj23}	[nΩ]	-	-		305	-
R_{pj34}	[nΩ]	-	-		-	24

The total inductance (L_c) of the field poles was calculated to be approximately 32.9 mH using the relationship between the inductive voltage (E_L) and current ramp rate (di/dt), i.e., $E_L = L_c \times di/dt$, as shown in Fig. 4.8.

Fig. 4.9 shows the current versus voltage and center magnetic field density (I–V and I–B_z) curves measured at the V_{12}, V_{23}, and V_{34} voltage taps, as shown in Fig. 4.5 and the Hall sensor in first pole shoe. The slope of this I–V curve represents the R_{pj} values in the three joints. The values of R_{pj} among the four HTS SPCs, i.e., R_{pj12}, R_{pj23}, and R_{pj34}, were measured to be approximately 23, 305, and 24 nΩ, respectively.

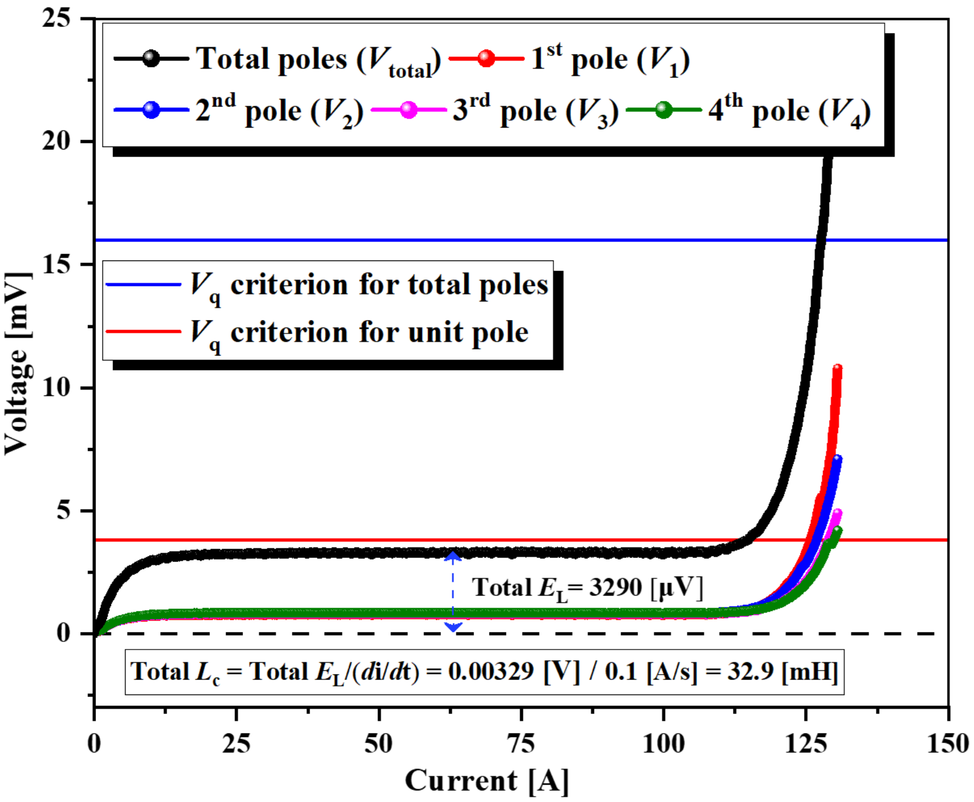

Fig. 4.8. I_c measurement results of 2G HTS field SPCs

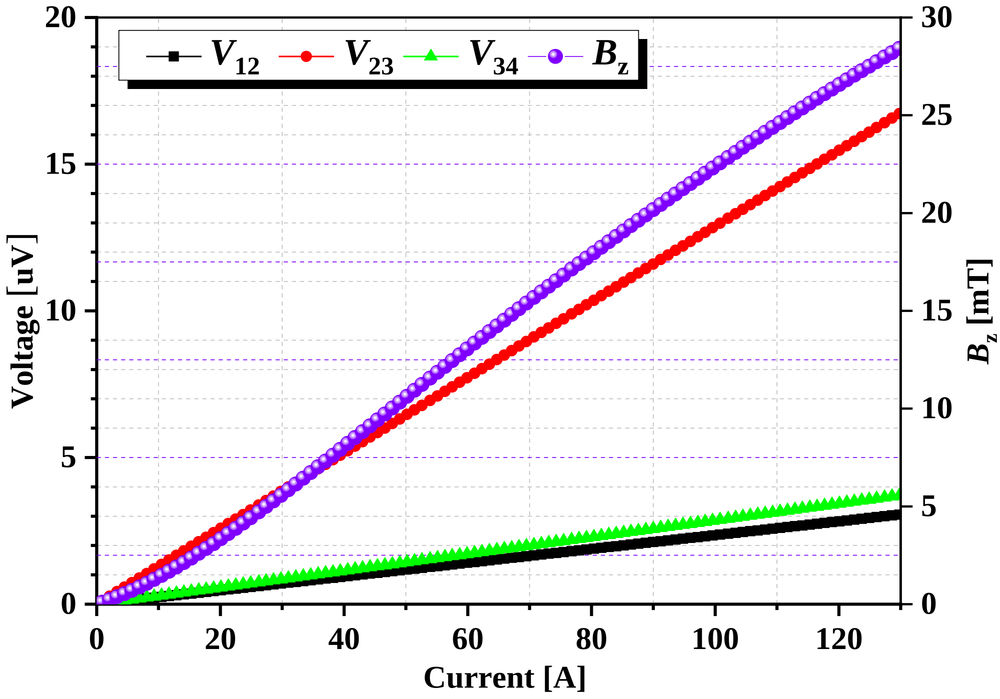

Fig. 4.9. R_{pj} and B_z measurement results

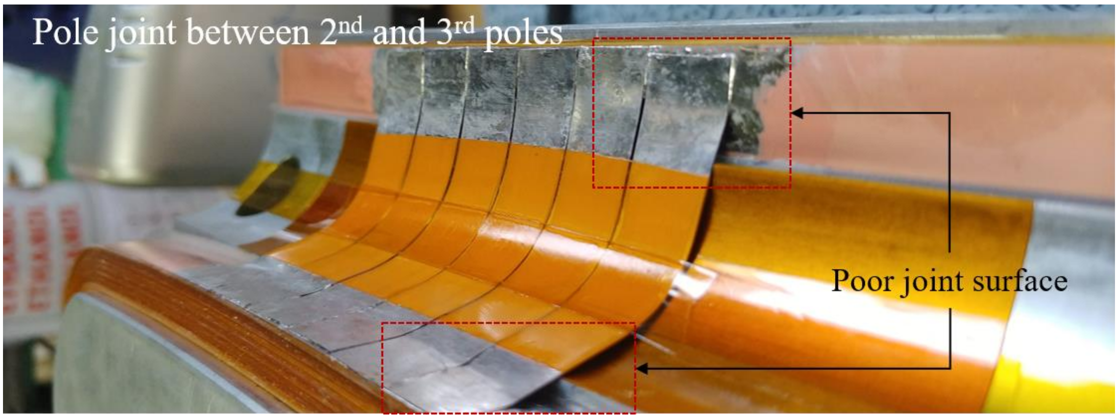

Fig. 4.10. Pole joint condition between 2nd and 3rd poles with six HTS bridge wires

Fig. 4.10 shows an image of the pole joint between second and third poles, with six-parallel bridge wires, which was brazed using In-Bi soldering. In particular, R_{pj23} was relatively higher than R_{pj12} and R_{pj34} because of insufficient pole joint between the outermost wire surfaces of the second and third poles, as shown in Fig. 4.10. Moreover, the magnitude of B_z, which was measured at the first pole shoe was 5.6 mT at 30 A, which is the rated I_f value of the 1 kW class HTSRM.

4.2. Field current charging test with contactless superconducting field exciter

This subsection presents the practical results of the fabrication and performance test of full-scale FCs for 1 kW class HTSRM which is charged by CSFE. This rotating machine with a 1 kW power capacity has already been designed and analyzed in Chapter 3. Moreover, a prototype CSFE was developed and experimentally tested to investigate its fundamental operating characteristics and optimal charging methods of the HTS FCs of the 1 kW class HTSRM [38]–[41], [47], [73]–[74].

In this subsection, it mainly focused on the design, fabrication, and performance characteristic test of the major components, which consisted of the rotor assembly of the 1 kW class HTSRM, such as the rotor field-pole of the rotating machine and the rotor and stator components of the CSFE. In particular, to confirm the technical feasibility of CSFE on application to the 1 kW class HTSRM, the HTS FCs were charged under various operating conditions of the CSFE in a stationary flux-pump mode.

First, to verify the current-charging performance of this noncontact excitation method before the final assembly of a full system, the component parts of the rotor field pole and CSFE were individually fabricated and assembled. Further, a preliminary test setup was constructed to excite the HTS field winding of the 1 kW class HTSRM using CSFE in a stationary flux-pumping mode. The charging performance of I_f was evaluated under various operating conditions of the CSFE. Preferentially, during the first charging test, two types of 2G HTS wires were considered to choose a suitable conductor for the rotor winding of the CSFE, which can ultimately saturate the magnitude of I_f. Furthermore, to control the charged I_f, various cases of current charging were tested by considering the operating parameters of the CSFE, such as n_p, g_a, and S_r.

4.2.1. Design and fabrication of contactless superconducting field exciter

As shown in Fig. 4.11(a), the current-charging system with CSFE in this dissertation can be simply modeled by R–L electric circuit which is already conceptually discussed in subsection 2.1.1 of Chapter 2. This simple circuit, which is composed of the CSFE stator, CSFE rotor, and HTSRM rotor, can be formulated by the Faraday and Kirchhoff laws as follows [27]–[29], [31]–[33]:

$$V_{\mathrm{emf}} = -\frac{d\varphi}{d\mathrm{t}} = R_{\mathrm{e}} I_{\mathrm{p}} + L_c \frac{dI_{\mathrm{p}}}{d\mathrm{t}} \tag{4.1}$$

where the output of CSFE consists of series connected 8-V_{emf} sources and 8-R_d, as shown in Figs. 4.11(a) and (b). V_{emf} refers to the V_{dc} source in Eq. (2.3) to charge the HTS FCs and represents the total V_{emf} from V_{emf1} to V_{emf8} at HTS strands from 1st to 8th, respectively. Moreover, total R_d is internal resistance in CSFE and is considered as the sum of R_{d1} to R_{d8}. In addition, Φ is the total magnetic flux applied into the HTS strands of the CSFE rotor, and it can be supplied by the PM or electromagnet in the CSFE stator with a constant rotation period because of the relatively rotating CSFE rotor. R_e is the total resistance of the R–L circuit and represents the sum of R_d, loop joint resistance between the HTS strands and HTS SPCs (R_{lj}), and R_{pj}, i.e., $R_e = R_d + R_{\mathrm{lj}} + R_{\mathrm{pj}}$. I_p is the pumping current.

From (1), I_p, which flows into the R–L closed circuit in the superconducting state at LN2 temperature, can be supplied to the HTS SPCs and is expressed as follows [28]–[29], [31]–[33]:

$$I_{\mathrm{p}}(t) = \frac{V_{\mathrm{emf}}}{R_{\mathrm{e}}}\left(1 - e^{-\frac{R_{\mathrm{e}}}{L_{\mathrm{c}}}t}\right) = I_{\mathrm{s}}\left(1 - e^{-\frac{t}{\tau}}\right) \tag{4.2}$$

where I_s is the saturation current, i.e., rated I_f in the HTS field winding, and is proportional to V_{emf} and inversely proportional to R_e. τ is a time constant, which determines the saturation or charging time of I_s. Therefore, by supplying current to the HTS load coils in a noncontact manner, the CSFE can replace the existing PS, which is located outside the HTSRM at room temperature.

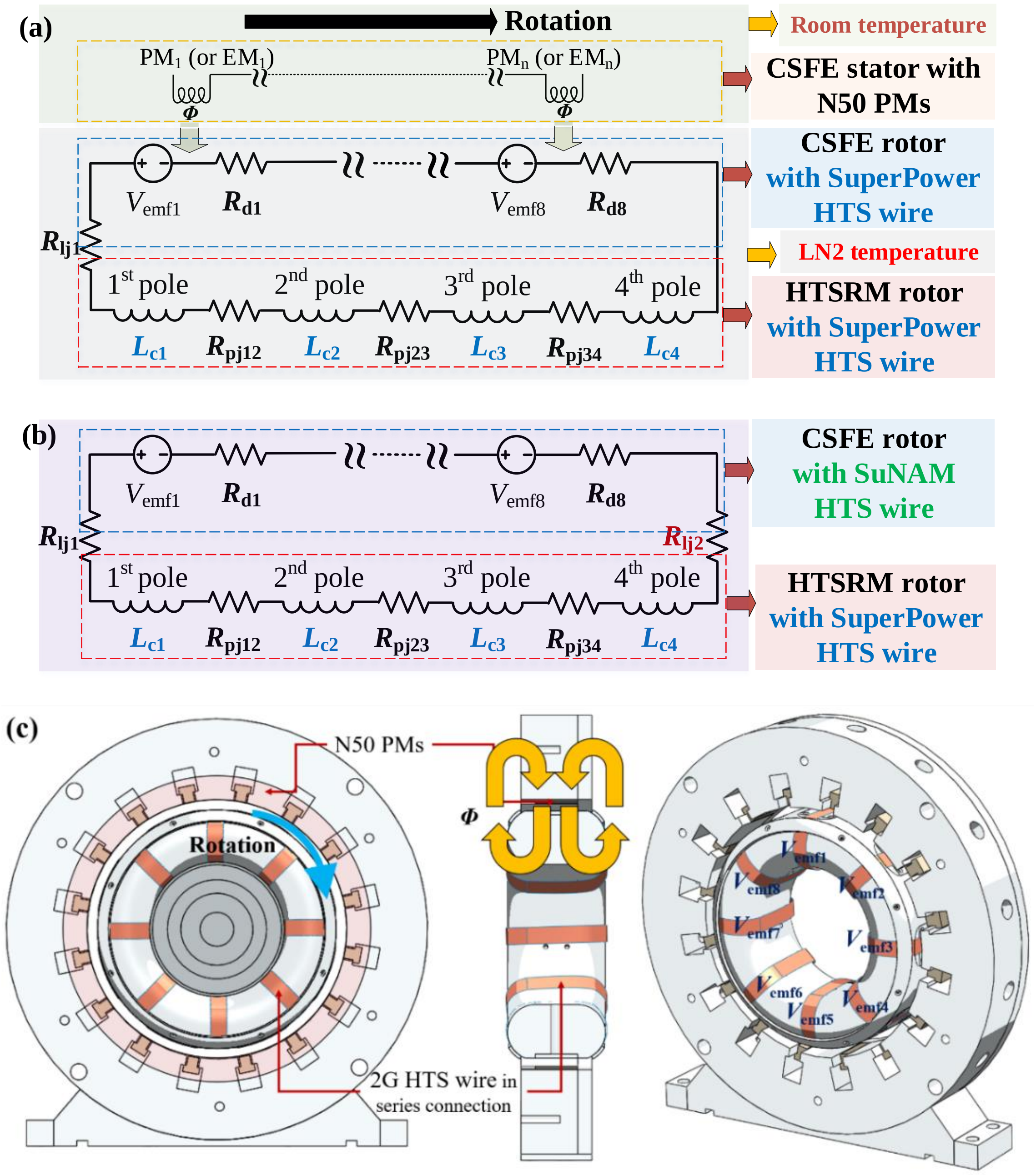

Fig. 4.11. Schematic circuit diagrams of the noncontact current-charging system with CSFE using (a) SuperPower and (b) SuNAM HTS wires as the HTS strands of the CSFE rotor, and (c) concept of circuit diagram in 3D modelling

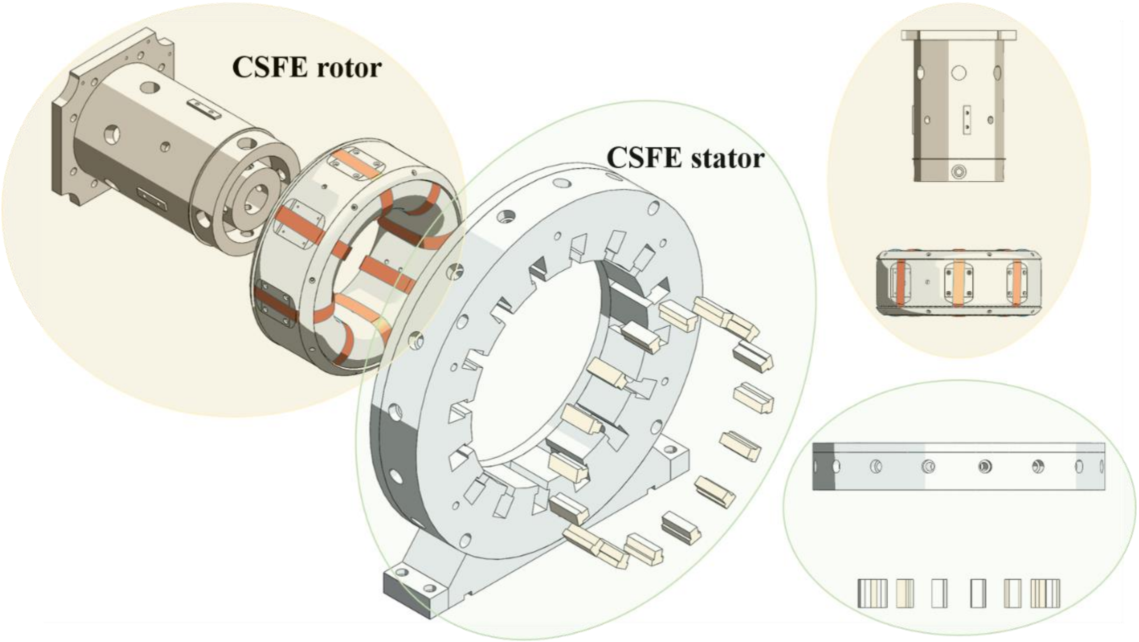

Fig. 4.12. 3D configuration of CSFE

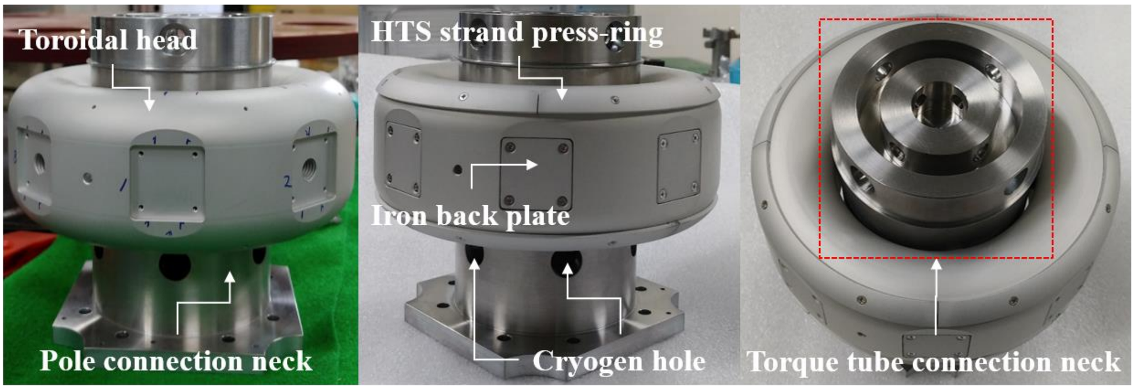

(a) Toroidal type rotor part of CSFE without HTS strands

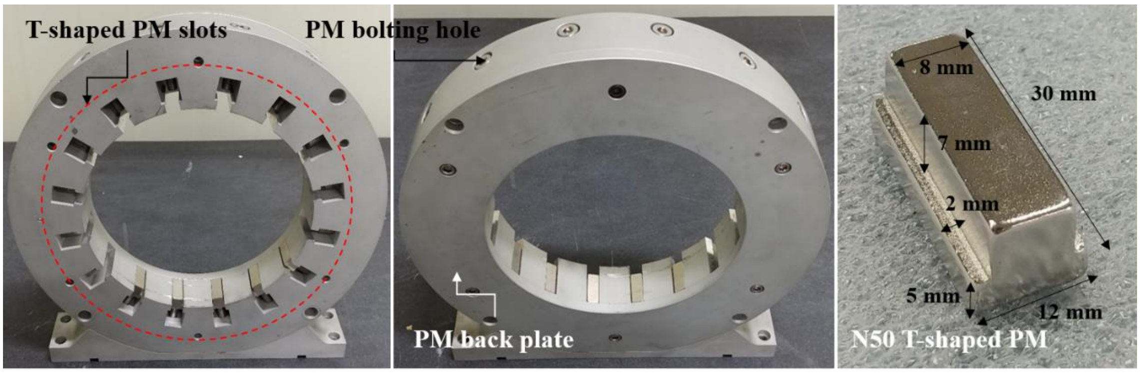

(b) Cylinder type stator part of CSFE with N50 PM

Fig. 4.13. Images of fabricated configuration parts of CSFE

Fig. 4.12 shows 3D modeling for fabricating CSFE for the 1 kW class HTSRM, which consists of rotary and stationary parts, such as the rotating machine configuration. Moreover, Figs. 4.13(a) and 4.13(b) show the machined and temporarily assembled rotor and stator of CSFE, respectively. In the CSFE rotor, a toroidal head, which was used to wind the HTS strands in a toroidal shape, was bolted with a pole-connection neck. Thin press rings structurally guided and fixed the HTS strands to surface of the toroidal head. The cryogen holes were arranged in the outer circumference of the pole connection neck to pass the liquid cryogen, i.e., LN2 which is to cool HTS strands of CSFE rotor. Finally, the load-side shaft and torque tube can be connected to CSFE through connection neck, as shown in red-dashed box of Fig. 4.13(a). A stainless-steel material (SUS304) was used for the pole connection neck to decrease the amount of heat shrinkage in the axial direction of rotating machine. In the CSFE stator, a maximum of up to 16 pieces of T-shaped slots were arranged in the inner circumference of the CSFE stator, to mount the PMs, as shown in red-dashed circle of Fig. 4.13(b). These PMs were fixed by bolts inserted in the outer circumference of CSFE stator, as shown in red dashed-box of Figs. 4.15(a) and 4.15(b). In addition, PM back plate supported T-shaped PMs to prevent escape of PM in axial direction. Thus, PMs can be aligned with the center of HTS strands in CSFE rotor.

Figs. 4.14 and 4.15 show images of the fabrication result of the CSFE rotor and stator in the assembly process using the HTS field poles of the rotating machine. A summary of the final major parameters is listed in Table 4.5. In the design and fabrication of CSFE, three technical methods were applied to maximize I_s charged by the CSFE. It is observed that the overall effectiveness of these methods was studied and proven in [38]–[41], [73]–[74].

First, we considered the magnetic plate with S45C material at the background of the HTS strands to increase the magnetic-flux linkage that passed through the HTS strands, which could increase the pumping current to the load, as shown in Figs. 4.13(a) and 4.14(b). Second, a toroidal structure and the corresponding winding method were considered, as shown in Fig. 4.14(a). A previous study [41] reported that I_s increased as the number of HTS strands (n_c) increased. Thus, we considered the toroidal-head structure of the CSFE rotor to wind the HTS strands to be within the limited size of the CSFE rotor. By considering the twisted angle of the HTS wire in the inner and outer diameters of the toroidal head, eight HTS strands were finally arranged in series on the surface of the toroidal head, as shown in Fig. 4.14(a). The aluminum material (Al6061) with excellent heat transfer performance was used for the toroidal head and press-ring to efficiently cool HTS strands which directly exchanges heat with the surface of toroidal head.

Finally, a series-connected type, which can minimize the number of joint-spot between the CSFE and load coils, was used as a winding connection structure between the HTS strands and HTS SPCs. Thus, the HTS strand was continuously wound on the surface of the toroidal head, as shown in Fig, 4.14(c), and its two ends were joined to the HTS SPCs to form a single electrically closed loop among the rotor components, as shown in Fig. 3.14(d).

For the preliminary charging test, two type 2G HTS wires (SC12050 model from SuperPower Inc. and SCN12550 model from SuNAM Co., Ltd) were considered as HTS strands of CSFE rotor and their technical parameters are listed in Tables 4.2 and 4.5, respectively. Moreover, Fig. 4.16 shows I_c profiles along the 30 m spool of SCN12559 model, which were finally used for HTS strands after preliminary charging test. The maximum and minimum values of I_c are 730 and 701 A, respectively, which were measured and guaranteed by manufacturer, i.e., SuNAM Co., Ltd.

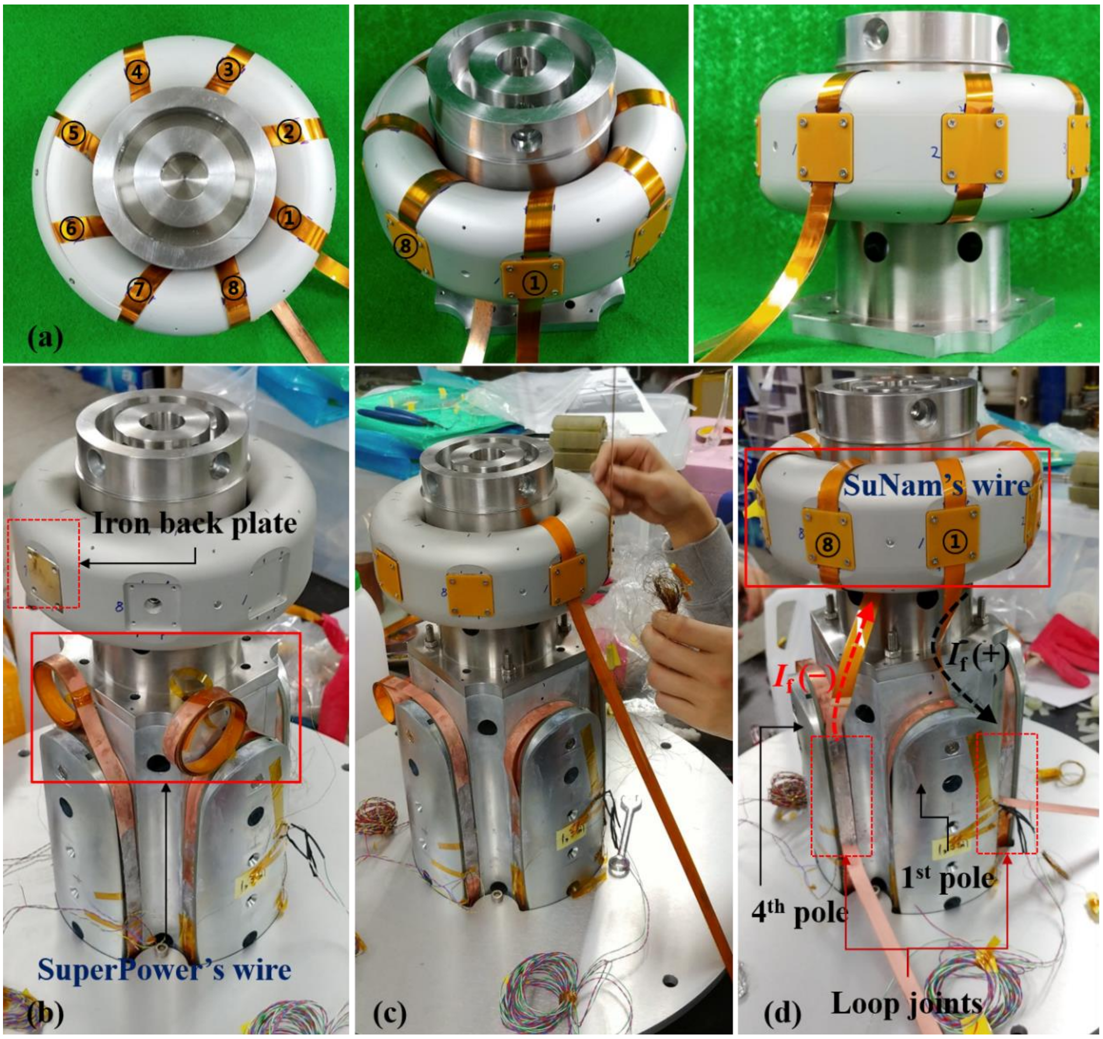

Fig. 4.14. Images of (a) toroidal winding of eight HTS strands on the CSFE rotor, (b) temporarily assembled rotors, (c) HTS strand winding work, and (d) final rotor assembly with HTS strands connection

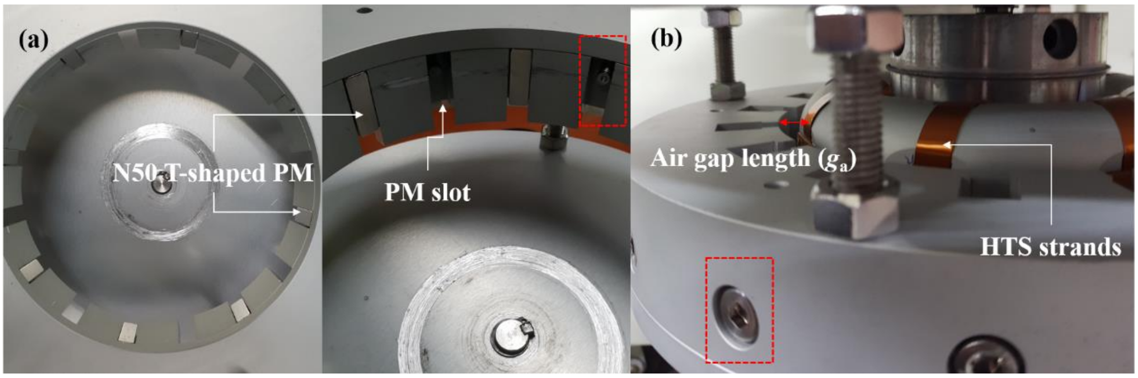

Fig. 4.15. Images of (a) PM arrangement in CSFE stator and (b) enlarged view of the air gap between CSFE rotor and stator

Table 4.5. Major parameters of HTS CSFE

Parameters	**Unit**	**Values**
	CSFE Rotor	
Conductor manufacturer	-	SuNAM
Conductor model	-	SCN12550
Conductor width	[mm]	12.1±0.1
Conductor thickness	[mm]	0.15±0.02
Bare-substrate magnetic property	-	Non-magnetic
Max/Min I_c at 77 K, 0 T	[A]	730/701
Critical temperature	[K]	91
Coefficient of variation	[%]	0.8
HTS strand connection type	-	Series
Number of HTS strands	-	8
Material of iron back plate	-	S45C
Material of toroidal head	-	Al6061
Material of pole neck	-	SUS304
	CSFE Stator	
PM type	-	NdFeB N50
Surface magnetic flux density	[T]	0.52
B at 77 K, 7 mm g_a	[T]	0.15
Number of PM slots	-	Max. 16
Material of stator	-	Al6061

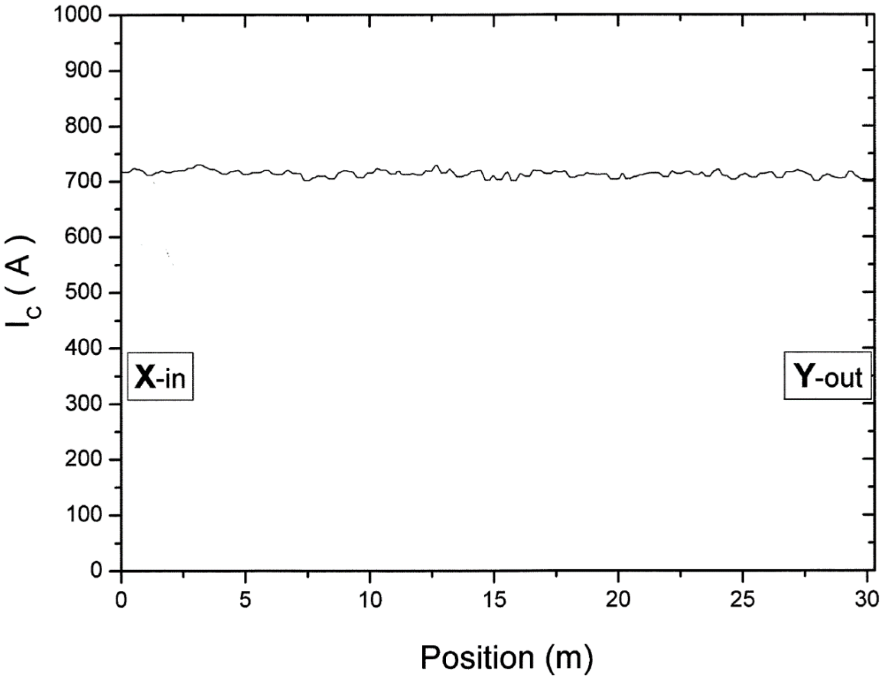

Fig. 4.16. I_c raw data of SCN12550 model used in CSFE rotor

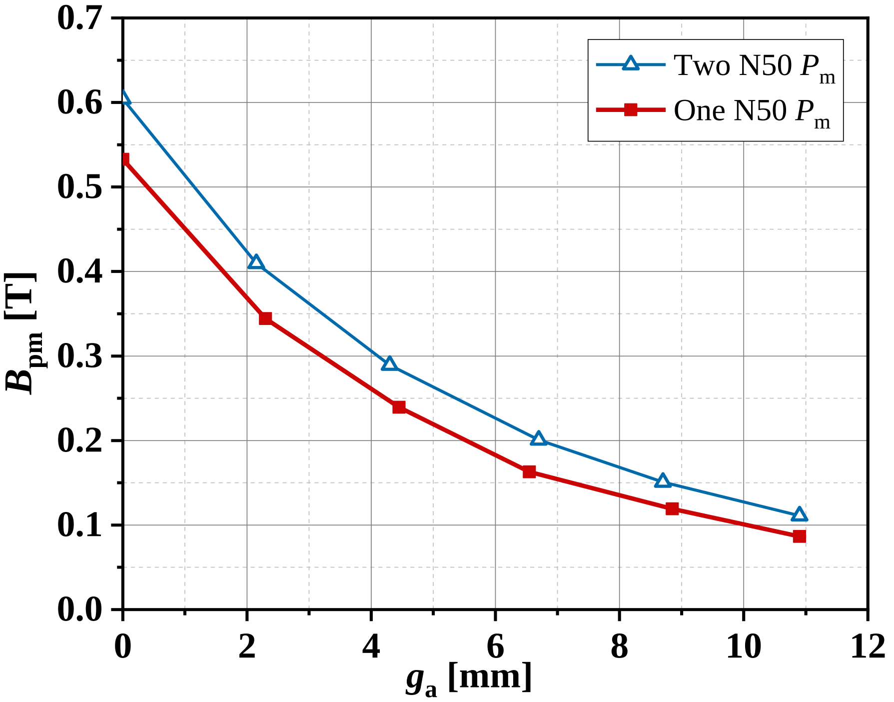

Two PMs							
g_a	mm	0	2.15	4.3	6.7	8.7	10.9
B_{pm}	T	0.60412	0.40954	0.28932	0.20069	0.1577	0.11104
One PM							
g_a	mm	0	2.3	4.45	6.55	8.85	10.9
B_{pm}	T	0.5328	0.34434	0.23941	0.163	0.11919	0.0865

Fig. 4.17. B_{pm} profiles measured at 77 K according to g_a change

The CSFE stator simply consisted of T-shaped PMs, which delivered time-varying magnetic flux to the HTS strands when the rotor rotated with constant S_r, and a supporting structure to hold the PMs. The T-shaped PMs were circumferentially inserted into the stator slots, as shown in Fig. 3.15(a). The neodymium rare-earth magnet was used as a T-shaped PM in the CSFE stator. The grade of this PM was N50, which is the highest readily available grade among the PM shapes that can be fabricated into a T-shape. Its surface magnetic flux density was approximately 0.5236 T at room temperature. The effective width and length of T-shaped PM were 8 and 30 mm, respectively, as shown in Fig. 4.13(b), and the effective surface area where the magnetic-flux linkage occurs with HTS strands was 24 mm^2.

The size of g_a was set to 8 mm, which is the minimum gap length that considers the values of the cross-sectional thickness of the rotor cryostat, cryogen jacket, and vacuum layers, as shown in Fig. 4.15(b). The magnetic field density of the PM (B_{Pm}) for the N50 grade, which was measured at LN2 temperature, i.e., 77 K and 7 mm g_a, was approximately 0.15 T, as shown in Fig. 4.17.

4.2.2. Experimental cases and setup with contactless superconducting field exciter

A. Experimental cases

To perform the no-load test of the HTSRM, the amount of current charged into the HTS field winding must be changed and controlled by any PS. However, the CSFE with PM could not directly control the magnitude and charging speed of the current compared with the current charging using a DC PS in a constant-current mode. Therefore, it needs to confirm the controllable current ranges through a preliminary experiment and then apply it to the no-load test of the HTSRM. Both magnitude and charging speed of I_s charged by CSFE could be determined and controlled using the design parameters of CSFE and the load coil, which were considered as active and passive control parameters, respectively. The active parameters could be considered as controllable parameters because of their easiness in terms of parameter change and control at outside, i.e., CSFE stator. According to these parameters, g_a and B_{pm} directly affected the amount of magnetic-flux linkage that passed through the HTS strands. In addition, the period of the magnetic-flux linkage was affected by n_p and S_r. In contrast, the passive parameters, such as L_c and R_j, were difficult to apply in controlling the magnitude and charging speed of I_s because these parameters were initially determined by the design and fabrication process of the application system. Therefore, we chose n_p, S_r, and g_a as control parameters of I_s to evaluate the charging performance of the HTS field winding. In particular, the controllable ranges of I_s charged into the HTS field winding were investigated according to the changes in the control parameters. The following three experimental cases were considered and conducted.

1) Consideration of the 2G HTS wire type in the CSFE rotor: The different types of 2G HTS

wire, as shown in Fig. 4.18(a), were investigated to select a suitable wire for HTS strands of the CSFE, which can ultimately saturate the magnitude of I_{op}. The SuperPower HTS wire (SCS 12050 model) and SuNAM HTS wire (SCN12550 model) for HTS strands in the CSFE rotor were considered to compare the amount of I_{s} charged into the HTS field winding. In the SuperPower HTS wire case, the extra wire lengths were additionally wound at the two ends of the first and fourth HTS SPCs in the rotor field pole, respectively, during the winding work, as shown in red solid box of Fig. 4.14(b). From ⑧ of Figs. 4.14(a) or 4.14(b), the extra wires in the fourth HTS SPCs started to wind in series on the toroidal head and then its end in opposite side as shown in ① of Fig. 4.14(a) was connected to end of the first HTS SPCs using In–Bi soldering. This process created an electrically closed loop with the HTS SPCs with only one loop joint, as shown in Fig. 4.11(a). Meanwhile, in the SuNAM HTS wire case, two loop joints were formed because of joints of different HTS wires in HTS SPCs and CSFE rotor, as shown in Figs. 4.11(b) and red dashed-boxes of 4.14(d). The technical parameters of the two 2G HTS wires are listed in Tables 4.2 and 4.5, respectively. We note that parameters of SuperPower HTS wire, which was tested as HTS strands of CSFE rotor, were equal to that of HTS wire used in HTS SPCs.

2) Consideration of the number of PMs in the CSFE stator (n_{p}): V_{emf} is proportional to the rotation frequency (f_{r}) of Φ applied from the PMs of the CSFE stator [24]–[41]. This parameter can be changed by n_{p} and S_{r}; thus, the magnitude and charging speed of I_{s} can be controlled by changing n_{p}. The available ranges of S_{r} were limited in the actual operation because the output power of the rotating machine was dependent on operational S_{r}. Accordingly, in this experiment, we changed n_{p} from 4 to 16, as shown in Fig. 4.18(b), to investigate the effect of the changes in f_{r} on the charging characteristic and performance of I_{s}.

3) Consideration of the air-gap length between the rotor and stator of CSFE (g_{a}): The intensity of the magnetic-flux linkage, which can determine the amount of I_{s} charged from the CSFE, decreased with the increase in g_{a} [28]. In this experiment, we adjusted g_{a} using a thin sheet made of fiber reinforced plastic with a thickness of 1 mm, as shown in Fig. 4.18(c). Thus, I_{s} performance was tested at g_{a} values of 7, 8, and 9 mm.

B. Experimental setup

Fig. 4.19 shows the schematic diagram of the experimental setup for the preliminary charging test of the HTS field winding of the 1 kW class HTSRM using the CSFE. In this test, the stationary flux-pumping mode of the CSFE was considered for simplicity of the test environment. Thus, the CSFE stator where the N50 PMs were installed was the only rotating part in this test, as shown in Fig. 4.19(a). A servomotor operated and controlled this rotating part and its S_{r}.

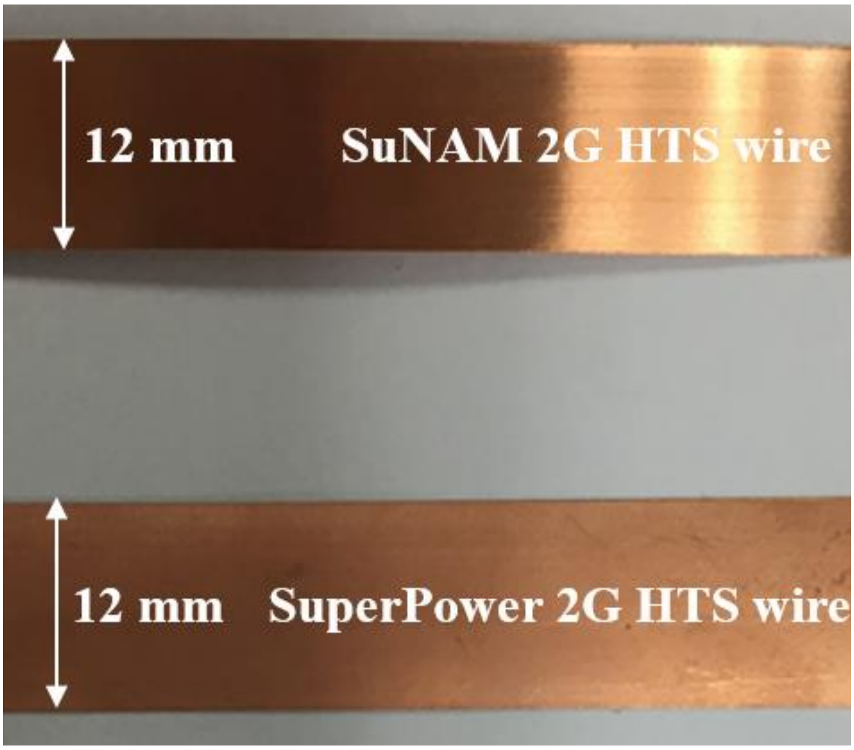

(a) Consideration of the 2G HTS wire type

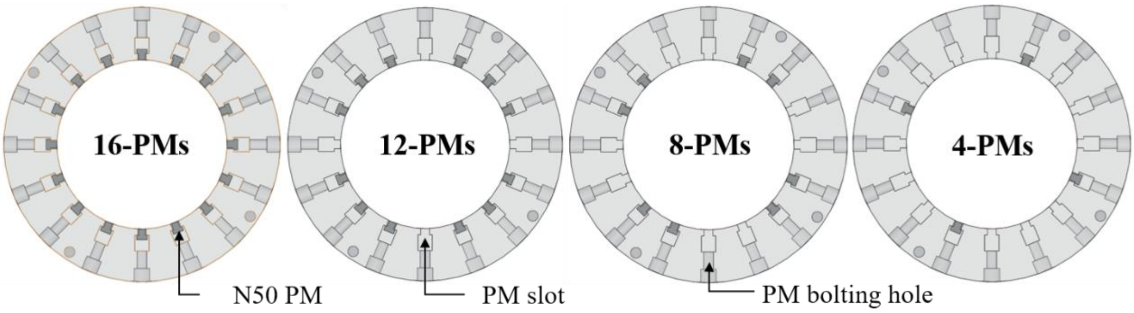

(b) Consideration of the number of PMs (n_p)

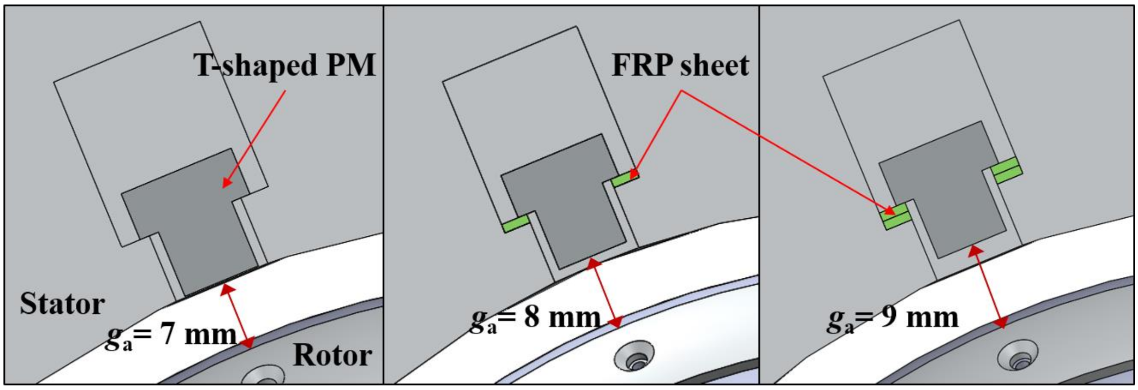

(c) Consideration of the air-gap length (g_a)

Fig. 4.18. Experiment cases

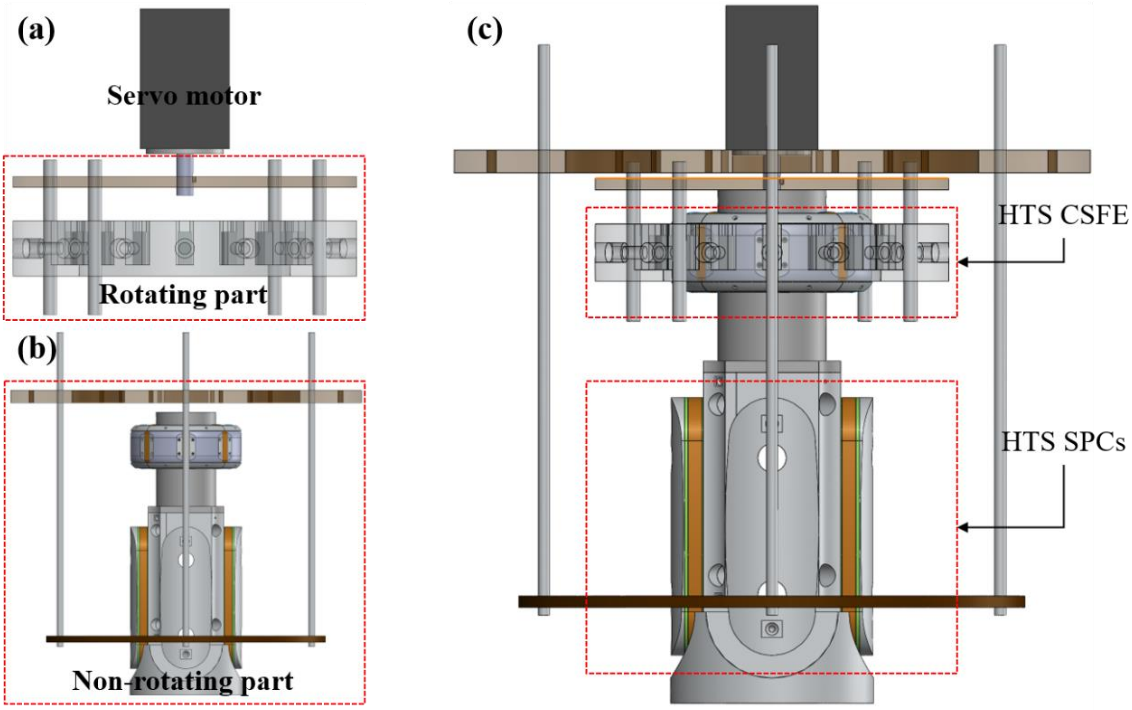

Fig. 4.19. Schematic diagram of experimental setup for the preliminary charging test in the stationary flux-pumping mode. (a) Rotating part in the stationary flux-pump mode, (b) non-rotating part in the stationary flux-pump mode, and (c) fully assembled setup

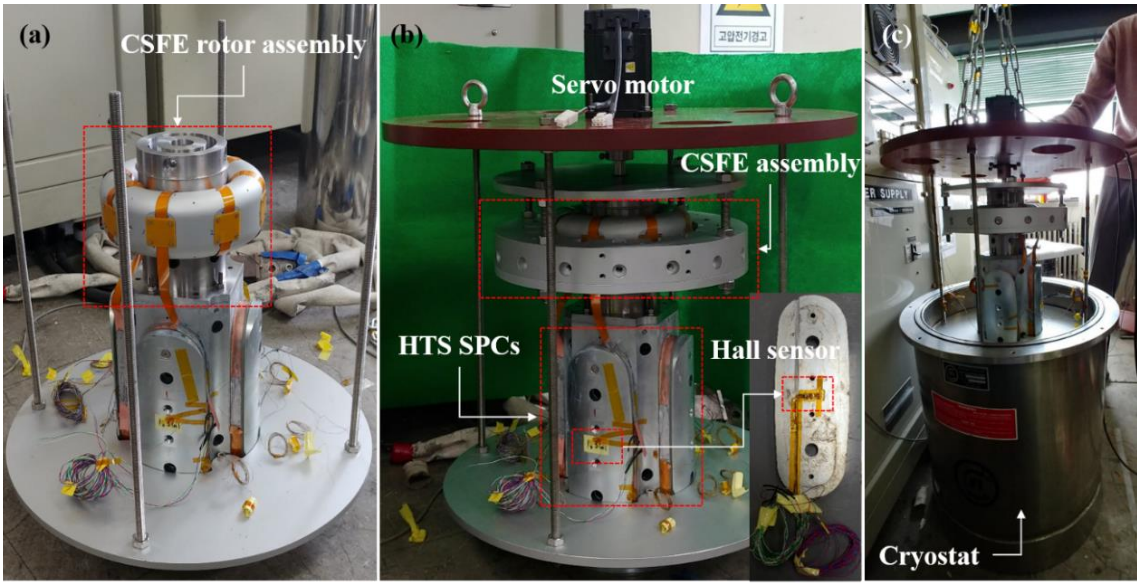

Fig. 4.20. Real experimental setup of the preliminary charging test in the stationary flux-pumping mode. (a) Assembly with CSFE rotor and salient pole body, (b) fully assembled experimental setup without the LN2 cryostat, and (c) assembly with the LN2 cryostat

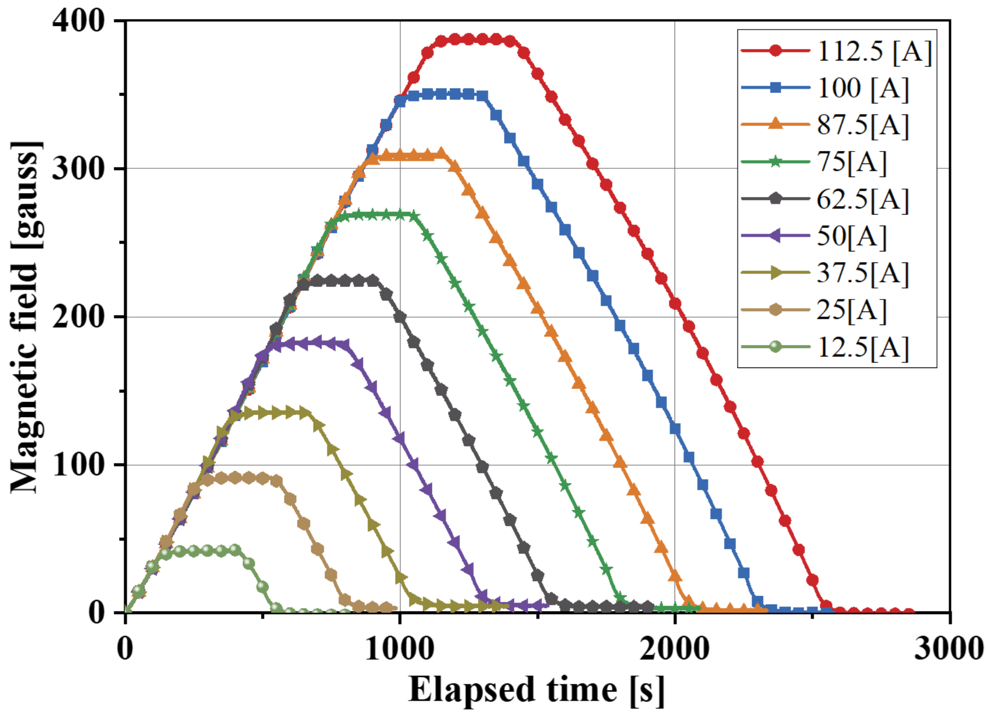

Current (A)	0	12.5	25	37.5	50	62.5	75	87.5	100	112.5
Magnetic field (G)	0	42	91	135.5	182.5	224.5	269.5	309.5	350.5	387

Fig. 4.21. Magnetic field profiles of the second field winding with various current supplies

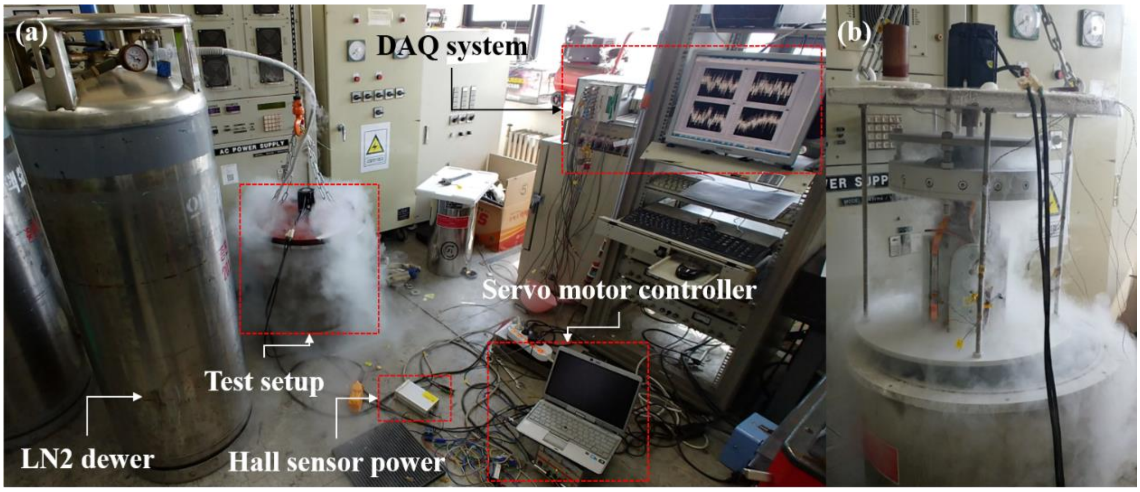

Fig. 4.22. Preliminary current-charging test in the stationary flux-pumping mode. (a) The whole view of test configuration and (b) warm-up of test setup from LN2

Fig. 4.20 shows images of the real-experimental setup for the preliminary charging test. The assembly with CSFE and HTS SPCs was finally inserted into the cylindrical SUS-cryostat, as shown in Fig. 4.20(c). To measure I_s charged by the noncontact method of the CSFE, Hall sensors were installed at the center of the pole cover, i.e., pole shoe, as shown in Fig. 4.20(b). Its reference data, i.e., hall voltage versus magnetic field density, on the charging current versus corresponding magnetic field density were previously calibrated by a DC PS in a constant-current mode, as shown in Fig. 4.21. Thus, charged I_s could be indirectly predicted using the reference data.

Fig. 4.22 shows the whole experiment view for the preliminary current-charging test in the stationary flux-pumping mode. The fully assembled experimental setup was batched and cooled by LN2 stored in cryostat as shown in Fig. 4.22(a). All voltage signals were monitored and measured using the data-acquisition (DAQ) system from NATIONAL INSTRUMENTS, which consisted of NI SCXI devices and the LabVIEW software.

4.2.3. Experimental results on current charging characteristic with contactless superconducting field exciter

A. Effect of the 2G HTS wire type in the CSFE rotor

Fig. 4.23 shows the comparison results of charged I_s using SuperPower and SuNAM HTS wires on the HTS strand of CSFE. For the charging test results, in the case of the SuperPower HTS wire, the values of the fully saturated current were measured to be approximately 17.8 and 18.4 A at S_r values of 100 and 200 rpm, respectively. Moreover, in the case of the SuNAM HTS wire, the values of the charged current were fully saturated to approximately 68 and 70 A at S_r values of 100 and 200 rpm, respectively.

The number of loop joints in the SuperPower HTS wire case with one joint was smaller than that in the SuNAM HTS wire case with two joints; however, the I_s values that used the SuperPower HTS wire were approximately 3.8 times lower than those that used the SuNAM HTS wire at both S_r values of 100 and 200 rpm. The values of R_d can be roughly estimated by the calculated R_e ($=L_c/\tau$) using measured I_p profiles, as shown in Fig. 4.23. The estimated values of R_d were 102.14 and 220.45 μΩ in SuperPower HTS wire case and 61.96 and 108.23 μΩ in SuNAM HTS wire case at S_r values of 100 and 200 rpm, respectively. It is concluded that it occurred because in the SuperPower HTS wire case, R_d in the HTS strands, which determines the magnitude of I_s, was higher than that in the SuNAM HTS wire case. Further fundamental study on the charging characteristics of the HTS rotary flux pump that considered various HTS wire types was conducted in detail in [43]. The SuNAM HTS wire was finally selected as the winding strands of the CSFE rotor to increase the I_{op} performance of the HTS field winding of the rotating machine.

In case of SuNAM HTS wire at S_r values of 100 rpm, as shown by the red curve with circles in Fig. 4.23, the slop of I_s was temporarily decreased, as shown in red-dashed box of Fig. 4.23. This is because superconducting state in R–L circuit cannot be thermally maintained because of insufficient cooling, which is caused by LN2 shortage, especially at CSFE rotor. The slop was back again recovered with refilling LN2 into cryostat. This behavior is technically attractive feature in stable operation of 2G HTS coil because it can be considered as self-protecting characteristic. If HTS coils are charged by the contact-type excitation method, i.e., constant current mode of DC PS (PS), if PS does not provide a reliable current-control according to cooling state of HTS coil, i.e., changes of T_{op}, the HTS coil may be permanently damaged by over I_{op} above I_c. However, in case that HTS coils are charged by contactless excitation method, i.e., CSFE, even if the cooling condition is not well for T_{op}, HTS coil can reduce the amount of I_s, i.e., I_{op}, by itself and then protect itself from permanent damage.

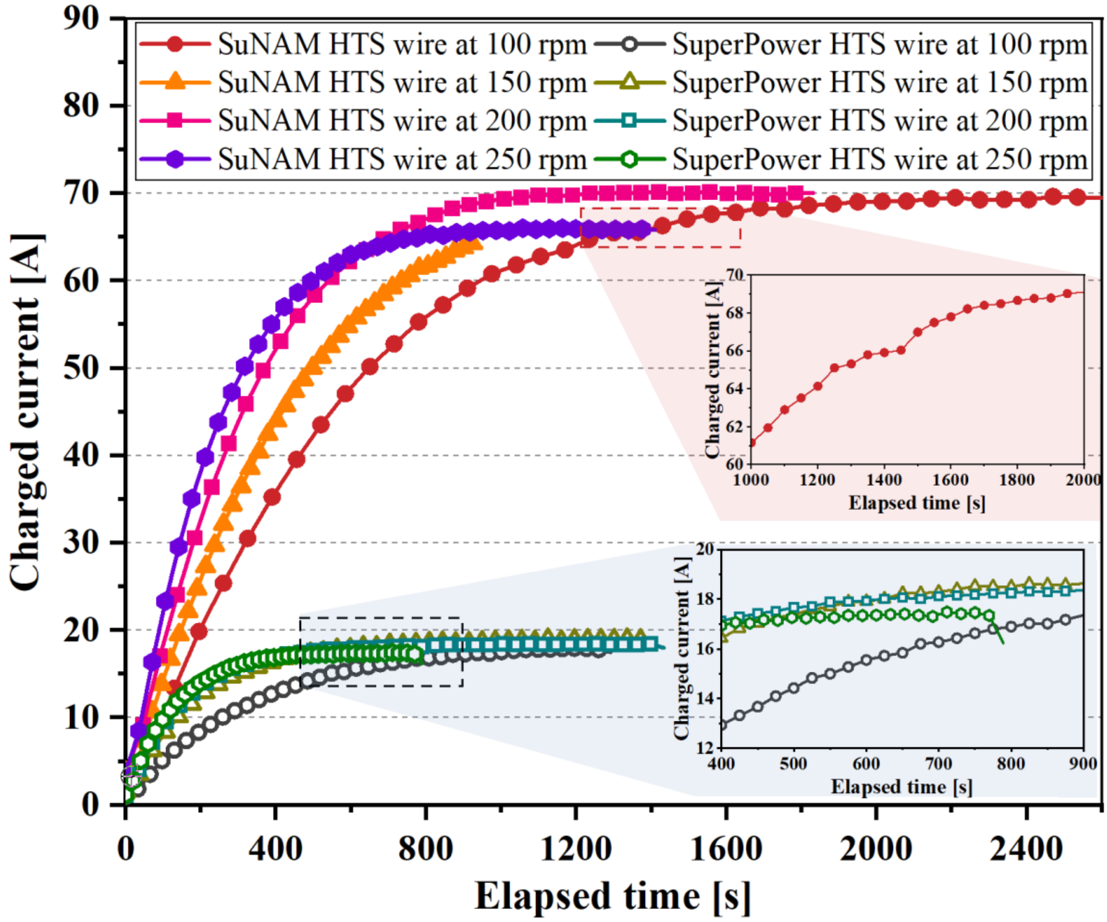

Fig. 4.23. Comparison of charged I_s that uses SuperPower and SuNAM HTS wires on the HTS strand of CSFE at S_r = 100, 150, 200, and 250 rpm; and g_a = 7 mm (eight HTS strands in the rotor and 16 PMs in the stator)

In both HTS wires, the charging behaviors that the magnitude of I_s decreases, were observed above a constant charging speed. In case of SuperPower HTS wire, maximum I_s started to decrease above S_r = 150 rpm and especially such behavior becomes remarkable at S_r = 250 rpm, as shown in black-dotted box of Fig. 4.23. In case of SuNAM HTS wire, maximum I_s started to decrease above S_r of 200 rpm and the magnitude of I_s at S_r of 250 rpm was approximately 5.72% smaller than that of S_r of 200 rpm as shown in comparison between violet curve with hexagons and pink curve with squares of Fig. 4.23. These behaviors were similarly observed in other researches and they reasoned that this is because heat generations because of eddy-current occurs in 2G HTS wire and iron back plate when a time-varying magnetic field with relatively high-frequency is applied to HTS wires [29], [33], [44], [48]. Thus, operating condition of HTSRM, which is excited by CSFE, carefully considered and designed because I_{op} of field winding can be restricted by S_r of CSFE.

B. Effect of the number of PMs in the CSFE rotor

Fig. 4.24 shows the results of the current charging test according to the changes in n_p from 4 to 16 with different values of S_r (100, 150, and 200 rpm) and at 7 mm g_a. Generally, the magnitude and charging speed of the charged current is enhanced as the rotation frequency ($f_r = (n_p \times S_r)/60$) increases. However, the increment in the magnitude of I_s was not proportional to the increase in f_r because of the leakage or lack of penetrating magnetic flux into the HTS strands [14]. The magnitude and saturation speed of the current profiles must ideally be the same at equal f_r; however, the test results of f_r cases of 13.3 and 20 Hz were inconsistent with that in the ideal case, as shown by the red dashed boxes in Fig. 4.25. It is concluded that this was because of technical problems, such as the joint-resistance changes caused by re-soldering between the two ends of the HTS strand and HTS SPCs., insufficient cooling caused by LN2 shortage, irregular air gap caused by rotational vibration, measurement errors caused by signal noise, and other causes that occurred in the repeated experiments.

The controllable ranges of I_s were approximately from 49.5 to 70.4 A at f_r values from 6.7 to 53.3 Hz, as shown in Fig. 4.25 and summarized in Table 4.6. Moreover, the charging times (t_τ) were calculated based on the time constant during circuit charging, which means the charging time to reach 63.2% of I_s, and they were compared in Table 4.6. It was observed that t_τ was generally accelerated with increase of f_r. Finally, it concluded that to control the I_s values below 49.6 A, the magnetic flux linked to the HTS strands of the CSFE rotor should be decreased by controlling g_a.

C. Effect of the air-gap length between the rotor and stator of CSFE

Fig. 4.26 shows the results of the current-charging test when g_a was set to 7-, 8-, and 9-mm at f_r values of 13.3 and 26.7 Hz. It noted that the HTS strand on the toroidal head of the CSFE rotor was repetitively rewound using new HTS wires because they were unfortunately damaged during the repeated tests. Thus, the values of I_s were different compared with those in the equivalent test condition, i.e., cases of 13.3 and 26.7 Hz f_r, as shown in Fig. 4.24, because of technical problems above explained in subsection 4.2.4-B of Chapter 4, especially, the changes of R_{lj} because of re-soldering among them.

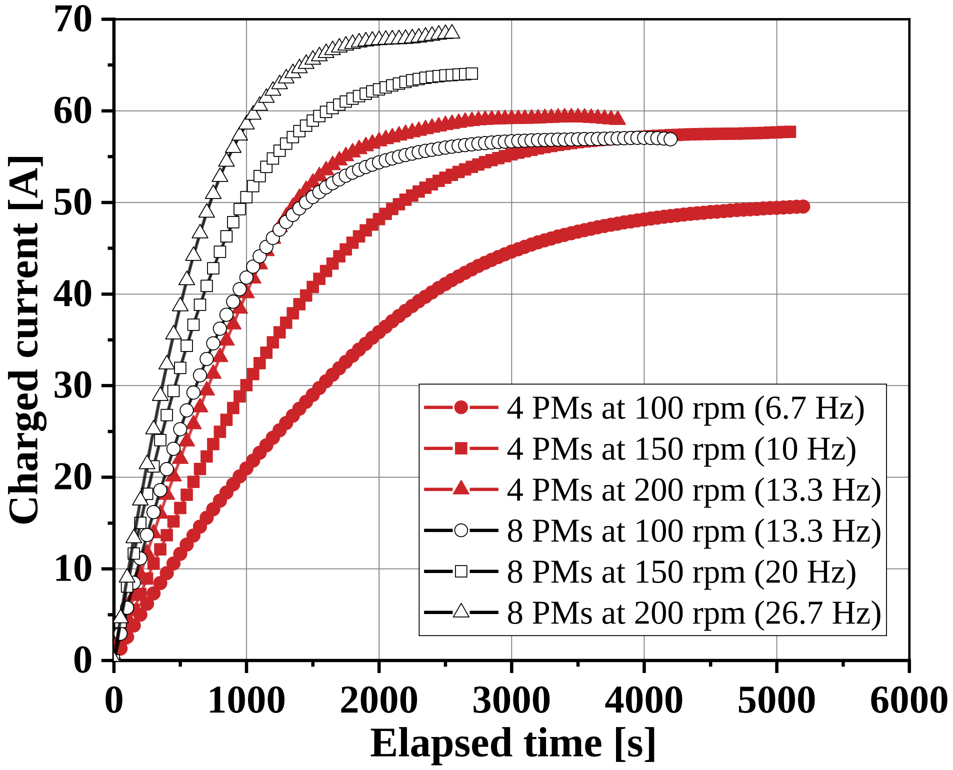

(a) Test cases with $n_p = 4$ and 8 at $g_a = 7$ mm and S_r =100, 150, and 200 rpm

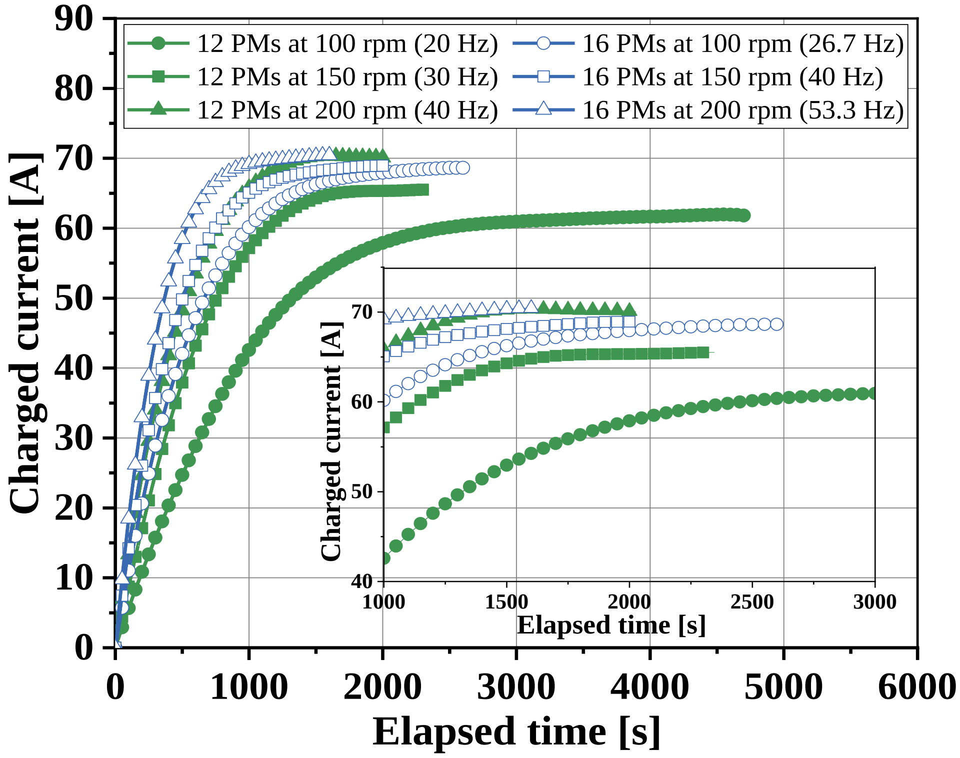

(b) Test cases with $n_p = 12$ and 16 at $g_a = 7$ mm, and S_r =100, 150, and 200 rpm

Fig. 4. 24. Charged current curves according to changes in n_p and S_r

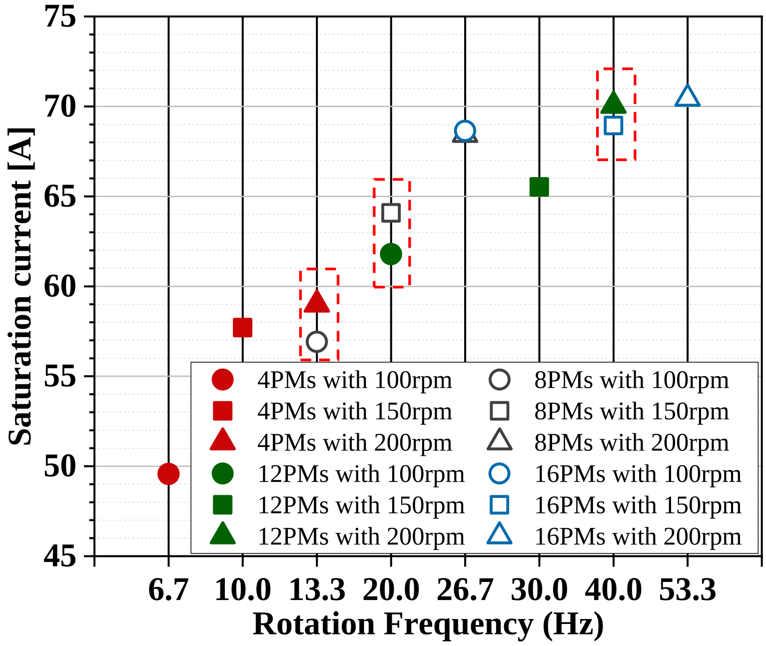

Fig. 4.25. I_s ranges according to the changes in f_r (= (n_p × S_r)/60)

Table 4.6. Charging test results according to the changes in f_r (= (n_p × S_r)/60)

Charging cases	**Charging time[†]/current[#] [s]/[A]**	**Max. charging current [A]**
4 PMs at 100 rpm (6.7 Hz)	1660/31.3	49.5
4 PMs at 150 rpm (10 Hz)	1280/36.5	57.7
4 PMs at 200 rpm (13.3 Hz)	922/37.5	59.3
8 PMs at 100 rpm (13.3 Hz)	795/36.1	57
8 PMs at 150 rpm (20 Hz)	690/40.5	64.1
8 PMs at 200 rpm (26.7 Hz)	582/43.3	68.4
12 PMs at 100 rpm (20 Hz)	886/39.2	62
12 PMs at 150 rpm (30 Hz)	564/41.4	65.5
12 PMs at 200 rpm (40 Hz)	439/44.5	70.4
16 PMs at 100 rpm (26.7 Hz)	524/43.4	68.6
16 PMs at 150 rpm (40 Hz)	400/43.6	68.9
16 PMs at 200 rpm (53.3 Hz)	304/44.5	70.4

[†]: Charging time to reach $0.632I_s$, [#]: $0.632I_s$

From the test results, in the 13.3 Hz f_r case, the I_s values were measured to be 63.7, 48.4, and 35.6 A at 7, 8, and 9 mm g_a, respectively, as shown in Fig. 4.26(a). In the 26.7-Hz f_r case, the I_s values were measured to be 76.4, 53, and 49 A at 7, 8, and 9 mm g_a, respectively, as shown in Fig. 4.26(b). Generally, the magnitude and charging speed of I_s decreased as g_a increased because the amount of magnetic flux that penetrated into the HTS strands was reduced by the increase in the reluctance in the air gap according to the increase in g_a.

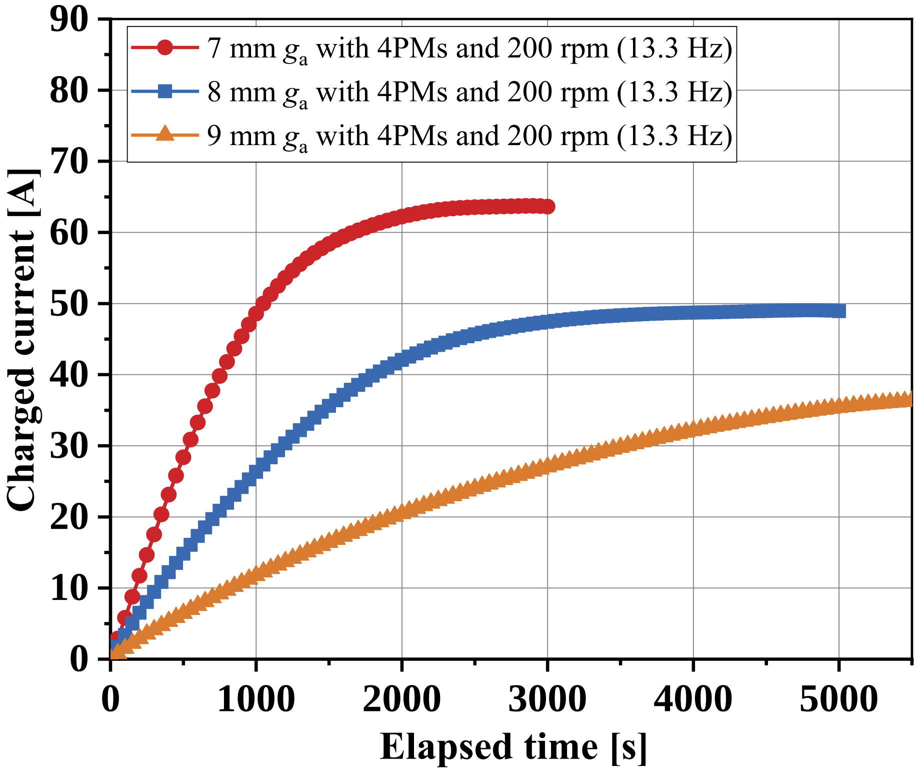

(a) Test cases with g_a = 7, 8, and 9 mm at 13.3 Hz f_r

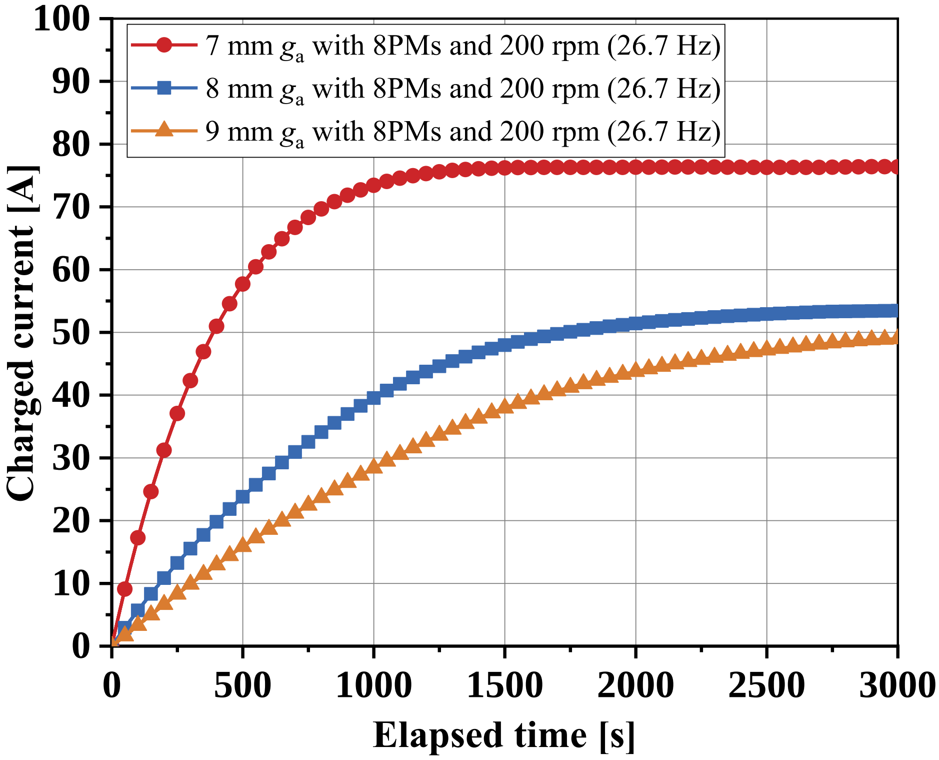

(b) Test cases with g_a = 7, 8, and 9 mm at 26.7 Hz f_r

Fig. 4.26. Charged current curves according to the changes in g_a

4.3. Results and discussion

In this subsection, the rotor, which composed the rotating machine field pole and rotary part of CSFE, was successfully developed for a 1 kW class HTSRM system. In addition, an experimental setup in a stationary flux-pumping mode was built using a fabricated rotor assembly to evaluate the current-charging performance of the HTS field winding using a noncontact excitation method. For the test results, the HTS field winding was successfully charged by the CSFE. Moreover, the current-charging characteristics were investigated according to the changes in n_p, S_r, and g_a to confirm the available current ranges in the HTS field winding. The controllable ranges of the charged current were expected to be approximately between 49.6–70.4 A by considering n_p and S_r, i.e., f_r. In addition, for the other test cases that considered g_a and f_r, the controllable ranges of the charged current were expected to be approximately from 35.6 to 76.4 A. Through preliminary experiment, I_f increases in practical HTS FCs for the 1 kW class HTSRM. Maximum I_f of 76.3 A is two times larger than that of $I_f \geq 30$ A in design process of HTSRM. The following causes are considered for such results:

1. Increase in maximum n_p from 8 in prototype to 16 in full-scale HTS flux pump. This increase in the charging speed and V_{emf}.
2. Decrease in minimum g_a from 8 mm in prototype to 7 mm in full-scale HTS flux pump. This increases in V_{emf}.
3. Increase in I_c of the HTS coil used in the charging test from 65 A in prototype to 128 A in full-scale HTS flux pump

It is believed that these results can be applied for the given design specifications of the 1 kW class HTSRM of 30 A I_f and 400 rpm S_r because under the operating conditions of 7 mm g_a and 26.7 Hz f_r, It can charge a maximum current of 76.4 A into the HTS field winding, which is two times more current than rated I_f of 30 A; however, rated S_r can be decreased from 400 to 200 rpm. All results in this chapter will be used as a technical reference for no-load and loaded tests, which are to evaluate the output performance of the 1 kW class HTSRM.

Chapter 5. Implementation of HTS Generator by the Application of Contactless Superconducting Field Exciter

To confirm the technical feasibility of contactless excitation method on HTSRM, this chapter presents the results of the fabrication and performance test of the 1 kW class HTSG, which is charged by the contactless-type excitation technique, i.e., CSFE. An expensive dynamometer is required for measuring the output performance of HTSRM in the motor operation mode. Therefore, the operation mode in the generator was considered to simply configure the test environment, which is to measure the performances of the developed prototype-HTSRM. The 1 kW class M-G set was finally fabricated using the commercial induction motor and developed HTS generator. As the first step of configuring the test environment, a cryogenic cooling system using LN2 was fabricated and its cooling characteristics were tested with the HTSG. Further, various core components of the HTS generator, such as a salient rotor pole with HTS coils, rotating shafts, torque-transferring structures, and rotating and stationary parts for the CSFE, were manufactured and assembled to configure the 1 kW class HTSG system. In addition, the HTSG stator was fabricated with three-phase copper armature winding. In particular, the contactless field-excitation performance of the apparatus was verified before the final assembly of the HTSG system.

Further, the assembled machine was connected with a conventional induction motor and three-phase resistive load to build the M-G setup. The HTSG operating performance was evaluated using the M-G test setup.

In non-load tests, the characteristics of the open-circuit induced voltage (E_i) of the HTSG, which was generated and affected by contactless field excitation and operating speed, respectively, were tested and measured. In particular, the charge and discharge behaviors of the field current excited by the CSFE were experimentally analyzed based on the E_i profiles of the HTSG. Further, three-phase variable resistive loads were connected in the load test. The HTSG output characteristics were tested and measured by performing experiments on the constant load and constant speed characteristics, respectively.

5.1. Fabrication of LN2 cryogenic cooling system

This subsection presents the practical results of design and fabrication of the cryogenic cooling system with LN2 for the 1 kW class HTSG. The simple cooling system was considered readily to inject LN2 inside of HTS rotor without any complex devices for generation and circulation of cryogen. Based on similar devices in previous developments [14], [75]–[77], the cooling system was empirically designed and fabricated without any analytical or numerical approaches to save the resources while developing cooling systems.

Fig. 5.1 shows the configuration of cryogenic cooling system with LN2, which is composed of LN2 cryostat at generator outside and triple cooling pipe at generator inside. The direct injection of LN2 through the original pressure of the LN2 dewer could thermally and mechanically damage the ferro-fluid seal; thus, the additional cryostat was used to construct the cryogenic cooling system, which is capable of manually controlling the injection pressure of LN2 stored in the cryogenic vessel. By the pressures of GN2 in the external tank or naturally vaporized GN2 in LN2 cryostat, which are relatively lower than that of the original pressure of the LN2 dewer, LN2 is supplied to the LN2 feeding pipe inside the HTSRM. Fig. 5.2 shows the fabricated LN2 cryostat installed with level sensor inside the cryostat. The amount of LN2 is measured and monitored by the level sensor with PT-100, as shown in Fig. 5.2(b).

To naturally discharge the vaporized N2 outside the HTSG, the cryogen transfer pipe with triple-layers type was designed and fabricated. The assembly of triple cooling pipes consisted of LN2 feeding, GN2 discharge, and vacuum pipes, as shown in Figs. 5.1(a)–5.1(c), respectively. The feeding pipe is positioned at the innermost of this assembly to deliver LN2 inside the rotor and the discharge pipe is positioned outside the feeding pipe to discharge the vaporized N2, i.e., GN2, after cooling the HTS rotor. Finally, the vacuum pipe is positioned at the outmost of this assembly to thermally insulate the ferro-fluid seal against freezing caused by heat transfer of GN2. Moreover, the GN2 discharge port was separated to the ferro-fluid seal by at least 500 mm to prevent freezing of the ferro-fluid seal caused by the returned GN2 flowing in the discharge pipe. Finally, the assembled triple cooling pipes were vacuum tested by a rotary vacuum pump (GHP-150 from KOREA DIAVAC Co., Ltd.), and convection gauge (CG202 from ATOVAC Inc.). The vacuum level was measured to be maximum 9.8×10^{-4} with the operation of the vacuum pump and maintained at 1.5×10^{-3} with non-operation of vacuum pump. Consequently, this feeding pipe could successfully transfer LN2 without any icing on surfaces of the vacuum pipe.

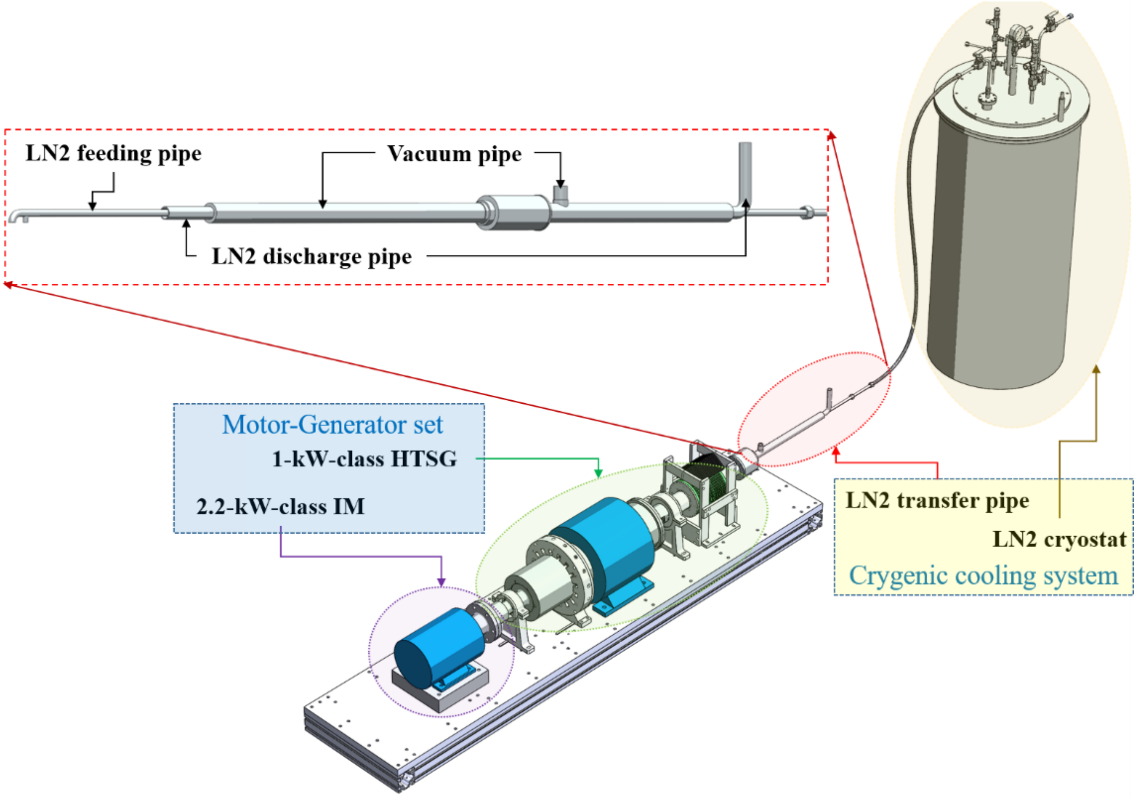

(a) 3D configuration diagram of the LN2 cooling system connected with the M-G set

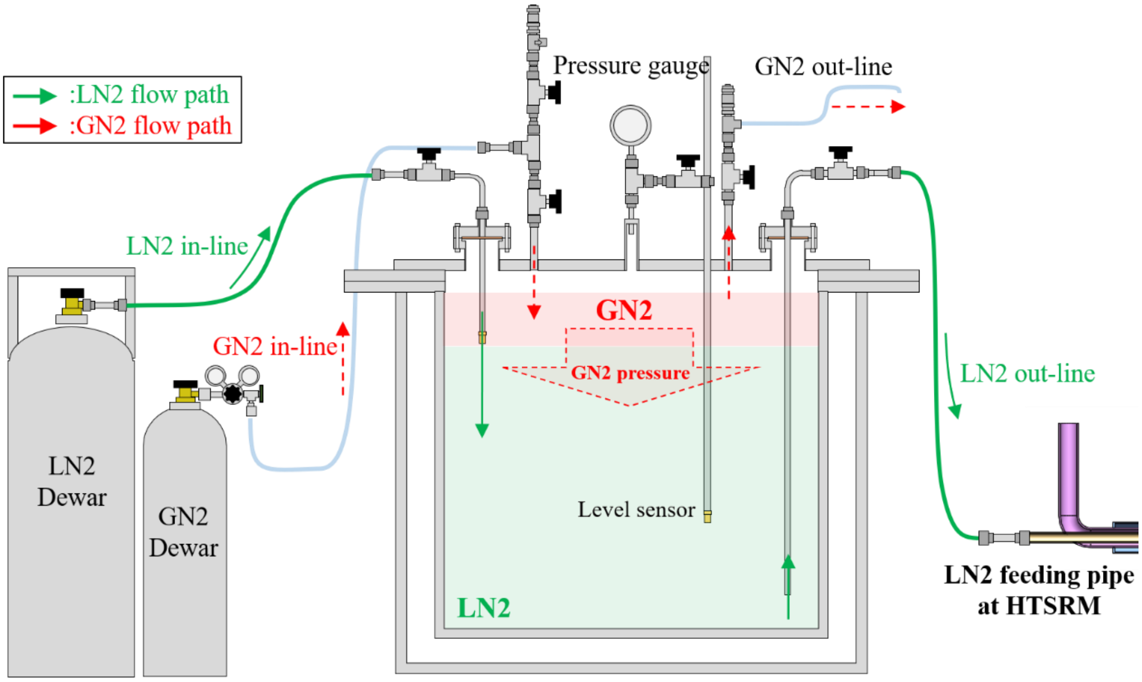

(b) Schematic diagram of the LN2 cryostat

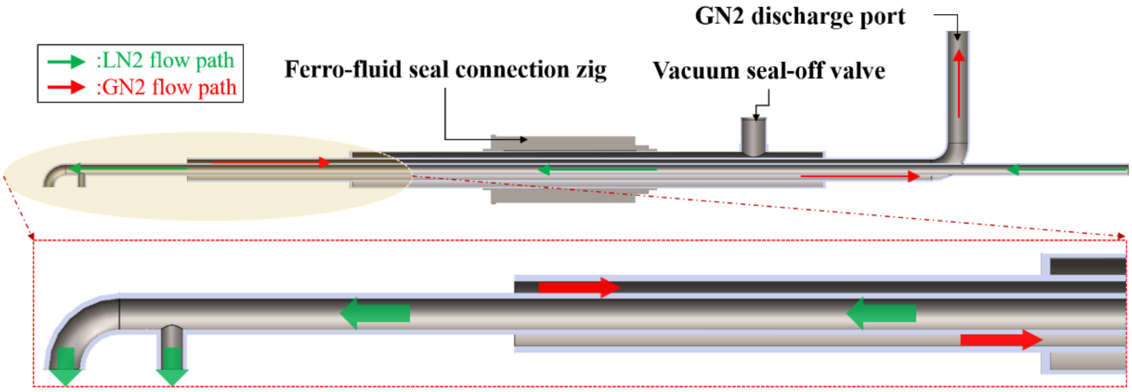

(c) Cross-sectional view of triple cooling pipes

Fig. 5.1. Configuration of the cryogenic cooling system for the 1 kW class HTSG

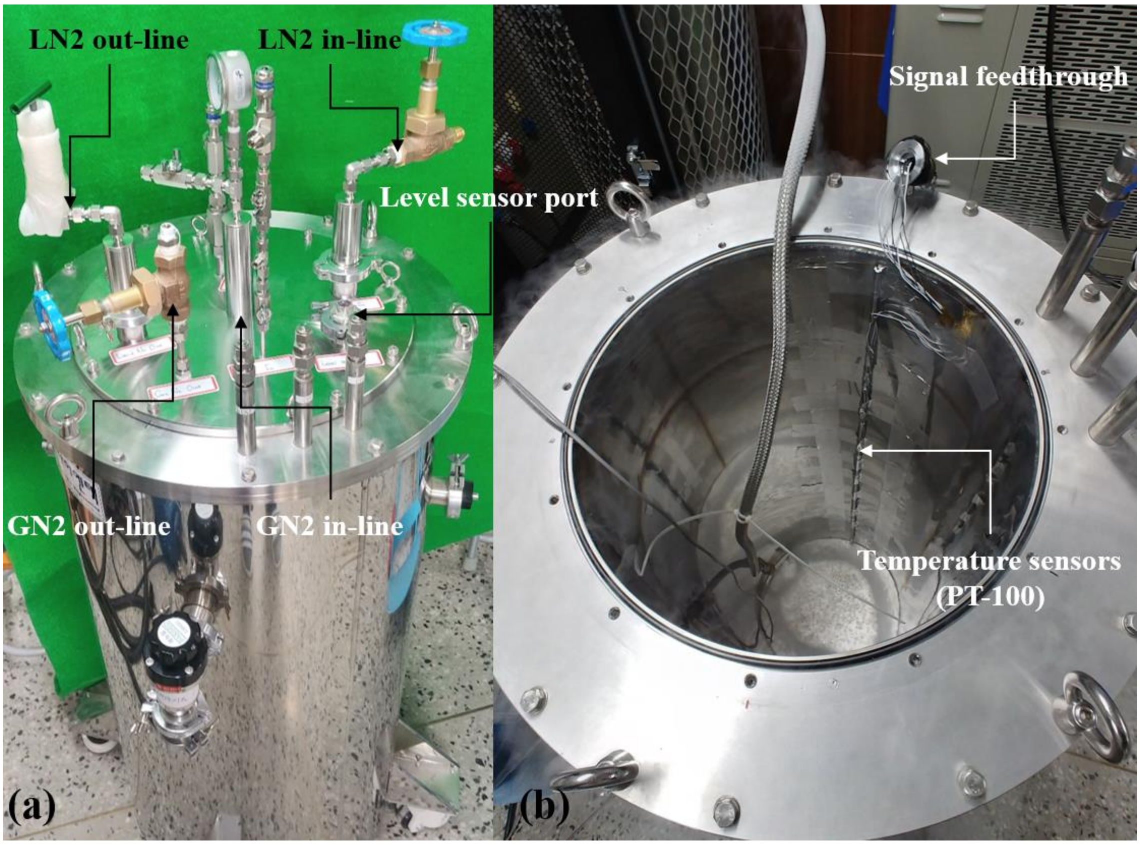

Fig. 5.2. Photographs of fabricated LN2 cryostat. (a) Overall configuration and (b) inside view of the cryostat with level sensor

5.2. Assembly of HTS generator system

This subsection presents the results of final fabrication of the HTS rotor and Cu stator for the 1 kW class HTSG. First, the preliminary rotor assembly, which was fabricated in Chapter 4, was fully assembled with other rotor components, such as torque disk and tube, rotating shafts, and cryostats. Further, based on the design results obtained in subsection 3.1.2 of Chapter 3, the three-phase coils were wound using Cu wires and the final stator assembly of the HTSG was fabricated with armature coils.

5.2.1. Assembly of the rotor with HTS field winding

Before the final assembly of rotor, Hall sensors were finally calibrated with epoxy impregnation to measure Hall signals at a constant position. Using DC PS, magnetic field density profiles were measured at 10 and 90 A charges, as shown in Fig. 5.3. Thus, the charged I_f could be indirectly predicted using the voltage signals corresponding to the magnetic field, i.e., at 10 and 90 A charges, as shown in Fig. 5.3.

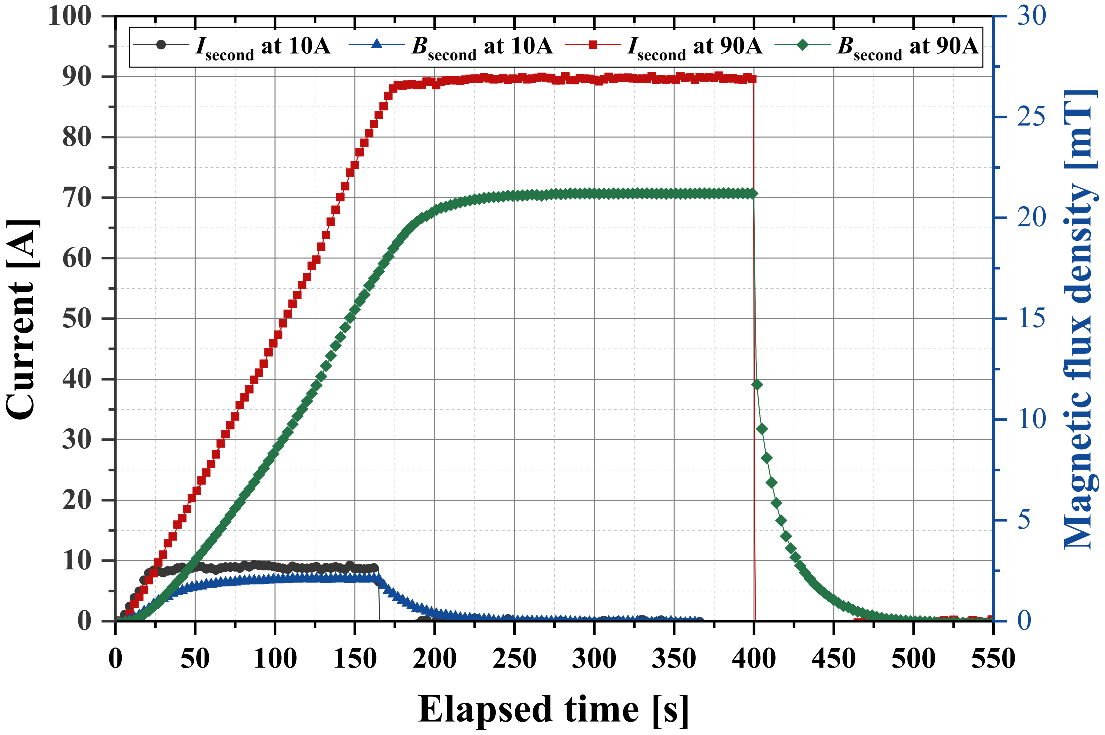

Fig. 5.3. Charge and discharge profiles of the second pole at 10 and 90 A by DC PS

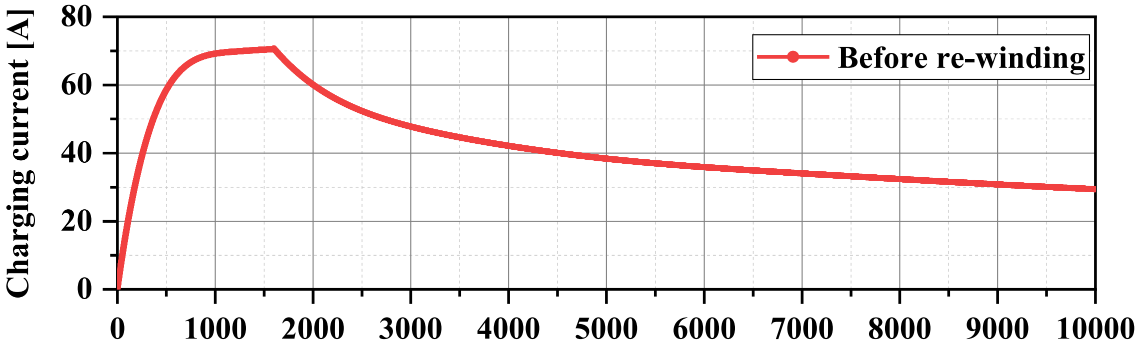

(a) Before re-winding the HTS wire on CSFE

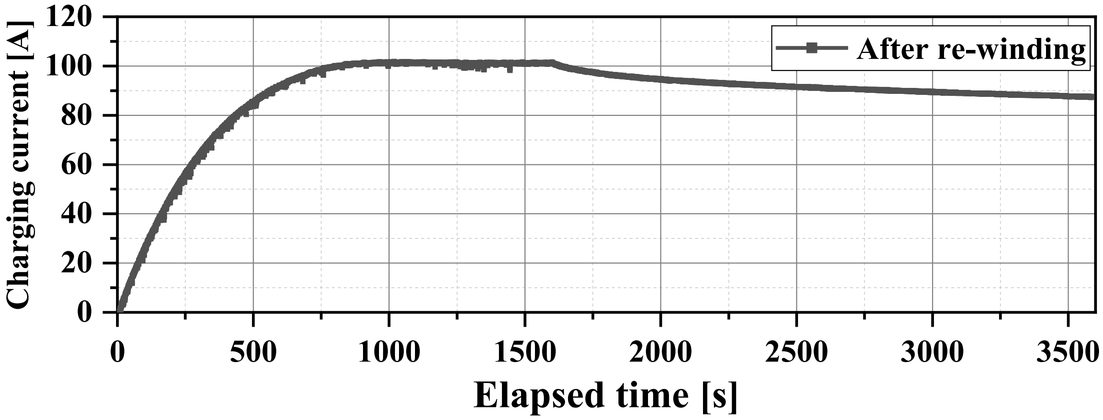

(b) After re-winding the HTS wire on CSFE

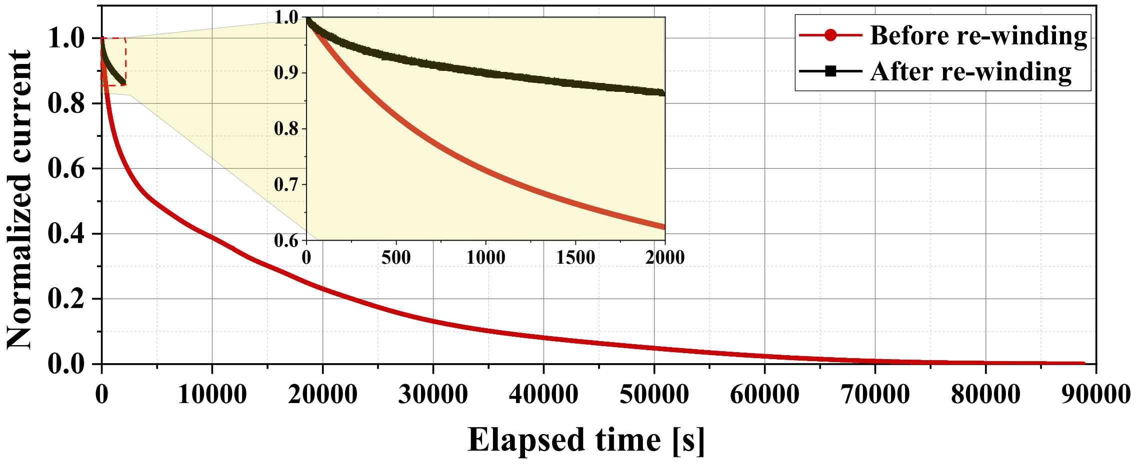

(c) Comparison of normalized discharging I_f

Fig. 5.4. Contactless charging and discharging characteristics of I_f excited by a 100 A class CSFE

Finally, the I_f profile was measured using Hall voltage in the second pole, as shown in Fig. 5.4(b). I_f is fully saturated at around 101 A and this value is approximately 32.2% higher than that of the test result in the preliminary charging test described in subsection 4.2.4 of Chapter 4, as shown in Fig. 5.4(a). The charging time to reach 101 A was 887 s and the current ramp up rate was 0.114 A/s. This is because the joint-resistances, (R_{lj1} and R_{lj2}) were decreased by re-winding, thereby causing re-soldering between the two ends of the HTS strand and HTS SPCs, as well as replacement with new 2G HTW wires. This is reasonably proven by normalized comparison of spontaneous discharged currents, as shown in Fig.5.4(c). The black curve, i.e., a discharging profile after the re-joint between the CSFE and the HTS field pole, is discharged slower than that of the red curve because of lower joint resistances in the superconducting closed circuit.

If HTS FCs are charged with currents of 70.4 and 101 A with a contact excitation system, the excitation losses in current lead pairs with round rods were estimated to be 8.46 and 13 W, respectively, with an assumption of 330 mm axial length, 3.1 mm diameter, 9.87 nΩ · m resistivity, and 411 W/mK thermal conductivity of Cu at 77 K.

However, if the HTS field pole is charged by the CSFE, the excitation losses were estimated to be 0.54 and 1.11 W, respectively, with an assumption of the total resistance of the superconducting circuit inside the HTS rotor (R_e) of 0.1086 and 0.1093 mΩ, respectively. It is observed that the values of R_e ($=L_c/\tau$) can be roughly calculated with the charged I_f profiles, as shown in Figs. 5.4(a) and 5.4(b). In an equal operating environment, the CSFE is expected to reduce the excitation loss by about 93.7% and 91.5% as compared to that by the conventional contact excitation system.

Fig 5.5 shows the images of the rotor assembly without rotating shafts and cryostat. The joint lead wires, which connect the HTS SPCs and CSFE, and various signal wires were impregnated by Stycast epoxy to mechanically protect them against whirlpool of LN2 when the HTSG rotates. Further, this assembly was finally covered and welded by SUS cylinder to contain LN2. After welding, the vacuum level of SUS cylinder inside was measured to determine if there was a leakage of vacuum, which was maintained at 1.5×10^{-3} with the non-operation of vacuum pump. The whole rotor assembly of 1 kW class HTSG was successfully fabricated with connection of bellows pipe, torque elements, rotating shafts, and cryostat, as shown in Fig. 5.6.

Bellows pipe, which contain the cooling pipe, was connected at pole end with indium sealing. Further, the rotating shafts were assembled at both ends of the rotor through torque tube and disk, as shown in Fig. 5.6(c). The assembly of the HTS rotor finally was finished by covering the cryostat, as shown in Fig. 5.6(d). The fully assembled HTS rotor was tested by helium detector to investigate the leak point in the HTS rotor. No leaks were detected, and the vacuum level was maintained at1.5×10^{-3} with non-operation of vacuum pump.

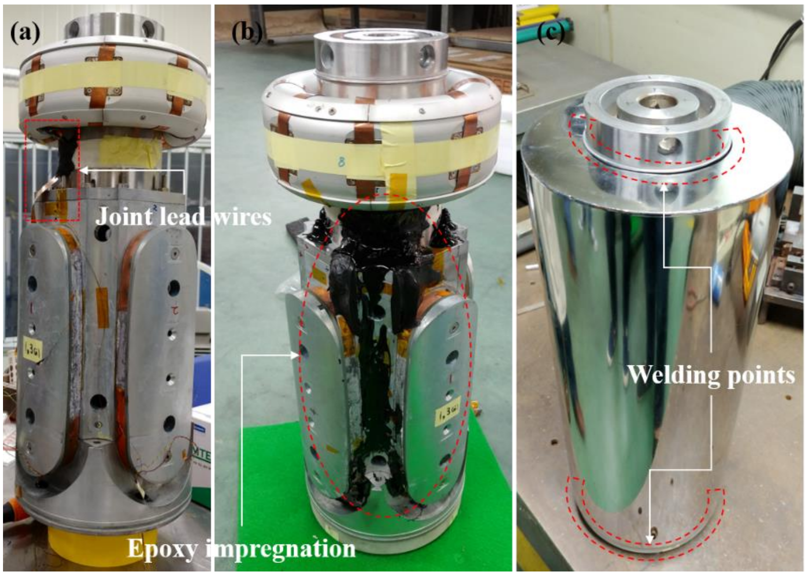

Fig. 5.5. Images of HTS rotor assembly I. (a) Before epoxy impregnation, (b) after epoxy impregnation, and (c) covering by SUS cylinder

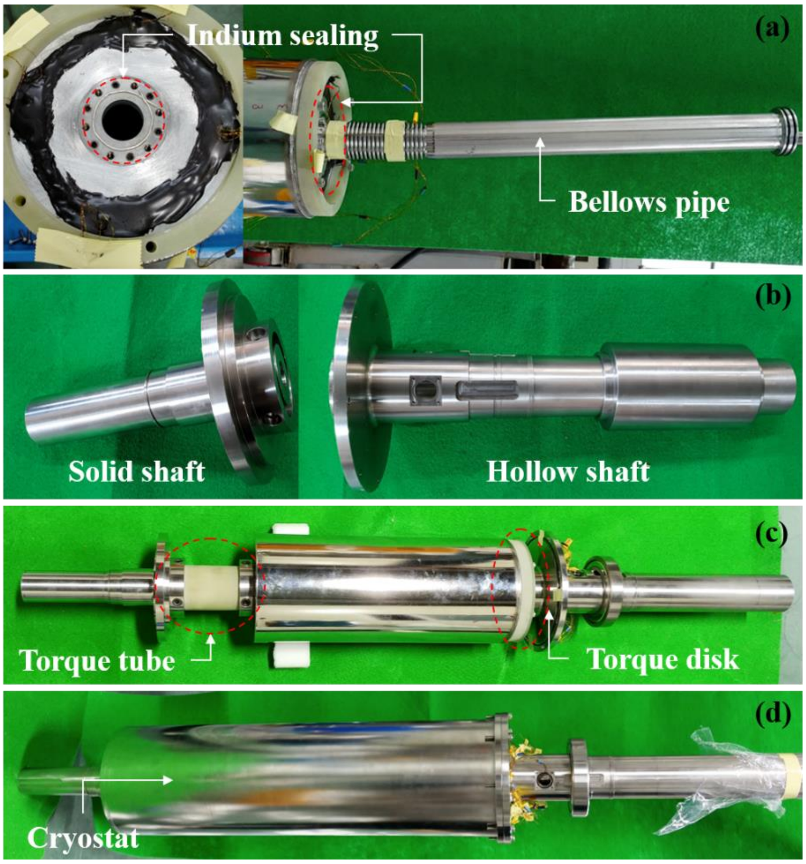

Fig. 5.6. Images of HTS rotor assembly II. (a) Sealing of bellows pipe by indium wire, (b) both rotating shafts, (c) connection of shafts and torque elements, and (d) final rotor assembly with cryostat

5.2.2. Assembly of the stator with armature winding

Based on the numerical design results obtained in subsection 3.1.2 of Chapter 3, this stator was finally fabricated, as shown in Fig. 5.7. The three-phase armature was designed and fabricated using double-layer winding, distribution winding with four slots per pole per phase (q) , and fractional pitch winding with 10/12 coil pitch. The module for each pole in one phase was wound to be 26 turns with two strands of enamel coated copper wire with 0.95 mm diameter. Each ends of phases were connected to create the star connection in armature and opposite ends of each phase are led to terminal box. The fabricated module coils were inserted in 48-slots of stator core and then the armature ends were insulated by insulation papers as shown in Fig. 5.7(c). The fill factor of armature coil was calculated to be approximately 40.7% and corresponding current density (J_a) of armature was estimated to 2.82 A/mm^2 with rated current (I_a) of 4 A$_{rms}$. Each phase resistance was measured to 3.3 Ω at room temperature. For final process, the stator was coated and electrically insulated by varnish bath to protect the armature winding.

Fig. 5.7. Photographs of fabricated stator for the 1 kW class HTSG. (a) Armature coil modules, (b) armature coil assembly with stator core, (c) insulation in armature ends, and (d) final assembly of the stator

5.3. Characteristic test on operational performance of HTS generator

This sub-chapter presents experimental results on operation characteristic of the 1 kW class HTSG which is charged by contactless excitation method. First of all, test environment was composed with M-G set, measurement devices, resistive load, and others. Then, the charging characteristics of I_f excited by CSFE and open-circuit characteristics of HTSG were tested and measured in no-loaded operation. In the loaded operation, the output characteristics of HTSG such as charged I_f, phase voltage (V_p), voltage regulation rate (V_r), phase current (I_p), active power (P_a), THDs, etc., were tested and measured by connecting three-phase variable resistor.

5.3.1. Configuration of characteristic test setup

Fig. 5.8 shows the test configuration to test the operation characteristic of the 1 kW class HTSG. The motor-generator (M-G) set was developed using a commercial 5.5-kW induction motor and fully assembled 1-kW HTSG.

In the initial field-charging mode, the I_f is started to be charged by contactless method because of injection of time-varying magnetic field by rotation of CSFE rotor, which is uniaxially connected with field-pole of HTSG and the maximum I_s in the field winding can be controlled by S_r in charging mode. Therefore, to control I_s in field winding as well as induced voltage of HTSG, a prime mover, i.e., induction motor, should be driven and controlled by an inverter with variable speed control.

The load characteristics of the 1 kW class HTSG can be experimentally analyzed by measuring the electrical outputs such as V_p, I_p, P_a, and etc., which are supplied to the three-phase resistive load with a capacity of a 1.5-kW connected to the stator of HTSG. The variable signals of output are measured and monitored by oscilloscope, i.e., HDO 4034A from TELEDYNE LECROY Co., Ltd., and power quality analyzer, i.e., DEWE-571 from DEWETRON Inc..

The cooling condition inside the HTS rotor and stability of field winding are detected through the temperature sensors in field-pole and terminal voltages in four-HTS SPCs and all signals inside the rotor are drawn through the slip-ring and brush set, which are coupled to hollow shaft, and monitored and recorded in the PC-DAQ system outside.

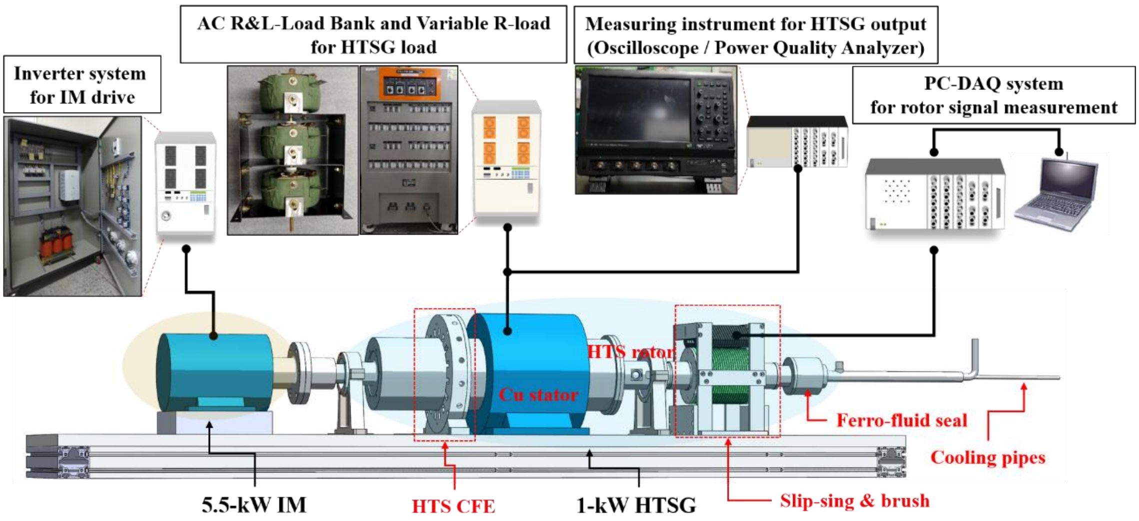

(a) 3D configuration diagram of characteristic test

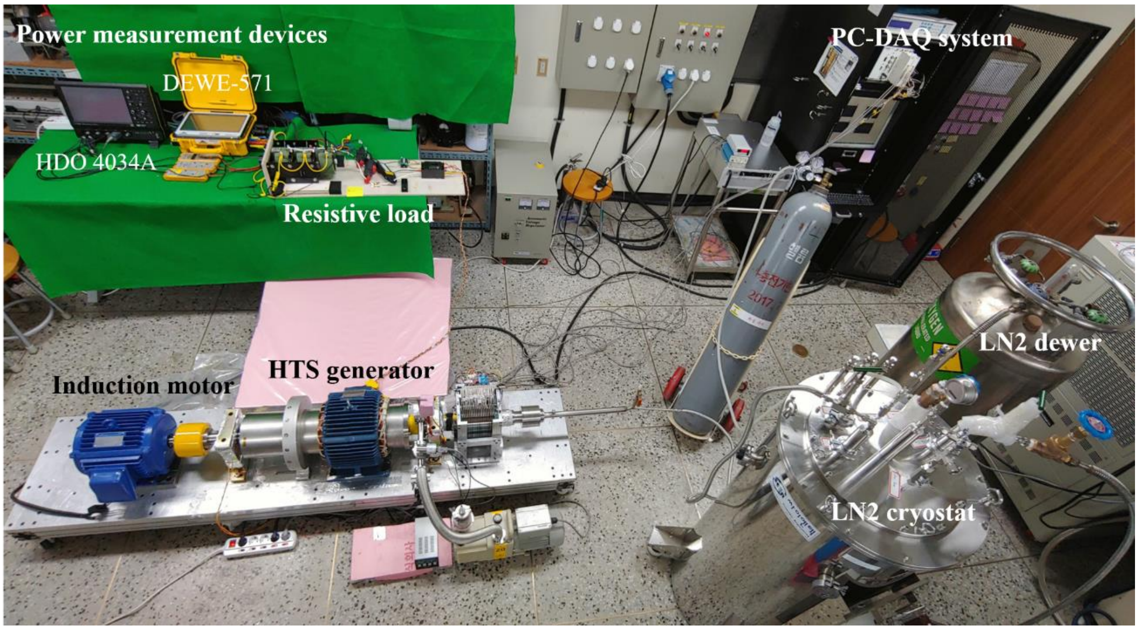

(b) Whole view of the characteristic test setup

Fig. 5.8. Configuration of characteristic test for the 1 kW class HTSG

5.3.2. Characteristic test in no-load mode

Unfortunately, the technical problems in slip-sing and brush set occurred during the rotation test, and thus, no out-put signals in the HTS rotor could not be measured during the generator test. Therefore, we analyzed the behavior of the measured E_i of HTSG to reasonably explain the test results without any I_f signals. In general, the E_i of the synchronous generator is proportional to the mechanical constant (K), S_r, and the magnetic flux (Φ) or I_f, i.e., $E_i = K\Phi(I_f)S_r$, before the iron cores are magnetically saturated. In other words, if S_r was continuously maintained along the elapsed time, the E_i of the HTSG would also exhibit the same behavior with I_f charged by the CSFE.

Through speed-up and -down tests without the resistive load, a continuous output data for a total of 7 h was measured and recorded with the power quality analyzer and oscilloscope. Fig. 5.9(a) shows the profiles of E_i which are generated in the open-circuited three-phase armature and measured as the root mean square value from the power quality analyzer (DEWE-571). After disconnecting the circuit breaker for switching to resistive load, the three-phase E_i of the HTSG was observed at successive changes of the S_r.

In the speed-up tests, the S_r was changed and increased from 200 rpm up to 900 rpm with 100 rpm interval after the E_i of HTSG was saturated and observed by the measurement devices. In the initial operation, the HTSG was operated at 100 rpm to cool down the rotor inside, and then, the S_r was increased and constantly maintained at 200 rpm after 3200 s to excite the HTS FCs in earnest.

In the rotation with 200 rpm, despite the constant S_r until 6000 s, the continuous increase in E_i of the HTSG was observed as shown in the black-dotted square in Fig. 5.9(a). This means that the I_f charged by CSFE is not saturated and is exponentially increasing to the saturation zone of the I_f. The E_i of HTSG was almost saturated and constantly maintained by the saturated I_f for approximately 6000 s. The value of I_s was expected to be 101 A based on the final current charging test as shown in Fig. 5.4.

In the speed-up tests from 200 rpm to 600 rpm, whenever the S_r of HTSG changed up to 600 rpm, the E_i was constantly maintained or slightly increased along the elapsed time, indicating that the I_f was charged at a constant or slightly higher rate, i.e., $I_f \geq 101$ A, as shown in the enlarged view of the blue-dashed square in Fig. 5.9(a). The magnitude of the E_i, which increases with each speed acceleration, was almost constant, and therefore, only the increase in the S_r appeared to affect the changes in the E_i of HTSG, as shown in Fig. 5.9(b). In conclusion, the maximum I_f was charged and saturated under the S_r of 600 rpm, and the operating current margin which is the ratio of I_c to I_f was calculated to be 0.789.

Through charge behaviors under N_s of 600 rpm, it is suggest-ed that unchanging characteristic in I_f within certain S_r of developed CSFE is suitable for industrial applications requiring constant speed operation because it operated like a PM generator or motor within a certain speed range. Fig. 5.10 shows the measurement results screened from DEWE-571 and HDO 4034A devices. The averaged E_i of the three-phase was measured to be 238 V_{rms} at the rated S_r, i.e., 400 rpm.

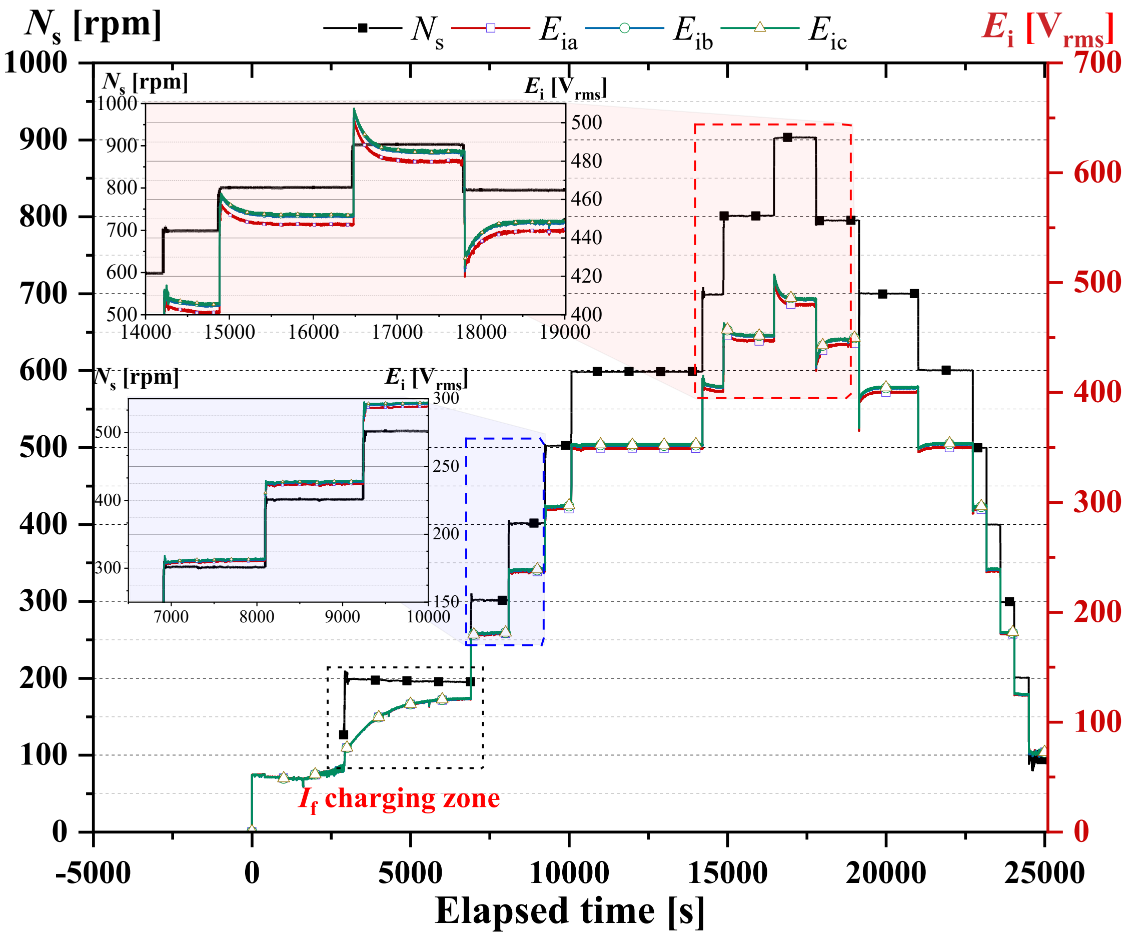

(a) E_i profiles according to the changes in S_r measured by power quality analyzer

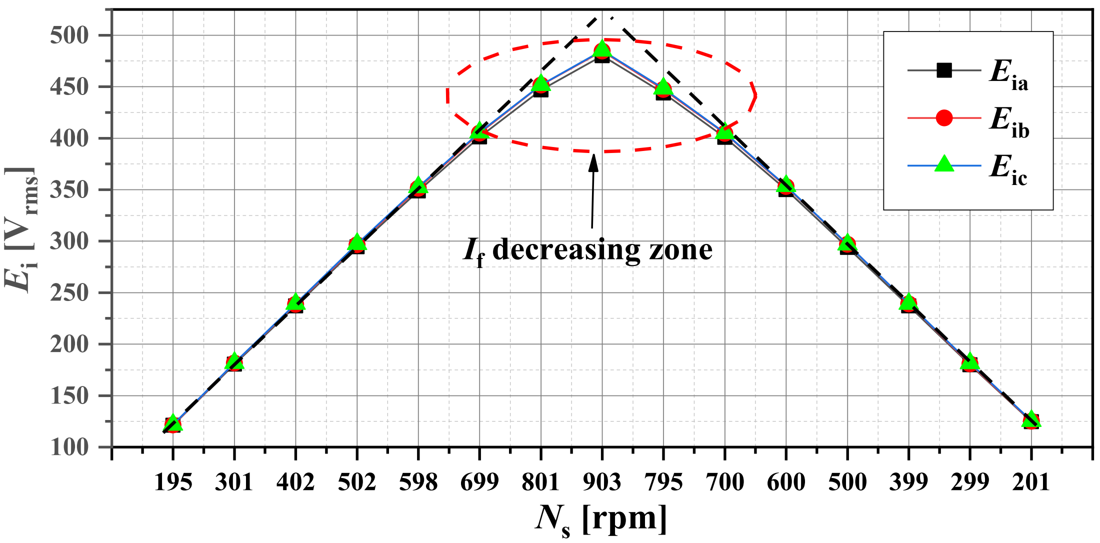

(b) E_i curve according to changes in S_r

Fig. 5.9. Characteristic test results of the 1 kW class HTSG in the non-loaded test ($S_r = N_s$)

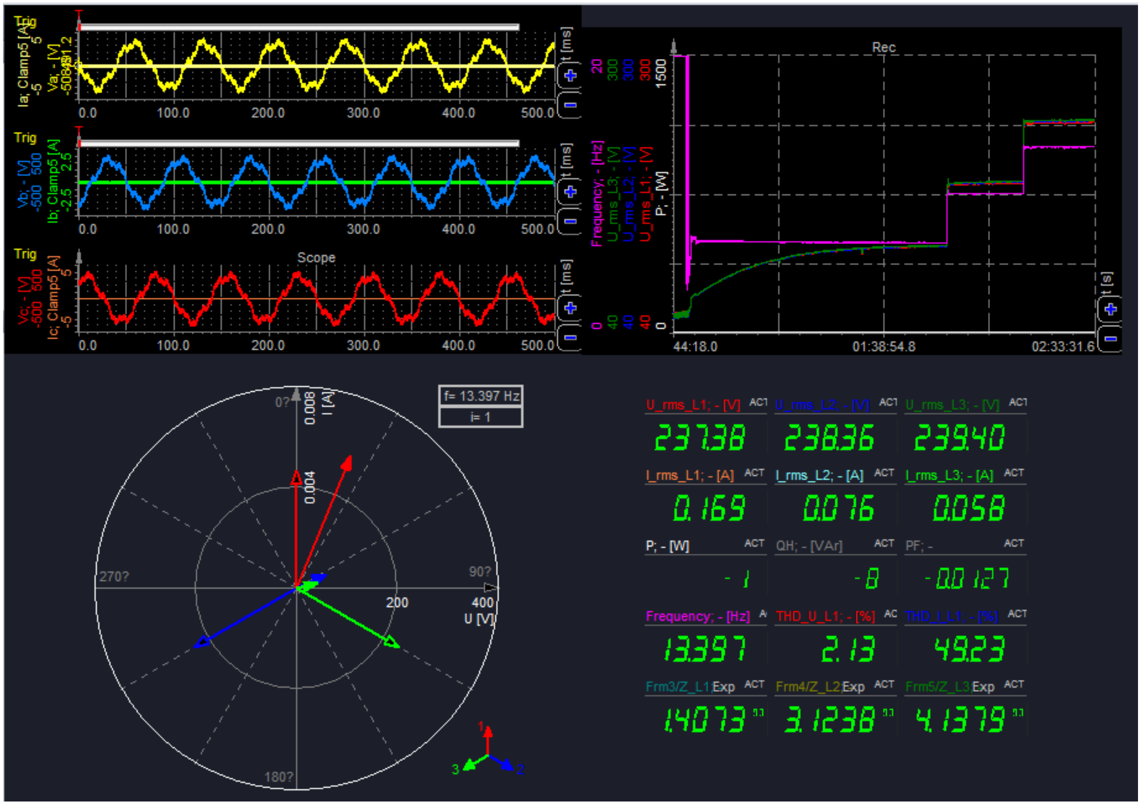

U_rms_L1; - [V] ACT 237.38
U_rms_L2; - [V] ACT 238.36
U_rms_L3; - [V] ACT 239.40
I_rms_L1; - [A] ACT 0.169
I_rms_L2; - [A] ACT 0.076
I_rms_L3; - [A] ACT 0.058
P; - [W] ACT -1
QH; - [VAr] ACT -8
PF; - ACT -0.0127
Frequency; - [Hz] 13.397
THD_U_L1; - [%] 2.13
THD_I_L1; - [%] ACT 49.23
Frm3/Z_L1;Exp ACT 1.4073
Frm4/Z_L2;Exp ACT 3.1238
Frm5/Z_L3;Exp ACT 4.1379

(a) Output characteristics in power quality analyzer (DEWE-571)

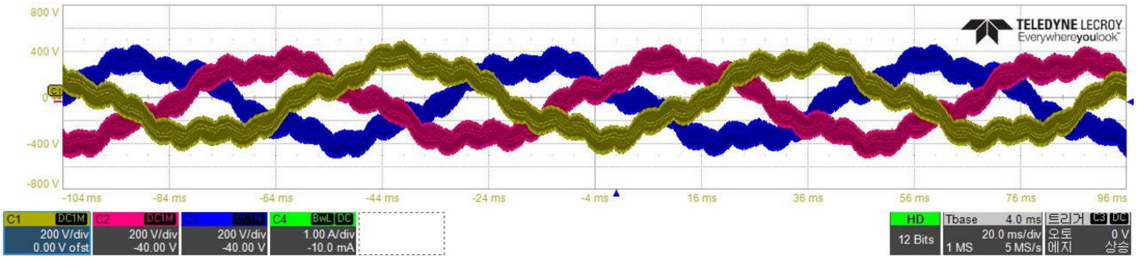

C1 DC1M 200 V/div 0.00 V ofst
C2 DC1M 200 V/div -40.00 V
C3 DC1M 200 V/div -40.00 V
C4 BwL DC 1.00 A/div -10.0 mA
HD 12 Bits
Tbase 4.0 ms 20.0 ms/div 1 MS 5 MS/s
트리거 C3 DC 오토 0 V 에지 상승

(b) Three phase E_i wave forms in the oscilloscope (HDO 4034A)

Fig. 5.10. Characteristic measurement screens in the non-loaded test of the 1 kW class HTSG

In the speed-up tests from 700 to 900 rpm, S_r was constant at the beginning of the speed changes; however, the behavior of E_i showed an exponential decrease after reaching the maximum value, as shown in the enlarged view of the red-dashed square in Fig. 5.9(a). It is concluded that this is because I_f decreased from the initial value and this is reasonably proven with a slope decrease in the E_i curve according to changes in S_r, as shown in the red-dashed circle of Fig. 5.9(a). It can be assumed as the demagnetizing effect caused by automatically field weakening control in HTS FCs at high speed levels. The inherent charging characteristic of the HTS flux pump employing iron structure and 2G HTS conductor, which is the amount of current charging that can be reduced under high-speed levels, or the uneven cooling of the rotor because of excessive centrifugal force during high-speed rotation are considered as a cause of this phenomenon. In [29], [33], [44], [48], such anomalous behaviors were reasonably expected to be caused by eddy currents at relatively higher S_r, which generate heat loss in iron structures and 2G HTS wire, thereby resulting in reduction in both V_{oc} and R_d by decreasing linkage flux and I_c, respectively. Moreover, the automatic demagnetizing effect caused by the decrease in I_f can be applied in HTSMs for electric traction and propulsion, which require field weakening control during high-speed operations. For S_r = 600 rpm and above, I_f was expected to decrease to 101 A or less, and the minimum value of I_f was charged and saturated at the S_r of 900 rpm.

In the speed-down tests, S_r was set to decrease from 900 to 200 rpm at 100 rpm intervals after E_i of the HTSG was saturated. In the speed-down tests from 900 to 700 rpm, S_r of HTSG was constant at the beginning of the speed changes; however, the behavior of E_i showed an exponential increase after reaching the minimum value, as shown in the enlarged view of the red-dashed square in Fig. 5.9(a). Thus, it can be concluded that this is caused by increasing I_f from the initial value. This means that this is a behavior wherein I_f, which has been saturated to the minimum value at 900 rpm, is re-charged at 800 rpm or 700 rpm above I_s at 900 rpm.

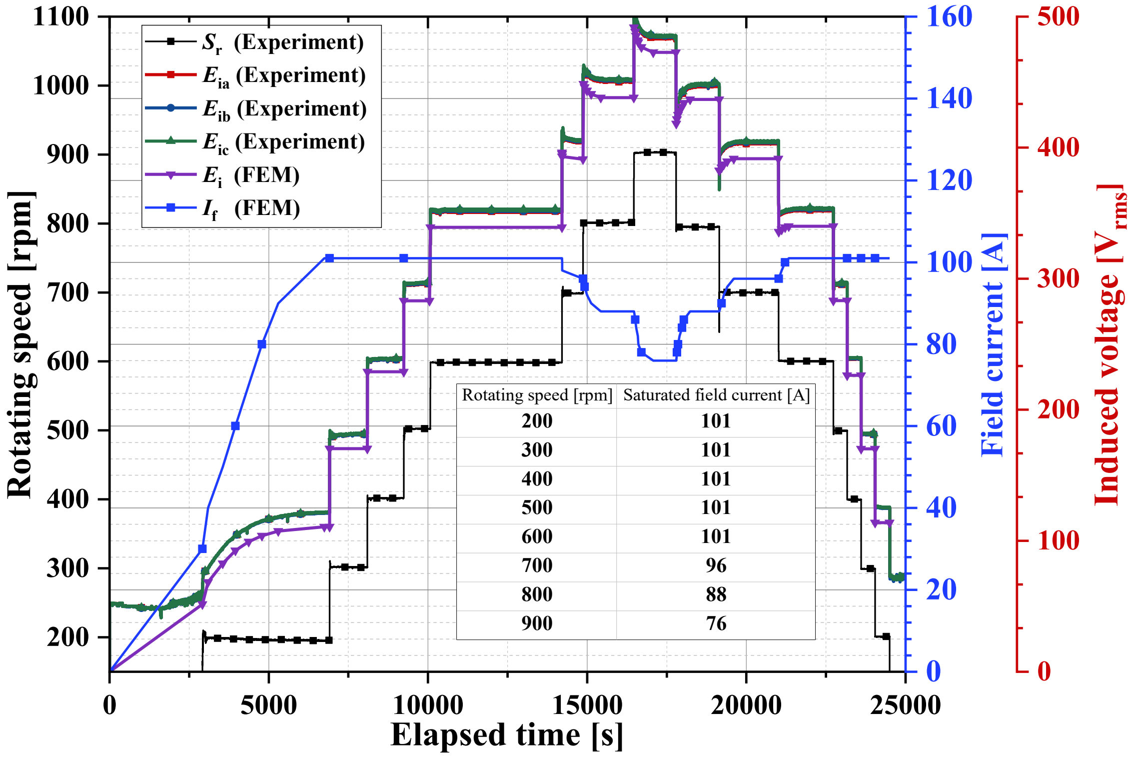

Rotating speed [rpm]	Saturated field current [A]
200	101
300	101
400	101
500	101
600	101
700	96
800	88
900	76

Fig. 5.11. Characteristic comparison of experiment- and FEA-results in results in non-loaded test and estimation results on the I_f

In the speed-down tests from 600 to 200 rpm, E_i of the HTSG at each S_r has the same value at the speed-up test, and the magnitude of E_i, which decreases with each speed drop, i.e., the slope of E_i curve, was also constant, as shown in Fig. 5.9(b). Therefore, only S_r affects the changes in E_i of the HTSG.

To understand the I_f behaviors more reasonably, the values of I_f were estimated based on test results of the E_i using 2D FEA. Fig. 5.11 shows the E_i and I_f profiles to compare the experimental approach with the numerical method. It is observed that the values of S_r, which are same in the x axis of Fig. 5.11, were used for 2D FE simulations to compare both results in equal operating conditions. Generally, difference in analysis results as compared to those of experiments was observed. It attributes this difference to the measurement errors for various output signal in experiments, as well as difference in the material property of magnetic cores. The difference in E_i between experiment and simulation is approximately 12 V_{rms}, thereby indicating that the E_i values in the experiment (E_{ia}: red line with square symbol, E_{ib}: green line with circle symbol, and E_{ic}: red line with triangle symbol) was 12 V_{rms} higher than those of simulations (E_i: violet line with inverse triangle symbol) on an average, as shown in Fig. 5.11. The values of saturated I_f are conversely estimated based on the E_i profile in the experiment, as shown by the blue line with square symbol in Fig. 5.11 and presented in Fig. 5.11. For values of S_r between 700 and 900 rpm, it was observed that saturated I_f decreases for each value of S_r. The values of I_f at 700, 800, and 900 rpm were estimated to be 96, 88, and 76 A, respectively.

5.3.3. Characteristic test in variable resistive load mode

The operating performance of the 1 kW class HTSG was verified by measuring the electrical outputs supplied to the three-phase variable resistive load with a capacity of 1.5 kW connected to the stator of the HTSG. Through the resistive loaded test, the continuous outputs from a total of 5 h were measured and recorded with a power quality analyzer and oscilloscope.

The CSC test was conducted with a constant S_r and variable load resistance (R_l). When E_i and I_f of HTSG were fully saturated by the rotation with constant S_r, the load test was conducted by putting R_l and then changing the values of R_l. The output parameters, i.e., V_p, V_r, I_p, P_a, THDs, and others were measured from 200 to 800 rpm at 100 rpm intervals; these values are listed in Table 5.1. Fig. 5.12 shows the profiles of the various output parameters that were generated in the CSC test and measured as root mean square values in the power quality analyzer (DEWE-571), at different values of S_r of 200, 400, 600, and 800 rpm. The rated P_a of HTSG, i.e., 1086 W was generated with I_p = 1.58 A, S_r = 400 rpm, and R_l = 150 Ω in the CSC test. Moreover, the THDs in V_p and I_p, and V_r were measured to be 0.86%, 0.85%, and 4.48%, respectively, at the rated output. The maximum P_a of 1779 W was confirmed at S_r = 600 rpm and R_l = 203 Ω in the CSC test. The maximum value of J_a with I_p = 1.72 A was calculated to be 1.21 A/mm^2. Both THDs in V_p and I_p

were measured to be approximately 1% level in the overall test ranges and especially, under 1% above that obtained with S_r = 400 rpm. Through experimental verification on superior THDs in V_p and I_p outputs, it was concluded that the current ripple of pulsating field excitation, which arise from CSFE, does not adversely affect output characteristic of HTSRM. Such valuable results can give the experimental understanding for [37], which numerically approached this similar concern. Moreover, the CLC test was conducted with constant R_l and S_r, as shown in Fig. 5.13. When E_i and I_f of the HTSG were fully saturated by rotation with constant speed, the load test was conducted by putting the constant R_l and then changing the S_r.

The output characteristics at S_r = 200 rpm and R_l = 100 Ω, S_r = 400 rpm and R_l = 150 Ω, S_r = 600 rpm and R_l = 300 Ω, and S_r = 800 rpm and R_l = 350 Ω were measured and screened from DEWE-571 and HDO 4034A devices, as shown in Figs. 5.14–5.17, respectively.

Table 5.1. Performance test results of constant speed characteristic test

S_r [rpm]	R_l † [Ω]	V_p† [V_{rms}]	V_r† [%]	I_p† [A_{rms}]	P_a [W]	VTHD†/ITHD† [%]
200	404	116	9.77	0.32	102.0	1.07/1.60
200	303	114	11.46	0.41	131.0	1.15/1.43
200	200	114.8	10.16	0.60	201.0	1.09/1.24
200	150	112.4	12.62	0.78	259.7	1.11/1.21
200	100	112	14.18	1.22	404.8	1.02/1.04
300	396	174	5.75	0.46	231.3	0.93/1.19
300	303	175.2	4.69	0.60	307.5	0.93/1.02
300	202	173.9	7.23	0.89	460.6	0.91/0.97
300	152	170.7	7.17	1.18	597.8	0.90/0.91
300	99	167.8	9.62	1.83	916.7	0.87/0.88
400	405	232.4	3.44	0.59	404.1	0.90/0.94
400	303	232.8	2.70	0.79	542.3	0.88/0.89
400	203	230.3	4.99	1.17	801.8	0.88/0.88
400	150	229.3	4.48	1.58	1085.6	0.86/0.85
500	400	289.2	2.36	0.74	630.4	0.86/0.87
500	300	289	2.34	0.97	833.5	0.86/0.85
500	203	287.9	2.71	1.42	1225.5	0.85/0.85
600	406	348.2	1.22	0.87	898.3	0.86/0.91
600	302	347.4	1.55	1.15	1196.5	0.85/0.89
600	203	345.4	2.19	1.72	1778.9	0.84/0.85
700	391	398.4	1.03	1.00	1190.7	0.86/0.88
700	302	399.0	1.06	1.30	1554.3	0.85/0.86
800	395	443.8	0.66	1.12	1484.9	0.89/0.91
800	350	441.9	0.89	1.26	1661.3	0.87/0.88

†: The average value in the three-phase

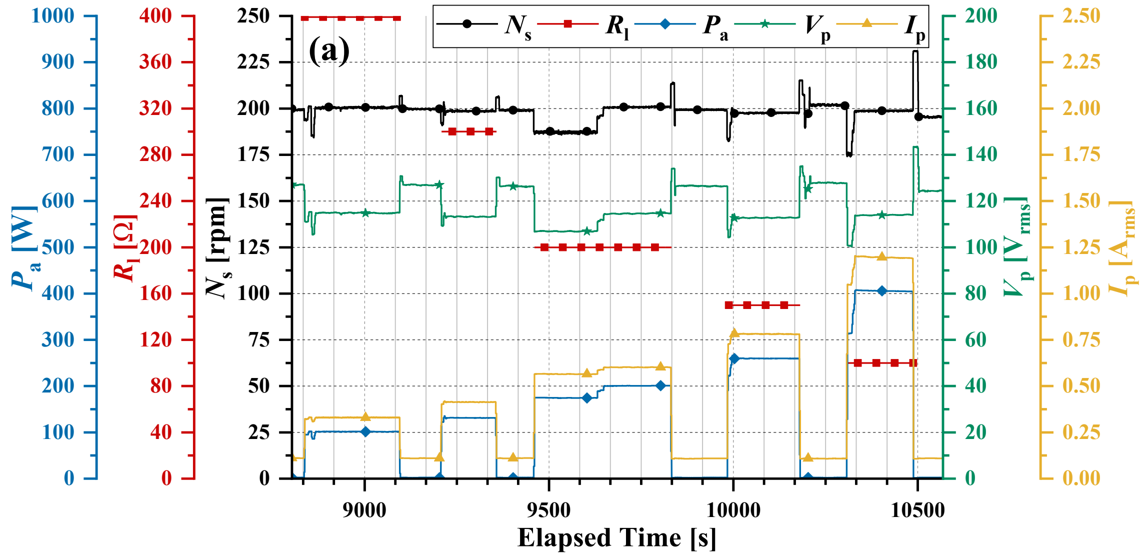
(a)
Ns
Rl
Pa
Vp
Ip
Pa [W]
0
100
200
300
400
500
600
700
800
900
1000
Rl [Ω]
0
40
80
120
160
200
240
280
320
360
400
Ns [rpm]
0
25
50
75
100
125
150
175
200
225
250
Vp [Vrms]
0
20
40
60
80
100
120
140
160
180
200
Ip [Arms]
0.00
0.25
0.50
0.75
1.00
1.25
1.50
1.75
2.00
2.25
2.50
9000
9500
10000
10500
Elapsed Time [s]

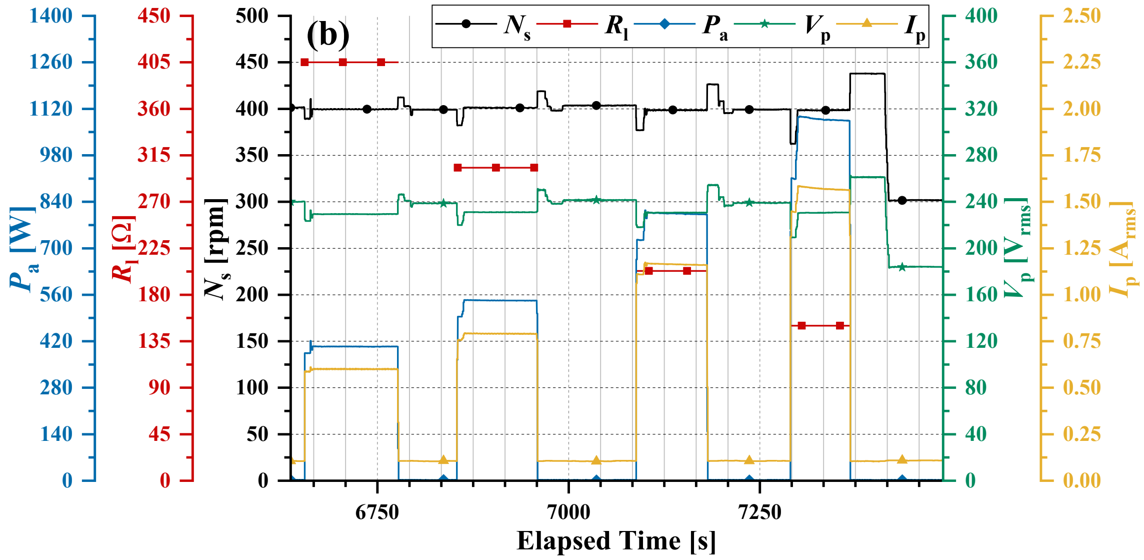
(b)
Ns
Rl
Pa
Vp
Ip
Pa [W]
0
140
280
420
560
700
840
980
1120
1260
1400
Rl [Ω]
0
45
90
135
180
225
270
315
360
405
450
Ns [rpm]
0
50
100
150
200
250
300
350
400
450
500
Vp [Vrms]
0
40
80
120
160
200
240
280
320
360
400
Ip [Arms]
0.00
0.25
0.50
0.75
1.00
1.25
1.50
1.75
2.00
2.25
2.50
6750
7000
7250
Elapsed Time [s]

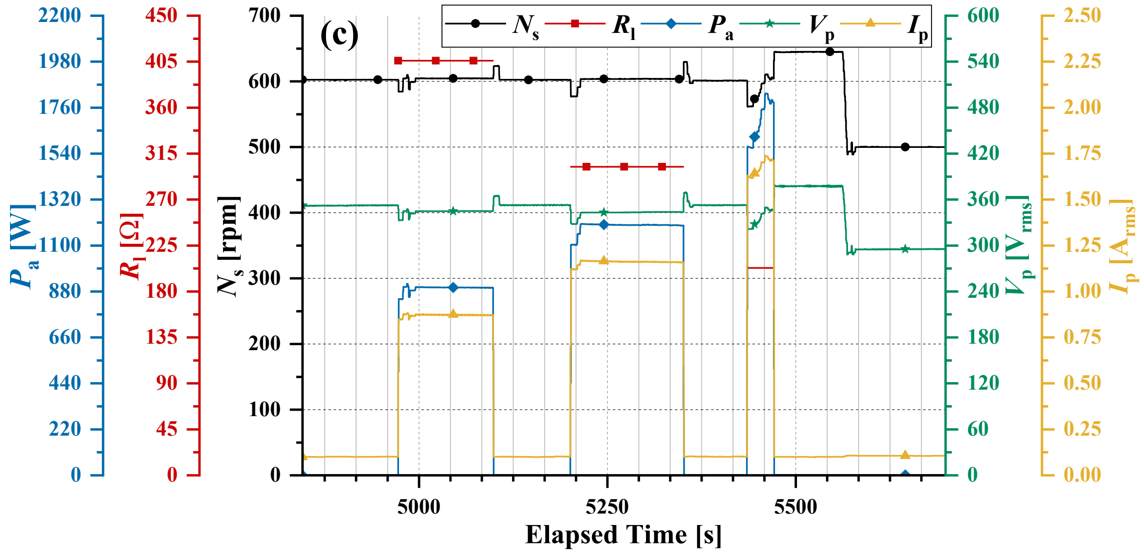
(c)
Ns
Rl
Pa
Vp
Ip
Pa [W]
0
220
440
660
880
1100
1320
1540
1760
1980
2200
Rl [Ω]
0
45
90
135
180
225
270
315
360
405
450
Ns [rpm]
0
100
200
300
400
500
600
700
Vp [Vrms]
0
60
120
180
240
300
360
420
480
540
600
Ip [Arms]
0.00
0.25
0.50
0.75
1.00
1.25
1.50
1.75
2.00
2.25
2.50
5000
5250
5500
Elapsed Time [s]

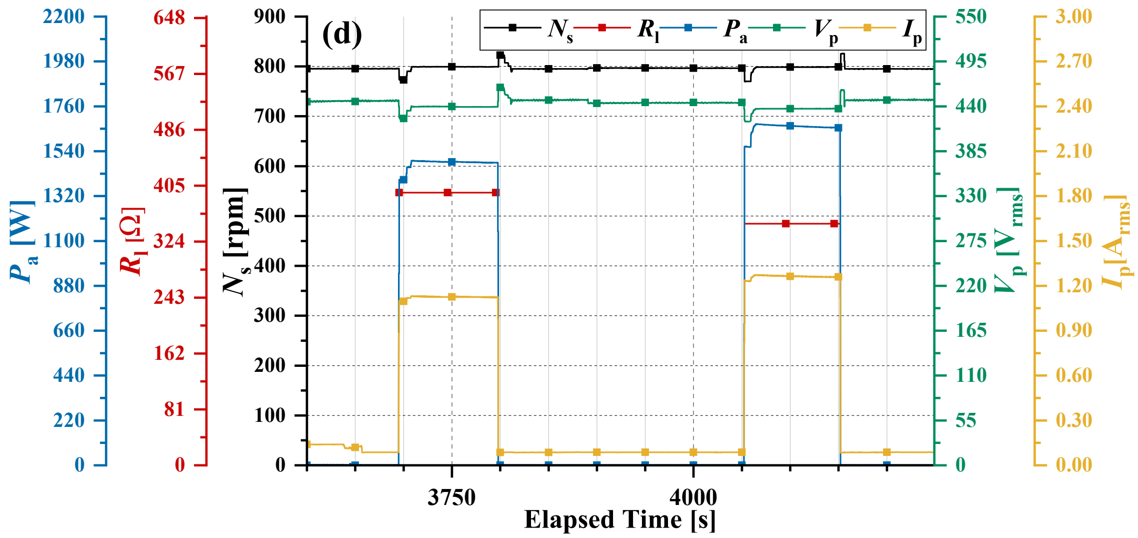

Fig. 5.12. Profiles of the output parameters of the 1 kW class HTSG at S_r = (a) 200, (b) 400, (c) 600, and (d) 800 rpm in the CSC test

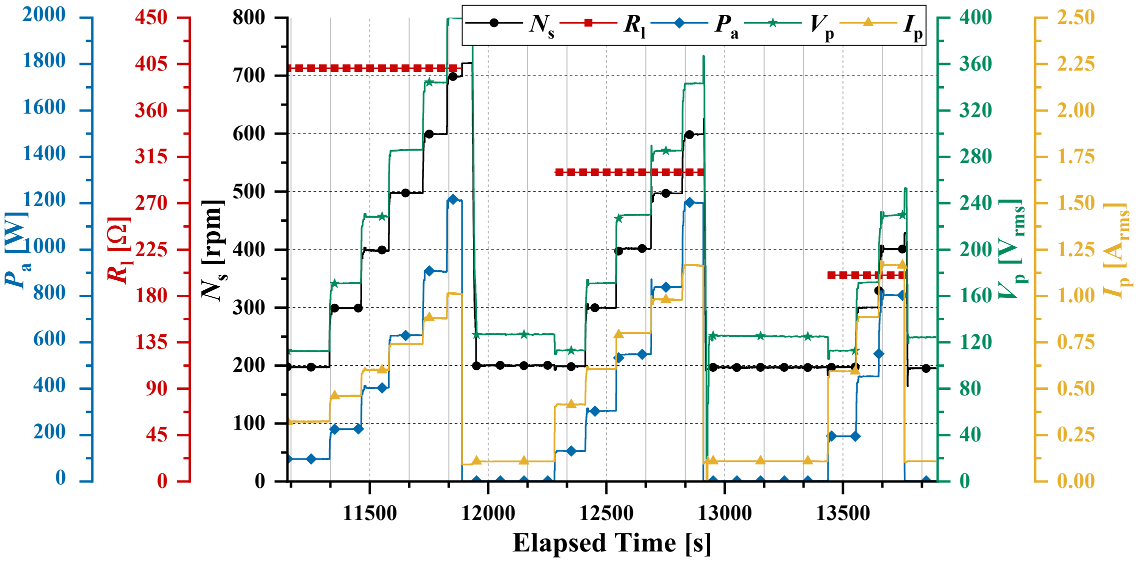

Fig. 5.13. Profiles of the output parameters of the 1 kW class HTSG at R_l = 400, 300, and 200 Ω in the CLC test

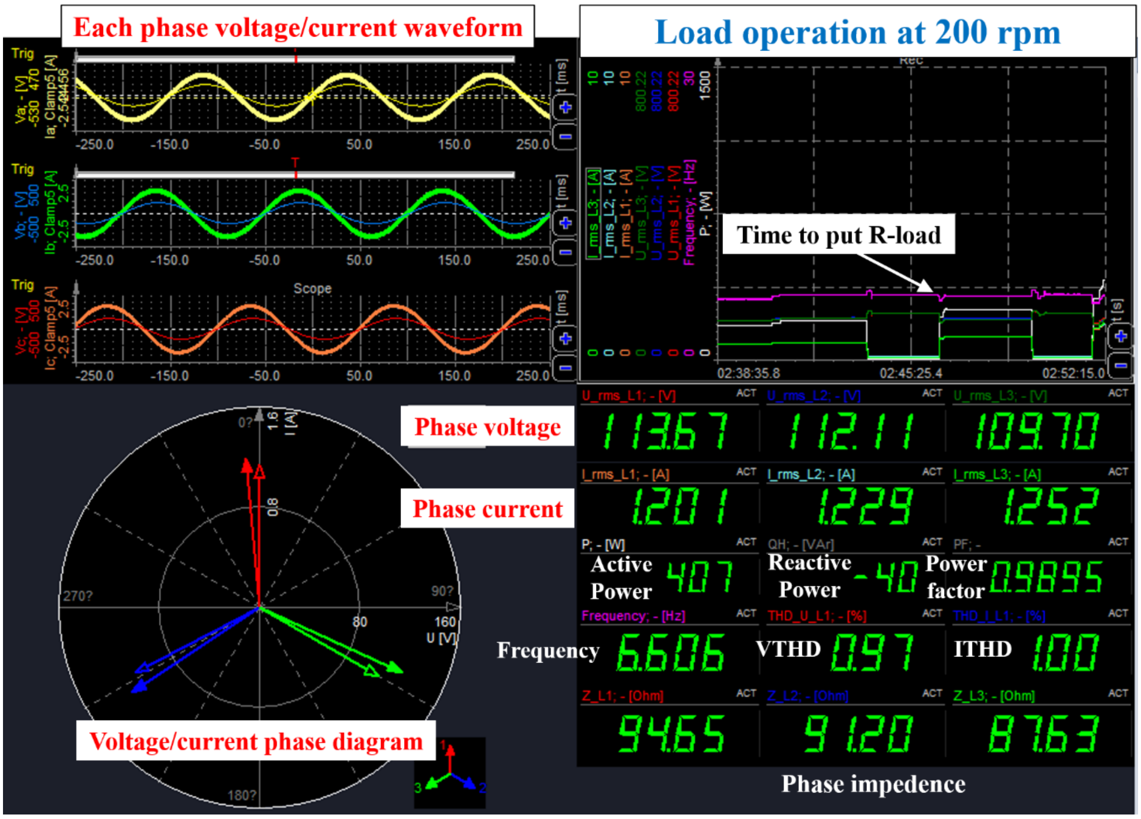

(a) Output characteristics in the power quality analyzer (DEWE-571)

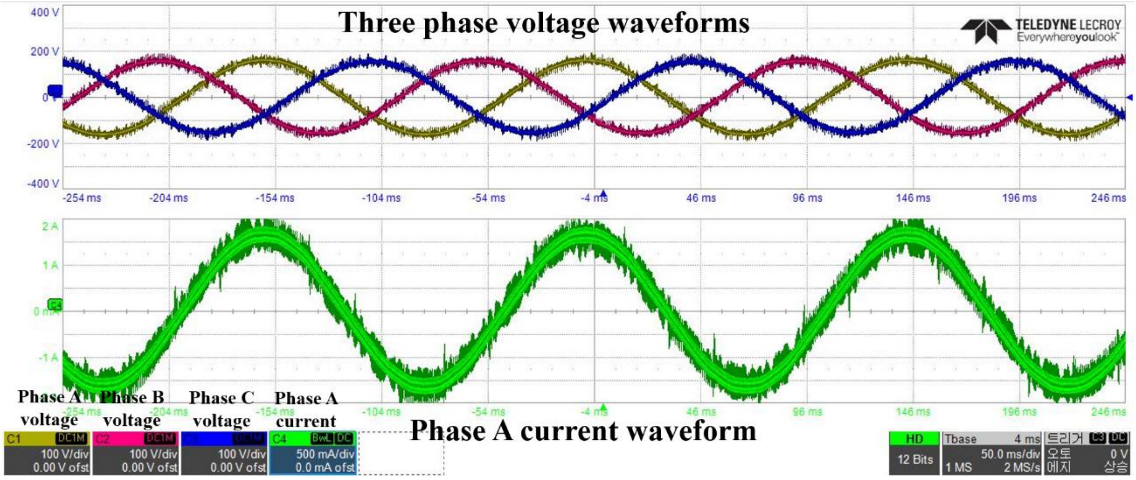

(b) V_p and I_p wave forms in the oscilloscope (HDO 4034A)

Fig. 5.14 Characteristic measurement screens in the loaded test of the 1 kW class HTSG (S_r = 200 rpm and R_l = 100 Ω)

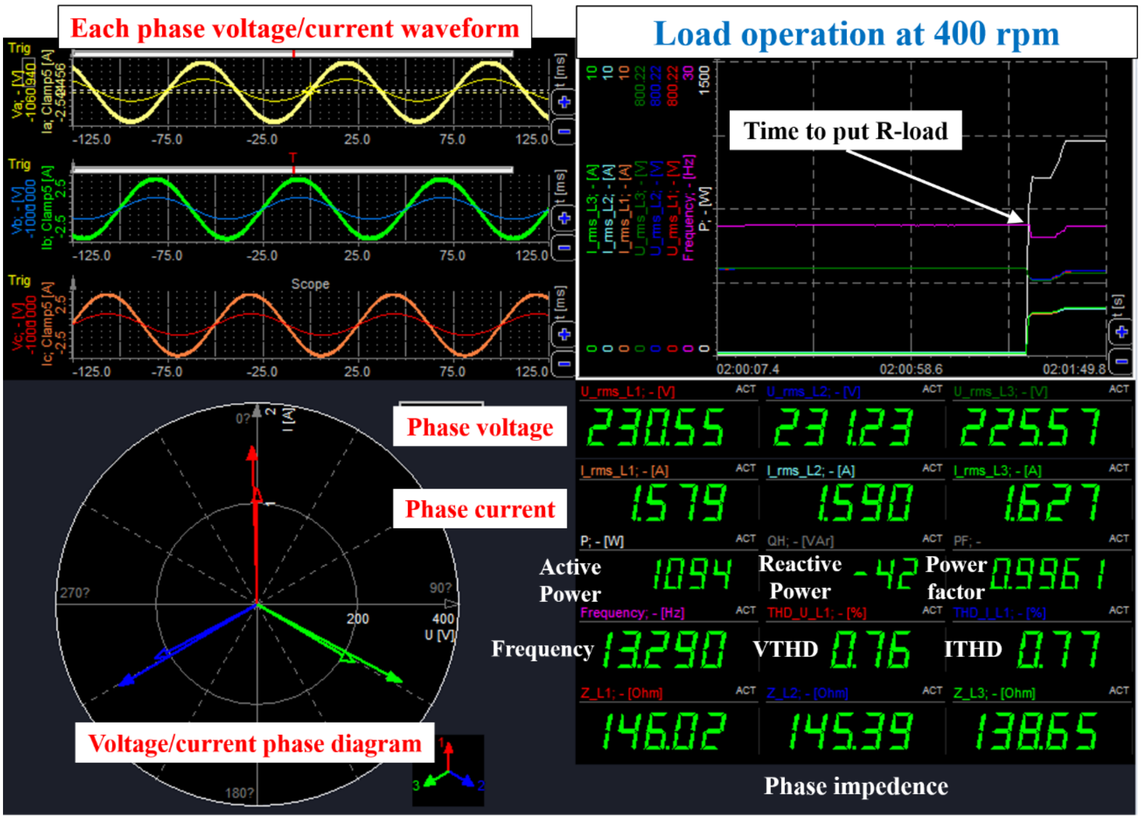

(a) Output characteristics in the power quality analyzer (DEWE-571)

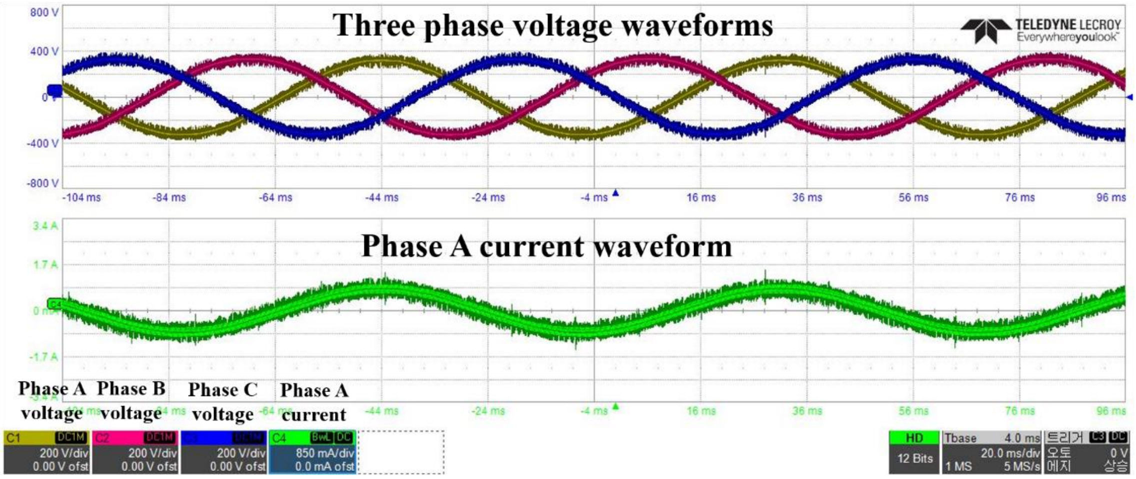

(b) V_p and I_p wave forms in the oscilloscope (HDO 4034A)

Fig. 5.15. Characteristic measurement screens in the loaded test of the 1 kW class HTSG (S_r = 400 rpm and R_l = 150 Ω)

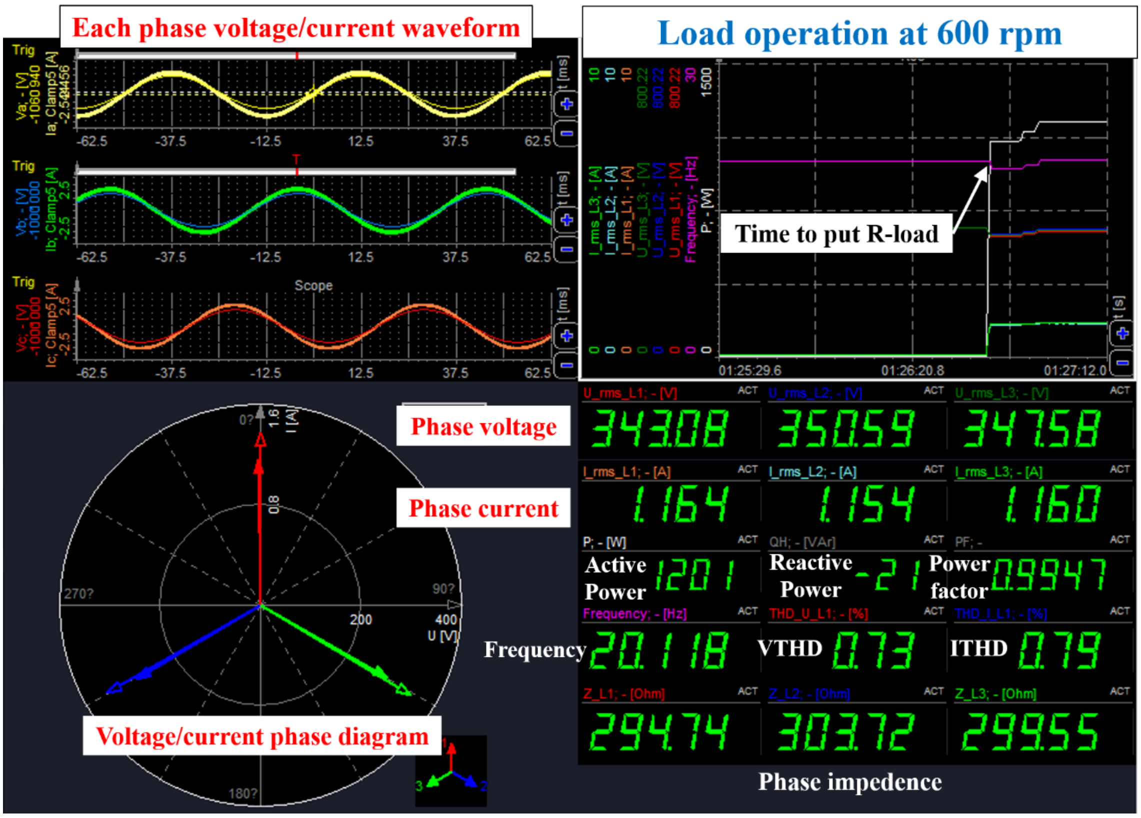

(a) Output characteristics in the power quality analyzer (DEWE-571)

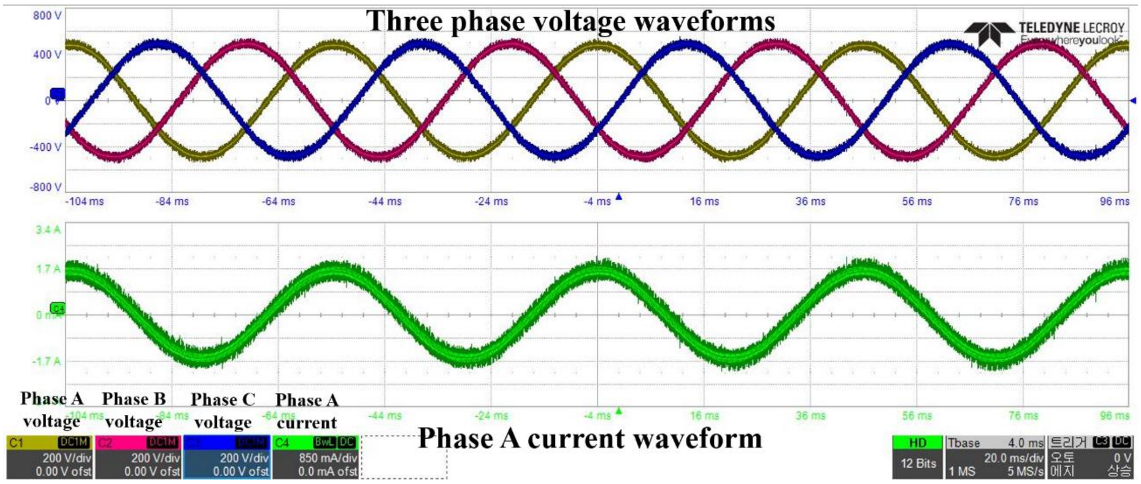

(b) V_p and I_p wave forms in the oscilloscope (HDO 4034A)

Fig. 5.16. Characteristic measurement screens in the loaded test of the 1 kW class HTSG (S_r = 600 rpm and R_l = 300 Ω)

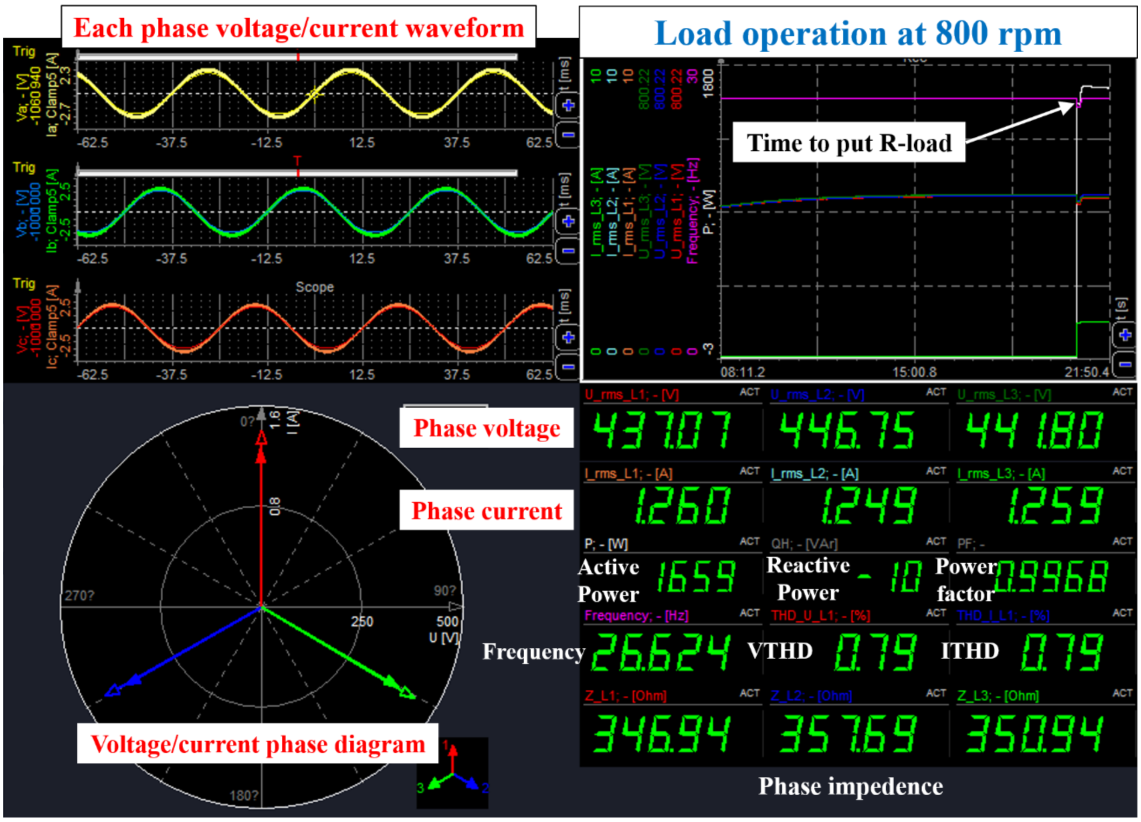

(a) Output characteristics in the power quality analyzer (DEWE-571)

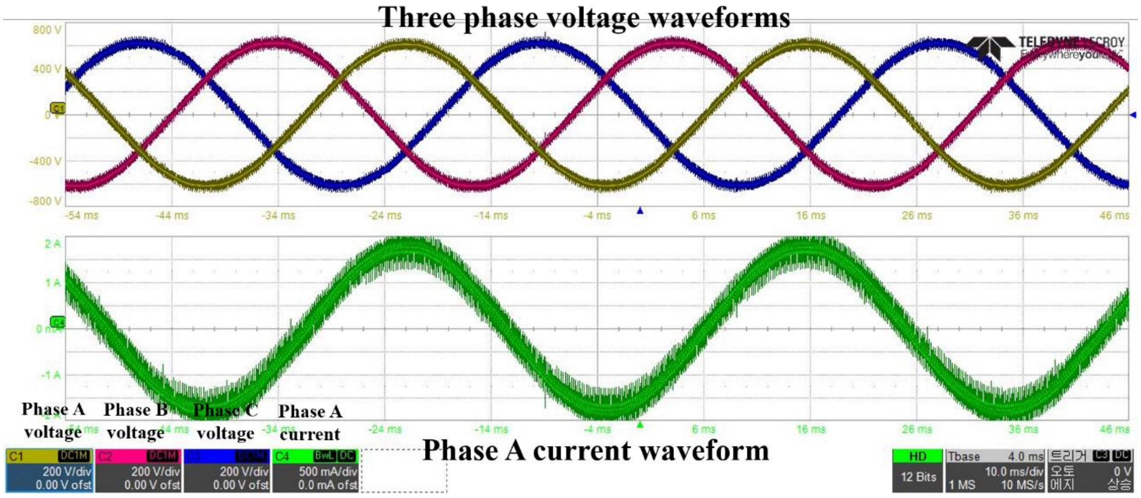

(b) V_p and I_p wave forms in the oscilloscope (HDO 4034A)

Fig. 5.17. Characteristic measurement screens in the loaded test of the 1 kW class HTSG (S_r = 800 rpm and R_l = 350 Ω)

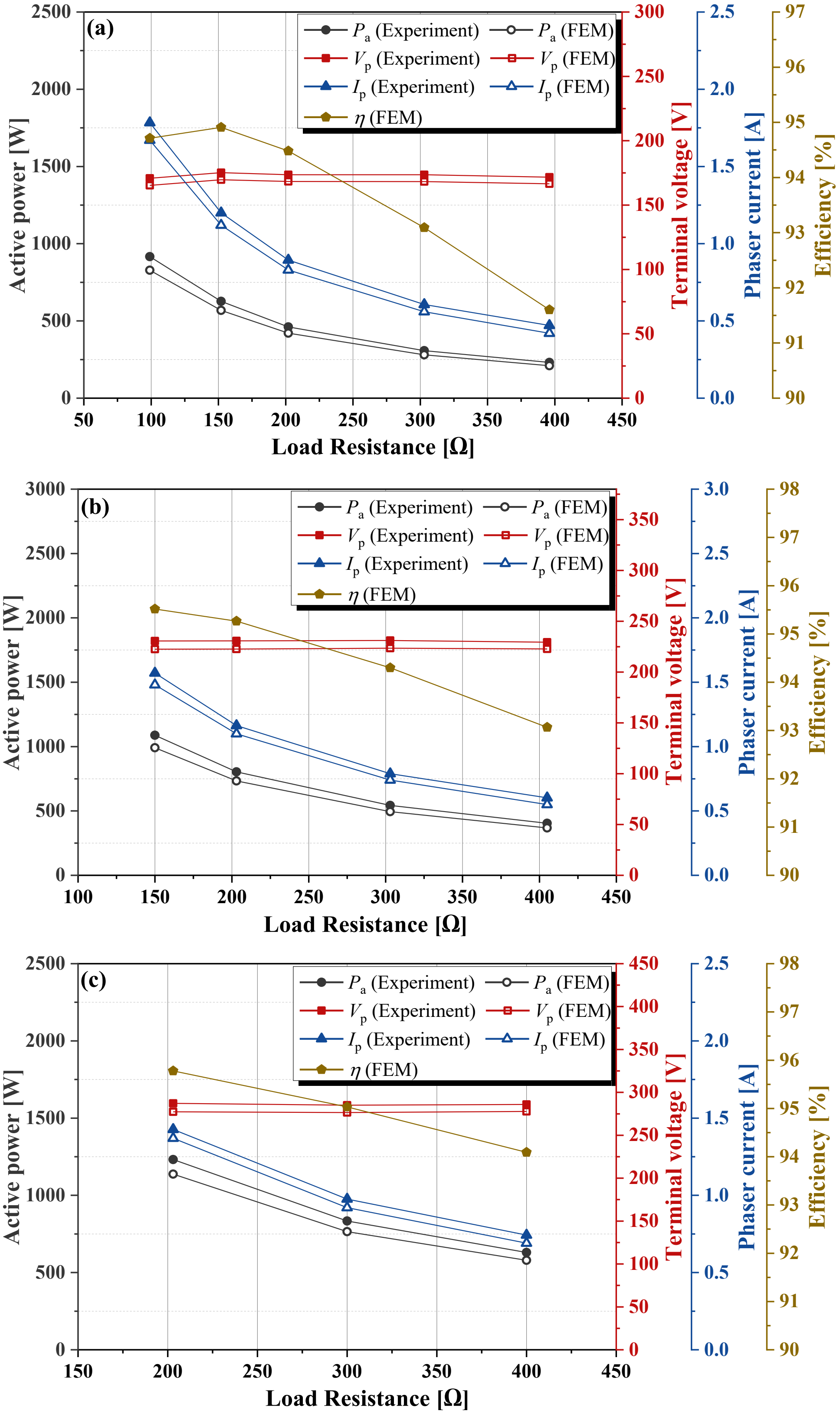

Fig. 5.18. Characteristic comparison between experiment and analysis in V_t, I_p, and P_a with different values of S_r of (a) 300, (b) 400, and (c) 500 rpm in the CSC test

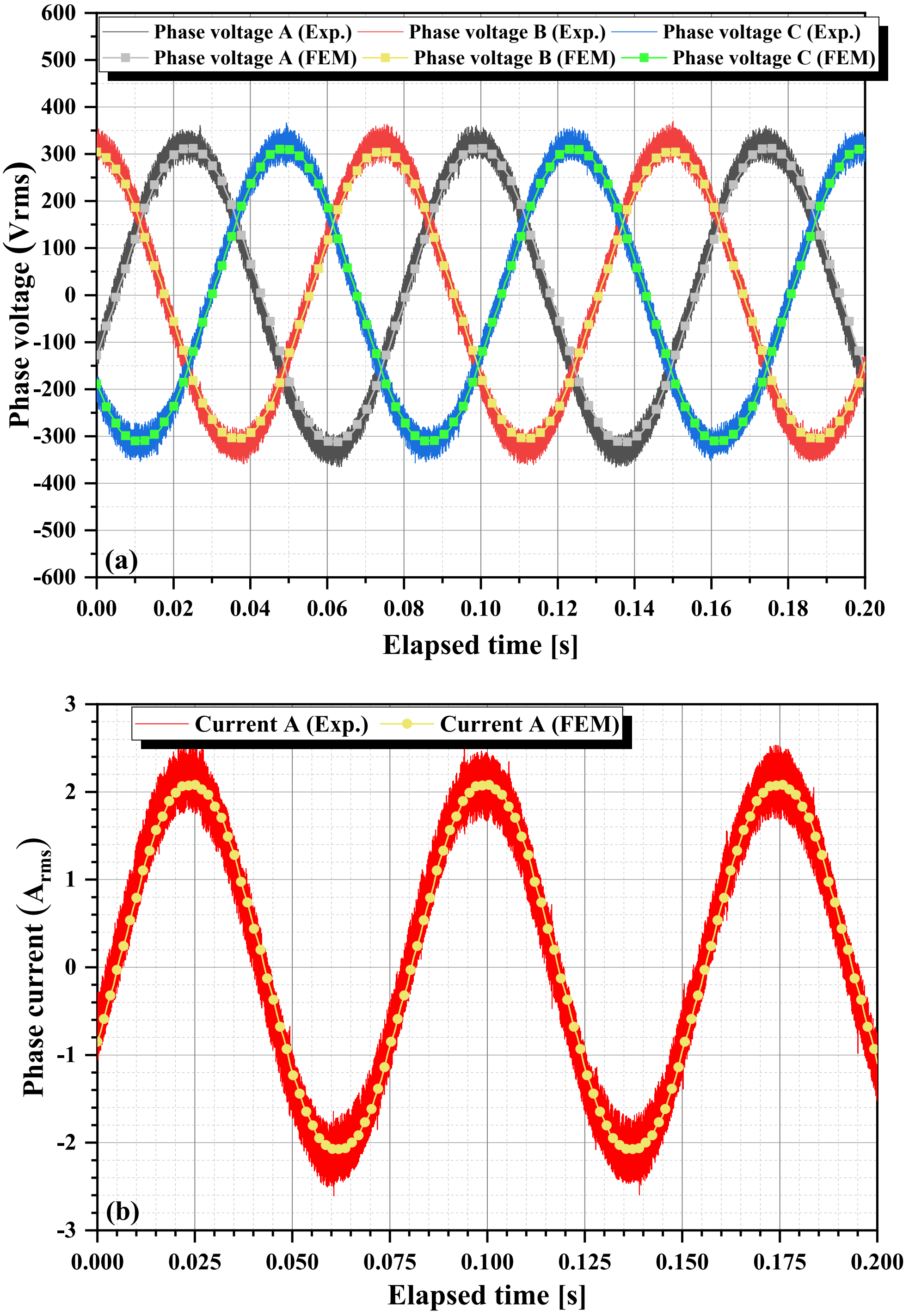

Fig. 5.19. Waveform comparisons in (a) V_p and (b) I_p with S_r = 400 rpm and R_l = 150 Ω

Finally, with equal S_r, phase R_l, and I_f used in each experiment, the simulation results in 2D FEA were compared with the experimental results, as summarized in Table 5.1. Fig. 5.18 shows the characteristic comparison between experiment and analysis in V_p, I_p, and P_r at different values of S_r (300, 400, and 500 rpm). Moreover, Fig. 5.19 shows waveform comparisons in V_p and I_p at S_r = 400 rpm and R_l = 150 Ω. In general, simulation results in P_a are 10% smaller than that in the experiments. It is believed that such differences are caused by difference in material property of the rotor core, i.e., the *B*-*H* curve of S45C, between R&D process and practical development, as well as decrease in magnetization characteristic of S45C at LN2, i.e., 77 K. Moreover, based on the copper and iron losses in the stator core calculated by 2D FEA, the values of η of 1 kW class HTSG were estimated in each operating condition. At rated operating conditions, i.e., S_r = 400 rpm, I_f = 101 A, and the values of R_l in each phase (R_{la}:150 Ω, R_{lb}:148 Ω, R_{lc}:143 Ω), the η of 1 kW class HTSG was calculated to be 95.41% with copper loss of 22.1 W in armature, the iron loss of 24.4 W in the stator, and the excitation loss of 1.11 W in CSFE, as shown in Fig. 5.18(b).

5.4. Results and discussion

In this subsection, the 1 kW class HTSG, which is charged and operated by a contactless excitation system, i.e., CSFE, was successfully fabricated and tested in the M-G test setup. The core components of HTSG were designed and fabricated, and the basic performances were tested before the full assembly of the HTSG system. Finally, the M-G test setup was constructed to investigate the operating characteristics of the 1 kW class HTSG, and the application feasibility of CSFE was verified through various performance tests.

The results indicated that the noncontact current charging performance of HTS FCs was confirmed at a charging speed of 53.3 Hz in the CSFE, (S_r = 200 rpm of the HTSG), and I_f was finally saturated at 101 A and its operating current margin in I_f was approximately 78.9% (101 A/128 A). The excitation loss of 100 A class CSFE was estimated to be 1.11 W, and this value is approximately 91.5% smaller than that of the two pairs of Cu current leads. If it considers the internal loss of external DC PS, the reduction effect in the excitation loss is expected to be even greater. In a non-loaded test above S_r = 200 rpm, the charging behavior of I_f was indirectly investigated through the analysis of the E_i behavior of HTSG. Up to 600 rpm, I_f seemed to maintain a constant level of 101 A or showed a slight increase with an increase in S_r. However, on and above 600 rpm, I_f seems to decrease slightly below 101 A with an increase in S_r. Moreover, the values of I_f were estimated based on the test results of E_i using 2D FEA. The values of I_f at 700, 800, and 900 rpm were estimated to be 96, 88, and 76 A, respectively.

In the resistive loaded test, the rated output of HTSG, i.e., 1086 W, was successfully confirmed at I_p = 1.58 A, S_r = 400 rpm, and R_l = 150 Ω in the CSC test. Moreover, the maximum output was measured to be 1779 W with I_p = 1.72 A, S_r = 600 rpm, and R_l = 203 Ω in the CSC tests. Moreover, the simulation results in 2D FEA were compared with the experimental results, and the simulation results in P_a were 10% smaller than that in experiments. The rated η of 1 kW class HTSG was estimated to be 95.41% by 2D FEA. By employing a contactless field exciter, the system efficiency of the HTSG improved by approximately 1.08% as compared to 94.33% efficiency, wherein the value was estimated based on calculation of excitation loss (13 W) of copper current leads in contact field exciter. Table 5.2 summarizes the major parameters of the final developed and tested 1 kW class HTSG and HTS field exciter.

Table. 5.2. Major parameters of the 1 kW class HTSG equipped with a 100 A class CSFE

Parameters	Unit	Value
HTS Synchronous Generator		
Machine type	-	Rotary HTS field / stationary Cu armature
Rated power	W	1086
Rated rotating speed	rpm	400
Number of field pole	-	4
Number of stator slots	-	48
Rated armature current	A_{rms}	1.58
Rated armature current density	A_{rms}/mm^2	1.11
Rated line voltage	V_{rms}	397
Voltage regulation	%	4.48
Voltage/current THD	%	0.86/0.85
Efficiency	%	95.41 (based on 2D-FEA)
HTS Field Winding		
Field pole type	-	Salient pole with S45C
Field-coil type	-	Racetrack HTS SPC
Used 2G HTS conductor	-	SCS 12050 (SuperPower)
Conductor width / thickness	mm	12/0.064
Insulation materials	-	Kapton Polyimide film
Winding turns per SPC	-	60
Total conductor length	m	120
Total coil inductance	mH	32.9
Operating temperature	K	77
Rated operating field current	A	101
Critical current / n-value	A/ -	Four FCs: 128/26
HTS Field Exciter		
Excitation source/method	-	DC voltage source / noncontact method
Exciter type	-	Rotary HTS flux pump
Exciter assignment	-	Single CSFE to four-FCs
Connection to F.C.	-	Series
Used 2G HTS conductor / PM types	-	SCN12550 (SuNAM) /NdFeB N50
Capacity	A	100
Operating temperature	K	77
Ramp rate at 200 rpm S_r	A/s	0.114
Excitation loss at 70.4 A / 101 A	W	0.54/1.11
Operating current margin (I_f/ I_c)	-	0.789

Chapter 6. Conclusion

6.1. Conclusion

In this dissertation, the feasibility of a novel HTSRM is demonstrated, which is excited and operated by a contactless field excitation system, i.e., rotating magnet-based HTS flux pump. The 1 kW class prototype HTSG and 100 A class CSFE were developed through draft design, analysis, detailed design, and basic characteristic test processes. Finally, both the full-scale prototypes were integrated in the M-G test bed and HTSRM feasibility was successfully verified by the operating characteristic tests in generator operation mode. This dissertation is concluded by summarizing the main results of each chapter as follows:

In Chapter 1, the background of contact-type excitation systems for 2G HTS magnet in stationary and rotary applications were discussed that motivated this dissertation. Further, the concept of CSFE was introduced to overcome the technical limitations in conventional contact-type field excitation systems. Moreover, the main objective and scope of the study were introduced to compose of this dissertation.

In Chapter 2, the operational mechanism and characteristics of rotary-type 2G HTS flux pump were introduced based on relevant studies to understand its mechanism, design parameters, control parameters, and other details. Further, some of the developments, which combined HTSRM and HTS flux pump, were overviewed and referred to devise a suitable design of CSFE for the HTSRM. The novel structure of HTSRM operated by CSFE was proposed considering the design purposes and technical countermeasures for novel CSFE. In Chapter 3, the overall structure of the 1 kW class HTSRM was designed based on analytical and numerical approaches. The core structures of HTS rotor, such as torque tube, rotating shaft, and rotor cryostat, were conceptually designed considering the mechanical and thermal characteristics of the HTS rotor. The structural shape of salient field-pole was designed and optimized by parametric 2D FEA to minimize the electromagnetic effect on the critical current performance of HTS field winding and satisfy the required specification of CSFE. Further, the final structure of the full system was modeled by 3D CAD based on 2D FEA results to develop a practical HTSRM prototype. The effective structure of the CSFE was empirically designed for maximizing the field current charged by CSFE. The output characteristics of the prototype machine were analyzed and estimated in generator operation. The various operating conditions were investigated to be referred in practical implementation and characteristic test of the prototype HTSRM.

In Chapter 4, the rotor assembly, which was composed of salient field-pole and rotary part of CSFE, was successfully fabricated for a 1 kW class HTSRM. To maximize the charged current, effective design factors, such as multiple and serial winding on 2G HTS wire, toroidal shape structure, and use of iron material, were considered and devised in design and fabrication of full-scale CSFE. An experimental setup was built by a fabricated rotor assembly to evaluate the current-charging performance of the HTS field winding with a contactless excitation technique. A current of maximum 76.4 A in the HTS field winding was successfully charged by 70 A class CSFE. Moreover, the control characteristics in contactless charged current were investigated according to control parameters, such as number of PMs, rotating speed, and air-gap length. The various test results provide the quantitative understandings to control the field current of the full-scale HTS field winding for the 1 kW class HTSRM. Moreover, a self-protecting characteristic of the HTS FC was observed, which maintain or reduce I_s by itself in a poor cooling state, i.e., at low level of LN2. This unique behavior of CSFE is expected to be a technically attractive feature in stable operation of 2G HTS magnets.

In Chapter 5, the 1 kW class HTSG with 100 A class CSFE was successfully fabricated and tested in the M-G test setup. The key components of HTSG were designed and fabricated, and their basic performances were tested before the full assembly of the HTSG system. Finally, the M-G test setup was constructed to investigate and verify the operating characteristics of the 1 kW class HTSG and the application feasibility of CSFE. The noncontact current charging performance of HTS field winding was confirmed at a charging speed of 53.3 Hz in the CSFE, i.e., S_r of 200 rpm of the HTSG, and I_f was finally saturated at 101 A. The operating current margin in the I_f is estimated to be 78.9%, which is relatively a higher value than that of other developments wherein the current margin is typically set at 70% or less to ensure the stability of the HTS coil in thermally, magnetically, and mechanically transient state. The excitation loss of 100 A class CSFE was estimated to be 1.11 W, which is approximately 91.5% smaller than that of the two pairs of Cu current leads. Finally, the rated output of HTSG, i.e., 1086 W, was successfully confirmed at I_p of 1.58 A, S_r of 400 rpm, and R_l of 150 Ω in the load test. Moreover, the maximum output was measured to be 1779 W with I_p of 1.72 A, S_r of 600 rpm, and R_l of 203 Ω in the load test. Through test results on THDs in V_p and I_p outputs (both at 1% levels), it is experimentally observed and validified that the current ripple of pulsating field excitation, which arise from CSFE, does not adversely affect the output characteristic of HTSRM. The rated η of 1 kW class HTSG was estimated to be 95.41% by 2D FEA. This value is approximately 1.08% higher than that of application case with contact-type field excitation system.

Furthermore, the valuable potential contributions with technical findings in this dissertation are as follows.

From qualitative advantage perspective, which is not verified and discussed in detail in this dissertation, the thermal stability may be excellent because of the removal of resistive current leads. Moreover, when disturbance is applied in the transient state, HTS coil charged by HTS flux pump may serve as self-protecting magnet because the amount of charging current reduces itself when the critical current in the superconducting loop decreases because of local or full quench.

From application perspective of rotating machine in industries, the field current control is passive in the exciter structure proposed in this dissertation; however, it is recommended to apply for industrial field requiring constant speed in rated operation because it operates like a PM generator or motor within a certain speed range. Furthermore, it can be used in HTS motors for electric traction and propulsion, which require field weakening control during high-speed operations because of its automatically demagnetizing effect caused by the decrease in I_f at high speed levels.

From R&D perspective, it is believed that this development is technically meaningful to relevant researchers because it's the world's first demonstration that is applicable for "rotating magnet based HTS flux pump" to the HTS rotating machine. Thus, this dissertation provides useful references or guidelines for design, fabrication, and test of this type of HTS rotating machine as well as various non-rotary 2G HTS magnet applications.

From an industrial perspective, it is expected that the contactless excitation and operation of the HTSRM may offer an opportunity to improve the efficiency, stability, and economic value of general superconducting rotating machinery systems as well as stationary superconducting magnet systems. In particular, it is very attractive to apply for offshore wind power generation, which emphasizes maintainability, and electric ship propulsion that requires silence.

6.2. Further study

It is believed that the practical results presented in this dissertation can contribute to relevant research works. However, the technical limitations in terms of current-controllability as well as design process are still remained. In order to accurately predict the chargeable current range and magnitude, it is necessary to establish cooperative design process between the HTSRM and flux pump designs. The following technical problems in current-controllability should be overcome to respond to the startup and load change in transient operation of an HTS generator or motor, and for its application in various industry fields:

1. In initial charging mode for both generator and motor, it is impossible to excite HTS field winding by itself without magnetic field injection by physical rotation. Thus, initial driving is necessary to excite field winding using any prime mover; thus, this leads to drawbacks in terms of size, fabrication, efficiency, and economics of facilities.
2. In drive mode with wide variable speed range for both generator and motor, it is difficult to control a constant field current because of the current changes according to rotating

speed changes when HTSRM drives in acceleration and deceleration of the rotating speed, thereby resulting in application limitation inside rotating machinery with constant speed operation.

3. In applications, such as electric ships or vehicle propulsions, where forward and reverse operations of the propulsion motor are required, it is impossible to maintain a constant field current because the current is slowly discharged by reversed voltage sources in CSFE caused by the reversal of the rotation direction.
4. In applications that require a field current control, such as a synchronous condenser, it is difficult to individually control the field current because of the integrated rotor structure of the HTSG and CSFE.

The above-mentioned technical issues are caused by non-independency in controllability of the rotating speed between HTSG and CSFE. Some practical alternatives to overcome such issues, which are not be considered in this dissertation, are presented below; the key points are independent generation and active control in time-varying magnetic field of CSFE:

1. Individual and physical rotation of PMs using a separate prime mover: The frequency of PMs of CSFE, which generate a time-varying magnetic field, are independently rotated and controlled by another motor drive to control the field current using the relative difference between the rotating speeds of HTSRM and PMs of CSFE.
2. Active generation and control of time-varying magnetic field using electromagnets: A rotating time-varying magnetic field is generated using electromagnets instead of PM without any physical rotation unlike solution 1. The field current is effectively charged and controlled by various sequences in the electromagnets, which govern the injected frequency, strength, and direction of the time-varying magnetic field.

The above-mentioned technical solutions can actively and sensitively control the charging speed, magnitude, compensation, and direction of the field current. Through a subsequent development, we can design a scaled-up HTSG system equipped with electromagnet-type CSFE to actively control the excitation in the HTS field winding.

DECLARATION

I herewith declare that this thesis was composed by myself under the supervision of Professor Ho Min Kim at Electrical Engineering Department, College of Engineering, Jeju National University from March 2014 to December 2019 without the prohibited assistance of third parties and without making use of aids other than those specified, and that this work has not been submitted for any other degree of professional qualification except as specified. Significant parts of the work outlined in this dissertation have been published and presented with participations as first- and co-author:

- Chapter 1 is partially based on following research papers entitled:
    - "Thermal design of a cryogenics cooling system for a 10 MW-class high-temperature superconducting rotating machine," *IEEE Trans. Appl. Supercond.*, vol. 25, no. 3, Jun. 2015, Art. no. 3800305.
    - "Design of indirect closed-cycle cooling scheme coupled with a cryocooler for a 3-MW-class high-temperature superconducting synchronous motor," *IEEE Trans. Appl. Supercond.*, vol. 26, no. 4, Jun. 2016, Art. no. 5204904.
    - "A compactly integrated cooling system of a combination dual 1.5-MW HTS motors for electric propulsion," *Progr. Supercond. Cryogenics*, vol. 18, no. 4, pp. 25–29, 2016.
    - "Conceptual design of cooling anchor for current lead on HTS FCs," *Progr. Supercond. Cryogenics*, vol. 19, no. 2, pp. 38–43, 2017.

- Chapter 2 is original contents in this dissertation based on relevant research papers.

- Chapter 3 is mainly based on following research papers and conference presentations entitled:
    - "Conceptual design and analysis of rotor for a 1 kW class HTS rotating machine," *Progr. Supercond. Cryogenics*, vol. 19, no. 4, pp. 45-50, 2017.
    - "Characteristic analysis of a 1 kW class HTS motor considering armature current information," *IEEE Trans. Appl. Supercond.*, vol. 28, no. 4, Jun. 2018, Art. no. 5207205.
    - "Design, analysis, and fabrication of salient field-pole for a 1 kW class HTS rotating machine," *Cryogenics*, vol. 97, pp. 126-132, 2019.
    - "3D electromagnetic design and analysis of a 1-HP-class HTS rotating machine integrated with a contactless excitation device," presented at 25th *Int. Conf. Magnet Technol.*, Amsterdam, Netherlands, 2017.
    - "Characteristic Analysis of a 1 kW class HTS Motor considering Armature Current

Information," presented at *Eur. Conf. Appl. Supercond.*, Geneva, Switzerland, 2017.

- "Electromagnetic effect analysis of salient-pole rotor on performance of HTS rotating machine," presented at *Int. Conf. Supercond. and Magnetism*, Antalya, Turkey, 2018.

■ Chapter 4 is mainly based on following research paper and conference presentations entitled:

- "Design, analysis, and fabrication of salient field-pole for a 1 kW class HTS rotating machine," *Cryogenics*, vol. 97, pp. 126-132, 2019.
- "Fabrication and charging test of HTS field windings using HTS contactless rotary excitation," *IEEE Trans. Appl. Supercond.*, vol. 29, no. 5, Aug. 2019, Art. no. 5203207.
- "Electromagnetic effect analysis of salient-pole rotor on performance of HTS rotating machine," presented at *Int. Conf. Supercond. and Magnetism*, Antalya, TURKEY, 2018.
- "Fabrication and preliminary tests of an 1 kW class HTS rotating machine with HTS contactless rotary excitation device," presented at *Appl. Supercond. Conf.*, Seattle, WA, USA, 2018.

■ Chapter 5 is mainly based on following conference presentations entitled:

- "Design and performance test of an 1 kW class HTS generator with contactless rotary excitation device," presented at 26th *Int. Conf. Magnet Technol.*, Vancouver, Canada, 2019.
- "Direct bath cooling structure and liquid nitrogen feeding device for an 1 kW class HTS generator with HTS contactless PS," presented at *CEC/ICMC* 2019, Hartford, CT, USA, 2019.

Ji Hyung Kim

December 2019

REFERENCES

[1] Y. H, Choi, "A study on high performance HTS magnet with enhanced thermal stability and self-protecting feature for development of megawatt-class superconducting wind turbine generator," PhD thesis in Korea University, 2017.

[2] Y. Iwasa, *Case studies in superconducting magnets: design and operational issues*, 2nd ed. New York, NY, USA: Springer-Verlag, 2009.

[3] H. W, Kim, "Utilization of metal-insulator transition material to improve stability and magnetic field efficiency of 2G HTS coils," PhD thesis in Ulsan University, 2016.

[4] Y. J, Hwang, "Design and fabrication of the high-T_c superconducting FC for homopolar synchronous generator with dual rotors," PhD thesis in Yonsei University, 2013.

[5] Y. Park *et al.*, "A superconducting joint for $GdBa_2Cu_3O_{7-\delta}$-coated conductors," *NPG Asia Materials*, 6. e98, 2014.

[6] G. D. Brittles *et al.*, "Persistent current joints between technological superconductors," *Supercond. Sci. Technol.*, vol. 28, no. 9, Aug. 2015, Art. no. 093001.

[7] K. Radcliff, "Mechanical properties of superpower and SuNAM REBCO coated conductors," M.S thesis in Florida State University, 2018.

[8] S. Yoon *et al.*, "26T 35mm all-$GdBa_2Cu_3O_{7-x}$ multi-width no-insulation superconducting magnet," *Supercond. Sci. Technol.*, vol. 29, no. 4, Mar. 2016, Art. no. 04LT04.

[9] S. HAHN *et al.*, "Current status of and challenges for no-insulation HTS winding technique," *TEION KOGAKU* (*J. Cry. Super. Soc. Jpn.*), vol. 53, no.1, pp. 2–9, 2018.

[10] S. Hahn *et al.*, "45.5-tesla direct-current magnetic field generated with a high-temperature superconducting magnet," *Nature*, vol. 570, pp. 496–499, Jun. 2019.

[11] S. Hahn *et al.*, "No-insulation multi-width winding technique for high temperature superconducting magnet," *Appl. Phys. Lett.*, vol. 103, Oct. 2013. Art. no. 173511.

[12] J. Y. Jang *et al.*, "Design, construction and 13 K conduction-cooled operation of a 3 T 100 mm stainless steel cladding all-REBCO magnet," *Supercond. Sci. Technol.*, vol. 30, no. 10, Sept. 2017. Art. no. 105012.

[13] J. B. Song *et al.*, "Over-current quench test and self-protecting behavior of a 7 T/78 mm multi-width no-insulation REBCO magnet at 4.2 K," *Supercond. Sci. Technol.*, vol. 28, no. 11, Sept. 2015. Art. no. 114001.

[14] T. D. Le *et al.*, "Thermal design of a cryogenics cooling system for a 10 MW-class high-temperature superconducting rotating machine," *IEEE Trans. Appl. Supercond.*, vol. 25, no. 3, Jun. 2015, Art. no. 3800305.

[15] T. D. Le *et al.*, "Design of indirect closed-cycle cooling scheme coupled with a cryocooler for a 3-MW-class high-temperature superconducting synchronous motor," *IEEE Trans. Appl. Supercond.*, vol. 26, no. 4, Jun. 2016, Art. no. 5204904.

[16] T. D. Le *et al.*, "A compactly integrated cooling system of a combination dual 1.5-MW HTS motors for electric propulsion," *Progr. Supercond. Cryogenics*, vol. 18, no. 4, pp. 25–29, 2016.

[17] M. P. Oomen *et al.*, "Transposed-cable coil & saddle coils of HTS for rotating machines: Test results at 30 K," *IEEE Trans. Appl. Supercond.*, vol. 19, no. 3, pp. 1633–1638, Jun. 2009.

[18] C. J. Hyeon *et al.*, "Conceptual design of cooling anchor for current lead on HTS FCs," *Progr. Supercond. Cryogenics*, vol. 19, no. 2, pp. 38–43, 2017.

[19] H. M. Kim, "Study on the characteristics of a discrete foil-type superconducting PS with the magnetic triggered switch," PhD thesis in Yonsei University, 2002.

[20] Y. S. Yoon, "A study on the characteristics of a high-T_c superconducting PS for the stabilization of superconducting magnets," PhD thesis in Yonsei University, 2001.

[21] T. K. Ko, "Study of the performance of a novel superconducting flux pump," PhD thesis in Case Western Reserve University, 1986.

[22] J. Geng, "Flux pumping for high-T_c superconducting (HTS) magnets," PhD thesis in Cambridge University, 2017.

[23] C. Hoffmann *et al.*, "Flux pump for HTS magnets," *IEEE Trans. Appl. Supercond.*, vol. 21, no. 3, pp. 1628–1631, Jun. 2011.

[24] C. Hoffmann *et al.*, "Design parameters for an HTS flux pump," *Phys. Proc.*, vol. 36, pp. 1324–1329, 2012.

[25] M. Sander, "Novel pulsed magnetization process for cryo-permanent magnets," *Physica C*, vol. 392–396, pp. 704–708, Oct. 2003.

[26] T. Coombs *et al.*, "A thermally actuated superconducting flux pump," *Physica C*, vol. 468, no. 3, pp. 153–159, Feb. 2008.

[27] Z. Jiang *et al.*, "Dynamic resistance of a high-T_c superconducting flux pump," *Appl. Phys. Lett.*, vol. 105, Sept. 2014. Art. no. 112601.

[28] Z. Jiang *et al.*, "Impact of flux gap upon dynamic resistance of a rotating HTS flux pump," *Supercond. Sci. Technol.*, vol. 28, no. 11, Sept. 2015. Art. no. 115008.

[29] C. W. Bumby *et al.*, "Development of a brushless HTS exciter for a 10 kW HTS synchronous generator," *Supercond. Sci. Technol.*, vol. 29, no. 2, Jan. 2016. Art. no. 024008.

[30] C. W. Bumby *et al.*, "Anomalous open-circuit voltage from a high-T_c superconducting dynamo," *Appl. Phys. Lett.*, vol. 108, no. 12, Mar. 2016. Art. no. 122601.

[31] Z. Jiang *et al.*, "A novel rotating HTS flux pump incorporating a ferromagnetic circuit," *IEEE Trans. Appl. Supercond.*, vol. 26, no. 2, Mar. 2016, Art. no. 4900706.

[32] C. W. Bumby *et al.*, "Frequency dependent behaviors of a dynamo-type HTS flux pump," *IEEE Trans. Appl. Supercond.*, vol. 27, no. 4, Jun. 2017, Art. no. 5200705.

[33] A. E. Pantoja *et al.*, "Impact of stator wire width on output of a dynamo-type HTS flux pump," *IEEE Trans. Appl. Supercond.*, vol. 26, no. 8, Dec. 2016, Art. no. 4805208.

[34] Z. Jiang *et al.*, "A rotating flux pump employing a magnetic circuit and a stabilized coated conductor HTS stator," *Journal of Magnetics*, vol. 21, no. 2, pp. 239–243, 2016.

[35] R. C. Mataira *et al.*, "Origin of the DC output voltage from a high-T_c superconducting dynamo," *Appl. Phys. Lett.*, vol. 114, no. 16, Apr. 2019. Art. no. 162601.

[36] C. W. Bumby *et al.*, "Through-wall excitation of a magnet coil by an external-rotor HTS flux pump," *IEEE Trans. Appl. Supercond.*, vol. 26, no. 3, Jun. 2016, Art. no. 0500505.

[37] R. Kulkarni, "Flux pump based field excitation for a high temperature superconducting synchronous generator," PhD thesis in Auckland University of Technology, 2017.

[38] J. Lee *et al.*, "Experimental analysis of charging characteristics of HTS FCs with HTS contactless rotary excitation device considering various HTS loads," *IEEE Trans. Appl. Supercond.*, vol. 28, no. 3, Apr. 2018, Art. no. 5203105.

[39] H. Jeon *et al.*, "Methods for increasing the saturation current and charging speed of a rotary HTS flux-pump to charge the FC of a synchronous motor," *IEEE Trans. Appl. Supercond.*, vol. 28, no. 3, Apr. 2018, Art. no. 5202605.

[40] H. Jeon *et al.*, "PID control of an electromagnet-based rotary HTS flux pump for maintaining constant field in HTS synchronous motors," *IEEE Trans. Appl. Supercond.*, vol. 28, no. 4, Jun. 2018, Art. no. 5207605.

[41] J. Lee, "Comparative characteristics of rotary HTS flux-pump considering rotational state of HTS load," presented at *Eur. Conf. Appl. Supercond.*, Geneva, Switzerland, 2017.

[42] J. H. Kim *et al.*, "Fabrication and charging test of HTS field windings using HTS contactless rotary excitation device," *IEEE Trans. Appl. Supercond.*, vol. 29, no. 5, Aug. 2019, Art. no. 5203207.

[43] S. Han *et al.*, "Charging characteristics of rotary HTS flux pump with several superconducting wires," *IEEE Trans. Appl. Supercond.*, vol. 29, no. 5, Aug. 2019, Art. no. 0603605.

[44] J. G. Storey *et al.*, "Optimizing rotor speed and geometry for an externally mounted HTS dynamo," *IEEE Trans. Appl. Supercond.*, vol. 29, no. 5, Aug. 2019, Art. no. 5202705.

[45] M. P. Oomen *et al.*, "Dynamic resistance in a slab-like superconductor with $J_c(B)$ dependence," *Supercond. Sci. Technol.*, vol. 12, no. 6, pp. 382–387, 1999.

[46] Y. B. Kim *et al*., “Critical persistent currents in hard superconductors,” *Phys. Rev. Lett.*, vol. 9, no. 7, Oct. 1962.

[47] J. Lee, “Development of contact-free current charging system for various high T_c superconducting magnet applications,” PhD thesis in Yonsei University, 2018.

[48] A. E. Pantoga, “Optimising rotor speed and geometry for an externally-mounted HTS dynamo,” presented at 25th *Int. Conf. Magnet Technol.*, Amsterdam, Netherlands, 2017.

[49] R. M.Walsh *et al*., “Characterization of current stability in an HTS NMR system energized by an HTS flux pump,” *IEEE Trans. Appl. Supercond.*, vol. 24, no. 3, Jun. 2014, Art. no. 4600805.

[50] W. Wang *et al.*, “Charging 2G HTS double pancake coils with a wireless superconducting DC PS for persistent current operation,” *IEEE Trans. Appl. Supercond.*, vol. 28, no. 3, Apr. 2018, Art. no. 0600804.

[51] Y. Gao *et al.*, “Design and study of a 2G HTS synchronous motor with brushless HTS flux pump exciters,” *IEEE Trans. Appl. Supercond.*, vol. 29, no. 5, Aug. 2019, Art. no. 5201705.

[52] Y. Gao *et al.*, “Design and study of a 2G HTS synchronous motor with brushless HTS flux pump exciters,” *IEEE Trans. Appl. Supercond.*, vol. 29, no. 5, Aug. 2019, Art. no. 5201705.

[53] Y. Gao, “Design, fabrication, and testing of a YBCO racetrack coil for an synchronous motor with brushless exciter,” presented at 26th *Int. Conf. Magnet Technol.*, Vancouver, Canada, 2019.

[54] G. D. Nam, “Design and performance analysis of a dynamo-type HTS flux pump for 10 kW superconducting generator,” presented at 26th *Int. Conf. Magnet Technol.*, Vancouver, Canada, 2019.

[55] H. -J. Sung *et al.*, “Design and heat load analysis for a 12 MW HTS wind power generator module employing brushless HTS exciter,” *IEEE Trans. Appl. Supercond.*, vol. 26, no. 4, Jun. 2016, Art. no. 5205404.

[56] H. -J. Sung *et al.*, “Design of a 12 MW HTS wind power generator including a flux pump,” *IEEE Trans. Appl. Supercond.*, vol. 26, no. 3, Apr. 2016, Art. no. 5206205.

[57] H. J. Park, “A Study on the torque disk structure design for MW- class low-speed high-torque HTS rotating machine,” PhD thesis in Changwon National University, 2017.

[58] T. D. Le *et al.*, “Design of indirect closed-cycle cooling scheme coupled with a cryocooler for a 3-MW-class high-temperature superconducting synchronous motor,” *IEEE Trans. Appl. Supercond.*, vol. 26, no. 4, 2016, Art. no. 5204904.

[59] T. D. Le *et al.*, “A compactly integrated cooling system of a combination dual 1.5-MW HTS motors for electric propulsion,” *Progr. Supercond. Cryogenics*, vol. 18, no. 4, pp. 25–29, 2016.

[60] J. H. Kim *et al.*, "Analysis of the mechanical characteristics of a 17-MW-class high-temperature superconducting synchronous motor," *J. Supercond. Nov. Magn.*, vol. 28, no. 2, pp. 671–679, 2015.

[61] J. M. Gere, *Mechanics of Materials*, 6th ed., INTERVISION, 2006.

[62] Material measurement laboratory in NIST. [Online] Available: http://cryogenics.nist.gov/MPropsMAY/G10%20CR%20Fiberglass%20Epoxy/G10CRFiberglassEpoxy_rev.htm

[63] Y. Iwasa, *Case Studies in Superconducting Magnets: Design and Operational Issues*, 2nd ed., New York, NY, USA: Springer-Verlag, 2009, pp. 248–250.

[64] Non-oriented electrical steel surface insulation, August. 22, 2017. [Online]. Available: http://www.posco.co.kr/homepage/docs/eng5/dn/company/product/e_electrical_pdf_2011.pdf

[65] Lorenz J, Fowler JT. "Synchronous generator subtransient reactance prediction using transient circuit coupled electromagnetic analyses and odd periodic symmetry," August 22, 2017. [Online]. Available: http://studylib.net/doc/18175531/synchronous-generator-subtransient-reactance.

[66] M. S. Sarma, *Electric Machine: Steady-State Theory and Dynamic Performance*, 2nd ed., Saint Paul, MN, USA: West Publishing Company, 1994, pp. 270–276.

[67] Spargo A, *et al.*, "Salient-pole rotor optimisations for synchronous generators using FEA software," presented at *the 2017 IEEE workshop on electrical machines design, control and diagnosis*, Nottingham, UK, Apr. 20–21, 2017.

[68] Y. Zhang, "Progress in production and performance of second generation (2G) HTS wire for practical applications," presented at *the IEEE 2013 int. conf. appl. supercond. electromagn. devices*, Beijing, China, 2013.

[69] H. S. Seol *et al.*, "Current control of WRSM considering magnetic saturation phenomenon," *IEEE Trans. Magn.*, vol. 52, no. 7, Jul. 2016, Art. no. 8204104.

[70] K. C. Kim, "A novel calculation method on the current information of vector inverter for interior permanent magnet synchronous motor for electric vehicle," *IEEE Trans. Magn.*, vol. 50, no. 2, Feb. 2014, Art. no. 7020504.

[71] W. Chai *et al.*, "Optimal design of wound field synchronous reluctance machines to improve torque by increasing the saliency ratio," *IEEE Trans. Magn.*, vol. 53, no. 11, 2017, Art. no. 8206604.

[72] S. W. Hwang *et al.*, "Torque improvement of wound field synchronous motor for electric vehicle by PM-assist," presented at *the 2016 IEEE Energy Conversion Congress and Exposition*, Milwaukee, WI, USA, Sept. 18-22, 2016.

[73] S. Han *et al.*, “Degradation of critical current in an HTS Tape with combined bending and torsion considering curvature of elliptical shape,” *IEEE Trans. Appl. Supercond.*, vol. 28, no. 3, Apr. 2018, Art. no. 8400405.

[74] S. Han *et al.*, “Degradation of critical current in an HTS coated conductor considering curvature of ellipse for rotating flux,” *Cryogenics*, vol. 89, pp. 141–146, 2018.

[75] Y. K. Kwon, “Development of HTS motor for industrial applications at KERI & DOOSAN,” presented at *2006 IEEE Power Engineering Society General Meeting*, Montreal, Que., Canada, 2006.

[76] H. J. Moon *et al.*, “Development of a MW-Class 2G HTS ship propulsion motor,” *IEEE Trans. Appl. Supercond.*, vol. 26, no. 4, Jun. 2016, Art. no. 5203805.

[77] H. J. Moon *et al.*, “An introduction to the design and fabrication progress of a megawatt class 2G HTS motor for the ship propulsion application,” *Supercond. Sci. Technol.*, vol. 29, no. 3, Feb. 2016, Art. no. 034009.

ABSTRACT IN KOREAN AND KEY WORDS

비접촉식 초전도 계자 여자기를 탑재한 1 kW 급 신개념 고온초전도 회전기 개발

제주대학교 일반대학원
에너지응용시스템학부 전기공학전공
김지형

본 논문은 영구 자석 기반의 회전형 고온초전도 플럭스 펌프를 응용한 비접촉식 여자 기술을 통하여 충전 및 운전되는 새로운 개념의 고온초전도 회전기의 세계 최초 구현을 위한 프로토타입 시스템의 설계, 제작 및 성능 시험에 관한 연구를 다룬다. 고온초전도체는 저온초전도체 대비 상대적으로 높은 온도 및 자기장에서 "영저항"의 특성을 보여 통전 전류의 감쇄없이 안정적으로 대전류 공급이 가능하므로, 저속 및 고토크 운전 특성을 갖는 해상 풍력발전기용 직접 구동식 발전기 및 전기 선박용 추진 전동기와 같이 고에너지 밀도가 요구되는 대용량 동기형 회전기 응용에 매우 적합하다. 고온초전도체 중 2세대 박막 도체인 희토류 바륨 구리 산화물 테이프는 회전자 계자 코일에 고밀도의 전류를 공급하여 기존 회전기와 동일 용량을 가지면서 좀 더 소형/경량화 된 시스템 제작을 가능하게 한다. 그러나 초전도 계자코일의 전원공급을 위해서는 종래의 접촉식 계자 여자 장치에 사용되는 슬립링/브러시 세트와 금속 전류도입선을 통한 상온의 직류전원 공급 장치와 극저온으로 냉각되는 계자코일 간의 전기적이며 기계적인 연결이 필수적으로 요구된다. 이러한 접촉식 여자 장치의 사용은 다음과 같은 기술적 한계를 지닌다.

1. 슬립링/브러시 세트의 기계적인 소음 및 진동으로 인한 빈번한 유지관리는 시스템의 신뢰성, 경제성 및 생산성을 저하시킨다.
2. 금속 전류도입선의 열손실은 국부적인 온도 상승을 야기하여 고온초전도 코일의 열적 안정성을 저하시킬 뿐만 아니라 증가된 극저온 냉각 부하 및 그에 따른 냉각 비용으로 시스템 효율성을 저하시킨다.

3. 직류 전원 공급을 위한 추가적인 외부 전원장치 및 발전기의 사용은 시스템의 효율성, 경제성, 및 유지보수성을 저하시킨다.

따라서 앞서 언급된 종래의 접촉식 여자 시스템의 문제를 근본적으로 해결하기 위해 비접촉 여자 시스템의 개발이 필수적으로 요구되는 실정이다. 이러한 관점에서 2세대 고온초전도 플럭스 펌프를 적용한 비접촉식 초전도 계자 여자기는 종래의 접촉식 여자기보다 다양한 산업 응용 분야에서 보다 효율적이고 안정적이며 경제적인 고온초전도 회전기를 구현할 수 있을 것으로 기대되고 있다. 고온초전도 회전자 내부에서 자체적으로 직류 전원 생성 및 공급이 가능한 온 보드 여자 시스템을 사용함으로써 접촉식 여자 시스템의 슬립링/브러쉬 세트, 금속 전류도입선 및 외부 전원장치를 제거할 수 있다. 계자 여자기로 사용된 고온초전도 플럭스 펌프는 상온에 위치한 종래의 접촉식 계자 여자 장치로부터 침투하는 열을 완전히 차단할 수 있으며 전류 여자 시 발생하는 줄 열을 크게 억제할 수 있다. 따라서 이 장치는 상온의 접촉식 여자 시스템과의 구조적인 연결을 제거하여 초전도 회전기 시스템 제작상의 비용절감 뿐만 아니라 운전상의 효율성, 신뢰성 및 경제성 향상을 가능하게 한다. 플럭스 펌프를 사용한 비접촉식 초전도 계자 여자기의 기술적인 장점은 다음과 같다.

1. 금속 전류도입선, 슬립링/브러시 조립 및 외부 전원을 제거하여 높은 시스템 효율성 및 경제성 제공.
2. 금속 전류도입선을 통한 열 침투를 완벽하게 제거하여 고온초전도 계자코일의 높은 전기적/열적 안정성 제공.
3. 금속 전류도입선의 상당량의 열손실을 제거함으로써 고온초전도 회전자 냉각 비용 대폭 절감.
4. 슬립링/브러시의 기계적인 마찰로 인한 소음 및 진동을 완벽하게 제거함으로써 뛰어난 시스템 내구성, 경제성, 유지보수성 및 생산성 제공.

이러한 고온초전도 플럭스 펌프의 기술적 장점을 통하여 고온초전도 회전기의 상업화 개발이 가능할 것으로 전망됨에도 불구하고, 현재까지 고온초전도 회전기 응용을 위한 초전도 비접촉식 여자 시스템의 실질적인 적용 및 구현은 수행되거나 보고되지 않고 있다. 따라서 본 논문에서는 비접촉식 초전도 계자 여자 기술을 적용한 고온초전도 회전기의 새로운 구조를 제안함과 더불어 세계 최초로 구현하고자 한다. 본 논문에서 제안하는 비접촉식 여자기는 이른바 회전형 자석 기반의 고온초전도 플럭스 펌프에서 비롯되었으며 초전도 직류 자석의 충전 및

운전을 위한 비접촉식 초전도 전원장치 중 하나이다. 본 논문에서 제안된 핵심 기술의 독창성 및 그에 따른 장점은 다음과 같다.

1. 회전기의 고온초전도 계자극과 비접촉식 초전도 계자 여자기의 직류 전원 생성부가 통합된 회전자 구조; 극저온 냉각 구조의 단순화를 통한 냉각 효율성 증대
2. DC 전원 여자를 위한 시변 자기장 생성을 위해 추가적인 회전 구동장치가 필요하지 않은 구조; 시스템 구조의 단순화를 통한 시스템 유지보수성 및 효율성 증대.
3. 상온의 원통형 시변 자기장 공급 장치를 가지는 구조; 상온에 위치한 영구자석의 제어를 통한 비접촉식 충전 전류 제어성 증대.
4. 비접촉식 초전도 계자 여자기용 회전자의 새로운 구조 (토로이달 형상 및 자성 재질의 구조물) 및 권선법 (무접합 직렬 다중권선); 한정된 크기의 회전자내에서 비접촉 충전 전류 증대.

본 논문에서는 고온초전도 회전기의 실질적인 운전을 위해 비접촉식 초전도 계자 여자기의 적용 가능성을 검증 및 평가하는 것을 목적으로, 계자 여자기의 직류 전원 생성부와 계자 코일이 통합된 고온초전도 회전자를 설계 및 제작하였으며 여자기의 비접촉 전류 충전 특성 및 출력 성능을 테스트하였다. 이를 위해 초전도 회전기의 기계적/열적/전자기적 특성을 고려한 1 kW 급 프로토타입 고온초전도 회전기의 설계를 수치 해석적 방법을 통하여 진행하였다. 또한 비접촉식 초전도 계자 여자기 개발을 위하여 외부 시변 자기장을 사용한 전류 펌핑 매커니즘을 도입하였으며 최종적으로 제작된 계자 여자기는 풀 스케일급의 초전도 계자코일과 결합하여 비접촉식으로 충전되는 전류의 충전 거동 특성과 성능을 실험적으로 분석 및 평가하였다. 테스트 결과, 부분적으로 수동적이긴 하지만 영구자석의 개수, 회전 속도 및 공극 길이의 변화를 통하여 특정 범위내에서 전류 제어가 가능함을 실험적으로 확인하였다. 또한 액체 냉매가 부족한 열적 과도상태에서 초전도 여자기의 자체적인 전류 제어 현상이 관측되었으며 이를 통해 전원 공급의 신뢰성 그리고 초전도 계자코일의 열적 안정도를 향상시킬 수 있을 것으로 사료된다.

최종적으로 개발된 회전기 시스템을 기반으로 개발 여자기와 회전기의 성능평가를 위한 M-G 세트를 구축하였다. 발전기 운전 시험을 통하여 초전도 계자 코일의 비접촉식 계자 충전을 성공적으로 검증하였으며 계자전류의 충전 거동을 실험적으로 분석하였다. 테스트 결과, 개발된 계자 여자기는 여자 손실을

현저히 감소시킴으로써 금속 전류도입선을 사용한 계자 충전시보다 시스템 효율을 약 1%가량 향상시킬 수 있음을 확인하였다. 또한, 400 rpm의 정격 회전 속도에서 1086 W의 발전기 출력 및 101 A의 계자 전류 충전을 달성하였 뿐만 아니라 2차원 전자기 유한 요소 해석 결과는 동일 운전 조건의 실험 결과와 약 90% 수준으로 일치함을 확인하였다. 발전기 왜형률은 1% 수준으로 측정되었으며 이를 통해 플럭스 펌프에 의한 비접촉식 충전전류의 맥동이 회전기 출력에 반영되지 않음을 실험적으로 확인하였다. 100 A급 초전도 계자 여자기의 비접촉식 충전 거동 특성을 분석한 결과, 개발 여자기는 특정 속도범위 내에서 영구 자석 발전기 또는 전동기와 같이 동작하기 때문에 정속도 운전이 필요한 응용분야에 적합할 것으로 판단된다.

핵심 주제어

고온초전도 회전기, 고온초전도 계자 코일, 무접합 직렬 다중권선, 비접촉식 전류 충전 기술, 비접촉식 초전도 계자 여자기, 2세대 고온초전도체, 토로이달 구조물, 회전형 고온초전도 플럭스 펌프

ACKNOWLEDGEMENTS

오랜 시간동안 많은 분들의 진심 어린 도움과 격려가 있어 박사 학위과정을 무사히 마칠 수 있었습니다. 저의 힘들었던 마음보다는 어렵고 불편한 일들 기꺼이 같이 견뎌 주신 마음들이 있었기에 이 자리까지 올 수 있지 않았나 생각합니다. 묵묵히 희생해주시고 기다려 주신 모든 분들께 이 지면을 통해 고개 숙여 감사의 인사를 드리고 싶습니다.

오랜 시간동안 못난 제자의 연구를 위해 전적으로 믿고 맡겨 주시는 김호민 교수님께 진심 어린 감사함을 전하고 싶습니다. 어떤 일을 하던지 주신 은혜에 부끄럽지 않은 제자가 되도록 노력하겠습니다. 앞으로도 많은 지도편달 부탁드리며 항상 건강하시길 바라겠습니다.

본 논문의 심사를 허락해 주시고 무사히 완성될 수 있도록 세심한 심사와 조언을 해주신 김일환 교수님, 김세호 교수님, 이개명 교수님께 진심으로 감사드립니다. 그리고 저희 전기공학과의 발전을 위해 물심양면 노력하시는 김호찬 교수님, 진영규 교수님, 그리고 학부시절부터 항상 격려해주시는 좌종근 교수님과 오성보 교수님께도 감사의 인사를 드립니다. 자랑스러운 제자가 되도록 노력하겠습니다.

먼 길을 마다하지 않고 본 논문의 심사를 허락해 주신 연세대 고태국 교수님께도 진심 어린 감사의 인사를 드립니다. 부족한 논문 채워 주시고 조언해주신 덕에 무사히 마칠 수 있었습니다. 항상 건강하시길 바라겠습니다.

학위를 무사히 마칠 수 있도록 오랫동안 도움주시고 이끌어 주신 신안산대 윤용수 교수님, 전적인 지원, 진심 어린 격려 아끼지 않으시는 전기연구원 조영식 박사님, 항상 본인 일처럼 신경 써 주시고 세심한 지도 아끼지 않으시는 두산중공업 박희주 박사님, 자주 뵙진 못하지만 항상 조언과 격려 주시는 서울대 한승용 교수님께 감사의 인사를 드립니다. 앞으로도 좋은 지도편달 부탁드리겠습니다. 항상 건강하시길 바라겠습니다.

국내 초전도 산업분야의 밝은 미래를 위해 국내외에서 좋은 연구 많이 해주고 계시는 송정빈 박사님, 김광록 박사님, 황영진 박사님, 최윤혁 박사님 에게도 감사의 인사를 드립니다. 항상 같은 눈높이에서 공감하고 응원해주신 점 많은 위로가 되었습니다. 형님들 본받아 좋은 연구자가 되도록 노력하겠습니다. 항상 감사드리며 응원하겠습니다.

항상 신세만 지는 친구들, 전기연구원 김형욱 박사와 윈디텍 이성훈 박사에게도 감사의 인사를 전합니다. 힘든 순간마다 너희들의 아낌없는 도움, 격려가 있어 먼 길을 완주할 수 있었던 것 같다. 지금 하고 있는 일에 최선을 다하는 만큼, 반드시 꽃피울 날이 올 거라 믿어 의심치 않는다. 항상 응원한다!

오랜 시간 동안 같은 연구과제 진행하면서 고생한 연세대 초전도응용연구실 연구원들에게도 감사의 인사를 전합니다. 과제 초창기에 고생 많았고 좋은 결실 얻은 이제열 박사, 이번에 같이 좋을 결실 맺는 전해룡 박사, 제일 오랫동안 고생해주고 있는 한승학 박사과정, 모두 고생 많았고 잘 따라주고 이끌어준 덕에 학위과정 무사히 마칠 수 있었던 것 같다. 앞으로도 잘 부탁하고 항상 응원한다!

후배 잘되라고 항상 여러모로 도움주시는 제주대 김도진 박사님, 제주국제대 부창진 교수님, 프리에너지 김대현 대표님, 거성전기 차우겸 대표님께도 감사의 인사를 드립니다. 힘들 때마다 형님들 계셔서 잘 이겨낼 수 있었던 것 같습니다. 하시는 일들 잘되도록 열심히 응원하며 돕겠습니다.

오랜 시간동안 동거동락하고 있는 제주대학교 전기공학과 식구들, 힘든 요구사항에 항상 최선을 다해주시는 조경훈, 장정민 조교 선생님과 밤낮으로 학과 발전을 위해 애쓰고 있는 각 연구실 동료분들에게도 감사의 인사 전합니다. 의젓한 버팀목이 되주시는 안진홍 선배님, 밤낮으로 고생이 많은 만큼 좋은 결실 있으실 겁니다. 항상 응원하겠습니다. 제일 오랜 시간 같이 고생해준 상헌이랑 민혁이, 궂은일 마다하지 않고 항상 잘 따라주고 도와줘서 여기까지 올 수 있지 않았나 싶다. 정말 고맙고 앞으로도 잘 해보자! 선배님들 잘 보필해주고 있는 기훈이, 현이, 창우, 민재 후배님들, 타지까지 와서 열심히 공부하고 있는 안크자야, 뭉크볼러, 줄만다크 후배님들도 열심히 한 보람 찾으시 길 바라며 항상 응원하겠습니다.

그리고 무엇보다 소중한 제주대학교 초전도응용연구실 식구들에게도 이자리를 빌어 감사의 인사를 전하고 싶습니다. 저의 부족한 부분을 항상 채워주는 너희들이 있어 학위과정을 무사히 마칠 수 있었던 것 같다. 연구실 초창기 무척이나 고생해준 사일이, 아직까지도 연구실 후배들 챙기는 네가 있어 언제나 든든하다. 너무 고맙고 항상 응원한다! 먼 곳 캐나다에서 항상 응원해주는 레탄등, 힘든 유학생활 잘 적응하고 맡은 바 최선을 다해주는 후릉, 묵묵히 잘 따라와주고 있는 정현이, 많은 살림살이 도맡아 챙겨주고 있는 홍비, 힘든 시기 잘 견뎌준 창주, 힘든 몸상태에도 궂은일 자처해준 재형이, 끝까지 남아 못난 형 보필해주고 있는 윤석이에게 진심으로 감사한 마음과 앞으로 더 발전하자는 격려와 다짐을 전합니다.

늦은 나이까지 공부하는 자식 뒤를 묵묵히 지켜주고 계시는 아버지와 어머니에게 감사하고 사랑한다는 말 전하고 싶습니다. 일찍 좋은 소식 전하지 못하여 죄송하고 앞으로 주신 은혜 보답하는 자랑스러운 아들이 되도록 노력하겠습니다. 오랫동안 건강하시길 진심으로 빌겠습니다. 그리고 바쁜 저 대신 보윤이, 민우 항상 아껴 주는 형님과 여동생 가족에게도 고맙다는 말 전하고 싶습니다. 형님은 빨리 좋은 보필 찾으셨으면 하고 지은이는 성훈이랑 아름이 잘 키우고 행복하길 바란다.

생전에 좋은 소식 드리지 못하여 항상 죄스러운 하늘에 계시는 장인어른, 장모님께도 늦은 감사의 마음을 전하고 싶습니다. 늦게나마 기뻐하실 모습 그려봅니다. 소연이, 보윤이, 민우 잘 보살피겠습니다. 걱정 마시고 편하시길 바랍니다. 그리고 바쁘다는 핑계로 자주 인사 드리지 못하는 태경 형님 가족, 소정처형 가족에게도 감사의 인사를 드립니다. 앞으로 자주 볼 수 있도록 노력하겠습니다.

마지막으로 한결같은 사랑을 주며 오랜 시간 희생해준 나의 아내 김소연에게 진심으로 감사하고 사랑한 다는 말 전하고 싶습니다. 너를 만나지 않았다면, 너와 결혼하지 않았다면 지금의 자리까지 올 수 없었을 것 같다. 너무 고마워! 앞으로 너의 시간에 집중할 수 있도록 열심히 외조하는 남편이 되도록 노력할께! 그리고 내 분신들, 첫째 보윤이, 둘째 민우에게 좋은 아빠가 되겠다는 다짐과 약속을 전합니다. 별 탈없이 건강히 자라주는 너희가 너무 자랑스럽다. 그동안 같이 보내지 못한 시간만큼 앞으로 너희들에게 집중할께! 사랑한다! 아들들!

이외에 제가 지금까지 성장하는데 있어 도움을 주신 모든 분들에게 미처 언급하지 못함을 죄송하게 생각하며 항상 최선을 다하는 모습으로 보답하도록 하겠습니다. 당찬 포부와 진지함은 퇴색하고 나태함과 요령으로 새로운 시작을 맞이하고 있는 것은 아닌지 다시금 마음을 가다듬으며 저를 아껴 주시는 마음에 누가 되지 않도록 성실히 살아가도록 하겠습니다.

2019년 12월

김 지 형 올림

VITA

Ji Hyung Kim
Applied Superconductivity Laboratory
Jeju National University
Department of Electrical Engineering
Mobile: +82-10-8664-8528
E-mail: jihkim@jejunu.ac.kr and rlawlgud54@naver.com

I. EDUCATION

[1] Jeju National University, Republic of Korea
B.S in Department of Electrical Engineering
March 1, 2003 — February 19, 2010

[2] Jeju National University, Republic of Korea
M.S in Department of Electrical Engineering (Prof. Ho Min Kim)
March 1, 2012 — February 20, 2014

[3] Jeju National University, Republic of Korea
Ph. D in Department of Electrical Engineering (Prof. Ho Min Kim)
March 1, 2014 — February 14, 2020

II. PUBLICATIONS

International papers (SCI)

[1] **J. H. Kim**, C.-K. Jwa, Y. S. Jo, S. K. Baik, Y. K. Kwon, and H. M. Kim, "Conceptual design of a field coil for 5 MW HTS synchronous machine," *Journal of superconductivity and novel magnetism*, vol. 26, no. 4, pp. 1247–1251, 2013.

[2] Y. H. Choi, O. J. Kwon, Y. -G. Kim, J. -B. Song, **J. H. Kim**, H. M. Kim, and H. Lee, "Thermal quench behaviors of no-insulation coils wound using GdBCO coated conductor tapes with various lamination materials," *IEEE Trans. Appl. Supercond.*, vol. 24, no. 3, Jun. 2014, Art. no. 8800105.

[3] **J. H. Kim** S. I. Park, T. D. Le, K. L. Kim, H. Lee, Y. -S. Jo, Y. S. Yoon, and H. M. Kim, "Characteristic analysis of various structural shapes of superconducting field coils," *IEEE Trans. Appl. Supercond.*, vol. 25, no. 3, Jun. 2015, Art. no. 5201105.

[4] **J. H. Kim**, S. I. Park, T. D. Le, H. C. Jo, Y. -S. Jo, Y. H. Choi, H. Lee, H. M. Kim, "Analysis of the mechanical characteristics of a 17-MW-class high-temperature superconducting synchronous motor," *Journal of Superconductivity and Novel Magnetism*, vol. 28, no. 2, pp. 671–679, 2015.

[5] K. L. Kim, Y. H. Choi, D. G. Yang, D. H. Kang, **J. H. Kim**, H. M. Kim, and H. G. Lee, "Analytical and empirical studies on the characteristic resistances of no-insulation GdBCO racetrack pancake coil under various operating currents," *Current Applied Physics*, vol. 15, no. 1, pp. 8–13, Jan. 2015.

[6] T. D. Le, **J. H. Kim**, S. J. Lee, G. -M. Lee, S. H. Kim, H. -C. Kim, and H. M. Kim, "Thermal Analysis of a cooling system for a high-temperature superconducting magnet system," *INFORMATION*, vol. 18, no. 7, pp. 3133–3139, 2015.

[7] T. D. Le, **J. H. Kim**, S. I. Park, D. -H. Kang, H. Lee, Y. -S. Jo, Y. S. Yoon, and H. M. Kim, "Thermal design of a cryogenics cooling system for a 10 MW-class high-temperature superconducting rotating machine," *IEEE Trans. Appl. Supercond.*, vol. 25, no. 3, Jun. 2015, Art. no. 3800305.

[8] H.-W. Kim, J. Hur, S. -W. Kim, D. -W. Ha, R. -K. Ko, J. -P. Hong, **J. H. Kim**, H. M. Kim, J. -H. Joo, S.-B. Kim, and Y. -S. Jo, "Electrical characteristic analysis according to contact resistance between turns of HTS Coil," *IEEE Trans. Appl. Supercond.*, vol. 26, no. 3, Apr. 2016, Art. no. 4601504.

[9] Y. H. Choi, J. -B. Song, D. G. Yang, Y. -G. Kim, **J. H. Kim**, H. M. Kim, and H. Lee, "Cooling performance and thermal characteristics of no-insulation GdBCO magnet cooled by a mixed cryogen cooling system," *IEEE Trans. Appl. Supercond.*, vol. 26, no. 4, Jun. 2016, Art. no. 4600705.

[10] T. D. Le, **J. H. Kim**, D. J. Kim, C. -J. Boo, Y. -S. Jo, Y. S. Yoon, K. Y. Yoon, Y. H. Choi, H. Lee, and H. M. Kim, "Design of indirect closed-cycle cooling scheme coupled with a cryocooler for a 3-MW-class high-temperature superconducting synchronous motor," *IEEE Trans. Appl. Supercond.*, vol. 26, no. 4, Jun. 2016, Art. no. 5204904.

[11] **J. H. Kim** , T. D. Le, D. J. Kim, C. -J. Kim, Y. -S. Jo, Y. S. Yoon, K. Y. Yoon, and H. M. Kim, "Economic analysis of a 1.5-MW-class HTS synchronous machine considering various commercial 2G CC tapes," *IEEE Trans. Appl. Supercond.*, vol. 26, no. 4, Jun. 2016, Art. no. 5206105.

[12] **J. H. Kim**, T. D. Le, D. J. Kim, C. -J. Boo, Y. -S. Jo, Y. S. Yoon, K. Y. Yoon, Y. H. Choi, H. Lee, and H. M. Kim, "Effects of stabilizer thickness of 2G HTS wire on the design of a 1.5-MW-class HTS synchronous machine," *IEEE Trans. Appl. Supercond.*, vol. 26, no. 4, Jun. 2016, Art. no. 5206705.

[13] Y. H. Choi, S.-G. Kim, S.-H. Jeong, **J. H. Kim**, H. M. Kim, and H. Lee, “A study on charge–discharge characteristics of no-insulation GdBCO magnets energized via a flux injector,” *IEEE Trans. Appl. Supercond.*, vol. 27, no. 4, Jun. 2017, Art. no. 4601206.

[14] **J. H. Kim**, C. J. Hyeon, S. H. Chae, D. J. Kim, C. -J. Boo, Y. -S. Jo, Y. S. Yoon, S. -G. Kim, H. Lee, and H. M. Kim, “Design and analysis of cooling structure on advanced air-core stator for megawatt-class HTS synchronous motor,” *IEEE Trans. Appl. Supercond.*, vol. 27, no. 4, Jun. 2017, Art. no. 5202507.

[15] S.-G. Kim, Y. H. Choi, D. G. Yang, S. -H. Jeong, **J. H. Kim**, H. M. Kim, Y. S. Choi, and H. Lee, “Study on thermal-quench behaviors of GdBCO coils wound with silicon grease as an insulation material,” *IEEE Trans. Appl. Supercond.*, vol. 27, no. 4, Jun. 2017, Art. no. 4700905.

[16] S. Han, J. Lee, H. Jeon, **J. H. Kim**, C. J. Hyeon, H. M. Kim, H. Kang, T. K. Ko, Y. S. Yoon, “Degradation of critical current in an HTS tape with combined bending and torsion considering curvature of elliptical shape,” *IEEE Trans. Appl. Supercond.*, vol. 28, no. 3, Apr. 2018, Art. no. 8400405.

[17] J. Lee, H. Jeon, S. Han, **J. H. Kim**, C. J. Hyeon, H. M. Kim, T. K. Ko, D. K. Park, and Y. S. Yoon, “Experimental analysis of charging characteristics of HTS field coils with HTS contactless rotary excitation device considering various HTS loads,” *IEEE Trans. Appl. Supercond.*, vol. 28, no. 3, Apr. 2018, Art. no. 5203105.

[18] H. Jeon, J. Lee, S. Han, **J. H. Kim**, C. J. Hyeon, H. M. Kim, D. K. Park, Y. D. Chung, T. K. Ko, and Y. S. Yoon, “Methods for increasing the saturation current and charging speed of a rotary HTS flux-pump to charge the field coil of a synchronous motor,” *IEEE Trans. Appl. Supercond.*, vol. 28, no. 3, Apr. 2018, Art. no. 5202605.

[19] **J. H. Kim**, C. J. Hyeon, H. L. Quach, S. H. Chae, J. Lee, H. Jeon, S. Han, T. K. Ko, Y. S. Yoon, H. -W. Kim, Y. -S. Jo, and H. M. Kim, “Characteristic analysis of a 1-kw-class HTS motor considering armature current information,” *IEEE Trans. Appl. Supercond.*, vol. 28, no. 4, Jun. 2018, Art. no. 5207205.

[20] H. Jeon, J. Lee, S. Han, **J. H. Kim**, C. J. Hyeon, H. M. Kim, H. Kang, T. K. ko, and Y. S. Yoon, “PID control of an electromagnet-based rotary HTS flux pump for maintaining constant field in HTS synchronous motors,” *IEEE Trans. Appl. Supercond.*, vol. 28, no. 4, Jun. 2018, Art. no. 5207605.

[21] C. J. Hyeon, **J. H. Kim**, H. L. Quach, H. -W. Kim, S. -W. Kim, Y. -S. Jo, and H. M. Kim, “Quench behavior of 2G HTS coils with polyimide film and MIT material under over pulse-current,” *IEEE Trans. Appl. Supercond.*, vol. 28, no. 4, Jun. 2018, Art. no. 4603906.

[22] S. Han, J. Lee, H. Jeon, T. K. Ko, H. M. Kim, **J. H. Kim**, C. J. Hyeon, and Y. S. Yoon, "Degradation of critical current in an HTS coated conductor considering curvature of ellipse for rotating flux pump," *Cryogenics*, vol. 89, pp. 141–146, Jan. 2018.

[23] J. M. Kim, J. C. Kim, Y. G. Kim, S. J. Hong, S. J. Park, **J. H. Kim**, H. M. Kim, Y. S. Choi, and H. G. Lee, "Investigation about the effects of metal-clad winding on the electromagnetic characteristics of the GdBCO racetrack coils in a time-varying magnetic field," *Results in Physics*, vol. 11, pp. 400–405, 2018.

[24] **J. H. Kim**, H. L. Quach, C. -J. Boo, Y. S. Yoon, H. Jeon, S. Han, T. K. Ko, H. -W. Kim, Y. -S. Jo, H. J. Park, J. Lee, H. Lee, and H. M. Kim, "Fabrication and charging test of HTS field windings using hts contactless rotary excitation device," *IEEE Trans. Appl. Supercond.*, vol. 29, no. 5, Aug. 2019, Art. no. 5203207.

[25] H. L. Quach, **J. H. Kim**, Y. S. Chae, J. H. Moon, J. H. Ko, S. H. Chae, J. H. Ahn, E. -H. Kim, S. H. Kim, Y. G. Jin, H. -W. Kim, Y. -S. Jo, and H. M. Kim, "Analysis on electrical and thermal characteristics of a no–insulation HTS coil considering heat generation in steady and transient states," *IEEE Trans. Appl. Supercond.*, vol. 29, no. 5, Aug. 2019, Art. no. 4701506.

[26] **J. H. Kim**, C. J. Hyeon, H. L. Quach, S. H. Chae, Y. S. Chae, J. H. Moon, C. -J. Boo, Y. S. Yoon, J. Lee, H. Jeon, S. Han, Y. -G. Kim, H. Lee, and H. M. Kim, "Design, analysis, and fabrication of salient field-pole for a 1-kW-class HTS rotating machine," *Cryogenics*, vol. 97, pp. 126–132, Jan. 2019.

[27] S. Han, J. Lee, H. Jeon, H. M. Kim, **J. H. Kim**, Y. -S. Jo, H. -W. Kim, T. K. Ko, and Y. S. Yoon, "Charging characteristics of rotary HTS flux pump with several superconducting wires," *IEEE Trans. Appl. Supercond.*, vol. 29, no. 5, Aug. 2019, Art. no. 0603605.

[28] H. L. Quach, **J. H. Kim**, C. J. Hyeon, Y. S. Chae, J. H. Moon, C. -J. Boo, H. -W. Kim, Y. -S. Jo, S. -W. Kim, and H. M. Kim, "Electrical and thermal analyses of a second generation high temperature superconducting magnet with vanadium III oxide and Kapton polyimide film insulation materials under an over-pulse current," *Supercond. Sci. Technol.*, vol. 32, no. 6, May 2019, Art. no. 065006.

International papers (SCOPUS)

[1] **J. H. Kim**, S.-I. Park, and H.-M. Kim, "Magnetic field analysis of the field coil for 10 mw class superconducting wind turbines," *Progr. Supercond. Cryogenics*, vol. 14, no. 3, pp. 18–22, 2012.

[2] **J. H. Kim** and H. M. Kim, "Electromagnetic design of 10 MW class superconducting wind turbine using 2G HTS wire," *Progr. Supercond. Cryogenics*, vol. 15, no. 3, pp. 29–34, 2013.

[3] S. I. Park, **J. H. Kim**, T. D. Le, and H. M. Kim, “Comparison of superconducting generator with 2G HTS and MgB2 wires,” *Progr. Supercond. Cryogenics*, vol. 15, no. 4, pp. 48–52, 2013.

[4] **J. H. Kim**, S. I. Park, S. H. Im, and H. M. Kim, “Analysis of mechanical characteristics of superconducting field coil for 17 MW class high temperature superconducting synchronous motor,” *Progr. Supercond. Cryogenics*, vol. 15, no. 3, pp. 13–19, 2013.

[5] T. D. Le, **J. H. Kim**, S. I. Park, and H. M. Kim, “Conceptual design of current lead for large scale high temperature superconducting rotating machine,” *Progr. Supercond. Cryogenics*, vol. 16, no. 2, pp. 54–58, 2014.

[6] **J. H. Kim**, S. I. Park, T. D. Le, and H. M. Kim, “3D electromagnetic design and electrical characteristics analysis of a 10-MW-class high-temperature superconducting synchronous generator for wind power,” *Progr. Supercond. Cryogenics*, vol. 16, no. 2, pp. 47–53, 2014.

[7] S. I. Park, **J. H. Kim**, T. D. Le, D. H. Lee, D. J. Kim, Y. S. Yoon, K. Y. Yoon, and H. M. Kim, “Analysis of losses within SMES system for compensating output fluctuation of wind power farm,” *Progr. Supercond. Cryogenics*, vol. 16, no. 4, pp. 57–61, 2014.

[8] T. D. Le, **J. H. Kim**, S. I. Park, D. J. Kim, H. G. Lee, Y. S. Yoon, Y. S. Jo, K. Y. Yoon, and H. M. Kim, “Transient characteristics of current lead losses for the large scale high-temperature superconducting rotating machine,” *Progr. Supercond. Cryogenics*, vol. 16, no. 4, pp. 62–65, 2014.

[9] T. D. Le, **J. H. Kim**, D. J. Kim, C. J. Boo, and H. M. Kim, “Status of the technology development of large scale HTS generators for wind turbine,” *Progr. Supercond. Cryogenics*, vol. 17, no. 2, pp. 18–24, 2015.

[10] T. D. Le, **J. H. Kim**, C. J. Hyeon, D. K. Kim, Y. S. Yoon, J. Lee, Y. G. Park, H. Jeon, H. L. Quach, and H. M. Kim, “A compactly integrated cooling system of a combination dual 1.5-MW HTS motors for electric propulsion.” *Progr. Supercond. Cryogenics*, vol. 18, no. 4, pp. 25–29, 2016.

[11] C. J. Hyeon, **J. H. Kim**, H. L. Quach, S. H. Chae, Y. S. Yoon, J. Lee, S. H. Han, H. Jeon, Y. H. Choi, H. G. Lee, and H. M. Kim, “Conceptual design of cooling anchor for current lead on HTS field coils,” *Progr. Supercond. Cryogenics*, vol. 19, no. 2, pp. 38–43, 2017.

[12] **J. H. Kim**, C. J. Hyeon, H. L. Quach, Y. S. Chae, J. H. Moon, C. -J. Boo, and H. M. Kim, “Conceptual design and analysis of rotor for a 1-kW-Class HTS rotating machine,” *Progr. Supercond. Cryogenics*, vol. 19, no. 4, pp. 45–50, 2017.

[13] H. L. Quach, **J. H. Kim**, Y. S. Chae, J. H. Moon, J. H. Ko, H. -W. Kim, S. -W. Kim, Y. -S. Jo, and H. M. Kim, “Analytical and numerical simulation on charging behavior of no-

insulation REBCO pancake coil," *Progr. Supercond. Cryogenics*, vol. 20, no. 4, pp. 16–19, 2018.

III. AWARDS

The outstanding paper awards

[1] "Technology trend of large-scale wind power generators" at Jeju Conference on IT & Power Engineering 2012 organized by The Korean Institute of Electrical Engineers (KIEE)

[2] "Analysis of mechanical characteristics of superconducting field coil for 17 MW class high superconducting synchronous motor" at 2013 Summer Conference on the Korea Institute of Applied Superconductivity and Cryogenics organized by The Korea Institute of Applied Superconductivity and Cryogenics (KIASC)

[3] "Comparison of superconducting generator with 2G HTS and MgB2 wires" at Progress in Superconductivity and Cryogenics (Vol. 15, No. 4, 2013) organized by The Korea Institute of Applied Superconductivity and Cryogenics (KIASC)

[4] "Technology and trend of superconducting generator for wind power" at Jeju Conference on IT & Power Engineering 2015 organized by The Korean Institute of Electrical Engineers (KIEE)

[5] "Current lead design for 3 MW class HTS rotating machine" at Jeju Conference on IT & Power Engineering 2015 organized by The Korean Institute of Electrical Engineers (KIEE)

[6] "Development trends of large scale HTS generators for wind turbine" at 2017 Autumn Conference on Korea Wind Energy Association organized by Korea Wind Energy Association (KWEA)

IV. PATENTS

[1] Ho Min Kim and Ji Hyung Kim, "열전도 개폐스위치를 이용한 초전도 회전기의 비상 냉각 제어 시스템 (Cooling system of super conduction generator using heat conduction switch gear)," Korea patent, App. No. 10-1376708, March 14, 2014.

[2] Ho Min Kim and Ji Hyung Kim, "극저온 냉매 강제순환용 초전도 극저온 펌프 (The pump for the cryogenic fluid circulation)," Korea patent, App. No. 10-1441875, September 12, 2014.

[3] Ho Min Kim and Ji Hyung Kim, "초전도 회전기 계자코일의 전류리드용 냉각 및 지지부재 (Apparatus for cooling current leads of a superconducting rotating machine)," Korea patent, App. No. 10-1518974, May 04, 2015.

[4] Ho Min Kim and Ji Hyung Kim, “초전도 회전기용 공심형 전기자코일의 자기냉동식 냉각구조 (Apparatus of cooling for stator coils of superconducting motor or generator),” Korea patent, App. No. 10-1518977, May 04, 2015.

[5] Ho Min Kim, Yong Soo Yoon, Ji Hyung Kim, Chang Ju Hyeon, Jeyull Lee, Haeryong Jeon, and Seunghak Han, “비접촉식 회전형 여자장치를 적용한 고온 초전도 회전기 (High temperature superconducting rotating machine with a contactless rotary excitation device),” Korea patent, App. No. 10-1766684, August 03, 2017.

[6] Ho Min Kim and Ji Hyung Kim, “고온초전도 회전기용 초전도 코일의 성능평가 장치 (Performance evaluation device of superconducting coil for high temperature superconducting rotating machine),” Korea patent, App. No. 10-1850042, April 12, 2018.

[7] Ho Min Kim and Ji Hyung Kim, “고온초전도 회전기용 초전도 코일의 성능평가 방법 (Performance evaluation method of superconducting coil for high temperature superconducting rotating machine),” Korea patent, App. No. 10-1924391, November 27, 2018.

[8] Ho Min Kim and Ji Hyung Kim, “고온초전도 회전기용 초전도 코일의 성능평가 장치 및 상기 장치에 의한 초전도 코일의 성능평가 방법 (Performance evaluation device and method of superconducting coil for high temperature superconducting rotating machine),” PCT patent, App. No. PCT/KR2018/004663, April 23, 2018.